

Universiteit
Leiden
The Netherlands

A multidirectional approach to optimize morphogenesis and barrier characteristics of human skin equivalents

Mieremet, A.

Citation
Mieremet, A. (2019, November 14). *A multidirectional approach to optimize morphogenesis and barrier characteristics of human skin equivalents*. Retrieved from https://hdl.handle.net/1887/80612

Version:	Publisher's Version
License:	Licence agreement concerning inclusion of doctoral thesis in the Institutional Repository of the University of Leiden
Downloaded from:	https://hdl.handle.net/1887/80612

Note: To cite this publication please use the final published version (if applicable).

Cover Page



Universiteit Leiden



The handle http://hdl.handle.net/1887/80612 holds various files of this Leiden University dissertation.

Author: Mieremet, A.
Title: A multidirectional approach to optimize morphogenesis and barrier characteristics of human skin equivalents
Issue Date: 2019-11-14

A multidirectional approach to optimize morphogenesis and barrier characteristics of human skin equivalents

Arnout Mieremet

A multidirectional approach to optimize morphogenesis and barrier characteristics of human skin equivalents

Arnout Mieremet

The research described in this thesis was performed at the Department of Dermatology of the Leiden University Medical Center (LUMC) and at the Division BioTherapeutics of the Leiden Academic Centre for Drug Research (LACDR), Leiden University (Leiden, The Netherlands). The research was financially supported by the Netherlands Organization for Scientific Research (NWO) domain Applied and Engineering Sciences (TTW) (project number 13151), which is partly funded by the Ministry of Economic Affairs and Climate Policy, and the Ministry of Education, Culture and Science.

Printing of this thesis was financially supported by Stichting Proefdiervrij and TTW.

Cover design: Arnout Mieremet
Layout and design: Renske Hortensius, persoonlijkproefschrift.nl
Printing: Ridderprint BV, www.ridderprint.nl

© Copyright, Arnout Mieremet, 2019
ISBN: 978-94-6375-545-0
All rights reserved. No part of this book may be reproduced in any form or by any means without permission of the author.

A multidirectional approach to optimize morphogenesis and barrier characteristics of human skin equivalents

Proefschrift

Ter verkrijging van de graad van Doctor aan de Universiteit Leiden,
op gezag van Rector Magnificus prof. mr. C.J.J.M. Stolker,
volgens besluit van het College voor Promoties
te verdedigen op donderdag 14 november 2019
klokke 11.15 uur

door

Arnout Mieremet

Geboren te Delft in 1990

Promotor:
Prof. dr. J.A. Bouwstra

Co-promotor:
Dr. A. El Ghalbzouri

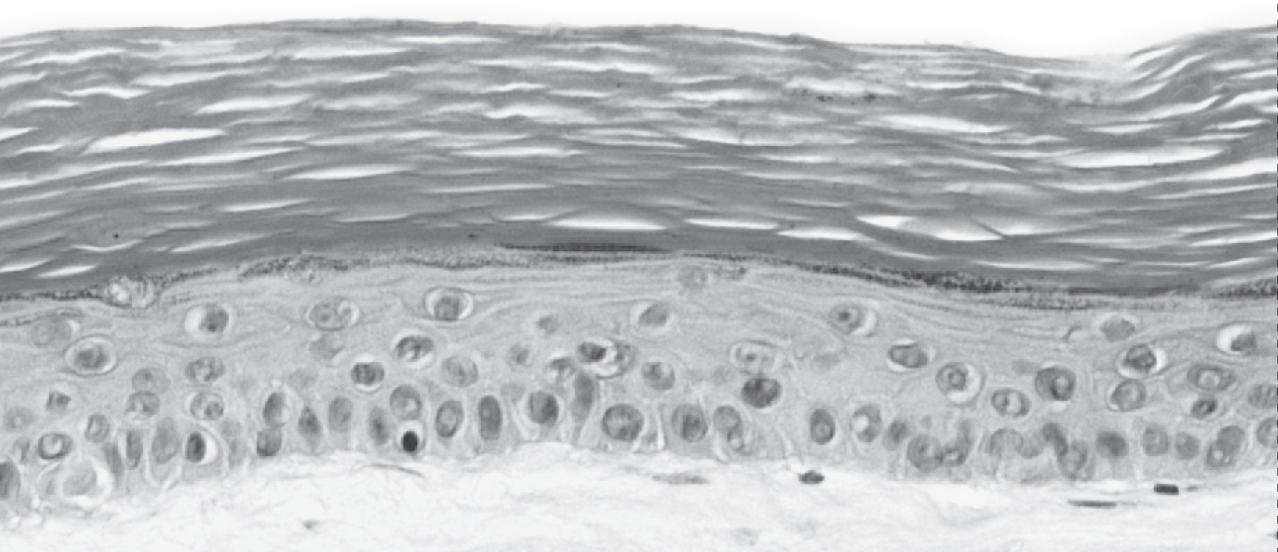
Promotiecommissie:
Prof. dr. H. Irth, *Leiden Academic Centre for Drug Research (LACDR)* (Chairman)
Prof. dr. A.P. IJzerman, *Leiden Academic Centre for Drug Research (LACDR)* (Secretary)
Prof. dr. M.H. Vermeer, *Leiden University Medical Center (LUMC)*
Prof. dr. M. Schäfer-Korting, *Free University Berlin*
Prof. dr. P.S. Hiemstra, *Leiden University Medical Center (LUMC)*
Dr. R. Rissmann, *Centre for Human Drug Research (CHDR)*

Contents

Chapter 1	Introduction	7
	Part I	
Chapter 2	Recapitulation of native dermal tissue in a full-thickness human skin model using human collagens	33
Chapter 3	Improved epidermal barrier formation in human skin models by chitosan modulated dermal matrices	57
	Part II	
Chapter 4	Characterization of human skin equivalents developed at body's core and surface temperatures	89
Chapter 5	Human skin equivalents cultured under hypoxia display enhanced epidermal morphogenesis and lipid barrier formation	113
Chapter 6	Unravelling effects of relative humidity on lipid barrier formation in human skin equivalents	139
Chapter 7	Shedding light on the effects of 1,25-dihydroxyvitamin D3 on epidermal lipid barrier formation in three-dimensional human skin equivalents	165
	Part III	
Chapter 8	Contribution of palmitic acid to epidermal morphogenesis and lipid barrier formation in human skin equivalents	193
Chapter 9	Multitargeted approach for the optimization of morphogenesis and barrier formation in human skin equivalents	223
Chapter 10	Summary and perspectives	251
Chapter 11	Nederlandstalige samenvatting (Dutch Summary)	270
	Curriculum Vitae	280
	List of publications	281

1

General introduction



1. Structure and function of the human skin

The human skin is the largest organ of the human body with an approximate total surface of 1.5 m^2 in adults and consists of the dermis and the epidermis. Main functions of the native human skin (NHS) are to limit water and heat loss from the body and to protect it against pathogenic entrees or external aggravations. To do so, there are multiple defence mechanisms of the skin including the microbial, chemical, immunological, and physical barrier [1]. These defence mechanisms are mainly located within or on top of the epidermis. Yet, deeper skin layers are as important for the development and maintenance of these barrier components.

1.1. Dermis and dermal-epidermal junction

The dermis ranges from dermal white adipose tissue, also referred to as hypodermis, to the reticular and papillary zones. In the dermal white adipose tissue, intradermal adipocytes are the main resident cells [2]. This layer is distinct from subcutaneous fatty tissue, which serves mainly as thermal insulation of the body as reported by Driskell *et al.* [2]. The skin resident adipocytes contribute to a range of skin functions including hair follicle regeneration and wound healing [3, 4]. Main parts of the dermis are the reticular and papillary region (**Fig. 1 a**). Resident cell types are fibroblasts, endothelial cells, and dermal dendritic cells. Fibroblasts were often regarded as a single cell type, but extensive characterization by Sorrel *et al.* [5], El Ghalbzouri *et al.* [6, 7], and Watt *et al.* [8-10] revealed morphological, transcriptional, and aetiological differences in the fibroblast population, indicating the existence of different subpopulations [11, 12]. This is often linked to their position in either the reticular or the papillary dermis. The deeper reticular dermis contains a low cell density and a compact extracellular matrix (ECM), which functions mainly as structural component contributing to skin strength and elasticity. Reticular fibroblasts have the ability to form structured collagens, being crucial for maintenance of the dermis [7]. Furthermore, reticular fibroblasts play a key role during wound healing [10]. The papillary layer contains a higher cell density with a loose dermal ECM. This dermal layer contributes mostly to reciprocal signalling with the epidermis, including maintenance of keratinocyte proliferation capacity and preservation of the dermal-epidermal junction (DEJ) [6, 9, 10]. All fibroblasts are of mesenchymal origin and therefore express vimentin which serves as biomarker to analyse the dermal distribution of fibroblasts. Other important features of the dermis are the presence of nervous, microvasculature, and lymphatic systems.

The DEJ links the epidermis with the underlying dermis in a characteristic rete ridges appearance. It is a continuous structural layer at the basal side of keratinocytes which is composed of hemidesmosomes, anchoring filaments, anchoring fibrils, and structural proteins [13, 14]. Main functions include the

formation of anchoring structures for proper polarity of keratinocytes, formation of a barrier between the epidermis and the dermis, and connecting the dermis to the epidermis. Both keratinocytes and fibroblasts contribute to the formation of the compact DEJ by deposition of structural and signalling proteins [15-18]. These various proteins are amongst others laminin 332, collagen types IV, VII, and XVII [19]. Small genetic alterations in genes carrying information for proteins of the basement membrane are causing serious skin diseases [20], emphasizing the importance of the DEJ.

1.2. Epidermis

The epidermis is the uppermost layer of the skin and contains four distinguishable layers, which from basal to apical side are the stratum basale (SB), the stratum spinosum (SS), the stratum granulosum (SG), and the stratum corneum (SC) (**Fig. 1 b**) [21-23]. Main cell types within the epidermis are keratinocytes, melanocytes, and Langerhans cells. Keratinocytes are the most abundant cells present in the epidermis and ultimately differentiate into corneocytes [24]. Keratinocytes display characteristic features for each epidermal layer to govern tissue preservation and homeostasis [25]. These are proliferation in the basal layer, early differentiation in the spinous layer, late differentiation in the granular layer, and terminal differentiation starting from the interface between SG and SC.

As the epidermis is renewed continuously, tight regulation of epidermal proliferation and differentiation is crucial for long-term viability. In the basal layer, keratinocytes divide both symmetrically and asymmetrically, regulating the epidermal renewal and maintaining the proliferative potential of the NHS, as reviewed by Poulson and Lechler [26]. A cellular biomarker for proliferation is the Ki67 protein. Postmitotic keratinocytes initiate the early differentiation program within the spinous layer, associated with loss of proliferative capacity and the expression of the keratins 1 and 10 [21]. Epidermal hyperproliferation or increased cell activation can trigger the expression of keratins 6, 16, and 17 at the expense of keratins 1 and 10. The keratin expression pattern in each epidermal layer is reviewed by Homberg and Magin [21]. When keratinocytes enter the late terminal differentiation program, these also express characteristic cornification proteins including (pro-)filaggrin, involucrin, and loricrin. At this differentiation stage, keratinocytes characteristically contain a high number of keratohyalin granules and lamellar bodies [27, 28]. The latter are secreted into the SG-SC interface, extruding a mixture of lipids and lipid processing enzymes. At the SG-SC interface, these lipids are processed to form a highly organized intercellular lamellar matrix. The SC consists of 10-20 cornified cell layers and is often analogized as brick-and-mortar structure, where the corneocytes are considered as bricks and the lipid matrix is regarded as mortar [29]. Severe protein cross linking occurs at the periphery of the corneocyte cell body creating a cornified

envelope, thereby establishing an impermeable appearance of the corneocytes. Also, these corneocytes are linked to each other by protein complexes, termed corneodesmosomes [28, 30, 31]. Around the cornified envelope, a lipid envelope is formed by a monolayer of lipids chemically linked to the cornified envelope proteins [32]. The lipid envelope functions as template for the orientation of the lipid lamellae within the intercorneocyte space. Importantly, this lipid matrix is the only continuous pathway for diffusion through the SC.

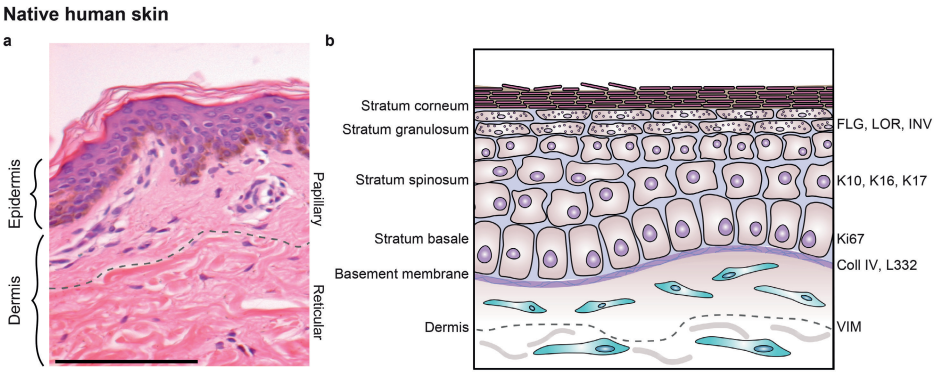


Figure 1. Morphology of the NHS. (**a**) Haematoxylin and eosin stained cross section of the native human skin. Characteristic is the presence of the dermis and epidermis with rete ridges structure. Scale bar indicates 100 µm (**b**) Schematic structure of NHS with indicated epidermal layers. Protein biomarkers for terminal differentiation (filaggrin (FLG), loricrin (LOR), involucrin (INV)), early differentiation (keratin 10 (K10)), epidermal activation (keratin 16 and 17 (K16, K17)), proliferation (Ki67), basement membrane (collagen type IV (Coll IV), laminin 332 (L332)), and fibroblast distribution (vimentin (VIM)) are indicated.

2. Barrier of the human skin

2.1. Functionality

The skin harbours multiple lines of defence including the physical, chemical, immunological, and microbial barrier [1]. The complete functionality of the skin is based on these four barriers. In this thesis the focus will be on the physical barrier of the skin, which is primarily formed by the SC. This uppermost skin layer functions as a physical barrier based on the almost impermeable structure of corneocytes together with a highly organized lipid matrix [33]. Functional properties of the skin can be evaluated with various experimental techniques, as reviewed by Cropek and Karande [34]. The inside-out barrier can be determined by measuring trans-epidermal water loss (TEWL) [35]. The outside-in functionality can be examined by compound diffusion studies. In these studies, topically applied compounds partition into the SC and subsequently diffuse through the various layers of the skin. Selection of appropriate molecules and detection methods allow measurement of compound diffusion rate. More details on the

barrier functionality, integrity, or absorption tests are described or reviewed elsewhere [36-38].

2.2. Lipid organization

Both the inside-out and outside-in skin barrier functionality are affected by the lipid matrix. This lipid matrix fills the intercorneocyte space entirely and is structured in both a lamellar and a lateral organization (**Fig. 2 a, b**). First observations of the lipid lamellar stackings were performed using freeze fracture electron microscopy [39]. Thereafter, the broad-narrow-broad stackings of lipid lamellae were visualized after ruthenium tetroxide fixation of the SC [40-42]. Even later, the SC was studied using small-angle X-ray diffraction (SAXD) [43]. This revealed two lamellar phases, one with a repeat distance of around 6 nm termed the short periodicity phase (SPP), and one with a repeat distance of around 13 nm termed the long periodicity phase (LPP) (**Fig. 2 c**) [43, 44]. The presence of the LPP contributes highly to the functionality of the skin barrier [45]. Within the lamellae, the lipid matrix is structured in the lateral organization (**Fig. 2 d**). The lipids can assemble in three different types of lateral organization, namely in the liquid, hexagonal, or orthorhombic lateral packing [46]. In human SC at physiological temperature, both liquid, hexagonal and orthorhombic domains co-exist, although most lipids assemble in the most dense orthorhombic lateral packing [47, 48].

2.3. Lipid composition

Major determinant for the lipid organization is the composition of the lipid matrix. There are various classes of lipids within the lipid matrix, of which the most prevalent are ceramides, free fatty acids, and cholesterol. Multiple subclasses of the ceramides and free fatty acids exist, as these lipids can vary in their headgroup architecture and carbon chain length. More details about the main lipid classes, will be covered in this section. Other lipid classes present in the SC lipid matrix (diglycerides, triglycerides) are described elsewhere [49].

2.3.1. Ceramides

Ceramides are sphingolipids consisting of a sphingoid base amide linked to a very long acyl chain, which contribute approximately 50-60% by mass to the SC lipid matrix [50, 51]. Ceramides vary in headgroup architecture, which determines in which subclass these are categorized [52]. The ceramide population consists of fifteen well characterized subclasses (**Fig. 3 a**). The ceramides have either a sphingosine (S), dihydrosphingosine (dS), phytosphingosine (P), or hydroxyl-sphingosine (H) sphingosine base. These are linked to a non-hydroxy (N) or an α-hydroxy (A) acyl chain classified as CER[non-EO], or to a ω-esterified linoleic acid (EO) acyl chain classified as CER[EO]. Ceramides containing an ω-hydroxy (O) acyl chain are classified as CER[O], which are present in low amounts in the

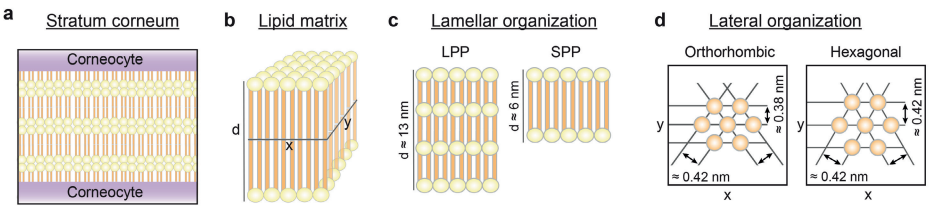


Figure 2. Lipid organization in the stratum corneum. (a) Illustration of the SC showing the intercorneocyte lipid matrix. **(b)** Schematic overview of the 3D lipid matrix shown by lipid head group regions as yellow spheres and hydrocarbon chain regions as orange columns. **(c)** Representation of the lamellar organization. Long periodicity phase (LPP) and short periodicity phase (SPP) are characterized by a specific repeat distance (d). **(d)** Lateral organization of the hydrocarbon chains of the lipids. The orthorhombic organization is a very dense ordered packing, whereas the hexagonal organization is less dense ordered. These are characterized with a specific distance between the hydrocarbon chains.

lipid matrix as free CER[O], as the majority is esterified to cornified envelope proteins contributing to the lipid envelope. Several other ceramide subclasses have been identified recently (e.g. dihydroxy sphinganine (CER[T]) and 1-O-acylceramides (CER[1-O-E])), but these are present in low quantities in the SC and/or have a yet to be discovered biophysical role [53-55]. Furthermore, each ceramide subclass comprises of a wide carbon chain length distribution, resulting in numerous ceramide entities within a single subclass [56-59]. The total ceramide carbon chain lengths range from C32 (ceramides with 32 carbon atoms) to C56 for CER[non-EO] and C64 up to C78 for CER[EO] [53, 60, 61]. Additionally, various levels of unsaturation exist, resulting in the presence of unsaturated ceramides in the lipid matrix of the SC [57, 62].

2.3.2. Free fatty acids

The free fatty acids (FFAs) contribute approximately 15-20% by mass to the SC lipid matrix [50, 51]. FFAs cover a wide range of entities, due to variability in the level of hydroxylation (non or hydroxy), unsaturation (non, mono or poly), and carbon chain length (C12-C36) (**Fig. 3 b**) [60, 63, 64]. Most abundant FFAs are the saturated FFAs with a carbon chain length of C24 and C26 [60, 63, 65]. The amount of unsaturated or hydroxy FFAs is much lower as compared to saturated FFA, of which oleic (18:1) and linoleic (18:2) FFA are the most abundant unsaturated FFAs in the SC [62, 66, 67].

2.3.3. Cholesterol

The main sterol in the epidermis is cholesterol. By mass, cholesterol contributes 20-25% to the weight of the SC lipids (**Fig. 3 c**) [50, 51]. Characteristic for the epidermis is the high amount of cholesterol sulphate. This derivative is present in

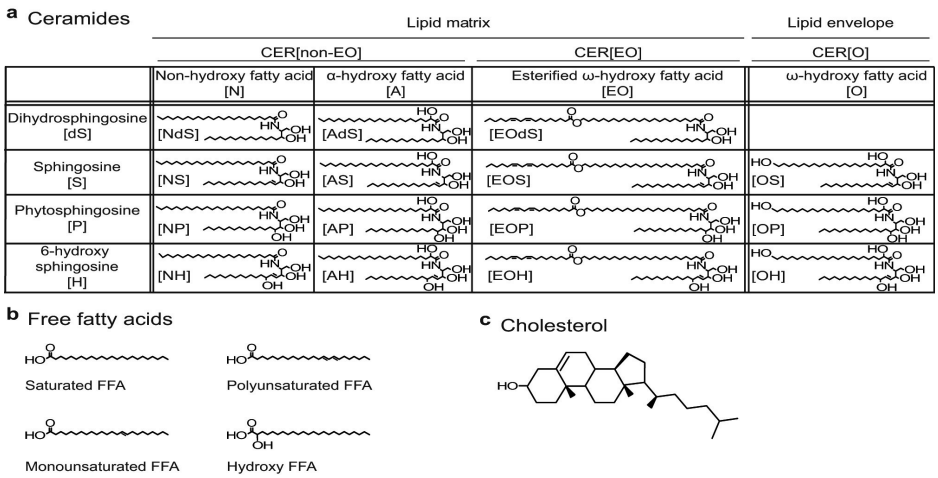


Figure 3. Molecular structures of main lipid classes in the SC. (a) Tabular overview of the fifteen most common ceramide subclasses in the SC with their structural formulas in the hairpin conformation. Nomenclature according to Motta *et al.* [52] is indicated. **(b)** Overview of the four main FFA subgroups covering saturated, monounsaturated, polyunsaturated, and hydroxy FFAs. **(c)** Molecular structure of cholesterol.

the SC 2-5% by mass and plays an important signalling role during desquamation of the corneocytes [68-70].

2.4. Biosynthesis of barrier lipids

The lipid composition is a result of diverse biosynthesis steps occurring in the viable epidermis [71]. Reviews by Breiden and Sandhoff [72], Elias and Feingold [73], Rabionet *et al.* [74], Van Smeden *et al.* [67], and Kihara [50] describe in detail the biosynthesis of major barrier lipids in the skin. In essence, the diversity in chain length of FFAs and ceramides is a result of lipid processing by the elongation of very long fatty acids (ELOVL) family [50]. These enzymes have a specificity to a small range of carbon chain lengths and are expressed in the endoplasmic reticulum of keratinocytes [56]. Synthesis of ceramides occurs in a cascade which is initiated by serine palmitoyltransferase, ultimately followed by members of ceramide synthase family yielding CER[dS]. Other subclasses (e.g. [S], [P], [H]) are generated after processing of ceramide CER[dS] by dihydro-Cer desaturase 1 (DES1) and 2 (DES2) or yet to be identified mediators. Esterification of linoleic acid forming CER[EO] is processed by several enzymes including PNPLA1 and CYP4F22, although additional involvement of unknown enzymes cannot be excluded [50, 75]. After synthesis of ceramides, these are processed by addition of a glucose or phosphocholine group to the ceramide by glucosylceramide synthase (GCS) and sphingomyelin synthase (SMS) respectively. These are packed in lamellar bodies, which release their content during terminal differentiation

at the SG-SC interface. There, the precursor lipids are terminally processed by β-glucocerebrosidase (GBA) or acid sphingomyelinase (aSMASE) producing ceramides for the lipid matrix.

3. Essentials of human skin equivalents

3.1. Historical perspective

Human skin equivalents (HSEs) are the most sophisticated three-dimensional (3D) models of NHS, which were developed during years of research. Already in the 1940's and 1950's it was reported that skin biopsies could be cultured for a limited lifetime *in vitro* [76, 77]. Isolation and culturing techniques for primary skin cells harvested from these biopsies were developed soon thereafter. A major technical breakthrough for maintaining viability of primary skin cell cultures was reached using irradiated 3T3 cells as feeder layer [78]. These keratinocyte monocultures, later also developed without feeder layer, provided robust experimental tools to study skin cell behaviour of human origin. Next, 3D skin equivalents were developed to study the stratification of the epidermis using air-exposed methods, which created skin model types more related to the native structure [79-81]. Thereafter, further developments were made in cell culture techniques to generate advanced HSEs, as described by Niehues *et al.* [1].

3.2. Types of human skin equivalents

Various types of HSEs were developed and these can be categorized based on their method of generation and cell types used (**Fig. 4**). The first category covers the epidermal models, which are the most uncomplicated version of a 3D HSE. This HSE type is generated with keratinocytes cultured on an acellular component (inert filter or collagen coated inert filter), which form a stratified epidermis at the air-liquid interface. Due to their quality and simplicity, epidermal models have many applications, as described in section 4 *Applications of human skin equivalents*. The second category covers the full thickness models (FTMs). These consists of a dermal and epidermal compartment, of which the former is made of ECM harbouring fibroblasts and the latter contains keratinocytes which over time form a fully stratified epidermis. FTMs are generated with a wide variety in dermal ECMs, such as decellularized/de-epidermized dermis (DED) [82-84], collagen type I [85-88], collagen mixed with glycosaminoglycans and/or chitosan [89-92], fibrin [93-96], fibroblast-derived matrix [7, 85, 97], and synthetic polymers [93] as reviewed by Sriram *et al.* [98]. Due to the presence of the two major cell types, the interaction between the dermis and epidermis can be studied thoroughly. Moreover, FTMs are widely characterized and extensively applied for research purposes. For these reasons, this HSE type has been selected for the studies described in this thesis. A third category is attributed to advanced HSEs. This involves co-cultures of more than two cell types, for example with melanocytes,

Langerhans cells, dermal dendritic cells, skin resident T-cells, neuronal cells, or endothelial cells as microvasculature [99-102]. Additionally, HSEs with topically applied bacterial strains can be generated to mimic host-microbiome interactions or epidermal wound infections [103, 104]. These advanced co-cultures better resemble the anatomy of NHS, although due to their complexity these models are less suitable for barrier related studies. More details about the different types of HSEs are described in various review articles [105-109].

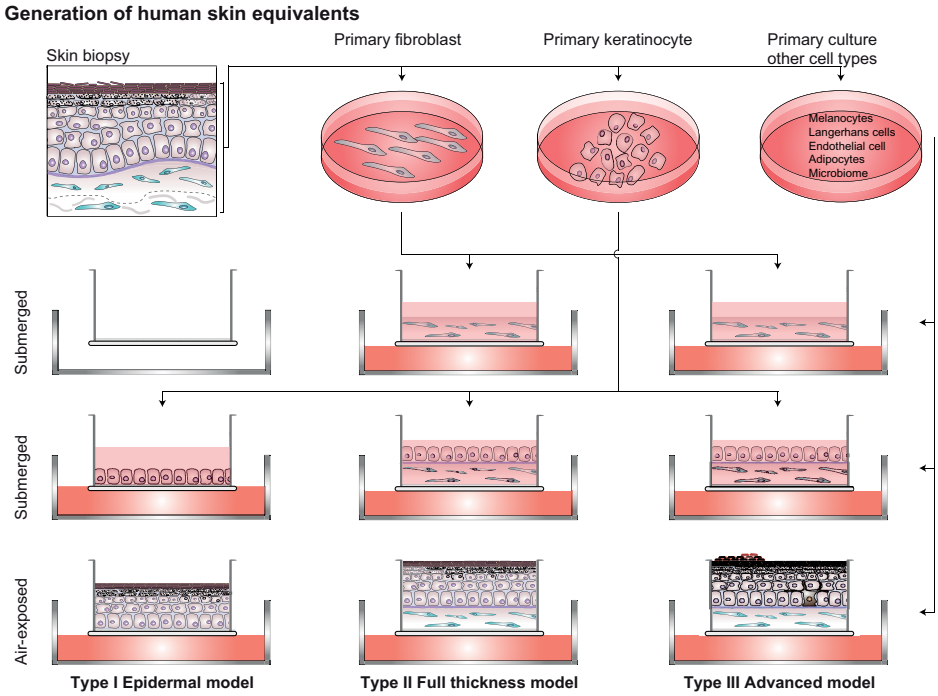


Figure 4. Generation of various types of HSEs. Primary cells are isolated from a skin biopsy and cultured in Petri dishes. Type I epidermal models are generated by seeding primary keratinocytes on an inert filter and culturing these submerged and subsequently at the air-liquid interface. Type II full thickness models are generated by seeding fibroblast in a collagen matrix, after which keratinocytes are seeded onto the dermal equivalents and cultured submerged and subsequently air-exposed. Type III advanced models are generated by equal procedures as type II FTMs with incorporation of additional cell types (illustrated with melanocyte and microbiome) harvested from the skin biopsy.

4. Applications of human skin equivalents

HSEs are versatile *in vitro* tools with applications not limited to a single field. Researchers use HSEs to obtain novel insights on human skin physiology and pathophysiology (e.g. wound healing, skin aging, atopic dermatitis, psoriasis

or cutaneous malignancies). Pathophysiologic conditions can be induced by utilization of disease specific cells (harbouring mutations/genetic aberrations) or by mimicking the inflammatory environment through addition of disease specific cytokines. Pathophysiological HSEs are primarily used to obtain a better understanding of pathogenesis and for low-throughput drug screening purposes in a physiological relevant 3D model [96, 102, 110-112].

Besides these applications, HSEs are widely used as *in vitro* tools for toxicity screenings. European Union legislation banned *in vivo* testing for cosmetic products, according to the seventh amendment of EU Cosmetics Directive 76/768 EEC, which entered into force in 2009. In line with this ban, *in vitro* testing is highly supported in the Registration, Evaluation, Authorisation and Restriction of Chemicals (REACH) legislation, or mandatory depending on the quantity produced per year. Methods for testing of chemicals are validated by the European Centre for the Validation of Alternative Methods (ECVAM) and are described in Organisation for Economic Co-operation and Development (OECD) test guidelines (TG) [113].

Toxicity screenings are performed with HSEs to determine skin corrosion and skin irritation, according to OECD TG 431 and OECD TG 438, respectively. Several validated commercial available models are used for these tests, including the EpiDerm™, EpiSkin™, SkinEthic™, EpiCS, Phenion® Full Thickness Skin Model, and LabCyte EPI-MODEL [114-116]. For each of these, specific adjustments in the OECD TG are described to maintain the defined reliability (based on within-laboratory validation, between-laboratory reproducibility) and predictive capacity (based on sensitivity, specificity and accuracy) [117-119]. In most assays, the single qualitative endpoint is based on mitochondrial metabolic activity (MTT assay). This is shown to be a robust and reproducible endpoint, yet non-specific. Another toxicological screening can be performed to predict skin sensitization [120]. However, skin sensitization is a result of intertwined multifactorial events, which include the covalent binding of the sensitizer, activation of keratinocytes, activation and migration of dendritic cells, and proliferation of antigen-specific memory T-cells [121]. These multiple key events are described in the Adverse Outcome Pathway (AOP) for skin sensitization [122]. Therefore, HSEs are utilized to predict the sensitization potential [123, 124], complementary to additional *in vitro* experiments to accurately predict this specific toxicity [125].

Although toxicological screenings using HSEs often outperform animal testing, the concordance of *in vitro* data to *in vivo* data is 70-75% in accuracy for skin irritation, which needs to be improved [126]. Furthermore, increased details on toxicity is obtained through an integrated approach on testing and assessment (IATA) that allow for the consideration of complementary information (e.g.,

physicochemical properties, QSARs), aiming to further minimize the use of animal testing [115, 127]. Besides the many commercially available models, there are HSEs which are developed at academic institutes, which include the HSEs described in this thesis. Also, an elegant initiative is the open source reconstructed epidermis (OS-REp), which is accompanied with openly accessible protocols for tissue production and is compatible for toxicity screenings [128, 129].

5. Morphology of human skin equivalents

The morphology of HSEs is comparable to that of NHS in many aspects. This includes the presence of the four distinguishable epidermal layers, the formation and maintenance of the basement membrane, and depending on HSE type the presence of fibroblasts in an ECM (**Fig. 5 a**). Morphogenesis can be studied using expression of protein biomarkers (**Fig. 5 b**). Nevertheless, there are also differences in morphogenesis between HSEs and NHS. In the dermis of HSEs, the presence of a homogeneous mesenchymal cell type contrasts with the heterogeneous mesenchymal cell population in the dermis of NHS [6, 98]. Moreover, a common difference is the lack of rete ridges present between the dermis and epidermis. Epidermal proliferation rates in HSEs are often increased as compared to NHS, also linked to epidermal hyperplasia. In various HSEs, the epidermis displays an activated or stressed phenotype. This activation can be reduced by modulation of the dermal equivalent (number of fibroblasts, ECM composition) [82, 97, 130]. Also, the late differentiation is altered, as the granular cells are enlarged in the HSEs and/or a higher number of granular cell layers is observed. Furthermore, involucrin is expressed in the spinous layer as well as in the granular layer in HSEs, in contrast to a restricted expression in the granular layer in NHS [85]. Due to the lack of desquamation in HSEs, the number of corneocyte layers accumulates over time. Therefore the thickness of the SC in HSEs mimics that of NHS only during a limited time period [132].

6. Barrier of human skin equivalents

The lipid barrier of HSEs is similar to that of NHS in several aspects, including the presence of all main SC lipid classes, within each class the presence of all subclasses, and the formation of the lamellar lipid organization [85, 131]. However, also differences were detected in the lipid barrier formation of HSEs as compared to NHS, thereby reducing the resemblance to NHS [133, 134]. In this section, more information is provided on the differences between HSEs and NHS regarding the barrier functionality, lipid organization, lipid composition, and epidermal lipid biosynthesis.

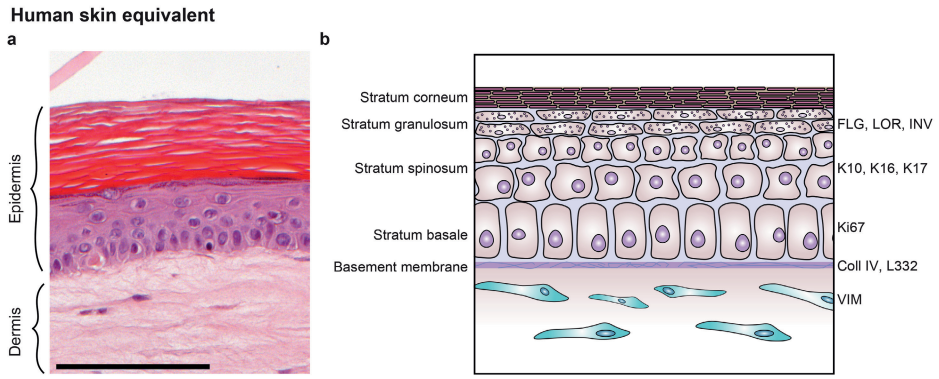


Figure 5. General morphology of HSEs. (**a**) Haematoxylin and eosin stained cross section of a FTM. Characteristic is the presence of the dermis and epidermis with a flat dermal-epidermal junction. Scale bar indicates 100 µm. (**b**) Schematic structure of a FTM with indicated protein biomarkers of terminal differentiation (FLG, LOR, INV), early differentiation (K10), epidermal activation (K16, K17), proliferation (Ki67), basement membrane (Coll IV, L332), and fibroblast distribution (VIM).

6.1. Functionality

The outside-in barrier functionality of HSEs has been examined by diffusion studies. These revealed an elevated penetration of compounds as compared to NHS, irrespective of the type of HSE [85, 135-138]. When comparing the various (commercial available) HSEs to each other, differences in barrier functionality were also detected, ascribed to variations in cell culture methodology or cell types present in these HSEs [85, 135-138]. Remarkably, barrier functionality in HSEs is reduced even when the thickness of the SC exceeds several times that of NHS [134]. The performance of the skin barrier of HSEs resembles that of NHS better for hydrophilic compounds and worse for hydrophobic compounds [139]. In contrast to the flux values, the qualitative barrier of HSEs concerning the rank order of compound diffusion resembles that of NHS to a high extent [140]. Small differences in permeability between compounds are more difficult to assess accurately using HSEs, which could also be limitation for *in vitro* testing of mixtures or cosmetic formulations [141, 142]. The inside-out barrier functionality is also altered, as the TEWL is higher *in vitro* as compared to *in vivo* [143].

6.2. Lipid organization in human skin equivalents

Investigations on the underlying factors regarding the reduced barrier functionality primarily focused on the SC. The protein barrier was investigated by assessment of the cornified envelopes of NHS and HSEs. These studies showed a high similarity in protein composition (loricrin, small proline-rich proteins, involucrin and filaggrin) [144, 145], which indicates a functional cornified envelope in HSEs. As a result, compound diffusion through the SC occurs via

the intercorneocyte space, as shown by confocal laser scanning microscopy [131, 146]. The lipid organization in the SC of HSEs also has been examined. Several similarities and some differences were observed, in part explaining the compromised barrier functionality of HSEs compared to NHS. When considering the lamellar organization, the LPP is detected in HSEs, likewise as in NHS. However, the repeat distance of the LPP is shorter in HSEs compared to NHS [85]. Furthermore, the SPP has not been detected in HSEs [43]. Studies on the lateral organization showed that the lipids assemble predominantly in the hexagonal packing in HSEs, in contrast to a predominant formation of the orthorhombic packing in the SC of NHS [85, 147]. Noteworthy, these alterations in lipid organization were also observed in skin biopsies cultured for a limited time period, emphasizing the effects of *in vitro* conditions on the induction of the aberrant lipid matrix organization [148-150].

6.3. Lipid composition in the stratum corneum of human skin equivalents

As the lipid organization is directly related to the composition, the lipid profile in the SC of HSEs was compared to that of NHS. This revealed the presence of the same lipid classes and subclasses within the SC of HSEs and NHS [85, 131]. However, several deviations between the lipid profiles were observed after detailed examination of the lipid matrix composition.

6.3.1. Ceramide composition in human skin equivalents

Ceramides vary in headgroup architecture, carbon chain length, and degree of unsaturation. These characteristics were initially analysed with gas chromatography and/or thin layer chromatography in NHS and HSEs. More recently, liquid chromatography coupled to mass spectrometry (LC-MS) has been employed [57, 60, 65, 151]. Similar in NHS and HSEs is the presence of all major subclasses and the presence of a wide range in carbon chain lengths in the SC lipid matrix. The most evident difference is the subclass profile, which includes a reduced presence of subclass [NP] and an increased presence of subclasses [NS], [AS], and [EOS] [62]. Also, the distribution of ceramide carbon chain length is different in HSEs compared to NHS, shown by the increased presence of short chain (≤C38) CER[non-EO] and the decreased presence of long chain (≥C44) CER[non-EO] [60]. This contributes to the reduction in mean carbon chain length of CER[non-EO] [60]. Furthermore, the level of C34-CER[non-EO] is increased in HSEs, which is correlated with an impaired barrier functionality *in vivo* [61, 152]. The CER[EO] carbon chain length distribution in the SC of HSEs closely resembles that of the SC in NHS [60]. Importantly, the level of monounsaturated ceramides is increased in HSEs compared to NHS [57, 62]. Additionally, the composition of CER[EO] was shown to be altered due to the esterification of the oleic acid instead of linoleic acid in HSEs [153].

6.3.2. Free fatty acid composition in human skin equivalents

Free fatty acids vary in headgroup architecture, carbon chain length and degree of unsaturation. These features were assessed in HSEs and compared to NHS, which revealed that FFAs are present with a wide carbon chain length distribution in the SC of HSE [62]. However, the FFA chain length distribution profile was altered, as well as a higher level of monounsaturated lipids FFAs in the SC of HSEs as compared to that in NHS [60, 154]. Furthermore, the level of FFAs in the SC lipid matrix is generally lower in HSEs [155]. The presence of hydroxy FFAs is still undetermined in HSEs [60].

6.3.3. Sterol composition in human skin equivalents

Although detailed investigations with LC-MS on the presence of cholesterol have not yet been performed, results obtained with thin layer chromatography indicated that there are high similarities in sterol composition in HSEs and NHS [85]. However, the presence of lanosterol, a precursor of the cholesterol biosynthesis pathway [156], is increased in HSEs [134]. Furthermore, the presence of cholesterol esters is much lower in HSEs [134]. Nevertheless, the presence of cholesterol in the lipid matrix of HSEs seems to resemble that of NHS better than the other major lipid classes, therefore cholesterol biosynthesis will not be further investigated in this thesis.

6.4. Barrier lipid biosynthesis in human skin equivalents

As the lipid composition in HSEs is altered, recent studies focussed on examination of the *in vitro* biosynthesis of barrier lipids. The ceramide subclass profile is a result of the orchestrated functionality of ceramide processing enzymes. Terminal ceramide processing in HSEs is performed by aSMASE and GBA, which are expressed similarly in NHS, HSEs, and skin explant models [149]. Furthermore, it has been shown that the expression of the lipid desaturase enzyme SCD-1 is upregulated in HSEs and skin explant models [62, 149, 154]. Characterization of biosynthesis pathways is of interest to determine novel promising targets for advanced optimization approaches and to gain better understanding on *in vitro* lipid barrier formation.

7. This thesis

7.1. Background

Preclinical screening of novel therapeutic compounds is currently performed using HSEs which mimic many properties of NHS, as described above and reviewed extensively before [1, 109, 157-160]. Furthermore, these have been used for studying diseased skin conditions, including but not limited to atopic dermatitis, hypertrophic scar formation, epithelial cancers, and genetic skin disorders [110,

161-164]. However, a limitation in preclinical studies is the compromised barrier formation which leads to a decreased barrier functionality [62, 85, 131, 165].

7.2. Objectives

The primary aim of this thesis is to determine whether epidermal morphogenesis and barrier formation of HSEs can mimic that of NHS better by optimization of *in vitro* culture conditions. In our analysis we used state-of-the-art experimental techniques to evaluate the dermal and epidermal morphogenesis, barrier formation, and functionality. The main objectives are:

a) to determine whether the dermal ECM affects epidermal lipid barrier formation
b) to investigate if culture conditions during generation of HSEs affect lipid barrier formation
c) to generate HSEs with optimized dermal ECM and external culture conditions in combination with improved cell culture medium composition

7.3. Outline

Part I focusses on studies of the dermal ECM in HSEs. Investigations on the effect of the non-human collagen source used for the dermal ECM is described in **chapter 2**. A method is reported to obtain soluble collagen from human abdominal dermis followed by utilization of it as a dermal ECM in FTMs. The so-called human collagen full thickness models (hC-FTMs) were developed and compared to the original FTM in which the dermal ECM consists of collagen isolated from rat tail tendons. Evaluations are described for dermal and epidermal morphogenesis, and the formation of the lipid barrier.

In **chapter 3 t**he effect of modulation of the dermal ECM by addition of the biopolymer chitosan is described. This biopolymer is added to the collagen solution in a single suspension, thereby establishing a novel dermal ECM. The collagen-chitosan full thickness model (CC-FTM) is evaluated for dermal and epidermal morphogenesis. Furthermore, the barrier composition and organization are characterized and compared to the control FTM and to NHS. Additionally, the functionality of the barrier is assessed.

Part II reports on the optimization of cell culture conditions of HSEs. In **chapter 4**, studies are described in which the culture temperature is reduced from conventional body core temperature (37°C) to 35°C and 33°C during generation of FTMs, as these better approaches the *in vivo* skin surface temperature. The effect of this temperature reduction is monitored during four weeks after air-exposure. FTMs are examined for dermal and epidermal morphogenesis. Furthermore,

the lipid barrier formation is examined by analysing SC lipid composition and organization in FTMs and is compared to NHS.

Determination whether the external oxygen level affects dermal and epidermal morphogenesis of FTMs, mediated by the hypoxia inducible factor signalling pathway, is reported in **chapter 5**. Reduction of the external oxygen level during cell culturing is performed, followed by examination of hypoxia signalling pathway activation. This is studied in fibroblast and keratinocyte monocultures as well as in HSEs. Evaluations on morphogenesis and lipid barrier formation are described in FTMs and NHS.

In **chapter 6**, studies are described to determine whether a high or low relative humidity level improves the epidermal morphogenesis and lipid barrier formation. This is performed in two different types of HSEs, the FTM and the CC-FTM, of which the development of the latter is described in **chapter 3**.

Investigations on sunlight exposure as external factor is described in **chapter 7**. The lack of sunlight exposure during generation of FTMs is compensated through addition of the active metabolite of the ultraviolet light driven vitamin D signalling pathway (i.e. $1,25(OH)_2D_3$). The expression levels of the vitamin D receptor and target genes are determined, as well as effects of supplementation on epidermal morphogenesis and barrier formation, with focus on ceramide composition and lamellar organization.

Part III focusses on cell culture medium optimization and combinatory strategies. **Chapter 8** reports the influence of reduced supplementation of exogeneous palmitic acid. Inadequate supplementation levels of this FFA can lead to lipotoxic effects and altered lipid processing in the epidermis, potentially leading to altered barrier formation. Therefore, a ten and hundredfold reduction in palmitic acid level is compared to established concentrations and evaluated for epidermal morphogenesis and lipid barrier formation.

The additive or synergic effect of a combined approach of optimized culture conditions obtained in the previous chapters with optimized medium components is described in **chapter 9**. Data is presented for the development and assessment of a FTM which is optimized based on single, double, and triple targeted strategies. The approaches included the i) chitosan containing dermal ECM (CC-FTMs), ii) development at reduced oxygen level, and iii) supplementation with an inhibitor of the liver X receptor. Experimental analyses of epidermal morphogenesis, lipid composition, lipid organization, and barrier functionality are described for the various FTMs and NHS.

In **Chapter 10**, the insights obtained in this thesis are summarized and discussed. Additionally, suggestions for future studies are provided.

8. References

1. Niehues, H., et al., 3D skin models for 3R research: the potential of 3D reconstructed skin models to study skin barrier function. Experimental dermatology, 2018.
2. Driskell, R.R., et al., Defining dermal adipose tissue. Exp Dermatol, 2014. 23(9): p. 629-31.
3. Festa, E., et al., Adipocyte Lineage Cells Contribute to the Skin Stem Cell Niche to Drive Hair Cycling. Cell, 2011. 146(5): p. 761-771.
4. Hassan, W.U., U. Greiser, and W. Wang, Role of adipose-derived stem cells in wound healing. 2014. 22(3): p. 313-325.
5. Sorrell, J.M. and A.I. Caplan, Fibroblast heterogeneity: more than skin deep. Journal of Cell Science, 2004. 117(5): p. 667-675.
6. Janson, D.G., et al., Different gene expression patterns in human papillary and reticular fibroblasts. Journal of Investigative Dermatology, 2012. 132(11): p. 2565-2572.
7. Janson, D., et al., Papillary fibroblasts differentiate into reticular fibroblasts after prolonged in vitro culture. Experimental dermatology, 2013. 22(1): p. 48-53.
8. Driskell, R.R., et al., Distinct fibroblast lineages determine dermal architecture in skin development and repair. Nature, 2013. 504(7479): p. 277.
9. Philippeos, C., et al., Spatial and Single-Cell Transcriptional Profiling Identifies Functionally Distinct Human Dermal Fibroblast Subpopulations. Journal of Investigative Dermatology, 2018.
10. Rognoni, E. and F.M. Watt, Skin Cell Heterogeneity in Development, Wound Healing, and Cancer. Trends in Cell Biology, 2018.
11. Hu, M.S., A.L. Moore, and M.T. Longaker, A Fibroblast Is Not a Fibroblast Is Not a Fibroblast. The Journal of investigative dermatology, 2018. 138(4): p. 729-730.
12. Tabib, T., et al., SFRP2/DPP4 and FMO1/LSP1 Define Major Fibroblast Populations in Human Skin. Journal of Investigative Dermatology, 2018. 138(4): p. 802-810.
13. Burgeson, R.E. and A.M. Christiano, The dermal-epidermal junction. Curr Opin Cell Biol, 1997. 9(5): p. 651-8.
14. Breitkreutz, D., et al., Skin Basement Membrane: The Foundation of Epidermal Integrity; BM Functions and Diverse Roles of Bridging Molecules Nidogen and Perlecan. BioMed Research International, 2013. 2013: p. 16.
15. Smola, H., et al., Dynamics of basement membrane formation by keratinocyte–fibroblast interactions in organotypic skin culture. Experimental cell research, 1998. 239(2): p. 399-410.
16. Marinkovich, M.P., et al., Cellular origin of the dermal-epidermal basement membrane. Developmental Dynamics, 1993. 197(4): p. 255-267.
17. El Ghalbzouri, A. and M. Ponec, Diffusible factors released by fibroblasts support epidermal morphogenesis and deposition of basement membrane components. Wound repair and regeneration, 2004. 12(3): p. 359-367.
18. El Ghalbzouri, A., et al., Basement membrane reconstruction in human skin equivalents is regulated by fibroblasts and/or exogenously activated keratinocytes. Journal of investigative dermatology, 2005. 124(1): p. 79-86.
19. Varkey, M., J. Ding, and E.E. Tredget, Superficial Dermal Fibroblasts Enhance Basement Membrane and Epidermal Barrier Formation in Tissue-Engineered Skin: Implications for Treatment of Skin Basement Membrane Disorders. Tissue Engineering. Part A, 2014. 20(3-4): p. 540-552.
20. Turcan, I. and M.F. Jonkman, Blistering disease: insight from the hemidesmosome and other components of the dermal-epidermal junction. Cell and Tissue Research, 2015. 360(3): p. 545-569.
21. Homberg, M. and T.M. Magin, Chapter Six - Beyond Expectations: Novel Insights into Epidermal Keratin Function and Regulation, in International Review of Cell and Molecular Biology, K.W. Jeon, Editor. 2014, Academic Press. p. 265-306.
22. Simpson, C.L., D.M. Patel, and K.J. Green, Deconstructing the skin: cytoarchitectural determinants of epidermal morphogenesis. Nature Reviews Molecular Cell Biology, 2011. 12: p. 565.
23. Alibardi, L., Chapter Six - The Process of Cornification Evolved From the Initial Keratinization in the Epidermis and Epidermal Derivatives of Vertebrates: A New Synthesis and the Case of Sauropsids, in International Review of Cell and Molecular Biology, K.W. Jeon and L. Galluzzi, Editors. 2016, Academic Press. p. 263-319.
24. Lippens, S., et al., Death penalty for keratinocytes: apoptosis versus cornification. Cell Death And Differentiation, 2005. 12: p. 1497.
25. Candi, E., R. Schmidt, and G. Melino, The cornified envelope: a model of cell death in the skin. Nature Reviews Molecular Cell Biology, 2005. 6: p. 328.
26. Poulson, N.D. and T. Lechler, Asymmetric cell divisions in the epidermis, in International review of cell and molecular biology. 2012, Elsevier. p. 199-232.

27. Ishida-Yamamoto, A., S. Igawa, and M. Kishibe, Molecular basis of the skin barrier structures revealed by electron microscopy. Exp Dermatol, 2018.
28. Yokouchi, M., et al., Epidermal cell turnover across tight junctions based on Kelvin's tetrakaidecahedron cell shape. eLife, 2016. 5: p. e19593.
29. Elias, P.M., Epidermal Lipids, Barrier Function, and Desquamation. Journal of Investigative Dermatology, 1983. 80(1, Supplement): p. S44-S49.
30. Igawa, S., et al., Tight junctions in the stratum corneum explain spatial differences in corneodesmosome degradation. Exp Dermatol, 2011. 20(1): p. 53-7.
31. Kirschner, N. and J.M. Brandner, Barriers and more: functions of tight junction proteins in the skin. Ann N Y Acad Sci, 2012. 1257: p. 158-66.
32. Elias, P.M., et al., Formation and functions of the corneocyte lipid envelope (CLE). Biochim Biophys Acta, 2014. 1841(3): p. 314-8.
33. Matsui, T. and M. Amagai, Dissecting the formation, structure and barrier function of the stratum corneum. International Immunology, 2015. 27(6): p. 269-280.
34. Cropek, D.M. and P. Karande, Models, Methods, and Measurements in Transdermal Drug Delivery, in Percutaneous Penetration Enhancers Drug Penetration Into/Through the Skin: Methodology and General Considerations, N. Dragicevic and H. I. Maibach, Editors. 2017, Springer Berlin Heidelberg: Berlin, Heidelberg. p. 153-184.
35. Elkeeb, R., et al., Correlation of transepidermal water loss with skin barrier properties in vitro: comparison of three evaporimeters. Skin Research and Technology, 2010. 16(1): p. 9-15.
36. Guth, K., et al., Suitability of skin integrity tests for dermal absorption studies in vitro. Toxicology in Vitro, 2015. 29(1): p. 113-123.
37. OECD, Guidance Document for the Conduct of Skin Absorption Studies. 2004.
38. OECD, Test No. 428: Skin Absorption: In Vitro Method. 2004.
39. Breathnach, A., et al., Freeze-fracture replication of cells of stratum corneum of human epidermis. Journal of anatomy, 1973. 114(Pt 1): p. 65.
40. Elias, P.M. and D.S. Friend, The permeability barrier in mammalian epidermis. J Cell Biol, 1975. 65(1): p. 180-91.
41. Madison, K.C., et al., Presence of intact intercellular lipid lamellae in the upper layers of the stratum corneum. J Invest Dermatol, 1987. 88(6): p. 714-8.
42. Swartzendruber, D.C., et al., Molecular models of the Intercellular Lipid Lamellae in Mammalian Stratum Corneum. Journal of Investigative Dermatology, 1989. 92(2): p. 251-257.
43. Bouwstra, J.A., et al., Structural investigations of human stratum corneum by small-angle X-ray scattering. Journal of Investigative Dermatology, 1991. 97(6): p. 1005-1012.
44. Schreiner, V., et al., Barrier Characteristics of Different Human Skin Types Investigated with X-Ray Diffraction, Lipid Analysis, and Electron Microscopy Imaging. Journal of Investigative Dermatology, 2000. 114(4): p. 654-660.
45. Groen, D., et al., Is an orthorhombic lateral packing and a proper lamellar organization important for the skin barrier function? Biochimica et Biophysica Acta (BBA) - Biomembranes, 2011. 1808(6): p. 1529-1537.
46. Boncheva, M., The physical chemistry of the stratum corneum lipids. International journal of cosmetic science, 2014. 36(6): p. 505-515.
47. Bouwstra, J.A., et al., The lipid organisation in the skin barrier. Acta Derm Venereol Suppl (Stockh), 2000. 208: p. 23-30.
48. Boncheva, M., F. Damien, and V. Normand, Molecular organization of the lipid matrix in intact Stratum corneum using ATR-FTIR spectroscopy. Biochimica et Biophysica Acta (BBA) - Biomembranes, 2008. 1778(5): p. 1344-1355.
49. Radner, F.P. and J. Fischer, The important role of epidermal triacylglycerol metabolism for maintenance of the skin permeability barrier function. Biochim Biophys Acta, 2014. 1841(3): p. 409-15.
50. Kihara, A., Synthesis and degradation pathways, functions, and pathology of ceramides and epidermal acylceramides. Progress in Lipid Research, 2016. 63: p. 50-69.
51. Weerheim, A. and M. Ponec, Determination of stratum corneum lipid profile by tape stripping in combination with high-performance thin-layer chromatography. Archives of Dermatological Research, 2001. 293(4): p. 191-199.
52. Motta, S., et al., Ceramide composition of the psoriatic scale. Biochimica et Biophysica Acta (BBA)-Molecular Basis of Disease, 1993. 1182(2): p. 147-151.
53. t'Kindt, R., et al., Profiling and characterizing skin ceramides using reversed-phase liquid chromatography–quadrupole time-of-flight mass spectrometry. Analytical chemistry, 2011. 84(1): p. 403-411.
54. Moore, D.J. and A.V. Rawlings, The chemistry, function and (patho)physiology of stratum corneum barrier ceramides. Int J Cosmet Sci, 2017. 39(4): p. 366-372.
55. Rabionet, M., et al., 1-O-acylceramides are natural components of human and mouse epidermis. Journal of lipid research, 2013. 54(12): p. 3312-3321.
56. Mizutani, Y., et al., Ceramide biosynthesis in keratinocyte and its role in skin function. Biochimie, 2009. 91(6): p. 784-790.

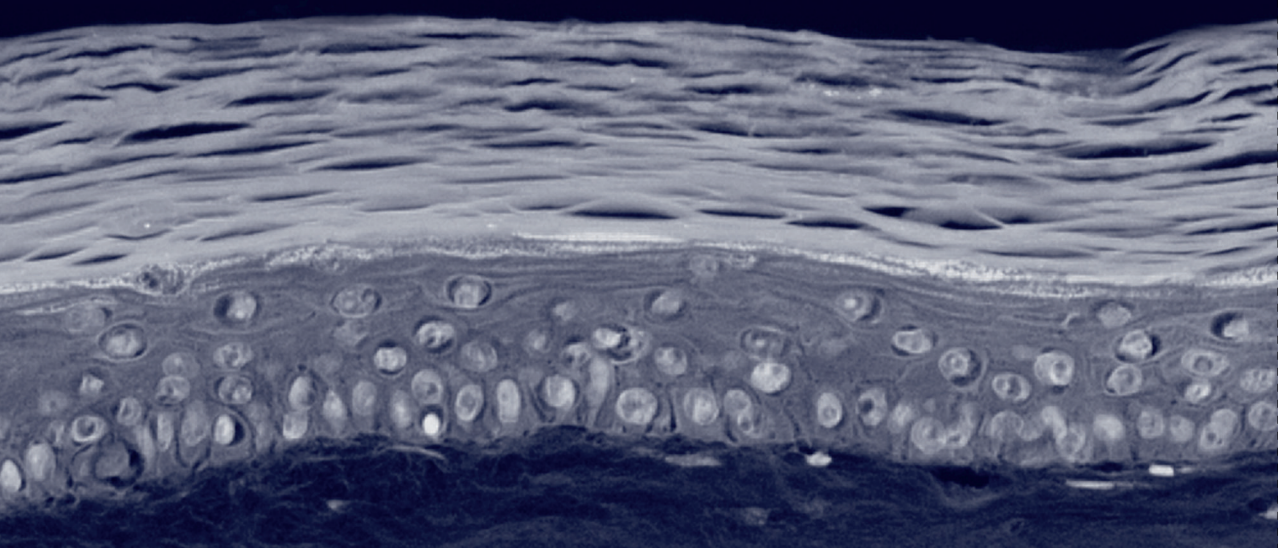
57. Boiten, W., et al., Quantitative analysis of ceramides using a novel lipidomics approach with three dimensional response modelling. Biochimica et Biophysica Acta (BBA) - Molecular and Cell Biology of Lipids, 2016. 1861(11): p. 1652-1661.
58. Pruett, S.T., et al., Thematic Review Series: Sphingolipids. Biodiversity of sphingoid bases ("sphingosines") and related amino alcohols. Journal of lipid research, 2008. 49(8): p. 1621-1639.
59. Maula, T., et al., Importance of the Sphingoid Base Length for the Membrane Properties of Ceramides. Biophysical Journal, 2012. 103(9): p. 1870-1879.
60. van Smeden, J., et al., Combined LC/MS-platform for analysis of all major stratum corneum lipids, and the profiling of skin substitutes. Biochimica et Biophysica Acta (BBA)-Molecular and Cell Biology of Lipids, 2014. 1841(1): p. 70-79.
61. Ishikawa, J., et al., Changes in the ceramide profile of atopic dermatitis patients. The Journal of investigative dermatology, 2010. 130(10): p. 2511-2514.
62. Thakoersing, V.S., et al., Increased presence of monounsaturated fatty acids in the stratum corneum of human skin equivalents. Journal of Investigative Dermatology, 2013. 133(1): p. 59-67.
63. Norlén, L., et al., A new HPLC-based method for the quantitative analysis of inner stratum corneum lipids with special reference to the free fatty acid fraction. Archives of dermatological research, 1998. 290(9): p. 508-516.
64. Wertz, P.W. and B. van den Bergh, The physical, chemical and functional properties of lipids in the skin and other biological barriers. Chemistry and physics of lipids, 1998. 91(2): p. 85-96.
65. Ponec, M., et al., New acylceramide in native and reconstructed epidermis. Journal of investigative dermatology, 2003. 120(4): p. 581-588.
66. Ansari, M., N. Nicolaides, and H. Fu, Fatty acid composition of the living layer and stratum corneum lipids of human sole skin epidermis. Lipids, 1970. 5(10): p. 838-845.
67. van Smeden, J., et al., The important role of stratum corneum lipids for the cutaneous barrier function. Biochimica et Biophysica Acta (BBA) - Molecular and Cell Biology of Lipids, 2014. 1841(3): p. 295-313.
68. Long, S., et al., Human stratum corneum polar lipids and desquamation. Archives of dermatological research, 1985. 277(4): p. 284-287.
69. Elias, P.M., et al., Role of cholesterol sulfate in epidermal structure and function: lessons from X-linked ichthyosis. Biochimica et Biophysica Acta (BBA)-Molecular and Cell Biology of Lipids, 2014. 1841(3): p. 353-361.
70. Sato, J., et al., Cholesterol sulfate inhibits proteases that are involved in desquamation of stratum corneum. Journal of investigative dermatology, 1998. 111(2): p. 189-193.
71. van Smeden, J., A breached barrier: analysis of stratum corneum lipids and their role in eczematous patients. 2013, Leiden Academic Center for Drug Research (LACDR), Faculty of Science, Leiden University.
72. Breiden, B. and K. Sandhoff, The role of sphingolipid metabolism in cutaneous permeabilitybarrier formation. Biochimica et Biophysica Acta (BBA) - Molecular and Cell Biology of Lipids, 2014. 1841(3): p. 441-452.
73. Feingold, K.R. and P.M. Elias, Role of lipids in the formation and maintenance of the cutaneous permeability barrier. Biochimica et Biophysica Acta (BBA) - Molecular and Cell Biology of Lipids, 2014. 1841(3): p. 280-294.
74. Rabionet, M., K. Gorgas, and R. Sandhoff, Ceramide synthesis in the epidermis. Biochimica et Biophysica Acta (BBA) - Molecular and Cell Biology of Lipids, 2014. 1841(3): p. 422-434.
75. Hirabayashi, T., et al., PNPLA1 has a crucial role in skin barrier function by directing acylceramide biosynthesis. Nature Communications, 2017. 8: p. 14609.
76. Billingham, R. and P.B. Medawar, The technique of free skin grafting in mammals. Journal of Experimental Biology, 1951. 28(3): p. 385-402.
77. Medawar, P., The cultivation of adult mammalian skin epithelium in vitro. QJ Microsc Sci, 1948. 89(Pt 2): p. 187-96.
78. Rheinwald, J.G. and H. Green, Seria cultivation of strains of human epidemal keratinocytes: the formation keratinizin colonies from single cell is. Cell, 1975. 6(3): p. 331-343.
79. Green, H., Terminal differentiation of cultured human epidermal cells. Cell, 1977. 11(2): p. 405-416.
80. Bell, E., et al., Living tissue formed in vitro and accepted as skin-equivalent tissue of full thickness. Science, 1981. 211(4486): p. 1052-4.
81. Mackenzie, I.C. and N.E. Fusenig, Regeneration of organized epithelial structure. J Invest Dermatol, 1983. 81(1 Suppl): p. 189s-94s.
82. El Ghalbzouri, A., E. Lamme, and M. Ponec, Crucial role of fibroblasts in regulating epidermal morphogenesis. Cell Tissue Res, 2002. 310(2): p. 189-99.
83. Lamb, R. and C.A. Ambler, Keratinocytes propagated in serum-free, feeder-free culture conditions fail to form stratified epidermis in a reconstituted skin model. PLoS One, 2013. 8(1): p. e52494.
84. Lee, D.Y. and K.H. Cho, The effects of epidermal keratinocytes and dermal fibroblasts on the formation of cutaneous basement membrane in three-dimensional culture systems. Arch Dermatol Res, 2005. 296(7): p. 296-302.

85. Thakoersing, V.S., et al., Unraveling barrier properties of three different in-house human skin equivalents. Tissue Engineering Part C: Methods, 2011. 18(1): p. 1-11.
86. Gangatirkar, P., et al., Establishment of 3D organotypic cultures using human neonatal epidermal cells. Nat Protoc, 2007. 2(1): p. 178-86.
87. Mori, N., Y. Morimoto, and S. Takeuchi, Skin integrated with perfusable vascular channels on a chip. Biomaterials, 2017. 116: p. 48-56.
88. Powell, H.M., D.M. Supp, and S.T. Boyce, Influence of electrospun collagen on wound contraction of engineered skin substitutes. Biomaterials, 2008. 29(7): p. 834-843.
89. Varkey, M., J. Ding, and E.E. Tredget, Differential collagen-glycosaminoglycan matrix remodeling by superficial and deep dermal fibroblasts: potential therapeutic targets for hypertrophic scar. Biomaterials, 2011. 32(30): p. 7581-91.
90. Varkey, M., J. Ding, and E.E. Tredget, Fibrotic remodeling of tissue-engineered skin with deep dermal fibroblasts is reduced by keratinocytes. Tissue Eng Part A, 2014. 20(3-4): p. 716-27.
91. Ding, C.-M., et al., Perfusion seeding of collagen–chitosan sponges for dermal tissue engineering. Process Biochemistry, 2008. 43(3): p. 287-296.
92. Auxenfans, C., et al., Adipose-derived stem cells (ASCs) as a source of endothelial cells in the reconstruction of endothelialized skin equivalents. Journal of tissue engineering and regenerative medicine, 2012. 6(7): p. 512-518.
93. Boehnke, K., et al., Effects of fibroblasts and microenvironment on epidermal regeneration and tissue function in long-term skin equivalents. European journal of cell biology, 2007. 86(11-12): p. 731-746.
94. Muffler, S., et al., A stable niche supports long-term maintenance of human epidermal stem cells in organotypic cultures. Stem Cells, 2008. 26(10): p. 2506-2515.
95. Stark, H.-J., et al., Authentic fibroblast matrix in dermal equivalents normalises epidermal histogenesis and dermo-epidermal junction in organotypic co-culture. European journal of cell biology, 2004. 83(11-12): p. 631-645.
96. Sriram, G., et al., Full-thickness human skin-on-chip with enhanced epidermal morphogenesis and barrier function. Materials Today, 2017.
97. El Ghalbzouri, A., et al., Replacement of animal-derived collagen matrix by human fibroblast-derived dermal matrix for human skin equivalent products. Biomaterials, 2009. 30(1): p. 71-78.
98. Sriram, G., P.L. Bigliardi, and M. Bigliardi-Qi, Fibroblast heterogeneity and its implications for engineering organotypic skin models in vitro. Eur J Cell Biol, 2015. 94(11): p. 483-512.
99. Cadau, S., et al., In vitro glycation of an endothelialized and innervated tissue-engineered skin to screen anti-AGE molecules. Biomaterials, 2015. 51: p. 216-225.
100. Ponec, M., et al., Endothelial network formed with human dermal microvascular endothelial cells in autologous multicellular skin substitutes. Angiogenesis, 2004. 7(4): p. 295-305.
101. Ouwehand, K., et al., Technical Advance: Langerhans cells derived from a human cell line in a full-thickness skin equivalent undergo allergen-induced maturation and migration. Journal of leukocyte biology, 2011. 90(5): p. 1027-1033.
102. van den Bogaard, E.H., et al., Crosstalk between keratinocytes and T cells in a 3D microenvironment: a model to study inflammatory skin diseases. J Invest Dermatol, 2014. 134(3): p. 719-727.
103. Drongelen, V., et al., Reduced filaggrin expression is accompanied by increased Staphylococcus aureus colonization of epidermal skin models. Clinical & Experimental Allergy, 2014. 44(12): p. 1515-1524.
104. Rademacher, F., et al., Skin microbiota and human 3D skin models. Experimental Dermatology, 2018. 27(5): p. 489-494.
105. Mathes, S.H., H. Ruffner, and U. Graf-Hausner, The use of skin models in drug development. Adv Drug Deliv Rev, 2014. 69-70: p. 81-102.
106. van den Broek, L.J., et al., Progress and Future Prospectives in Skin-on-Chip Development with Emphasis on the use of Different Cell Types and Technical Challenges. Stem Cell Rev, 2017. 13(3): p. 418-429.
107. Planz, V., C.M. Lehr, and M. Windbergs, In vitro models for evaluating safety and efficacy of novel technologies for skin drug delivery. J Control Release, 2016. 242: p. 89-104.
108. Yun, Y.E., et al., Artificial skin models for animal-free testing. Journal of Pharmaceutical Investigation, 2018: p. 1-9.
109. Gordon, S., et al., Non-animal models of epithelial barriers (skin, intestine and lung) in research, industrial applications and regulatory toxicology. Alternatives to Animal Experimentation: ALTEX, 2015. 32(4): p. 327-378.
110. Petrova, A., et al., 3D In vitro model of a functional epidermal permeability barrier from human embryonic stem cells and induced pluripotent stem cells. Stem Cell Reports, 2014. 2(5): p. 675-89.
111. Danso, M.O., et al., TNF-alpha and Th2 cytokines induce atopic dermatitis-like features on epidermal differentiation proteins and stratum corneum lipids in human skin equivalents. J Invest Dermatol, 2014. 134(7): p. 1941-1950.

112. Abaci, H.E., et al., Pumpless microfluidic platform for drug testing on human skin equivalents. Lab Chip, 2015. 15(3): p. 882-8.
113. OECD, performance standards for assessment of proposed similar or modified in vitro recondstructed human epidermis (RHE) test methods for skin corrosion (in relation to TG 431) http://www.oecd.org/chemicalsafety/testing/PerfStand-TG431-june14.pdf, 2014.
114. Alépée, N., M.H. Grandidier, and J. Cotovio, Sub-categorisation of skin corrosive chemicals by the EpiSkin™ reconstructed human epidermis skin corrosion test method according to UN GHS: Revision of OECD Test Guideline 431. Toxicology in Vitro, 2014. 28(2): p. 131-145.
115. Desprez, B., et al., Two novel prediction models improve predictions of skin corrosive sub-categories by test methods of OECD Test Guideline No. 431. Toxicology in Vitro, 2015. 29(8): p. 2055-2080.
116. Katoh, M., et al., Assessment of human epidermal model LabCyte EPI-MODEL for in vitro skin irritation testing according to European Centre for the Validation of Alternative Methods (ECVAM)-validated protocol. J Toxicol Sci, 2009. 34(3): p. 327-34.
117. Kandárová, H., et al., Assessment of the human epidermis model SkinEthic RHE for in vitro skin corrosion testing of chemicals according to new OECD TG 431. Toxicology in Vitro, 2006. 20(5): p. 547-559.
118. Kandárová, H., et al., The EpiDerm test protocol for the upcoming ECVAM validation study on in vitro skin irritation tests-an assessment of the performance of the optimised test. ATLA-NOTTINGHAM-, 2005. 33(4): p. 351.
119. Kandárová, H., et al., In vitro skin irritation testing: improving the sensitivity of the EpiDerm skin irritation test protocol. ATLA-Alternatives to Laboratory Animals, 2009. 37(6): p. 671.
120. Urbisch, D., et al., Assessing skin sensitization hazard in mice and men using non-animal test methods. Regulatory Toxicology and Pharmacology, 2015. 71(2): p. 337-351.
121. Bergers, L.I.J.C., et al., Immune-competent human skin disease models. Drug Discovery Today, 2016. 21(9): p. 1479-1488.
122. OECD, The Adverse Outcome Pathway for Skin Sensitisation Initiated by Covalent Binding to Proteins. 2014.
123. Saito, K., et al., Development of a new in vitro skin sensitization assay (Epidermal Sensitization Assay; EpiSensA) using reconstructed human epidermis. Toxicology in Vitro, 2013. 27(8): p. 2213-2224.
124. Saito, K., et al., An in vitro skin sensitization assay termed EpiSensA for broad sets of chemicals including lipophilic chemicals and pre/pro-haptens. Toxicology in Vitro, 2017. 40: p. 11-25.
125. Reisinger, K., et al., Systematic evaluation of non-animal test methods for skin sensitisation safety assessment. Toxicology in Vitro, 2015. 29(1): p. 259-270.
126. Dagmar, J., et al., Comparison of human skin irritation patch test data with in vitro skin irritation assays and animal data. Contact Dermatitis, 2010. 62(2): p. 109-116.
127. OECD, New guidance document on an integrated approach on testing and assessment (IATA) for skin corrosion and irritation. http://www.oecd.org/officialdocuments/publicdisplaydocumentpdf/?cote=ENV/JM/MONO%282014%2919&doclanguage=en 2014.
128. Mewes, K.R., et al., Catch-up validation study of an in vitro skin irritation test method based on an open source reconstructed epidermis (phase I). Toxicology in Vitro, 2016. 36: p. 238-253.
129. Poumay, Y., et al., A simple reconstructed human epidermis: preparation of the culture model and utilization in in vitro studies. Arch Dermatol Res, 2004. 296(5): p. 203-11.
130. El-Ghalbzouri, A., et al., Effect of fibroblasts on epidermal regeneration. British journal of dermatology, 2002. 147(2): p. 230-243.
131. Ponec, M., et al., Barrier function in reconstructed epidermis and its resemblance to native human skin. Skin Pharmacology and Physiology, 2001. 14(Suppl. 1): p. 63-71.
132. Ponec, M., J. Kempenaar, and A. Weerheim, Lack of desquamation - the Achilles heel of the reconstructed epidermis. Int J Cosmet Sci, 2002. 24(5): p. 263-72.
133. Kandarova, H., Evaluation and validation of reconstructed human skin models as alternatives to animal tests in regulatory toxicology. 2006, Freie Universität Berlin.
134. Ponec, M., et al., Lipid and ultrastructural characterization of reconstructed skin models. International journal of pharmaceutics, 2000. 203(1-2): p. 211-225.
135. Lotte, C., et al., Permeation and Skin Absorption: Reproducibility of Various Industrial Reconstructed Human Skin Models. Skin Pharmacology and Physiology, 2002. 15(suppl 1) (Suppl. 1): p. 18-30.
136. Schafer-Korting, M., et al., Reconstructed human epidermis for skin absorption testing: results of the German prevalidation study. ATLA, 2006. 34(3): p. 283.
137. Wagner, H., et al., Interrelation of permeation and penetration parameters obtained from in vitro experiments with human skin and skin equivalents. Journal of Controlled Release, 2001. 75(3): p. 283-295.
138. Ackermann, K., et al., The Phenion® Full-Thickness Skin Model for Percutaneous Absorption Testing. Skin Pharmacology and Physiology, 2010. 23(2): p. 105-112.

139. Schmook, F.P., J.G. Meingassner, and A. Billich, Comparison of human skin or epidermis models with human and animal skin in in-vitro percutaneous absorption. International Journal of Pharmaceutics, 2001. 215(1): p. 51-56.
140. Regnier, M., et al., Barrier Function of Human Skin and Human Reconstructed Epidermis. Journal of Pharmaceutical Sciences, 1993. 82(4): p. 404-407.
141. Dreher, F., et al., Comparison of Cutaneous Bioavailability of Cosmetic Preparations Containing Caffeine or α-Tocopherol Applied on Human Skin Models or Human Skin ex vivo at Finite Doses. Skin Pharmacology and Physiology, 2002. 15(suppl 1)(Suppl. 1): p. 40-58.
142. Netzlaff, F., et al., Permeability of the reconstructed human epidermis model Episkin® in comparison to various human skin preparations. European Journal of Pharmaceutics and Biopharmaceutics, 2007. 66(1): p. 127-134.
143. Döge, N., et al., Assessment of skin barrier function and biochemical changes of ex vivo human skin in response to physical and chemical barrier disruption. European Journal of Pharmaceutics and Biopharmaceutics, 2017. 116: p. 138-148.
144. Ponec, M., Skin constructs for replacement of skin tissues for in vitro testing. Advanced Drug Delivery Reviews, 2002. 54: p. S19-S30.
145. Steinert, P.M., et al., Small Proline-Rich Proteins Are Cross-Bridging Proteins in the Cornified Cell Envelopes of Stratified Squamous Epithelia. Journal of Structural Biology, 1998. 122(1): p. 76-85.
146. Vičanová, J., et al., Normalization of epidermal calcium distribution profile in reconstructed human epidermis is related to improvement of terminal differentiation and stratum corneum barrier formation. Journal of investigative dermatology, 1998. 111(1): p. 97-106.
147. Bouwstra, J., et al., Characterization of stratum corneum structure in reconstructed epidermis by X-ray diffraction. Journal of lipid research, 1995. 36(3): p. 496-504.
148. Thakoersing, V.S., et al., Nature versus nurture: does human skin maintain its stratum corneum lipid properties in vitro? Experimental dermatology, 2012. 21(11): p. 865-870.
149. Danso, M.O., et al., An ex vivo human skin model for studying skin barrier repair. Experimental dermatology, 2015. 24(1): p. 48-54.
150. Danso, M.O., et al., Exploring the potentials of nurture: 2nd and 3rd generation explant human skin equivalents. Journal of dermatological science, 2015. 77(2): p. 102-109.
151. Ponec, M., et al., The Formation of Competent Barrier Lipids in Reconstructed Human Epidermis Requires the Presence of Vitamin C. Journal of Investigative Dermatology, 1997. 109(3): p. 348-355.
152. Janssens, M., et al., Increase in short-chain ceramides correlates with an altered lipid organization and decreased barrier function in atopic eczema patients. Journal of lipid research, 2012.
153. Vicanova, J., et al., Incorporation of linoleic acid by cultured human keratinocytes. Arch Dermatol Res, 1999. 291(7-8): p. 405-12.
154. Thakoersing, V.S., et al., Modulation of stratum corneum lipid composition and organization of human skin equivalents by specific medium supplements. Experimental dermatology, 2015. 24(9): p. 669-674.
155. Ponec, M., et al., Characterization of Reconstructed Skin Models. Skin Pharmacology and Physiology, 2002. 15(suppl 1)(Suppl. 1): p. 4-17.
156. Mitsche, M.A., et al., Flux analysis of cholesterol biosynthesis in vivo reveals multiple tissue and cell-type specific pathways. 2015. 4: p. e07999.
157. Flaten, G.E., et al., In vitro skin models as a tool in optimization of drug formulation. European Journal of Pharmaceutical Sciences, 2015. 75: p. 10-24.
158. Küchler, S., K. Strüver, and W. Friess, Reconstructed skin models as emerging tools for drug absorption studies. Expert opinion on drug metabolism & toxicology, 2013. 9(10): p. 1255-1263.
159. Poumay, Y. and A. Coquette, Modelling the human epidermis in vitro: tools for basic and applied research. Archives of dermatological research, 2007. 298(8): p. 361-369.
160. Van Gele, M., et al., Three-dimensional skin models as tools for transdermal drug delivery: challenges and limitations. Expert opinion on drug delivery, 2011. 8(6): p. 705-720.
161. Hogervorst, M., et al., A shift from papillary to reticular fibroblasts enables tumour–stroma interaction and invasion. British journal of cancer, 2018. 118(8): p. 1089.
162. Semlin, L., et al., In vitro models for human skin disease. Drug Discovery Today, 2011. 16(3): p. 132-139.
163. Wang, S., et al., SPINK5 knockdown in organotypic human skin culture as a model system for Netherton syndrome: effect of genetic inhibition of serine proteases kallikrein 5 and kallikrein 7. Exp Dermatol, 2014. 23(7): p. 524-6.
164. van den Broek, L.J., et al., Development, validation and testing of a human tissue engineered hypertrophic scar model. 2012.
165. van Drongelen, V., et al., Barrier properties of an N/TERT-based human skin equivalent. Tissue Engineering Part A, 2014. 20(21-22): p. 3041-3049.

Part I



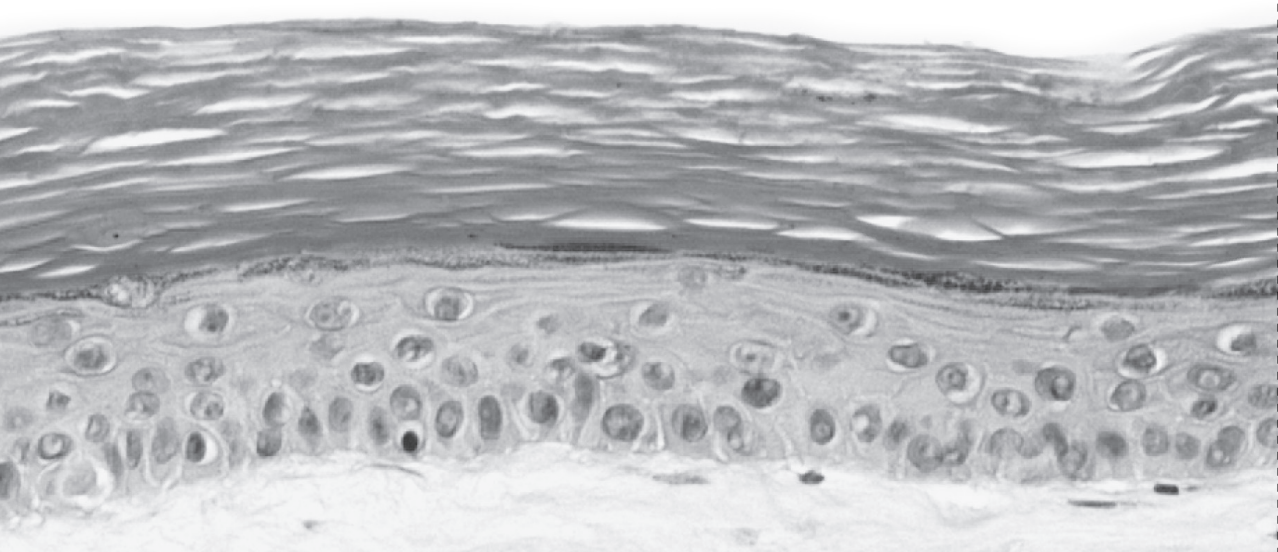
2

Recapitulation of native dermal tissue in a full thickness human skin model using human collagens

Arnout Mieremet
Marion Rietveld
Rianne van Dijk
Joke A. Bouwstra[+]
Abdoelwaheb El Ghalbzouri[+]

[+] Joint senior authorship

Tissue Engineering Part A 24 (11-12): 873-881
(2018)



Abstract

Objective Full thickness skin models are comprised of a three dimensional dermal equivalent based on an animal derived collagen matrix that harbours fibroblasts and an epidermal equivalent formed by keratinocytes. The functionality of both equivalents is influenced by many factors, including extracellular matrix composition and resident cell type. Animal-derived collagens differ from human collagens in amino acid composition and physico-chemical properties. This composition could alter the functionality of the dermal equivalent and epidermal morphogenesis with the barrier formation in full thickness models (FTMs). By replacement of animal-derived collagen for human collagen, we generated and characterized the animal material free human collagen full thickness models (hC-FTMs) that better mimics native dermal tissue.
Materials and Methods An isolation procedure to obtain soluble collagen from human abdominal dermis was developed. Both FTMs and hC-FTMs were generated with primary human fibroblasts and keratinocytes. Immunohistochemical analyses with biomarkers for the dermal matrix composition, basement membrane formation, epidermal proliferation, differentiation and activation were performed. The stratum corneum lipid composition was studied with liquid chromatography – mass spectrometry. Lipid lamellar organization was determined by small angle X-ray diffraction.
Results The FTMs and hC-FTMs exhibit many similarities, including the dermal matrix structure, basement membrane formation, epidermal basal layer proliferation and execution of differentiation programs. The stratum corneum contains a similar number of corneocyte layers and the same level of lipids. The ceramide chain length distribution and ceramide subclass profile showed only minor differences. Subsequently, this led to an unaltered lamellar organization.
Conclusion The animal material-free hC-FTM is generated successfully using collagens isolated from human abdominal dermis. Utilization of human collagens revealed that (epi-)dermal morphogenesis and lipid barrier formation resembled that of original FTMs. The hC-FTMs contain a dermal equivalent which mimics the native stromal tissue to a higher extent. Therefore these *in vitro* skin models can be used as promising tool for research purposes that contribute to animal-free experimentation.

Keywords: Human skin equivalent; Human collagen; Dermal microenvironment; Lipids; Epidermal barrier.

1. Introduction

The need for adequate skin models is high, due to the demands and goals of regulatory authorities and animal welfare organizations [1-3]. The architecture of the human skin is unique in nature and shares only some similarities with other primates and pigs. Therefore animal models should be used with restraint [4, 5]. *Ex vivo* human skin possesses all cell types resident in native human skin (NHS), yet the *ex vivo* skin model is limited available and exhibits a short lifespan [6, 7]. Therefore, *in vitro* developed human skin equivalents (HSEs) are preferably used for preclinical drug screenings. A widely used type of HSE is the full thickness model (FTM), which contains an epidermal and dermal equivalent. The former is made of keratinocytes generating a mature epidermis and the latter is composed of a collagen matrix harbouring the fibroblasts [8-10]. Progression in engineering of HSEs resulted in the resemblance of many characteristics of NHS *in vitro*. These include the presence of distinguishable epidermal layers, comparable basal cell proliferation rate, execution of differentiation programs, formation of the basement membrane (BM) and the presence of major lipid classes in the stratum corneum (SC) [11-13]. These similarities to NHS are established in our in-house developed HSEs as well as in several commercial available skin models. As such, several HSEs are validated tools for skin corrosion testing of chemicals as these meet criteria required by the OECD TG 431 [14], including SkinEthic, Epiderm™, epiCS® and Episkin™, whereas the Leiden epidermal skin model underwent a pre-validation [15, 16].

Complete *in vitro* reconstruction of the skin is not yet achieved. This is a complex procedure involving manifold developmental processes, culture conditions and nutritional factors. An important factor that could contribute to enhanced reconstruction of the skin *in vitro* is the dermal extracellular matrix of FTMs; this matrix is currently formed by collagen that originates from rat tail tendons. This animal source is used as it contains a high abundance of collagen fibrils, the standardized isolation procedures and efficacious matrices formed with it. However, collagen properties vary between tissues and species; there are variations in amino acid composition, thermal stability, and affinity for glycosaminoglycans which are important for the enzymatic resistance [17, 18]. Furthermore, the animal origin of the collagens could induce a biologic response to primary human stromal cells, but these effects are difficult to ascertain (18). Various other studies have been conducted to enhance epidermal reconstruction by optimizing the dermal matrix *in vitro*. The various dermal substitutes used include de-cellularized/de-epidermized dermis (DED) [19-21], collagen type I [8, 22-24], collagen mixed with glycosaminoglycans and/or chitosan [25-29], fibrin [30-32], fibroblast-derived matrix [8, 33, 34] and synthetic polymers [30], summarized in an excellent review article of Sriram *et al.* [35]. We hypothesize that the animal origin of collagen in

the dermal matrix of FTMs influences the (epi-)dermal homeostasis and barrier formation in FTMs.

Thorough characterization of the skin barrier is important to determine the effects of modulation in the dermal matrix. The skin barrier relies mainly in the SC, which consists of corneocytes embedded in a lipid matrix. The lipid matrix is the only continuous pathway through the SC and is regarded a major determinant for the barrier functionality [36]. Major constituents of the lipid matrix are ceramides (CERs), free fatty acids (FFAs) and cholesterol. The role and importance of each lipid subclass in the SC is extensively reviewed by van Smeden *et al.* [37]. In short, the CERs can be categorized into different subclasses, based on the type of sphingoid base coupled to a specific fatty acid chain, as illustrated by Janssens *et al.* [38]. The SC lipids fill the intercorneocyte space and are structured both in the lamellar and lateral organization [39, 40]. The SC lipid composition and organization play a key role in the functionality of the permeability barrier [41].

Our aim is to develop and characterize an animal material free FTM to better mimic the NHS. To do so, we designed an isolation procedure to obtain soluble collagen from human abdominal dermis. After generation of the human collagen full thickness models (hC-FTMs), evaluations between the established FTM, hC-FTM and NHS have been performed regarding epidermal morphology, proliferation, differentiation programs and BM formation. SC lipid characteristics were analysed in detail to provide insights about the SC lipid composition and organization of both FTM types. Hence, this study provides comprehensive information about the effects of the dermal microenvironment on the epidermal morphogenesis and barrier formation.

2. Materials and Methods

2.1 Isolation and culturing of primary skin cells

Isolation of primary human fibroblasts and keratinocytes was performed from surplus human breast skin as described before [11, 42]. Declaration of Helsinki principles are followed with obtainment of primary human skin cells from healthy adult donors. All isolated primary cells were tested negative for mycoplasma contamination.

2.2. Isolation and solubilisation of rat tail and human collagen

Rat tail collagen (4 mg/mL) was isolated from rat tail tendons through extraction of the collagen in 0.1% acetic acid, centrifugation and freeze drying. Isolation of soluble human collagen initiated with the removal of the epidermis from abdomen skin after one week at 37°C in PBS. The dermis was cut into small pieces and collagen was allowed to solubilize in a solution of 3% acetic acid and 0.1 mg/mL

pepsin (cat. no. p-7000, Sigma-Aldrich, Zwijndrecht, The Netherlands) at 4°C. After centrifugation at 12.000 rpm, the supernatant was freeze-dried and stored.

2.3. Preparation of the dermal equivalents

2.3.1. Rat tail collagen fibroblast-populated dermal equivalent

Development of dermal equivalents was performed as described earlier [8, 43]. In short, the hydrated collagen was mixed at 4°C with Hank's Buffered Salt Solution (HBSS) (Invitrogen), 0.1% acetic acid, 1M NaOH and FBS with and without cells to obtain a cell-free and cell-containing mixture. The cell-free mixture was polymerized at 37°C on a filter insert (Corning Transwell cell culture inserts, membrane diameter 24 mm, pore size 3 µm; Corning Life Sciences, The Netherlands). Sequentially the cell-containing (1,2 x 10^5 primary fibroblasts) suspension was allowed to polymerize on top. The dermal equivalent was cultured for 1 week.

2.3.2. Human collagen fibroblast-populated dermal equivalent

A concentration of 10 mg/mL hydrated human collagen was used for the preparation of human collagen dermal equivalents based on several pilot studies (data not shown). The dermal equivalent based on human collagen was prepared equally as the rat tail collagen fibroblast-populated dermal equivalent [8, 43]. Except the volume of 1M NaOH to induce the shift in acidity was increased slightly, based on phenol red indication.

2.4. Generation of FTMs and hC-FTMs

Primary keratinocytes (2.5 x 10^5/model) in their first passage were seeded onto each dermal equivalent. Four biological replicates were generated based on the use of four different primary cell donors. The development of the epidermal equivalent for both FTM types occurred similar as described by Mieremet *et al.* [43].

2.5. Statistics

Statistical analyses are conducted using GraphPad Prism version 6.00 for Windows (GraphPad Software, La Jolla, CA, USA). In general, statistical significance was calculated using paired Student's t-tests. Only the ceramide carbon chain length distribution and subclass profile were statistically tested using two-way ANOVA with a multiple comparison Holm-Šídák post-test. Statistical differences are noted as *, ** or ***, corresponding to $P<0.05$, <0.01, <0.001.

An expanded Materials and Methods is available as Supplementary Materials and Methods.

3. Results

3.1. Characterization of the epidermal morphogenesis in the hC-FTM

FTMs and hC-FTMs were generated by seeding primary keratinocytes on both types of dermal matrices. The characterization of epidermal homeostasis started by the examination of the morphology (**Fig. 1 a**). A well-organized epidermis was observed in both models, indicated by the presence of all four epidermal layers (i.e. stratum basale, stratum spinosum, stratum granulosum, and stratum corneum) (**Fig. 1 a**). Further characterization of the epidermal homeostasis in both FTM types and in NHS occurred through examination of the epidermal cell proliferation (Ki67), early (keratin 10) and late (loricrin) differentiation programs. As shown in **figure 1 a**, Ki67 positive cells were mainly confined in the basal layers of both FTM types and the NHS. Besides the localization, the proliferation index in both FTM types was also equal (**Fig. 1 b**). Keratin 10 showed a similar expression in the suprabasal cell layers, while loricrin was clearly expressed in the granular layer in both FTM types and NHS. Next, epidermal cell activation was examined by the expression of two hyper-proliferation associated keratin subtypes (i.e. keratin 16 and 17). These keratins are absent in NHS and only expressed during epidermal stress or activation. No difference in epidermal activation was observed between both FTM types. In addition, the number of corneocyte layers in the SC was similar in both FTM types (**Fig. 1 c**). When comparing the FTM types to NHS, some differences were observed, including the lack of rete ridges in the dermis, slight increased proliferation rate of keratinocytes and the enlarged cells in the granular layer. In addition, the epidermal cells were activated *in vitro,* but not *in vivo*, based on the expression of keratin 16.

3.2. Basement membrane formation in rat tail and human collagen based dermal equivalents

The composition of the dermal extracellular matrix was determined by both the initial supplemented collagen and other matrix components as well as by the deposition and rearrangement of proteins by the fibroblasts during the development of FTMs. To examine whether differences exist in the dermal matrix composition, the expression of major extracellular collagen types and the small leucine-rich proteoglycan decorin was examined in both FTMs and hC-FTMs (**Fig. 2**). The presence of collagen types I and III was similar in FTMs and hC-FTMs. Also decorin was present in both FTM types, although the fluorescence intensity appeared to be higher in the hC-FTM (*not quantified*). Next, the distribution of the fibroblasts in both FTM types was determined by the expression of vimentin. This fibroblasts marker was present throughout the dermis of both FTM types with similar distribution pattern. Thereafter, the formation of the basement membrane (BM) was assessed. The expression of collagen type VII, type IV and laminin 332 in both FTM types was equal and restricted to the epidermal-dermal junction.

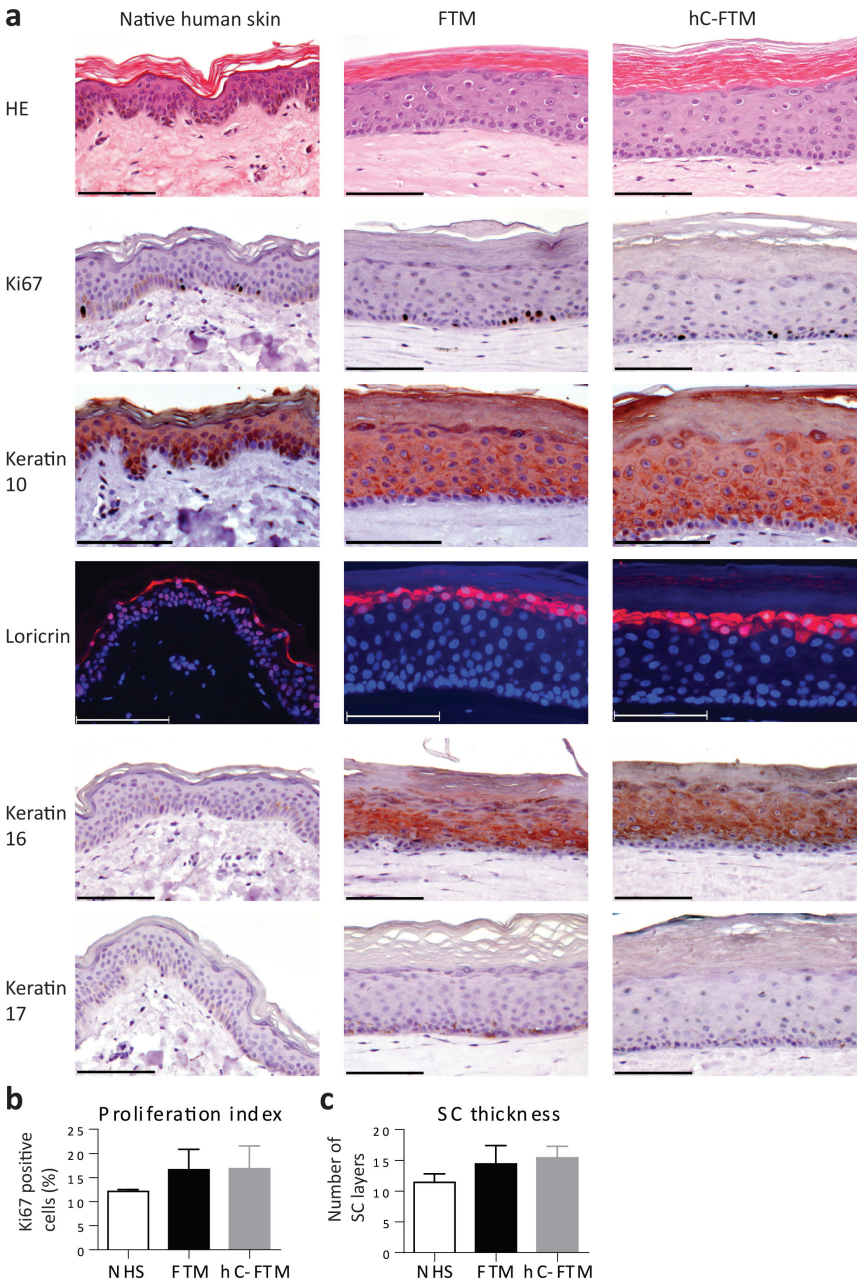


Figure 1. Epidermal homeostasis of NHS, FTM and hC-FTM. (a) Representative cross-sections examined for general morphology (HE), cell proliferation (Ki67), early (keratin 10) and late (loricrin) differentiation and epidermal cell activation (keratin 16 and 17). **(b)** Proliferation index based on the quantification of Ki67 positive cells in multiple regions of the basal layer. **(c)** Thickness of the SC in NHS, FTM and hC-FTM as determined with safranin red staining. Data represents mean ±SD, n=4, scale bar represents 100 µm.

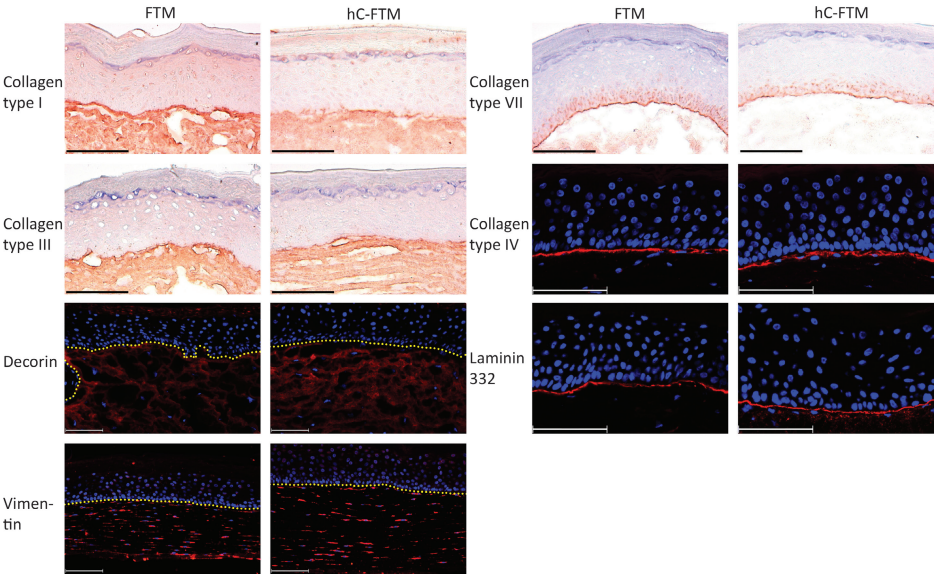


Figure 2. Dermal equivalent constituents and basement membrane formation in FTMs and hC-FTMs. Representative images of cross-sections of both FTM types, evaluated for the expression of proteins in the dermal matrix (collagen type I, III and decorin). Distribution of the fibroblasts is examined by vimentin expression. Formation of the basement membrane is analysed by collagen type VII, type IV and laminin 332 expression. Yellow dotted line indicates the dermal-epidermal junction. Scale bar represents 100 µm, n=4.

3.3. hC-FTMs show a similar ceramide chain length distribution as FTMs

After evaluation of the epidermal and dermal morphogenesis, we focussed on examination of the epidermal barrier characteristics. First, the weight percentage of total lipids in the SC was determined (**Fig. 3 a**). No significant difference in the level of total lipids in the SC of both FTM types was observed. Second, the CER chain length distribution in the SC of both FTM types was assessed. For this purpose, the CER composition in the total lipid extract was assessed with our in-house developed LC-MS analysis [44]. From the detected CER subclasses (**Supplementary fig. 1**), the carbon chain length distribution was examined. A wide distribution in the carbon chain length of all CER subclasses was observed in both FTM types. This distribution is mainly between 32 and 54 carbon atoms for the CER[non-EO] (**Fig. 3 b**) and between 62 and 78 carbon atoms for the esterified omega-hydroxylated ceramides (CER[EO]) (**Fig. 3 c**). When comparing the distribution of CERs between FTM and hC-FTM, no significant difference was observed for almost all CER carbon chain lengths. Only the level of short chain CER[non-EO] with 34 and that of CER[non-EO] with 42 carbon atoms was increased and the level of CER[non-EO] with 46 and 48 carbon atoms was reduced in the hC-FTM. To investigate whether these differences can be attributed to a particular subclass, the relative abundance of lipids with these four chain

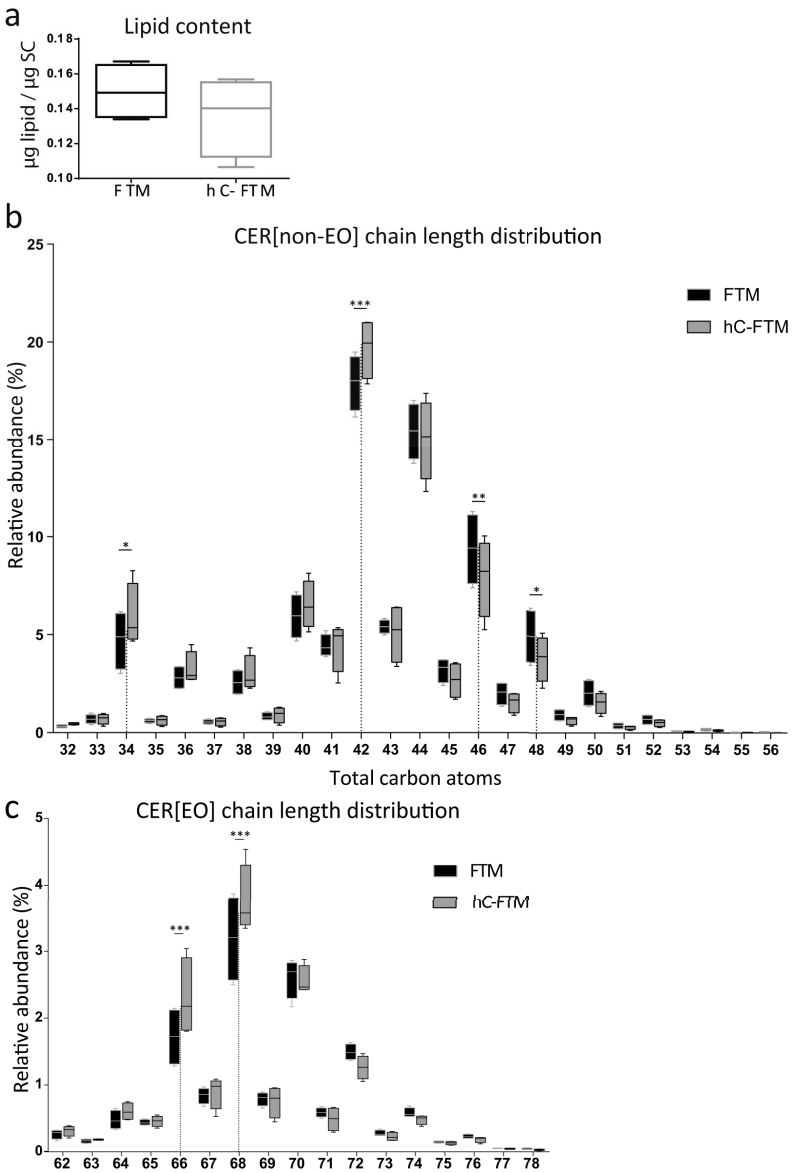


Figure 3. Lipid content and ceramide chain length distribution of FTMs and hC-FTMs. (a) The lipid content in the SC of the FTM and hC-FTM. **(b)** Box and whisker plot of CER[non-EO] with different number of C-atoms as relative abundance of the total AUC/internal standard (INST) of all CERs. In hC-FTMs, an increased relative abundance of C34 and C42 CER[non-EO] was detected, whereas there is a decrease in C46 and C48 CER[non-EO] was detected, both indicated by a dotted line. **(c)** CER[EO] carbon chain length distribution of FTMs and hC-FTMs. Box and whisker plot with indicated median of the CER[EO] as percentage of the relative abundance of total AUC/INST of all CERs. In hC-FTMs, an increase in the relative abundance of C66 and C68 CER[EO] is detected and indicated by a dotted line. Whiskers indicate the 95% confidence interval. Data is obtained from four independent experiments.

lengths was plotted for each CER[non-EO] subclass (**Supplementary fig. 2**). Nevertheless, there was no specific subclass to which these differences could be assigned to. Finally, the carbon chain length distribution for the high molecular weight CER[EO] was examined (**Fig. 3 c**). This revealed an increase in the relative abundance of the CER[EO] with 66 and 68 carbon atoms in the hC-FTMs.

3.4. Ceramide subclass profiles of FTMs and hC-FTMs

Next, the CER subclasses profile was determined for both FTM types. Besides the importance to study the distribution in CER carbon chain lengths, examination of the CER subclass profile provides additional insights on the CER composition in the lipid matrix. The CER subclass profile was determined after lipid separation by polarity and detection by mass. The profile of the twelve most abundant CER subclasses was determined and plotted for both FTM types (**Fig. 4**). After comparison of the CER subclass profile of the FTM and hC-FTM, only a significant change in CER[non-EO] subclass NS was observed. This subclass was more present in the hC-FTM. Next, the level of monounsaturated CERs of the CER[non-EO] subclasses AS and NS was examined which serves as major indicator for the level of monounsaturated CERs in all subclasses. The ratio between the saturated and monounsaturated CERs was calculated for the FTM and hC-FTM (**Supplementary fig. 3**). After comparing these ratios for both models, no difference in the level of monounsaturated CERs was observed. Besides the identified CER subclasses, several unidentified lipid entities were detected in the SC lipid matrix of both FTM types. These are indicated in **supplementary figure 1**, albeit not further analysed due to their unknown structure.

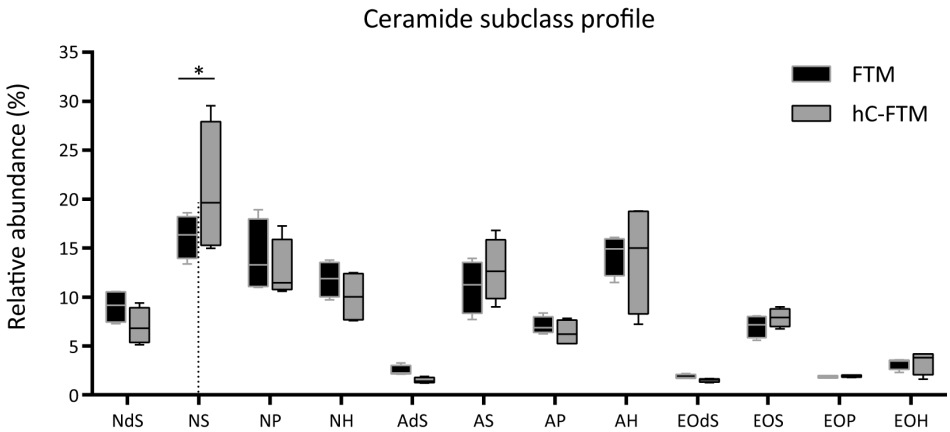


Figure 4. Ceramide subclass profile in FTMs and hC-FTMs. Box and whisker plot of each CER subclass as percentage of the relative abundance of total AUC/INST of all CERs. Significant difference in relative abundance is indicated, which is the increased relative abundance of NS. Whiskers indicate the 95% confidence interval. Data is obtained from four independent experiments.

3.5. Lamellar organization of the barrier lipids in the stratum corneum

The assessment of the SC lipid matrix was finalized by the determination of the SC extracellular lipid lamellar organization (**Fig. 5 a**). The lamellar organization of the SC lipids in the intercorneocyte space was characterized by a series of equidistant peaks in the X-ray diffraction pattern. Diffraction patterns of both FTM types contained peaks attributed solely to the LPP (**Fig. 5 b**). Moreover, in both FTM types two peaks were observed that could not be identified. The repeat distance of the long periodicity phase (LPP) was calculated and plotted based on the position of the diffraction peaks representing the 1st, 2nd and 3rd order of diffraction (**Fig. 5 c**). This revealed that the lamellar repeat distance in both FTM types was equal.

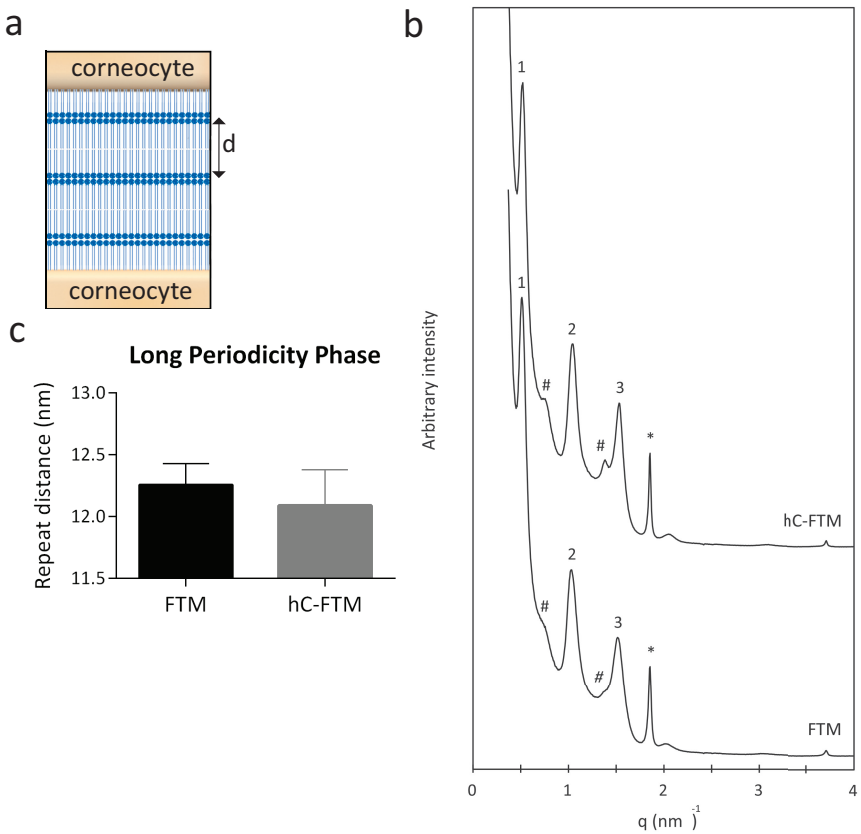


Figure 5. Lamellar lipid organization in the FTMs and hC-FTMs. (a) Schematic overview of the lamellae in the intercorneocyte space, where d indicates the repeat distance of the periodicity phase, adapted from van Smeden *et al.* [37]. **(b)** Representative diffraction pattern in which the first, second and third diffraction order of the long periodicity phase (LPP) are indicated. Separate crystalline cholesterol is indicated by the asterisk (*). Diffraction peaks of unknown phases are indicated with the number sign (#). **(c)** Barplot of the repeat distance of the LPP calculated based on the position of the first, second and third order of diffraction of the LPP. Data represents mean ±SD, n=4.

4. Discussion

To advance the resemblance of the *in vitro* developed full thickness models to NHS, we adapted the FTMs using collagen isolated from human abdominal dermis. This animal material free hC-FTM could be a valuable tool to better understand and study native stromal interactions. To form the dermal equivalent of the hC-FTM, a higher collagen concentration is used, since pepsinized human collagen self-assembles at delayed speed [45]. Yet, this higher collagen concentration in the dermal equivalent keeps the fibroblasts in the collagen matrix, as demonstrated by the heterogeneous distribution of the fibroblast throughout the dermis. The fibroblasts remodelled and cross-linked the dermal matrix during the one-week culturing period, which resulted in the formation of a dermal equivalent which is capable to support the developing epidermal equivalent [46, 47]. Despite the higher collagen concentration in the dermal equivalent of hC-FTMs, no major differences in collagen type I and III expression is deciphered. A proper collagen fibril formation in hC-FTMs is also supported by the expression of the small proteoglycan decorin in comparable levels as in the FTMs [48, 49].

As we solubilized human collagen to form the dermal extracellular matrix, the original microstructure of the dermis is not preserved in the hC-FTM, in contrast to skin models using DED as scaffold [19]. However, the morphogenesis of the hC-FTM is comparable to the morphogenesis of the DED models with centrifugal fibroblast seeding approach regarding the proliferation, differentiation programs and epidermal activation [19]. Major advantages of the hC-FTMs over the DED skin models are the circumvention of uncontrolled variation in dermal thickness and limited availability [34]. Another animal material free skin model is the fibroblast derived matrix model (FDM). In this model, the dermal scaffold is formed by secretion of matrix proteins by the fibroblast itself over time. The FDM mimics the NHS to the same extent as the FTM and hC-FTM, regarding epidermal morphogenesis [34] and epidermal barrier formation [8]. However, FDMs are more suitable for long-term cultures since collagen models often show severe contraction over time. In contrast, the major advantage of the hC-FTM is the shorter time period for the formation of the dermal equivalent.

In between the dermal and epidermal equivalent of the hC-FTM, a functional basement membrane is formed. This observation is consistent with the BM formation in FTMs, which is also previous reported [9, 49, 50]. Furthermore, the epidermis of the hC-FTM is well organized, in line with pioneering work of Auger *et al.* [51]. In hC-FTMs, the proliferation rate in the basal cell layer is equal and the execution of the differentiation program is similar to FTMs. Activation of the epidermis is comparable between hC-FTM and FTM, but elevated as compared to NHS.

In vitro barrier formation is determined through assessment of the SC lipid matrix composition and lamellar organization. The detection of the twelve well-known CER subclasses with concomitant wide distribution in CER carbon chain lengths in both FTM types indicates that the synthesis of CERs resembles that of NHS to a high degree [52, 53]. When focusing on the differences between the FTM and hC-FTM, only minor variations are detected in the CER carbon chain length distribution and in the CER subclass profile. The relative abundance of CER[EO] was underestimated in this study, since the unsaturated CER[EO] was not included in the analysis and no quantification occurred. Nonetheless, the conclusions of this study are not affected by this. When comparing the CER chain length and CER subclass distribution of the FTM types to NHS, elevated C34 CER[non-EO], a higher abundance of CER NS and CER AS and a lower level of CER NP are observed, similarly as previously reported [11, 50, 52]. The small changes in lipid composition did not alter the lamellar organization. In both FTMs and hC-FTMs, a LPP with a repeat distance of approximately 12.2 nm is observed which is similar as reported previously [50, 54]. Yet, there is still a gap to bridge to resemble the NHS in which the LPP is organized with a repeat distance of approximate 13 nm [39].

In conclusion, this comprehensive study shows that usage of human collagen in the dermal matrix leads to similar epidermal morphogenesis, barrier lipid composition and organization as conventional FTMs. For future work, the limited availability of human dermis as collagen source could be overcome through usage of recombinant human collagen [55, 56]. Further optimization of the composition and microstructure of the dermal matrix could lead to enhanced dermal and epidermal functionality and concomitant epidermal barrier formation. The developed animal component free hC-FTM can be used as promising tool to investigate native stromal interactions and contributes to innovative animal-free research.

5. Acknowledgements

This research was financially supported by Dutch Technology Foundation STW (grant no. 13151) , which is part of the Netherlands Organisation for Scientific Research (NWO), and which is partly funded by the Ministry of Economic Affairs. We like to thank Gert Gooris for performing the X-ray diffraction experiments and performing the analysis and the personnel at the DUBBLE beam line (BM26) at the ESRF for their support with the X-ray measurements. We thank the company Evonik (Essen, Germany) for their generous provision of CERs.

6. Author Disclosure Statement

No competing financial interests exist.

7. References

1. Organisation for Economic Co-operation and Development. Guidance Document for the Conduct of Skin Absorption Studies—OECD Series in Testing and Assessment. Number 28, 2004.
2. Organisation for Economic Co-operation and Development. Guideline for the Testing of Chemicals. Skin Absorption: In Vitro Method. Number 428, 2004
3. Kielhorn, J. and I. Mangelsdorf, Dermal absorption. 2006: World Health Organization.
4. Schmook, F.P., J.G. Meingassner, and A. Billich, Comparison of human skin or epidermis models with human and animal skin in in-vitro percutaneous absorption. International journal of pharmaceutics, 2001. **215**(1): p. 51-56.
5. Godin, B. and E. Touitou, Transdermal skin delivery: predictions for humans from in vivo, ex vivo and animal models. Advanced drug delivery reviews, 2007. **59**(11): p. 1152-1161.
6. Thakoersing, V.S., et al., Nature versus nurture: does human skin maintain its stratum corneum lipid properties in vitro? Experimental dermatology, 2012. **21**(11): p. 865-870.
7. De Wever, B., S. Kurdykowski, and P. Descargues, Human skin models for research applications in pharmacology and toxicology: Introducing NativeSkin®, the "missing link" bridging cell culture and/or reconstructed skin models and human clinical testing. Applied In Vitro Toxicology, 2015. **1**(1): p. 26-32.
8. Thakoersing, V.S., et al., Unraveling barrier properties of three different in-house human skin equivalents. Tissue Engineering Part C: Methods, 2011. **18**(1): p. 1-11.
9. Reijnders, C.M., et al., Development of a Full-Thickness Human Skin Equivalent In Vitro Model Derived from TERT-Immortalized Keratinocytes and Fibroblasts. Tissue Engineering Part A, 2015. **21**(17-18): p. 2448-2459.
10. El Ghalbzouri, A., et al., Fibroblasts facilitate re-epithelialization in wounded human skin equivalents. Laboratory investigation, 2004. **84**(1): p. 102-112.
11. Thakoersing, V.S., et al., Increased presence of monounsaturated fatty acids in the stratum corneum of human skin equivalents. Journal of Investigative Dermatology, 2013. **133**(1): p. 59-67.
12. Tfayli, A., et al., Comparison of structure and organization of cutaneous lipids in a reconstructed skin model and human skin: spectroscopic imaging and chromatographic profiling. Experimental dermatology, 2014. **23**(6): p. 441-443.
13. Ponec, M., et al., Lipid and ultrastructural characterization of reconstructed skin models. International Journal of Pharmaceutics, 2000. **203**(1–2): p. 211-225.
14. Development, O.f.E.C.-o.a., Test No. 431: In Vitro Skin Corrosion: Reconstructed Human Epidermis (Rhe) Test Method. 2004.
15. El Ghalbzouri, A., et al., Leiden reconstructed human epidermal model as a tool for the evaluation of the skin corrosion and irritation potential according to the ECVAM guidelines. Toxicology in Vitro, 2008. **22**(5): p. 1311-1320.
16. Desprez, B., et al., Two novel prediction models improve predictions of skin corrosive sub-categories by test methods of OECD Test Guideline No. 431. Toxicology in Vitro, 2015. **29**(8): p. 2055-2080.
17. Lin, Y.K. and D.C. Liu, Comparison of physical–chemical properties of type I collagen from different species. Food Chemistry, 2006. **99**(2): p. 244-251.
18. Angele, P., et al., Influence of different collagen species on physico-chemical properties of crosslinked collagen matrices. Biomaterials, 2004. **25**(14): p. 2831-2841.
19. El Ghalbzouri, A., E. Lamme, and M. Ponec, Crucial role of fibroblasts in regulating epidermal morphogenesis. Cell and Tissue Research, 2002. **310**(2): p. 189-199.
20. Lamb, R. and C.A. Ambler, Keratinocytes Propagated in Serum-Free, Feeder-Free Culture Conditions Fail to Form Stratified Epidermis in a Reconstituted Skin Model. PLOS ONE, 2013. **8**(1): p. e52494.
21. Lee, D.-Y. and K.-H. Cho, The effects of epidermal keratinocytes and dermal fibroblasts on the formation of cutaneous basement membrane in three-dimensional culture systems. Archives of dermatological research, 2005. **296**(7): p. 296-302.
22. Moulin, V., et al., What's New in Human Wound-Healing Myofibroblasts?, in Tissue Repair and Fibrosis: The Role of the Myofibroblast, A. Desmoulière and B. Tuchweber, Editors. 1999, Springer Berlin Heidelberg: Berlin, Heidelberg. p. 123-133.
23. Gangatirkar, P., et al., Establishment of 3D organotypic cultures using human neonatal epidermal cells. Nat. Protocols, 2007. **2**(1): p. 178-186.
24. Mori, N., Y. Morimoto, and S. Takeuchi, Skin integrated with perfusable vascular channels on a chip. Biomaterials, 2017. **116**: p. 48-56.

25. Varkey, M., J. Ding, and E.E. Tredget, Differential collagen–glycosaminoglycan matrix remodeling by superficial and deep dermal fibroblasts: Potential therapeutic targets for hypertrophic scar. Biomaterials, 2011. **32**(30): p. 7581-7591.
26. Varkey, M., J. Ding, and E.E. Tredget, Fibrotic remodeling of tissue-engineered skin with deep dermal fibroblasts is reduced by keratinocytes. Tissue engineering Part A, 2013. **20**(3-4): p. 716-727.
27. Varkey, M., J. Ding, and E.E. Tredget, Superficial dermal fibroblasts enhance basement membrane and epidermal barrier formation in tissue-engineered skin: implications for treatment of skin basement membrane disorders. Tissue Engineering Part A, 2013. **20**(3-4): p. 540-552.
28. Ding, C.-M., et al., Perfusion seeding of collagen–chitosan sponges for dermal tissue engineering. Process Biochemistry, 2008. **43**(3): p. 287-296.
29. Auxenfans, C., et al., Adipose-derived stem cells (ASCs) as a source of endothelial cells in the reconstruction of endothelialized skin equivalents. Journal of tissue engineering and regenerative medicine, 2012. **6**(7): p. 512-518.
30. Boehnke, K., et al., Effects of fibroblasts and microenvironment on epidermal regeneration and tissue function in long-term skin equivalents. European journal of cell biology, 2007. **86**(11): p. 731-746.
31. Muffler, S., et al., A Stable Niche Supports Long-Term Maintenance of Human Epidermal Stem Cells in Organotypic Cultures. Stem Cells, 2008. **26**(10): p. 2506-2515.
32. Stark, H.-J., et al., Authentic fibroblast matrix in dermal equivalents normalises epidermal histogenesis and dermo-epidermal junction in organotypic co-culture. European journal of cell biology, 2004. **83**(11-12): p. 631-645.
33. Janson, D., et al., Papillary fibroblasts differentiate into reticular fibroblasts after prolonged in vitro culture. Experimental dermatology, 2013. **22**(1): p. 48-53.
34. El Ghalbzouri, A., et al., Replacement of animal-derived collagen matrix by human fibroblast-derived dermal matrix for human skin equivalent products. Biomaterials, 2009. **30**(1): p. 71-78.
35. Sriram, G., P.L. Bigliardi, and M. Bigliardi-Qi, Fibroblast heterogeneity and its implications for engineering organotypic skin models in vitro. European journal of cell biology, 2015. **94**(11): p. 483-512.
36. Madison, K.C., Barrier function of the skin:"la raison d'etre" of the epidermis. Journal of Investigative Dermatology, 2003. **121**(2): p. 231-241.
37. Van Smeden, J., et al., The important role of stratum corneum lipids for the cutaneous barrier function. Biochimica et Biophysica Acta (BBA)-Molecular and Cell Biology of Lipids, 2014. **1841**(3): p. 295-313.
38. Janssens, M., et al., Increase in short-chain ceramides correlates with an altered lipid organization and decreased barrier function in atopic eczema patients. Journal of lipid research, 2012. **53**(12): p. 2755-2766.
39. Bouwstra, J.A., et al., Structural investigations of human stratum corneum by small-angle X-ray scattering. Journal of Investigative Dermatology, 1991. **97**(6): p. 1005-1012.
40. Damien, F. and M. Boncheva, The extent of orthorhombic lipid phases in the stratum corneum determines the barrier efficiency of human skin in vivo. Journal of Investigative Dermatology, 2010. **130**(2): p. 611-614.
41. Groen, D., et al., Is an orthorhombic lateral packing and a proper lamellar organization important for the skin barrier function? Biochimica et Biophysica Acta (BBA)-Biomembranes, 2011. **1808**(6): p. 1529-1537.
42. Haisma, E.M., et al., Inflammatory and Antimicrobial Responses to Methicillin-Resistant Staphylococcus aureus in an In Vitro Wound Infection Model. PLoS ONE, 2013. **8**(12): p. e82800.
43. Mieremet, A., et al., Improved epidermal barrier formation in human skin models by chitosan modulated dermal matrices. PloS one, 2017. **12**(3): p. e0174478.
44. Boiten, W., et al., Quantitative analysis of ceramides using a novel lipidomics approach with three dimensional response modelling. Biochimica et Biophysica Acta (BBA) - Molecular and Cell Biology of Lipids, 2016. **1861**(11): p. 1652-1661.
45. Wolf, K., et al., Collagen-based cell migration models in vitro and in vivo. Seminars in cell & developmental biology, 2009. **20**(8): p. 931-941.
46. Grinnell, F. and C.R. Lamke, Reorganization of hydrated collagen lattices by human skin fibroblasts. Journal of Cell Science, 1984. **66**(1): p. 51-63.
47. Grinnell, F. and W.M. Petroll, Cell motility and mechanics in three-dimensional collagen matrices. Annual review of cell and developmental biology, 2010. **26**: p. 335-361.
48. Zhang, G., et al., Decorin regulates assembly of collagen fibrils and acquisition of biomechanical properties during tendon development. Journal of cellular biochemistry, 2006. **98**(6): p. 1436-1449.
49. El Ghalbzouri, A., et al., Basement membrane reconstruction in human skin equivalents is regulated by fibroblasts and/or exogenously activated keratinocytes. Journal of investigative dermatology, 2005. **124**(1): p. 79-86.

50. van Drongelen, V., et al., Barrier Properties of an N/TERT-Based Human Skin Equivalent. Tissue Engineering Part A, 2014. **20**(21-22): p. 3041-3049.
51. Auger, F.A., et al., Skin equivalent produced with human collagen. In Vitro Cellular & Developmental Biology-Animal, 1995. **31**(6): p. 432-439.
52. van Smeden, J., et al., LC/MS analysis of stratum corneum lipids: ceramide profiling and discovery. Journal of lipid research, 2011. **52**(6): p. 1211-1221.
53. Masukawa, Y., et al., Characterization of overall ceramide species in human stratum corneum. Journal of lipid research, 2008. **49**(7): p. 1466-1476.
54. Bouwstra, J., G. Gooris, and M. Ponec, The Lipid Organisation of the Skin Barrier: Liquid and Crystalline Domains Coexist in Lamellar Phases. Journal of Biological Physics, 2002. **28**(2): p. 211-223.
55. Yang, C., et al., The application of recombinant human collagen in tissue engineering. BioDrugs, 2004. **18**(2): p. 103-119.
56. Yigit, S., N. Dinjaski, and D.L. Kaplan, Fibrous proteins: At the crossroads of genetic engineering and biotechnological applications. Biotechnology and bioengineering, 2015.
57. van Smeden, J., et al., Combined LC/MS-platform for analysis of all major stratum corneum lipids, and the profiling of skin substitutes. Biochimica et Biophysica Acta (BBA)-Molecular and Cell Biology of Lipids, 2014. **1841**(1): p. 70-79.

8. Supplementary Materials and Methods

8.1. Morphological and immunohistochemical analyses

8.1.1. Tissue preservation

To cryofixate samples, these were placed in a gelatine capsule containing Tissue-Tek® O.C.T.™ Compound (Sakura Finetek Europe B.V., Alphen aan den Rijn, The Netherlands) and snap frozen in liquid nitrogen. To paraffin embed the samples, these were fixed in 4% (w/v) formaldehyde solution (Added Pharma, Oss, The Netherlands), dehydrated and paraffin embedded.

8.1.2. Immunohistochemical analyses

Morphology analysis was performed on 5 µm paraffin embedded tissue cross-sections after staining with haematoxylin and eosin (HE; Klinipath, Duiven, The Netherlands). Immunohistochemical analyses of protein biomarkers Ki67 and the keratins 6, 10, 16 and 17 were performed on 5 µm paraffin embedded tissue sections. After deparaffinization and rehydration, heat-mediated antigen retrieval in citrate buffer occurred. Immunohistochemical analyses of collagen type I, III and VII were performed on 5 µm sliced cryofixated tissue sections after 10 min acetone fixation. Blocking occurred with 2% normal human serum (Sanquin, Leiden, The Netherlands). Stainings were performed using the streptavidin-biotin-peroxidase system (GE Healthcare, Buckinghamshire, United Kingdom), according to the manufacturer's instructions. Stainings were visualized with 3-amino-9-ethylcarbazole (AEC), counterstained with haematoxylin and sealed with Kaiser's glycerine. Specifications of primary and secondary antibodies are provided in **supplementary table 1**. Visualization of the sections occurred using a light microscope (Zeiss Axioplan 2, Zeiss, The Netherlands).

8.1.3. Immunofluorescence stainings

Immunofluorescence analyses of collagen type IV was performed on 5 µm paraffin embedded tissue sections followed by a 0.025% protease (Sigma) treatment for antigen retrieval. Immunofluorescence stainings of decorin, vimentin and laminin 332 were performed on 5 µm cryofixated sections which were dried overnight and initiated after 10 min acetone fixation. Blocking occurred with 2% normal human serum. Specifications of primary and secondary antibodies are provided in **supplementary table 1**. Sections were sealed with Vectashield containing DAPI (Vector Laboratories, The Netherlands). Imaging of the samples was performed using a fluorescence microscope (Leica CTR5000, Leica, The Netherlands).

8.2. Estimation of the proliferation index

The proliferation index (PI) was determined by counting the number of Ki67 positive nuclei among the total number of cells in the basal layer. A minimum of 100 basal cells were counted at three different regions of each section. The

resulted proliferation index indicates the percentage of positive stained nuclei. Data is presented as the mean of eight independent experiments and three NHS donors ±SD.

8.3. Counting the number of corneocyte layers in stratum corneum

Snap-frozen sections were sliced 5 µm using a cryotome (Leica CM3050S), dried overnight and fixed in acetone for ten min. Sections were stained for one min with a 1% (w/v) safranin O (Sigma) solution dissolved in Millipore water. After water washout, a 2% (w/v) KOH solution was applied on the sections for 25 min for NHS and 15 min for the FTMs to induce swelling of the corneocytes. Images were obtained right after enclosure with a cover glass at 400x magnification and SC layers were counted on at least four images each sample [43].

8.4. Stratum corneum isolation

The SC of both FTM types was isolated after overnight tissue incubation with a 0.1% (w/v) trypsin/PBS solution at 4°C followed by incubation at 37°C for 1 hr. The SC was peeled off and washed in a 0.1% trypsin inhibitor solution followed by sufficient Millipore water washing steps. The isolated SC was air-dried and stored in dry and inert conditions.

8.5. Small angle X-ray diffraction

Small-angle x-ray diffraction (SAXD) measurements were performed at the European Synchrotron Radiation Facility (ESRF, Grenoble, France) at station BM26B. After 24 hr hydration of the SC over a 27% (w/v) NaBr solution, the diffraction patterns were detected with a Frelon 2000 charge-coupled device (CCD) detector. This was done at room temperature for a period of 2 x 150 sec. Calculations of the repeat distance of the lamellar phase occurred as described in detail before [39, 41].

8.6. Lipid extraction and LC-MS analysis

Extraction of all the SC lipids was performed based on an adjusted Bligh and Dyer method as described by Boiten *et al.* [44]. The weight percentage of lipids in the SC was determined by measuring the SC dry weight before and after the lipid extraction. After extraction, solvents were evaporated under a gentle stream of nitrogen at 40°C. The obtained lipids were dissolved in a suitable volume of heptane:chloroform:methanol (95:2.5:2.5 v:v:v). The lipids were analysed by liquid chromatography – mass spectrometry (LC-MS) according to methods described elsewhere [57] and modified by Boiten *et al.* [44]. Briefly, CERs were separated and detected with an Acquity UPLC H-class (Waters, Milford, MA, USA) coupled to an XEVO TQ-S mass spectrometer (Waters). Separation of CERs occurred in normal phase on a PVA-Sil column (5 µm particles, 100 x 2.1 mm i.d.)(YMC, Kyoto, Japan) using a gradient starting with 98% heptane towards 50% (Hep:IPA:EtOH,

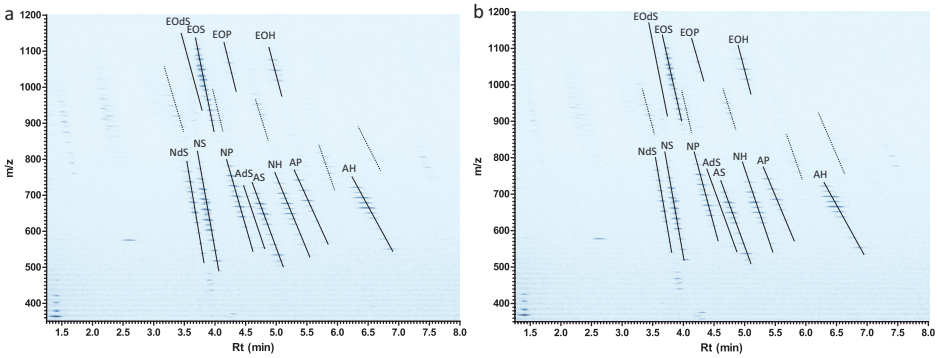
50:25:25, v:v:v) [57] and a flow rate of 0.8 mL/min. Detection was performed using APCI in positive ion mode, measuring in full scan from mass 350-1200 between 1.25-12.5 min. The total lipid concentration of all samples was set at 0.3 mg/mL and the injection volume was set to 5 µL. Monoisotopic integration has been performed. Presented values are AUCs divided by the internal standard (INST) of CER N(24deuterated)S(18).

Supplementary table 1. Specifications of antibodies used for immunohistochemical and immunofluorescence staining

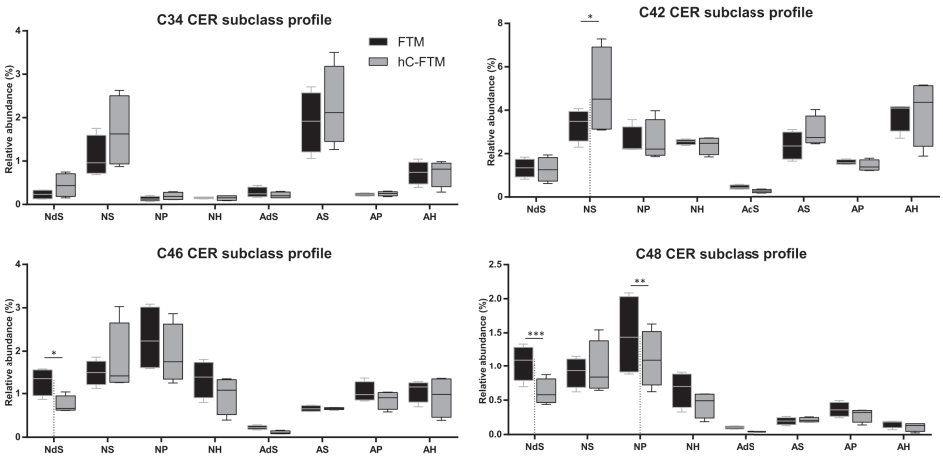
Immunohistochemistry	Origin	Clone	Dilution	Secondary antibody	Manufacturer
Primary antibody					
Ki67	Mouse	MIB1	1:100	A	DAKO, Denmark
Cytokeratin 6	Mouse	KS6.KA12	1:100	A	Sanbio BV, The Netherlands
Cytokeratin 10	Mouse	DE-K10	1:50	A	Labvision/Neomarkers, USA
Cytokeratin 16	Mouse	LL025	1:50	A	Serotec, UK
Cytokeratin 17	Mouse	CK-E3	1:25	A	Novus Biologicals, USA
Collagen type I	Goat	polyclonal	1:20	B	Southern Biotechnology, USA
Collagen type III	Goat	polyclonal	1:20	B	Southern Biotechnology, USA
Collagen type VII	Mouse	LH7.2	1:15	A	Chemicon, Australia
Secondary antibody					
A) Biotinylated goat anti-mouse	Goat		1:200		Southern Biotechnology, USA
B) Biotinylated rabbit anti-goat	Rabbit		1:200		DAKO, Denmark
Immunofluorescence	**Origin**	**Clone**	**Dilution**	**Secondary antibody**	**Manufacturer**
Primary antibody					
Loricrin	Rabbit	AF62	1:1000	C	Covance, The Netherlands
Vimentin	Mouse	V6630	1:50	D	Sigma-aldrich, The Netherlands
Decorin	Rabbit	polyclonal	1:1000	C	GeneTex, Taiwan

Supplementary table 1 (continued)

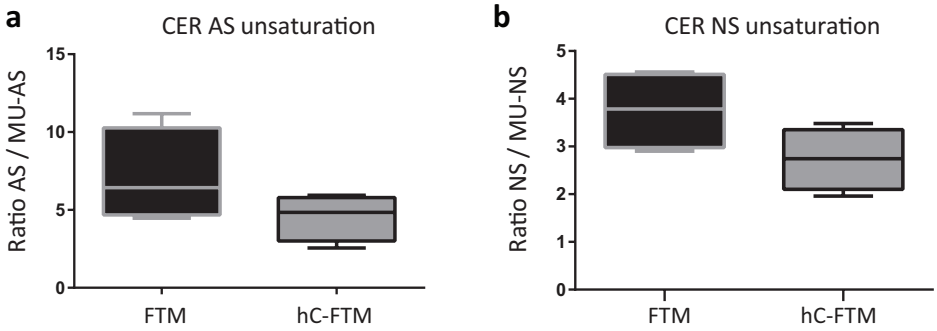
Immunofluorescence	Origin	Clone	Dilution	Secondary antibody	Manufacturer
Secondary antibody					
C) Cy3-conjugated anti-rabbit	Goat		1:500		Jackson immunoresearch Laboratory, USA
D) Cy3-conjugated anti-mouse	Goat		1:1000		Jackson immunoresearch Laboratory, USA



Supplementary figure 1. Ion map of the ceramides isolated from the stratum corneum after separation and detection with LC-MS. The location and nomenclature of the twelve well-known ceramide subclasses are provided for the FTM (a) and the hC-FTM (b). Dashed lines indicate unknown lipid entities. Data is obtained from four independent experiments.



Supplementary figure 2. Ceramide subclass profile of FTMs and hC-FTMs. Box and whisker plot with indicated median of the relative abundance of indicated CERs, as percentage of the relative abundance of total AUC/INST of all CERs. In hC-FTMs, an increase in the relative abundance of C42 CER NS, a decrease in C46 CER NdS and a decrease in C48 CER NdS and NP is detected and indicated by a dotted line. Whiskers indicate the 95% confidence interval. Data is obtained from four independent experiments.



Supplementary figure 3. Unsaturation index of ceramide subclasses AS and NS in FTMs and hC-FTMs. Box and whisker plot with indicated median of the ratio between saturated and mono-unsaturated (MU) CERs. Whiskers indicate the 95% confidence interval. Data is obtained from four independent experiments.

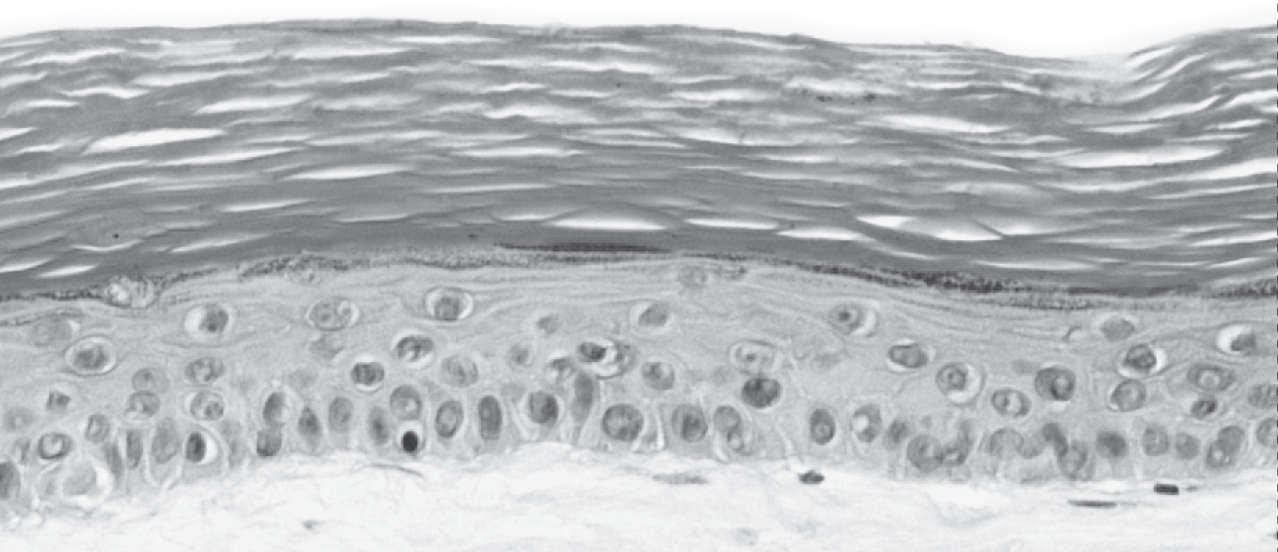
3

Improved epidermal barrier formation in human skin models by chitosan modulated dermal matrices

Arnout Mieremet
Marion Rietveld
Samira Absalah
Jeroen van Smeden
Joke A. Bouwstra[+]
Abdoelwaheb El Ghalbzouri[+]

[+] Joint senior authorship

PLoS ONE 12(3): e0174478: 1-20
(2017)



Abstract

Full thickness human skin models (FTMs) contain an epidermal and a dermal equivalent. The latter is composed of a collagen dermal matrix which harbours fibroblasts. Current epidermal barrier properties of FTMs do not fully resemble that of native human skin (NHS), which makes these human skin models less suitable for barrier related studies. To further enhance the resemblance of NHS for epidermal morphogenesis and barrier formation, we modulated the collagen dermal matrix with the biocompatible polymer chitosan. Herein, we report that these collagen-chitosan FTMs (CC-FTMs) possess a well-organized epidermis and maintain both the early and late differentiation programs as in FTMs. Distinctively, the epidermal cell activation is reduced in CC-FTMs to levels observed in NHS. Dermal-epidermal interactions are functional in both FTM types, based on the formation of the basement membrane. Evaluation of the barrier structure by the organization of the extracellular lipid matrix of the stratum corneum revealed an elongated repeat distance of the long periodicity phase. The ceramide composition exhibited a higher resemblance to NHS, based on the carbon chain-length distribution and subclass profile. The inside-out barrier functionality indicated by the transepidermal water loss is significantly improved in the CC-FTMs. The expression of epidermal barrier lipid processing enzymes is marginally affected, although more restricted to a single granular layer. The novel CC-FTM resembles the NHS more closely, which makes it a promising tool for epidermal barrier related studies.

1. Introduction

Human skin equivalents (HSEs) are *in vitro* developed three dimensional models of the human skin, resembling many characteristics of the native human skin (NHS). Applications of HSEs include basic research about skin biology, skin diseases, and determination of the toxicological profile of novel molecular entities. Furthermore, HSEs are reliable alternative to animal testing [1]. However, the barrier functionality of current HSEs deviates from NHS, which potentially causes ambiguity for the *in vitro* - *in vivo* correlation. To improve the applicability of HSEs, these should mimic the barrier formation and organization of NHS more closely.

The permeability barrier function of the human skin relies mainly on the outermost layer of the epidermis, in which the corneocytes are embedded in a lipid matrix, known as the stratum corneum (SC). The lipid matrix in the SC is the only continuous pathway for compound penetration and is therefore important in the functionality of the skin barrier. Major constituents of the lipid matrix are ceramides (CERs), free fatty acids (FFAs) and cholesterol. The CERs consist of a large number of subclasses, based on the type of sphingoid base coupled to a specific fatty acid chain [2]. Within the SC, the FFA and CER subclasses span a broad characteristic range of entities, based on the carbon chain length and head group architecture [3, 4]. Together, the SC lipids are highly organized and form crystalline lamellar phases. Both a short periodicity phase (SPP) with a repeat distance of around 6 nm and a long periodicity phase (LPP) with a repeat distance of around 13 nm are present in the SC of NHS [5, 6].

When comparing the SC lipid matrix of HSEs to that of NHS, many similarities are observed. Amongst others, the presence of the twelve well-known CER subclasses is similar, which are detected in NHS as well as in the HSEs [7]. The differences include the increased level of monounsaturated CERs and FFAs, reduced carbon chain lengths of CERs and FFAs, and an altered CER subclass profile [7, 8]. Consequently, the SPP is not formed, the LPP repeat distance is reduced, and the lateral packing of the lipids is less dense (hexagonal) compared to NHS (primarily orthorhombic) [8]. According to our hypothesis, these deviations in the lipid matrix reduce the permeability barrier in HSEs, including increased transepidermal water loss (TEWL) [8, 9]. Furthermore, in HSEs the epidermal homeostasis is altered, based on the expression of the hyper-proliferative associated marker keratin 16 (K16), the altered localization of terminal differentiation markers [8, 10, 11] and several lipid processing enzymes [7].

A widely used type of HSE is the full thickness human skin model (FTM), which consists of primary fibroblasts in the dermal equivalent and primary

keratinocytes in the epidermal equivalent. Incorporation of both dermis and epidermis resembles the NHS tissue architecture to a high extent. In FTMs, the fibroblast-keratinocyte cross talk is essential for epidermal morphogenesis and formation of the basement membrane (BM) [12]. This BM directs the polarity, proliferation, differentiation and migration of the keratinocytes.

Several types of dermal equivalents are described, where the dermal matrix ranges from artificial scaffolds [13, 14], fibroblast-derived dermal matrix [15] to de-epidermised or de-cellularised dermis [16, 17]. Each offers its advantages and disadvantages, as each dermal matrix affects the attachment, morphology and activity of the incorporated fibroblasts. Due to the dermal-epidermal cross talk, the dermal matrix could have a high impact on the epidermal homeostasis and barrier formation [18, 19]. Therefore, modulation of the dermal matrix offers an interesting method to enhance the barrier formation in HSEs.

The aim of this study is to advance the resemblance to native skin architecture and barrier properties in FTMs by modulating the dermal matrix. For this purpose, the dermal matrix of the FTM is modulated with the biopolymer chitosan to enhance the functionality of the dermal matrix. This approach resulted in the development of the collagen-chitosan full thickness human skin model (CC-FTM). Chitosan is biodegradable, easily available and serves as an excellent substrate for cell adhesion [20]. Ionic interactions between the amine groups of chitosan and the carboxyl groups of the collagen will form a stabilized dermal matrix during preparation [21-23]. In addition, during CC-FTM development, cationic sites on the chains of chitosan are still present and could benefit cellular adhesion [24]. The biocompatibility of chitosan in HSEs has been demonstrated by the reported incorporation of chitosan in a sponge-like dermal matrix [25-27]. Incorporation of chitosan in the dermal matrix potentially enhances the functionality of the dermal and epidermal equivalent and therefore could be advantageous for the overall homeostasis and ultimately the barrier formation.

In this study, evaluations between the novel CC-FTM, the established FTM and NHS have been performed regarding epidermal morphology, proliferation, differentiation programs, BM formation and barrier lipid processing enzymes. Detailed analyses of the SC lipid characteristics and barrier functionality revealed improved epidermal barrier formation in the novel FTM type.

2. Materials and methods

2.1. Primary cell isolation and culture

Isolation of primary human fibroblasts and keratinocytes was performed from surplus human breast skin [15]. Declaration of Helsinki principles are followed

with obtainment of primary human skin cells from healthy donors, exactly as stated and described before [28]. Once fat tissue was removed, the dermis and epidermis were separated after overnight incubation of the skin in 2.4 U/mL dispase II (Roche, Almere, The Netherlands). Primary keratinocytes were isolated from the epidermis after treatment with 0.05% (w/v) trypsin (BD Falcon, Breda, The Netherlands) and cultured as described before [15]. Primary fibroblasts were isolated after incubation of the dermis in a 3:1 (w/w) mixture of collagenase (Gibco, Landsmeer, The Netherlands) and dispase II (Roche) for 2 hr at 37°C and cultured as described before [15, 29]. All isolated primary cells were tested and found negative for mycoplasma contamination.

2.2. Dermal equivalent preparation

2.2.1. Fibroblast-populated collagen matrix

Development of dermal equivalents was performed as described earlier [8]. The hydrated collagen (4 mg/mL) was isolated from rat tail tendons. Obtainment of rat tail tendons occurred as described before [28]. Below a 1 mL cell-free collagen mixture with on top a 3 mL fibroblasts containing mixture (1.2-1.5 x 10^5 fibroblasts in each dermal equivalent) were produced onto filter inserts (Corning Transwell cell culture inserts, membrane diameter 24 mm, pore size 3 µm; Corning Life Sciences, The Netherlands) and allowed to polymerize at 37°C. After polymerization, the dermal equivalents were cultured as described elsewhere [8, 29] with fresh supplementation of 45 µM vitamin C (Sigma).

2.2.2. Fibroblast-populated collagen-chitosan matrix

Chitosan (cat. no. 448877, Sigma) was dissolved in 0.1% acetic acid at 4°C. Based on pilot studies, a final chitosan concentration of 5 mg/mL was used. The collagen-chitosan dermal equivalent was generated in a single step by mixing the 4 mg/mL collagen solution with the 5 mg/mL chitosan solution in a 3:1 (v/v) ratio, HBSS, 1M NaOH and a fibroblast containing FBS solution. Four mL of this mixture (equals 1.3-1.6 x 10^5 cells fibroblasts each dermal equivalent) was allowed to polymerize at 37°C. Subsequently, equal procedures were followed as the fibroblast-populated collagen matrix.

2.3. Generation of FTMs

Primary keratinocytes (2.5 x 10^5/model) in their first passage were seeded onto each dermal equivalent as described before [8, 29]. The FTMs were kept submerged for total of four days. Hereafter, the FTMs were lifted to the air-liquid interface and developed for 14-17 days [30].

2.4. Tissue imaging

2.4.1. Fixation of the tissue

Cross-sections of each FTM were either snap frozen for cryofixation or fixated with formaldehyde for paraffin embedding. For cryofixation, the tissue was placed in a gelatine capsule containing Tissue-Tek® O.C.T.™ Compound (Sakura Finetek Europe B.V., Alphen aan den Rijn, The Netherlands) and snap frozen in liquid nitrogen. For paraffin embedding, the tissue was fixed in 4% (w/v) formaldehyde (Added Pharma, Oss, The Netherlands), dehydrated and embedded in paraffin.

2.4.2. Immunohistochemical analyses

General morphological analysis was performed with 5 µm paraffin embedded tissue sections through staining with haematoxylin and eosin (HE; Klinipath, Duiven, The Netherlands). Immunohistochemical analyses of Ki67, keratin 10 and 16 were performed on 5 µm paraffin embedded tissue sections. After deparaffinization and rehydration, heat-mediated antigen retrieval in citrate buffer was performed, followed by blocking with 2% normal human serum (Sanquin, Leiden, The Netherlands). Stainings were performed using the streptavidin-biotin-peroxidase system (GE Healthcare, Buckinghamshire, United Kingdom), according to the manufacturer's instructions. Stainings were visualized with 3-amino-9-ethylcarbazole (AEC), counterstained with haematoxylin and sealed with Kaiser's glycerine. Specifications of the primary and secondary antibodies are provided in **supplementary table 1**. Visualization of the sections occurred using a light microscope (Zeiss Axioplan 2, Zeiss, The Netherlands).

2.4.3. Immunofluorescence analyses

Immunofluorescence staining of loricrin, collagen type IV, β-glucocerebrosidase (GBA), acid sphingomyelinase (aSMase), ceramide synthase 3 (CER-S3) and elongation of very long chain fatty acids protein 1 (ELOVL1) was performed with 5 µm formalin-fixed paraffin embedded sections. After deparaffinization and rehydration, heat-mediated antigen retrieval in citrate buffer was performed and followed by blocking with 2% normal human serum (Sanquin). During the collagen type IV staining, a protease treatment using a 0.025% protease solution (Sigma) was performed before incubation with the primary antibody. The sections were incubated with the primary antibody overnight at 4°C directly after blocking. After phosphate-buffered saline (PBS) washout secondary antibody was applied for 1 hr at RT and subsequently the sections were mounted with Vectashield containing DAPI for visualization of the nuclei (Vector Laboratories, The Netherlands). Immunofluorescence stainings of vimentin and laminin 332 were performed on 5 µm thick frozen sections, which were dried overnight and fixed in acetone for 10 min. Primary and secondary antibody application is equal as paraffin embedded sections as well as mounting. Visualization of the

sections occurred using a fluorescence microscope (Leica CTR5000, Leica, The Netherlands).

2.5. Determination of the epidermal thickness and proliferation index

The epidermal thickness was determined through quantification of eight images of each FTM type of various tissue regions after HE staining with 200x magnification. The outline of the epidermal area was determined with Adobe Photoshop (CS6 version 13.0) and the number of pixels in the epidermal area was measured. This was transformed to the area in squared micrometres. The proliferation index (PI) was determined by counting the number of Ki67 positive nuclei among the total number of cells in the basal layer. A minimum of 100 basal cells were counted at three different regions of each section. The resulting proliferation index is the percentage of positive stained nuclei. For both estimations, the data is presented as the mean of four independent experiments ±SD.

2.6. Counting stratum corneum layers

Cryofixated sections were sliced 5 µm using a cryotome (Leica CM3050S), dried overnight and fixed in acetone for 10 min. Sections were stained for one min with a 1% (w/v) safranin O (Sigma) solution dissolved in Millipore water. After water washout, a 2% (w/v) KOH solution was applied on the sections for 25 min to swell the corneocytes. After removal of the KOH solution, the glass slides were washed with Millipore water and enclosed with Kaiser's glycerine. Images were obtained with 400x magnification.

2.7. Stratum corneum isolation

The SC of FTMs was isolated through overnight incubation with a 0.1% (w/v) trypsin/PBS solution at 4°C followed by incubation at 37°C for 1 hr. The SC was isolated and washed with 0.1% trypsin inhibitor and Millipore water. The SC was air-dried and stored under Argon gas over silica until further use.

2.8. Small angle X-ray diffraction analysis

Small-angle x-ray diffraction (SAXD) measurements were performed at the European Synchrotron Radiation Facility (ESRF, Grenoble, France) at station BM26B as described in detail elsewhere [31]. The SC was hydrated over a 27% (w/v) NaBr solution during 24 hr at RT. SAXD patterns were detected with a Frelon 2000 charge-coupled device (CCD) detector at RT for a period of 2 x 150 sec. The scattering intensity (I) was measured as a function of the scattering vector q (in reciprocal nm). The latter is defined as $q=(4\pi\sin\theta)/\lambda$, in which θ is the scattering angle and λ is the wavelength. From the positions of a series of equidistant peaks (located at q_n), the periodicity, or d-spacing, of a lamellar phase was calculated using the equation $q_n=2n\pi/d$, n being the order number of the diffraction peak

[5]. The repeat distance of the lamellar phases was calculated based on the first, second and third order diffraction peak of the lamellar phase.

2.9. Lipid extraction and LC-MS analysis

Extraction of total SC lipids was performed based on an adjusted Bligh and Dyer method as described by Boiten *et al.* [32]. To determine the weight percentage of lipids in the SC, dry SC weight was measured before and after extraction. Nomenclature of the CER subclasses is followed according to Motta *et al.* [2] and listed (**Supplementary fig. 1**) [33, 34]. To analyse the CER subclasses and chain length distribution in each of the subclasses, the organic phase was collected and evaporated under a stream of nitrogen at 40°C. The obtained lipids were dissolved in a suitable volume of heptane:chloroform:methanol (95:2.5:2.5 v:v:v). The lipids were analysed by liquid chromatography – mass spectrometry (LC-MS) according to the method described elsewhere ([35] modified by Boiten *et al.* [32]). Briefly, CERs were separated and detected with an Acquity UPLC H-class (Waters, Milford, MA, USA) coupled to an XEVO TQ-S mass spectrometer (Waters, Milford, MA, USA). Separation of CERs occurred in normal phase on a PVA-Sil column (5 µm particles, 100 x 2.1 mm i.d.)(YMC, Kyoto, Japan) using a gradient starting with 98% heptane towards 50% (Hep:IPA:EtOH, 50:25:25, v:v:v) [35]. A flow rate of 0.8 mL/min was used. Detection was performed using APCI in positive ion mode, measuring in full scan from mass 350-1200 between 1.25-12.5 min. The total lipid concentration of all samples was around 0.3 mg/mL and the injection volume was set to 5 µL. Relative abundance of the FTMs and CC-FTMs was determined through quantification of the AUCs followed by a correction using a single internal standard as in Boiten *et al.* [32]. Relative abundance of benchmark values for NHS was determined based on quantification of the AUCs of a mixture of lipid extracts from eight different donors.

2.10. Transepidermal water loss measurements

Isolated SC was placed in a flow-through diffusion cells (PermeGear, Inc, Bethlehem, USA) filled with Millipore water with tubes connected to prevent the diffusion cell to leak or dry out. After a 30 min incubation period, the closed chamber evaporimeter (Aqua Flux AF200: Biox Systems Ltd, London, UK) [36] was placed on top of the SC for 15 min. Next, transepidermal water loss (TEWL) measurements were performed after every 20 sec during a time period of 900 sec.

2.11. Ethics statement

This ethics statement is identical to that of Haisma *et al.* [28]. All primary human skin cells from healthy donors used by the Department of Dermatology are isolated from surplus tissue collected according to article 467 of the Dutch Law on Medical Treatment Agreement and the Code for proper Use of Human Tissue of the Dutch Federation of Biomedical Scientific Societies. According to

article 467 surplus tissue can be used if no objection is made by the patient. This means that the patient who will undergo plastic surgery is well informed on the research. In case he/she refuses the patient has to sign the inform consent form, if they agree they do not sign. This approach differs from other countries. None of the authors were involved in the tissue sampling and only birth date, gender and skin type of the subjects was known. The Declaration of Helsinki principles were followed when working with human tissue. The rat tails were obtained from rats of the Animal Facility (Proef Dier Centrum) of the Leiden University Medical Center, The Netherlands. Rats came from the breeding facility, or were control animals of other studies and died by CO_2 asphyxiation. Because no living animals were used for the purpose of this study, no approval was needed from the Institutional Animal Care and Use Committee. This is in agreement with the European directive for the protection of animals used for scientific purposes (2010/63/EU).

2.12. Statistics

Statistical analyses are conducted using GraphPad Prism version 6.00 for Windows (GraphPad Software, La Jolla, CA, USA). In general, statistical significance was determined using a paired Student's t-tests or one-way ANOVA. The CER carbon chain length distribution, CER subclass profile and TEWL were statistically tested using two-way ANOVA with multiple comparison Holm-Šídák post-test. Statistical differences are noted as *, ** or ***, corresponding to $P<0.05$, <0.01, <0.001.

3. Results

3.1. Characterization of the epidermal homeostasis

To evaluate the effect of the modulated dermal matrix on epidermal organization and morphogenesis, full thickness human skin models with solely collagen as a dermal matrix (FTMs) and FTMs with the collagen-chitosan dermal matrix (CC-FTMs) are generated. After keratinocyte seeding onto the dermal matrices, these fully developed into a stratified epidermis. The epidermal morphology was evaluated and compared to NHS. Both dermal matrices enabled the formation of a well-organized epidermis, since the presence of all four epidermal strata (including stratum basale, stratum spinosum, stratum granulosum and stratum corneum (SC)) was observed (**Fig. 1 a**). However, the addition of chitosan resulted in a decreased epidermal thickness (**Fig. 1 b**), independent of the different fibroblast and keratinocyte donors used.

Next, basal cell proliferation (Ki67), early (keratin 10; K10) and late (loricrin; LOR) differentiation and the activation of the epidermis (K16) were examined, together providing information on epidermal homeostasis. Compared to

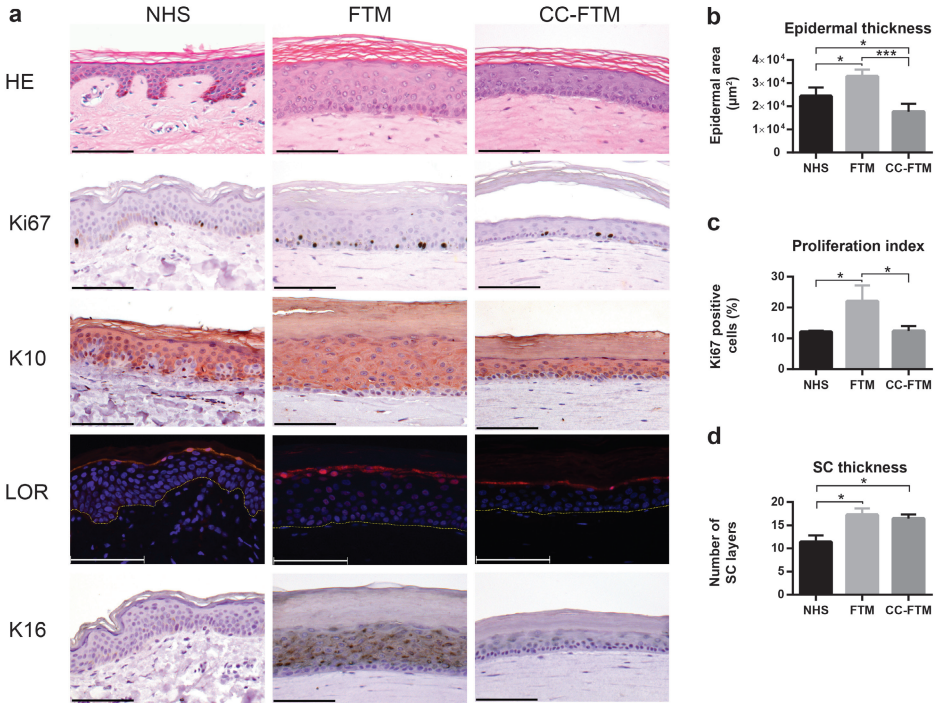


Figure 1. Epidermal morphogenesis in NHS, FTMs and CC-FTMs. (a) Cross-sections are examined for general morphology (HE), proliferation (Ki67), early (K10) and late (LOR) differentiation and epidermal cell activation (K16) using immunohistochemistry or immunofluorescence. The expression of loricrin (LOR) is depicted in red and the nuclei in blue, whereas the yellow dotted line indicates the dermal-epidermal junction. **(b)** Quantification of the epidermal thickness based on the HE staining. **(c)** Basal cell proliferation quantified based on the Ki67 positive cells in multiple regions of the epidermis. **(d)** Safranin red staining was quantified by counting the amount of corneocyte layers in the SC. Scale bar represents 100µm. *indicates $p<0.05$. Data represents mean ±SD of four independent experiments or skin donors.

FTMs the basal cell proliferation was reduced in CC-FTMs, based on the Ki67-proliferation index (PI) (**Fig. 1 c**), with a PI of 22.00 ±5.14 versus a PI of 12.33 ±1.67, respectively. The proliferation index of the CC-FTM became equal to that of NHS. The equal suprabasal expression of K10 in FTMs and CC-FTMs indicates an unaltered execution of the early differentiation program. The expression of the late differentiation marker LOR is more restricted to a single granular layer in CC-FTMs (**Fig 1 a**), more similar to NHS. A clear difference is observed when focusing on the epidermal cell activation. The expression of K16 in CC-FTMs is strongly reduced compared to FTMs and matches expression levels of NHS. Finally, the number of corneocyte layers in the SC was determined based on the safranin staining. In both FTM types, an equal number of corneocyte layers in the SC was observed (**Fig. 1 d**), which is increased as compared to NHS.

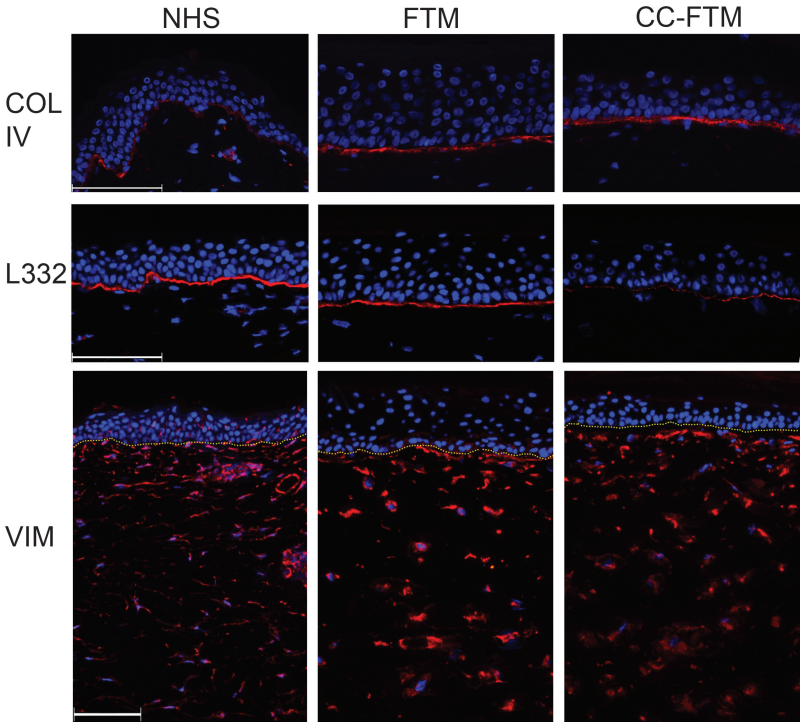


Figure 2. The dermal-epidermal linkage and fibroblast distribution. Cross-sections of NHS, FTMs and CC-FTMs are analysed by immunofluorescence. Collagen type IV (COL IV) is similarly expressed at the BM in both FTMs and CC-FTMs, while laminin 332 shows a delayed expression in CC-FTMs. Similar fibroblast distribution throughout the dermis is shown by vimentin (VIM). Proteins are visualized in red, nuclei are stained blue using DAPI and the yellow dotted line indicates the dermal-epidermal junction. Scale bar: 100 µm. Representative pictures are shown of four independent experiments.

3.2. Basement membrane formation and fibroblast distribution

Next, we examined whether the modulated dermal matrix affects the basement membrane (BM) formation. For this purpose the deposition of two BM proteins with distinct functions was examined by immunohistochemistry (**Fig. 2**). Collagen type IV, a major lamina densa structural protein, is continuously expressed at the dermal-epidermal junction in NHS and both FTM types. In contrast, the deposition of a key component of the lamina lucida/lamina densa interface, laminin 332 (L332) is reduced in CC-FTMs. To evaluate if this was a result of an altered fibroblast distribution in the chitosan-supplemented dermal matrix or a characteristic of the CC-FTMs, we examined the fibroblasts distribution using the fibroblast cytoskeleton protein vimentin (VIM). As shown in **figure 2**, VIM is detected similarly throughout the dermal matrices in both models, indicating a homogeneous distribution of fibroblasts.

3.3. Lamellar organization in the extracellular matrix of the stratum corneum

To evaluate the formation and organization of the lipid matrix in the epidermal barrier, we first studied the lamellar organization of the lipids in the stratum corneum (SC). Based on the unique X-ray diffraction pattern of the lipid lamellae, the identification and characterization of the lamellar phases was performed. In the obtained peak profile, the first, second and third orders of diffraction of the LPP were identified (**Fig. 3 a**). The repeat distance of the LPP was determined by the peak position of the first, second and third order of diffraction, which revealed elongation in CC-FTMs (**Fig. 3 b**). In addition to the LPP, the presence of crystalline cholesterol was also detected. Furthermore, an additional peak with unidentified origin was detected in the diffraction profile of the FTM, which is absent in CC-FTMs.

3.4. Lipid content and ceramide chain length distribution in CC-FTMs

After the observation that modulation of the dermal matrix positively influenced the SC lamellar organization, the total lipid content of the SC and the ceramide (CER) composition were determined. The level of total lipids in the SC of both models remained equal (**Fig. 4 a**), which suggests that the addition of chitosan to the dermal matrix did not affect the quantity of total lipids in the SC.

Subsequently, the composition of the CERs of both FTM types was investigated, to provide more insight in the barrier formation. To this end, the lipids were extracted from the isolated SC, separated by mass and polarity using a detailed LC-MS approach to determine the CER profiles. First, the twelve well known ceramide subclasses were detected in both FTM types and in a mixture of lipid extracts from NHS. Furthermore, several unidentifiable species were detected (**Supplementary fig. 2**), although due to their unknown nature these are not analysed in detail. The overall CER chain length distribution is compared for both FTM types and plotted separately for (non ω-esterified) CER[non-EO] (**Fig. 4 b**) and (ω-esterified) CER[EO] (**Supplementary fig. 3**) together with the benchmark values of NHS. When focusing on the differences between the FTM types, a reduction in CER[non-EO] with a total of 34 carbon atoms in the two chains (C_{34} CERs) was detected in the CC-FTM. Furthermore, an increase in the level of C_{44}, C_{46} and C_{48} CER[non-EO] was observed. These alterations improved the resemblance of the CER[non-EO] chain length distribution in CC-FTMs to NHS. To obtain more detailed knowledge about which CER[non-EO] subclasses mainly contribute to these differences, the subclass profiles of the specific CER[non-EO] was determined (**Supplementary fig. 4**). This reveals that the decreased relative abundance of C_{34} CER[non-EO] is attributed to the subclasses NS and AS. The increased relative abundance of C_{44}, C_{46} and C_{48} CERs is mainly attributed to the CER[non-EO] subclasses NdS, NP and NH. When focusing on the CER[EO]

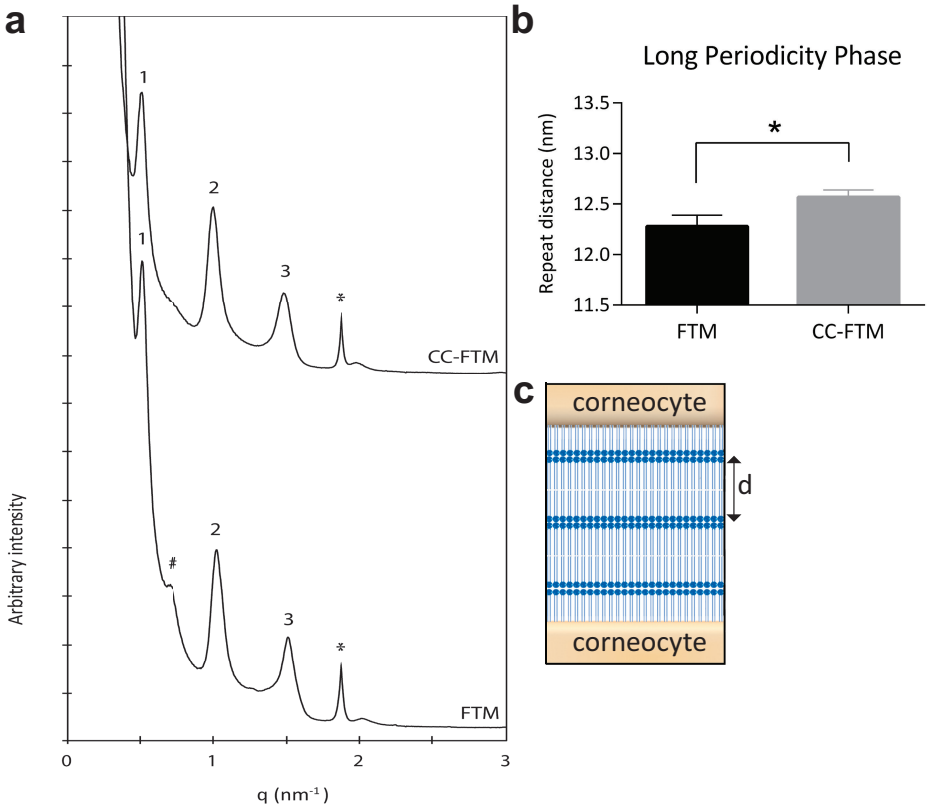


Figure 3. Lamellar organization of the extracellular lipid matrix in the stratum corneum (SC). (a) Representative diffraction pattern of the lipids in the SC of FTMs and CC-FTMs. The first, second and third order of diffraction are detected, as well as diffraction peaks attributed to separate crystalline cholesterol, indicated by the asterisk (*). In FTMs, an extra peak is observed, indicated by the pound sign (#). **(b)** Barplot of the original repeat distance of the LPP, which is elongated in the CC-FTM. Data represents mean ±SD of four independent experiments. **(c)** Drawing of lamellar organization in the intercorneocyte space, where d indicates the length of the periodicity phase, adapted from van Smeden *et al.* [34].

chain length distribution, a reduction in the level of C66, C68 and C70 CER[EO] was observed in CC-FTMs. These observations indicate that modulation of the dermal matrix affects the CER chain length distribution.

3.5. Profile of the ceramide subclasses in CC-FTMs

Besides the importance to mimic the CER chain length distribution, the overall CER subclass profile should also resemble that of NHS. Based on the separation and detection of the CERs with the LC-MS analysis, the relative abundance of each CER subclass in the SC was determined. The relative abundance of each CER subclass was plotted for both FTM types (**Fig. 5**). Several differences in the relative abundance of the CER subclasses were observed. The most significant changes

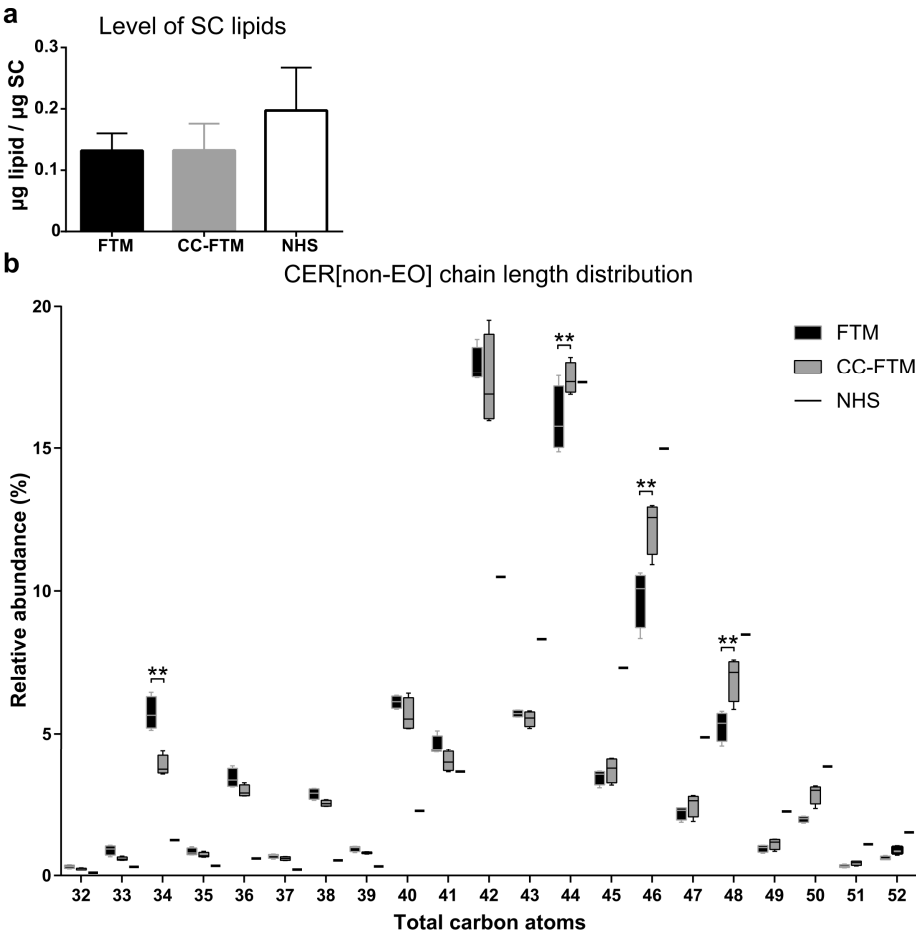


Figure 4. Lipid content and relative abundance of ceramides with specific carbon chain length. (a) The level of lipids in the SC of the FTM and CC-FTM is equal. **(b)** Box and whisker plot of CER[non-EO] as function of number of C-atoms in the total hydrocarbon chain, with indicated benchmark values of NHS. In CC-FTMs, a decreased abundance of C34 CER[non-EO] is indicated, whereas there is an increase in C44, C46 and C48 CER[non-EO]. Whiskers indicate the 95% confidence interval. Data is obtained from four independent experiments.

were the reduction in the level of the NS and AS subclasses in the CC-FTM. Compensatory, an increased level of NdS, NH and notably NP in the CC-FTM was observed. The relative abundance of AdS, AP, AH, and CER[EO] remained equal in both FTM types. The significant alterations in the CER subclass profile induces that the profile of NHS is more mimicked by the CC-FTM than the FTM.

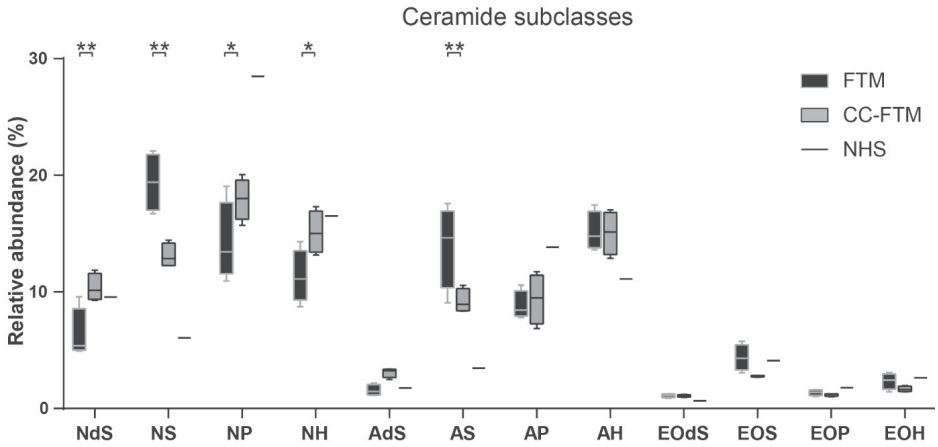


Figure 5. Ceramide subclass profile in FTMs and CC-FTMs. Box and whisker plot of CER subclasses with indicated benchmark values of NHS. Significant differences in relative abundance are indicated, which are the reduction in NS and AS and an increase of NdS, NP and NH in SC of CC-FTMs compared to FTMs. Whiskers indicate the 95% confidence interval. Data is obtained from four independent experiments.

3.6. Inside-out barrier functionality of the CC-FTMs

Followed by the detailed examination of the SC lipid barrier organization and CER composition, the barrier functionality of the NHS, FTMs and CC-FTMs was determined. Stable measurements of the transepidermal water loss (TEWL) over time revealed a significant reduction of the TEWL in the CC-FTMs compared to the FTMs (**Fig. 6**). The adjustment of the dermal matrix induced an improved inside-out barrier functionality based on TEWL values of both FTM types and NHS.

3.7. Expression of major lipid processing enzymes

The observed alterations in both CER chain length distribution and CER subclass profile could be a result of an altered expression of the major lipid processing enzymes. We therefore examined the expression GBA, aSMase, CER-S3 and ELOVL1 in NHS and both FTM types (**Fig. 7**). The expression of GBA and aSMase, both critical in the final step of ceramide processing, is localized in the granular layer of the epidermis in both FTM types, similar to NHS. The restriction to a single granular layer of GBA in CC-FTMs mimics more closely the expression of GBA in NHS. In addition, the expression of aSMase in the CC-FTM is more localized towards the granular layer. The expression of CER-S3, important in the formation of ceramides through linkage of the sphingoid backbone to very long chain fatty acids, is restricted to the granular layer in both models and in NHS. Finally, the expression of ELOVL1, which plays a role in the elongation of FFA chains, is localized in all epidermal layers equally for NHS, FTM and CC-FTM.

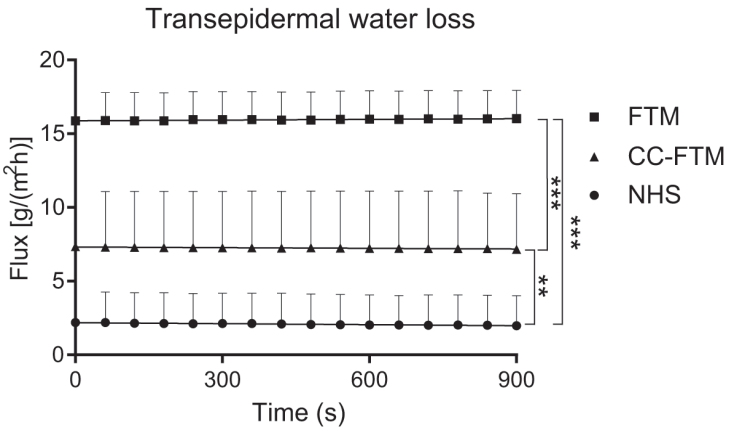


Figure 6. Transepidermal water loss of NHS, FTMs and CC-FTMs. TEWL was measured over 900 sec time period and plotted as mean values +SEM. Data is obtained from three independent experiments and three NHS samples.

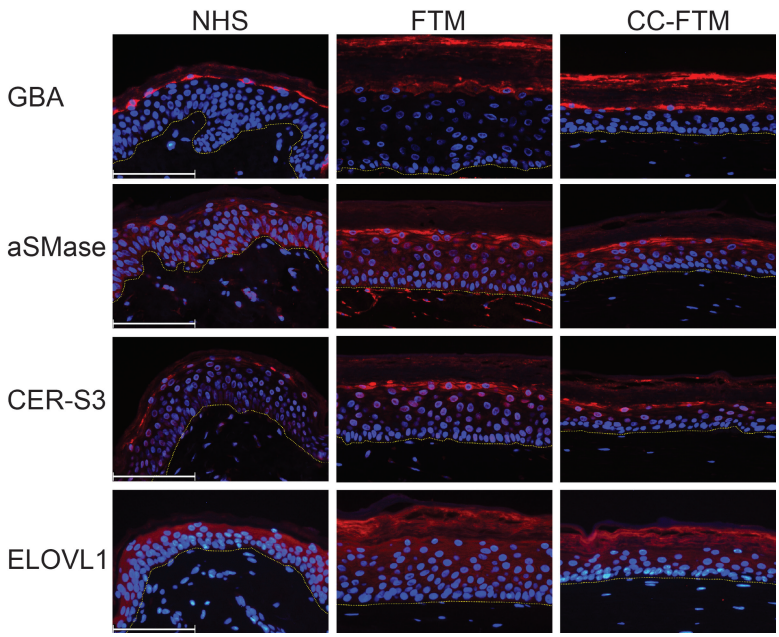


Figure 7. Expression of lipid processing enzymes in NHS, FTM and CC-FTM. Tissue sections of NHS, FTMs and CC-FTMs are analysed by immunofluorescence for the expression of lipid processing enzymes GBA, aSMase, CER-S3 and ELOVL1 (red). Representative images show the localization of GBA, aSMase and CER-S3 in the stratum granulosum, while the expression of ELOVL1 is more diffuse throughout the epidermis. Nuclei are stained blue using DAPI, the yellow dotted line indicates the dermal-epidermal junction. Scale bar represents 100 µm.

4. Discussion

Many properties of the native human skin (NHS) are mimicked *in vitro* in the range of existing HSEs. However, there is still an urgent need for HSEs that resemble the epidermal barrier properties very closely. In this work, CC-FTMs were developed through modulation of the dermal matrix by incorporation of the biopolymer chitosan. A major practical advantage of the collagen-chitosan dermal equivalent is the generation of it in a single fully hydrated preparation step, instead of a double preparation step for the FTMs. This novel FTM type is thoroughly analysed for epidermal morphogenesis and barrier formation and compared to the established FTM.

The epidermis of both FTM types is well-organized, based on the distinguishable presence of all four epidermal layers. In the CC-FTM, the epidermal thickness is reduced as well as the proliferation in the basal layer. However, the PI of both FTM types is within the reported range of PIs for NHS [37]. The epidermal differentiation program maintained regulated in both FTM types, although the granular layer in CC-FTM is reduced to approximately a single layer in CC-FTMs. The epidermal hyper-proliferation associated K16 is detected in FTMs and in several commercially available models [38], but is absent in CC-FTMs and in NHS [39], indicative for an improved epidermal homeostasis. Previously, it has been shown that the expression of K16 depends on the number of fibroblasts present in the dermal matrix [39], demonstrating a highly significant role for the fibroblasts and their microenvironment in the regulation of epidermal homeostasis and subsequent epidermal functionality.

The crucial role of the epidermal-dermal communication in both FTM types was analysed through expression of major BM proteins. The presence of the BM was detected in both FTM types, although the modulation of the dermal matrix attenuates the deposition of laminin 332 (L332). The major biological function of L332 is to facilitate epidermal attachment [40-42]. The reduced deposition of L332 in the CC-FTMs cannot be induced by an altered fibroblast distribution, based on the similar detection of the mesenchymal marker vimentin throughout the dermis of both FTM types. The reduced deposition of L332 could be explained by a functional overlap of L332 and chitosan, where both could act as substrate for keratinocyte adhesion. This could reduce the necessity for the deposition of L332 in CC-FTMs. This altered adhesion in turn could affect basal cell proliferation. Direct interaction of keratinocytes with a chitosan film has been observed before [24]. However, the direct attachment of keratinocytes to chitosan in the collagen-chitosan matrix should be investigated in detail in future studies.

The functionality of the epidermal barrier in the SC highly depends on terminally differentiated keratinocytes in concert with the SC extracellular lipid matrix. Expression of loricrin as major cornified envelope protein is similar in both FTM types, as well as the level of total lipids in the SC. The number of corneocyte layers in the SC of both FTM types is equal, although not similar to NHS [43].

The lamellar organization of the SC lipids was determined revealing an increased repeat distance of the LPP in CC-FTMs. Since the repeat distance of the LPP in NHS is approximately 13 nm [44], this indicates that the lamellar organization of CC-FTMs resembles that of NHS to a higher extent but still not completely. Moreover, the additional unknown lamellar phase in FTMs, possibly explained by phase separated CERs, is not present in CC-FTMs and NHS [8]. The SPP of approximately 6 nm has been identified in NHS, but has not yet been detected in any human skin model [5, 44].

To possibly explain the altered lipid organization and to gain more insight in the lipid barrier formation, the CER composition was analysed. First, the CER chain length distribution was assessed, revealing a wide range in CER carbon chain lengths in both FTM types. This demonstrates once more that the synthesis of variable CER entities in FTMs is functional, which is a major characteristic of NHS. When comparing both FTM types, there is a decreased relative abundance of C34 CER[non-EO] in CC-FTMs detected. Compensatory, an increment in the relative abundance of C44, C46 and C48 CER[non-EO] in CC-FTM was observed. A comparison is made with the CER chain length distribution of NHS, based on the benchmark values reported here and values described in literature [3, 35]. The reduced relative abundance of C34 CER[non-EO] and the increased relative abundance of C44, C46 and C48 CER[non-EO] in the CC-FTM compared to FTM resemble the chain length distribution of NHS more closely. An increase in the chain length of CERs has been correlated with a decrease in transepidermal water loss (TEWL) and thus an improved skin barrier [45]. This indicates that the CER composition influences the functionality of the epidermal barrier and that the barrier in CC-FTMs is superior to FTMs.

Second, the CER subclass profiles of both FTM types are compared to each other. In the CC-FTM, the CER subclass NP is increased to a level where this subclass is relatively the most abundant. Also CER NdS and NH are relatively more abundant. In contrast, the relative abundance of both AS and NS are reduced in the SC of CC-FTMs. The presence of CER[EO] is lower than reported before in HSEs [7], which is ascribed to the utilized data corrections. In this study, the level of CER[EO] was underestimated, since no chain length corrections have been performed and no quantification occurred. However, this did not affect the conclusions of our present study. To evaluate to which order the CER subclass profiles resembles that

of NHS, we compared the FTM and CC-FTM CER subclass profiles to the CER subclass profile of NHS [45]. The CER subclass profile in NHS has been studied extensively before with increased precision based on technical progress [3, 35, 46-49]. In NHS, the CER subclass NP is most abundant, which is most similar to the CC-FTM. In addition, the decreased relative abundance of CER subclasses AS and NS, as in the CC-FTMs, is more close to the CER subclass profile of NHS [3, 35, 46-49]. Altogether, the CER composition in the SC of CC-FTMs resembles that of NHS better, based on the CER chain length distribution and CER subclass profile.

Several interesting observations are made when comparing the obtained results from both FTM types to the epidermal barrier formation of skin in an unbalanced or diseased state. This is performed through comparing with atopic dermatitis (AD), a skin condition which is studied extensively regarding epidermal barrier formation [45, 50]. Although the aetiology is different, several similarities are observed. The epidermis of AD, most profound in lesional AD, as well as the FTMs, shows an elevated expression of K16 and increased proliferation [51], both indicative for an epidermis which is not in homeostasis. Furthermore, the increased relative abundance of CER subclasses AS, NS and the C34 CERs are observed in AD and FTMs, but are more normalized in the CC-FTMs. Therefore the chitosan modulated dermal matrix seems to be highly beneficial for the epidermal homeostasis, including the epidermal barrier formation.

This is further emphasized by the barrier functionality assay. TEWL measurements are widely applied and regarded indicative for the skin barrier integrity [34, 36, 52]. In the CC-FTMs the TEWL is significantly reduced, which may be a result of the altered SC lipid composition. This underlines the importance of the SC lipid composition in the formation of a competent barrier.

Finally, the expression of CER processing enzymes was studied, to evaluate if the altered CER composition is a direct effect of differently expressed enzymes. This was determined through analysis of the expression of GBA and aSMase. The localization of GBA at the interface of the stratum granulosum and stratum corneum is in agreement with the site where the conversion of CER precursors occurs. The intensity and restriction to a single granular layer of GBA in CC-FTMs mimics more the NHS. The localization of aSMase is not affected by the modulated dermal matrix. Although the level of AS and NS is reduced in CC-FTMs, this cannot be linked to an altered expression by aSMase, which processes the sphingomyelin into the CER subclasses AS and NS [53, 54]. However, the functionality of both enzymes can still be affected. The expression and localization of CER-S3 and ELOVL1 is highly similar in both FTM types and NHS [55], indicating that the major lipid metabolism pathways are unaffected *in vitro*. The expression of major lipid processing enzymes in the CC-FTM is highly

comparable to the FTMs, although the expression in the granular layer is more restricted to a single layer in CC-FTMs and NHS, which could be beneficial for the functionality of these enzymes.

5. Conclusion

The epidermal barrier properties of human skin models needs to resemble the NHS barrier properties to a higher extent, in order to fully mimic the NHS *in vitro*. In this work, the development of CC-FTMs is described, through modulation of the dermal matrix by the biopolymer chitosan. The CC-FTM resembles NHS to a higher extent regarding epidermal morphogenesis. The formation of the epidermal barrier, based on the organization and composition of the SC lipids and the inside-out barrier functionality, mimics the NHS more closely, although not entirely. The novel CC-FTMs are a promising tool to be used in epidermal barrier related studies.

6. Acknowledgements

The authors would like to thank Gert Gooris and the personnel at the DUBBLE beam line (BM26) at the ESRF for their support with the X-ray measurements. We thank the company Cosmoferm (Evonik) for their generous provision of CERs.

7. References

1. El Ghalbzouri A, Siamari R, Willemze R, Ponec M. Leiden reconstructed human epidermal model as a tool for the evaluation of the skin corrosion and irritation potential according to the ECVAM guidelines. Toxicology in Vitro. 2008;22(5):1311-20. doi: http://dx.doi.org/10.1016/j.tiv.2008.03.012.
2. Motta S, Monti M, Sesana S, Caputo R, Carelli S, Ghidoni R. Ceramide composition of the psoriatic scale. Biochimica et Biophysica Acta (BBA) - Molecular Basis of Disease. 1993;1182(2):147-51. doi: http://dx.doi.org/10.1016/0925-4439(93)90135-N.
3. van Smeden J, Hoppel L, van der Heijden R, Hankemeier T, Vreeken RJ, Bouwstra JA. LC/MS analysis of stratum corneum lipids: ceramide profiling and discovery. Journal of Lipid Research. 2011;52(6):1211-21. doi: 10.1194/jlr.M014456.
4. Masukawa Y, Narita H, Sato H, Naoe A, Kondo N, Sugai Y, et al. Comprehensive quantification of ceramide species in human stratum corneum. Journal of Lipid Research. 2009;50(8):1708-19. doi: 10.1194/jlr.D800055-JLR200.
5. Bouwstra JA, Gooris GS, van der Spek JA, Bras W. Structural Investigations of Human Stratum Corneum by Small-Angle X-Ray Scattering. J Investig Dermatol. 1991;97(6):1005-12.
6. Damien F, Boncheva M. The Extent of Orthorhombic Lipid Phases in the Stratum Corneum Determines the Barrier Efficiency of Human Skin In Vivo. J Invest Dermatol. 2009;130(2):611-4. doi: http://www.nature.com/jid/journal/v130/n2/suppinfo/jid200927251.html.
7. Thakoersing VS, van Smeden J, Mulder AA, Vreeken RJ, El Ghalbzouri A, Bouwstra JA. Increased Presence of Monounsaturated Fatty Acids in the Stratum Corneum of Human Skin Equivalents. J Invest Dermatol. 2013;133(1):59-67. doi: http://www.nature.com/jid/journal/v133/n1/suppinfo/jid201226251.html.
8. Thakoersing VS, Gooris GS, Mulder A, Rietveld M, El Ghalbzouri A, Bouwstra JA. Unraveling barrier properties of three different in-house human skin equivalents. Tissue engineering Part C, Methods. 2012;18(1):1-11. doi: 10.1089/ten.TEC.2011.0175.
9. Netzlaff F, Kaca M, Bock U, Haltner-Ukomadu E, Meiers P, Lehr C-M, et al. Permeability of the reconstructed human epidermis model Episkin® in comparison to various human skin preparations. European Journal of Pharmaceutics and Biopharmaceutics. 2007;66(1):127-34. doi: http://dx.doi.org/10.1016/j.ejpb.2006.08.012.
10. Ponec M, Boelsma E, Gibbs S, Mommaas M. Characterization of Reconstructed Skin Models. Skin Pharmacology and Physiology. 2002;15(suppl 1)(Suppl. 1):4-17.
11. Yuki T, Komiya A, Kusaka A, Kuze T, Sugiyama Y, Inoue S. Impaired tight junctions obstruct stratum corneum formation by altering polar lipid and profilaggrin processing. Journal of Dermatological Science. 2013;69(2):148-58. doi: http://dx.doi.org/10.1016/j.jdermsci.2012.11.595.
12. El Ghalbzouri A, Jonkman MF, Dijkman R, Ponec M. Basement Membrane Reconstruction in Human Skin Equivalents Is Regulated by Fibroblasts and/or Exogenously Activated Keratinocytes. J Investig Dermatol. 2004;124(1):79-86.
13. Boehnke K, Mirancea N, Pavesio A, Fusenig NE, Boukamp P, Stark H-J. Effects of fibroblasts and microenvironment on epidermal regeneration and tissue function in long-term skin equivalents. European Journal of Cell Biology. 2007;86(11–12):731-46. doi: http://dx.doi.org/10.1016/j.ejcb.2006.12.005.
14. Stark H-J, Boehnke K, Mirancea N, Willhauck MJ, Pavesio A, Fusenig NE, et al. Epidermal Homeostasis in Long-Term Scaffold-Enforced Skin Equivalents. J Investig Dermatol Symp P. 2006;11(1):93-105.
15. El Ghalbzouri A, Commandeur S, Rietveld MH, Mulder AA, Willemze R. Replacement of animal-derived collagen matrix by human fibroblast-derived dermal matrix for human skin equivalent products. Biomaterials. 2009;30(1):71-8. doi: 10.1016/j.biomaterials.2008.09.002.
16. Regnier M, Prunieras M, Woodley D. Growth and differentiation of adult human epidermal cells on dermal substrates. Front matrix biol. 1981;9:4-35.
17. Ponec M, Weerheim A, Kempenaar J, Mommaas AM, Nugteren DH. Lipid composition of cultured human keratinocytes in relation to their differentiation. Journal of Lipid Research. 1988;29(7):949-61.
18. Sorrell JM, Baber MA, Caplan AI. Site-matched papillary and reticular human dermal fibroblasts differ in their release of specific growth factors/cytokines and in their interaction with keratinocytes. Journal of Cellular Physiology. 2004;200(1):134-45. doi: 10.1002/jcp.10474.
19. Maas-Szabowski N, Szabowski A, Stark H-J, Andrecht S, Kolbus A, Schorpp-Kistner M, et al. Organotypic Cocultures with Genetically Modified Mouse Fibroblasts as a Tool to Dissect Molecular Mechanisms Regulating Keratinocyte Growth and Differentiation. J Investig Dermatol. 2001;116(5):816-20.

20. Mao JS, Cui YL, Wang XH, Sun Y, Yin YJ, Zhao HM, et al. A preliminary study on chitosan and gelatin polyelectrolyte complex cytocompatibility by cell cycle and apoptosis analysis. Biomaterials. 2004;25(18):3973-81. doi: http://dx.doi.org/10.1016/j.biomaterials.2003.10.080.
21. Parenteau-Bareil R, Gauvin R, Berthod F. Collagen-Based Biomaterials for Tissue Engineering Applications. Materials. 2010;3(3):1863.
22. Berthod F, Saintigny G, Chretien F, Hayek D, Collombel C, Damour O. Optimization of thickness, pore size and mechanical properties of a biomaterial designed for deep burn coverage. Clinical Materials. 1994;15(4):259-65. doi: http://dx.doi.org/10.1016/0267-6605(94)90055-8.
23. Rodríguez-Vázquez M, Vega-Ruiz B, Ramos-Zúñiga R, Saldaña-Koppel DA, Quiñones-Olvera LF. Chitosan and its potential use as a scaffold for tissue engineering in regenerative medicine. BioMed research international. 2015;2015:1.
24. Chatelet C, Damour O, Domard A. Influence of the degree of acetylation on some biological properties of chitosan films. Biomaterials. 2001;22(3):261-8.
25. Shahabeddin L, Berthod F, Damour O, Collombel C. Characterization of Skin Reconstructed on a Chitosan-Cross-Linked Collagen-Glycosaminoglycan Matrix. Skin Pharmacology and Physiology. 1990;3(2):107-14.
26. Dos Santos M, Metral E, Boher A, Rousselle P, Thepot A, Damour O. In vitro 3-D model based on extending time of culture for studying chronological epidermis aging. Matrix Biology. 2015;47:85-97. doi: http://dx.doi.org/10.1016/j.matbio.2015.03.009.
27. Berthod F, Hayek D, Damour O, Collombel C. Collagen synthesis by fibroblasts cultured within a collagen sponge. Biomaterials. 1993;14(10):749-54. doi: http://dx.doi.org/10.1016/0142-9612(93)90039-5.
28. Haisma EM, Rietveld MH, de Breij A, van Dissel JT, El Ghalbzouri A, Nibbering PH. Inflammatory and antimicrobial responses to methicillin-resistant Staphylococcus aureus in an in vitro wound infection model. PloS one. 2013;8(12):e82800. doi: 10.1371/journal.pone.0082800.
29. van Drongelen V, Danso MO, Mulder A, Mieremet A, van Smeden J, Bouwstra JA, et al. Barrier Properties of an N/TERT-Based Human Skin Equivalent. Tissue Engineering Part A. 2014;20(21-22):3041-9.
30. Ponec M, Weerheim A, Kempenaar J, Mulder A, Gooris GS, Bouwstra J, et al. The Formation of Competent Barrier Lipids in Reconstructed Human Epidermis Requires the Presence of Vitamin C. J Investig Dermatol. 1997;109(3):348-55.
31. Groen D, Poole DS, Gooris GS, Bouwstra JA. Is an orthorhombic lateral packing and a proper lamellar organization important for the skin barrier function? Biochimica et Biophysica Acta (BBA) - Biomembranes. 2011;1808(6):1529-37. doi: http://dx.doi.org/10.1016/j.bbamem.2010.10.015.
32. Boiten W, Absalah S, Vreeken R, Bouwstra J, van Smeden J. Quantitative analysis of ceramides using a novel lipidomics approach with three dimensional response modelling. Biochimica et Biophysica Acta (BBA)-Molecular and Cell Biology of Lipids. 2016.
33. van Smeden J, Janssens M, Boiten WA, van Drongelen V, Furio L, Vreeken RJ, et al. Intercellular skin barrier lipid composition and organization in Netherton syndrome patients. Journal of Investigative Dermatology. 2014;134(5):1238-45.
34. van Smeden J, Janssens M, Kaye ECJ, Caspers PJ, Lavrijsen AP, Vreeken RJ, et al. The importance of free fatty acid chain length for the skin barrier function in atopic eczema patients. Experimental Dermatology. 2014;23(1):45-52. doi: 10.1111/exd.12293.
35. van Smeden J, Boiten WA, Hankemeier T, Rissmann R, Bouwstra JA, Vreeken RJ. Combined LC/MS-platform for analysis of all major stratum corneum lipids, and the profiling of skin substitutes. Biochimica et Biophysica Acta (BBA) - Molecular and Cell Biology of Lipids. 2014;1841(1):70-9. doi: http://dx.doi.org/10.1016/j.bbalip.2013.10.002.
36. Elkeeb R, Hui X, Chan H, Tian L, Maibach HI. Correlation of transepidermal water loss with skin barrier properties in vitro: comparison of three evaporimeters. Skin Research and Technology. 2010;16(1):9-15. doi: 10.1111/j.1600-0846.2009.00406.x.
37. van Drongelen V, Danso MO, Out JJ, Mulder A, Lavrijsen AP, Bouwstra JA, et al. Explant cultures of atopic dermatitis biopsies maintain their epidermal characteristics in vitro. Cell and tissue research. 2015;361(3):789-97.
38. Boelsma E, Gibbs S, Faller C, Ponec M. Characterization and comparison of reconstructed skin models: morphological and immunohistochemical evaluation. Acta Derm Venereol. 2000;80(2):82-8.
39. El-Ghalbzouri A, Gibbs S, Lamme E, Van Blitterswijk CA, Ponec M. Effect of fibroblasts on epidermal regeneration. British Journal of Dermatology. 2002;147(2):230-43. doi: 10.1046/j.1365-2133.2002.04871.x.
40. Pulkkinen L, Christiano AM, Airenne T, Haakana H, Tryggvason K, Uitto J. Mutations in the γ2 chain gene (LAMC2) of kalinin/laminin 5 in the junctional forms of epidermolysis bullosa. Nature genetics. 1994;6(3):293-8.

41. Aberdam D, Galliano M-F, Vailly J, Pulkkinen L, Bonifas J, Christiano AM, et al. Herlitz's junctional epidermolysis bullosa is linked to mutations in the gene (LAMC2) for the γ2 subunit of nicein/kalinin (LAMININ–5). Nature genetics. 1994;6(3):299-304.
42. Nishiyama T, Amano S, Tsunenaga M, Kadoya K, Takeda A, Adachi E, et al. The importance of laminin 5 in the dermal–epidermal basement membrane. Journal of Dermatological Science. 2000;24, Supplement 1:S51-S9. doi: http://dx.doi.org/10.1016/S0923-1811(00)00142-0.
43. Bouwstra JA, de Graaff A, Gooris GS, Nijsse J, Wiechers JW, van Aelst AC. Water Distribution and Related Morphology in Human Stratum Corneum at Different Hydration Levels. Journal of Investigative Dermatology. 2003;120(5):750-8. doi: http://dx.doi.org/10.1046/j.1523-1747.2003.12128.x.
44. Thakoersing VS, Danso MO, Mulder A, Gooris G, El Ghalbzouri A, Bouwstra JA. Nature versus nurture: does human skin maintain its stratum corneum lipid properties in vitro? Experimental dermatology. 2012;21(11):865-70.
45. Janssens M, van Smeden J, Gooris GS, Bras W, Portale G, Caspers PJ, et al. Increase in short-chain ceramides correlates with an altered lipid organization and decreased barrier function in atopic eczema patients. Journal of lipid research. 2012;53(12):2755-66.
46. Pappinen S, Hermansson M, Kuntsche J, Somerharju P, Wertz P, Urtti A, et al. Comparison of rat epidermal keratinocyte organotypic culture (ROC) with intact human skin: Lipid composition and thermal phase behavior of the stratum corneum. Biochimica et Biophysica Acta (BBA) - Biomembranes. 2008;1778(4):824-34. doi: http://dx.doi.org/10.1016/j.bbamem.2007.12.019.
47. Masukawa Y, Narita H, Sato H, Naoe A, Kondo N, Sugai Y, et al. Comprehensive quantification of ceramide species in human stratum corneum. Journal of lipid research. 2009;50(8):1708-19.
48. Rabionet M, Bayerle A, Marsching C, Jennemann R, Gröne H-J, Yildiz Y, et al. 1-O-acylceramides are natural components of human and mouse epidermis. Journal of lipid research. 2013;54(12):3312-21.
49. Ponec M, Weerheim A, Lankhorst P, Wertz P. New acylceramide in native and reconstructed epidermis. Journal of investigative dermatology. 2003;120(4):581-8.
50. Ishikawa J, Narita H, Kondo N, Hotta M, Takagi Y, Masukawa Y, et al. Changes in the ceramide profile of atopic dermatitis patients. Journal of Investigative Dermatology. 2010;130(10):2511-4.
51. Gittler JK, Shemer A, Suárez-Fariñas M, Fuentes-Duculan J, Gulewicz KJ, Wang CQ, et al. Progressive activation of T H 2/T H 22 cytokines and selective epidermal proteins characterizes acute and chronic atopic dermatitis. Journal of Allergy and Clinical Immunology. 2012;130(6):1344-54.
52. Fluhr JW, Feingold KR, Elias PM. Transepidermal water loss reflects permeability barrier status: validation in human and rodent in vivo and ex vivo models. Experimental Dermatology. 2006;15(7):483-92. doi: 10.1111/j.1600-0625.2006.00437.x.
53. Uchida Y, Hara M, Nishio H, Sidransky E, Inoue S, Otsuka F, et al. Epidermal sphingomyelins are precursors for selected stratum corneum ceramides. Journal of lipid research. 2000;41(12):2071-82.
54. Rabionet M, Gorgas K, Sandhoff R. Ceramide synthesis in the epidermis. Biochimica et Biophysica Acta (BBA) - Molecular and Cell Biology of Lipids. 2014;1841(3):422-34. doi: http://dx.doi.org/10.1016/j.bbalip.2013.08.011.
55. Jennemann R, Rabionet M, Gorgas K, Epstein S, Dalpke A, Rothermel U, et al. Loss of ceramide synthase 3 causes lethal skin barrier disruption. Human molecular genetics. 2012;21(3):586-608.

8. Supporting Information

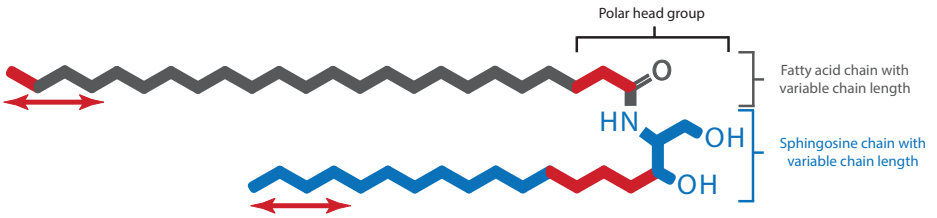
Supplementary table 1. Specification of antibodies used for immunohistochemical and immunofluorescence staining

Immunohistochemistry	Origin	Clone	Dilution	Secondary antibody	Manufacturer
Primary antibody					
Ki67	Mouse	MIB1	1:100	A	DAKO, Denmark
cytokeratin 10	Mouse	DE-K10	1:50	A	Labvision/Neomarkers, USA
cytokeratin 16	Mouse	LL025	1:50	A	Serotec, UK
Secondary antibody					
Biotinylated Goat anti-mouse (A)	Goat		1:200		Southern Biotechnology

Immunofluorescence	Origin	Clone	Dilution	Secondary antibody	Manufacturer
Primary antibody					
Loricrin	Rabbit	AF62	1:1000	B	Covance, The Netherlands
Vimentin	Mouse	V6630	1:50	C	Sigma-aldrich, The Netherlands
Collagen type IV	Mouse	24.12.8 (PHM-12)	1:75	C	Chemicon, Australia
Laminin 332	Mouse	BM165	1:75	C	Dr. M. Aumailley, Germany
GBA	Rabbit	EPR5142	1:150	D	Abcam, UK
aSMASE	Rabbit	Polyclonal	1:1000	D	Abcam, UK
CER-S3	Rabbit	Polyclonal	1:75	D	Sigma-aldrich, The Netherlands
ELOVL1	Rabbit	Polyclonal	1:300	D	Santa Cruz, USA

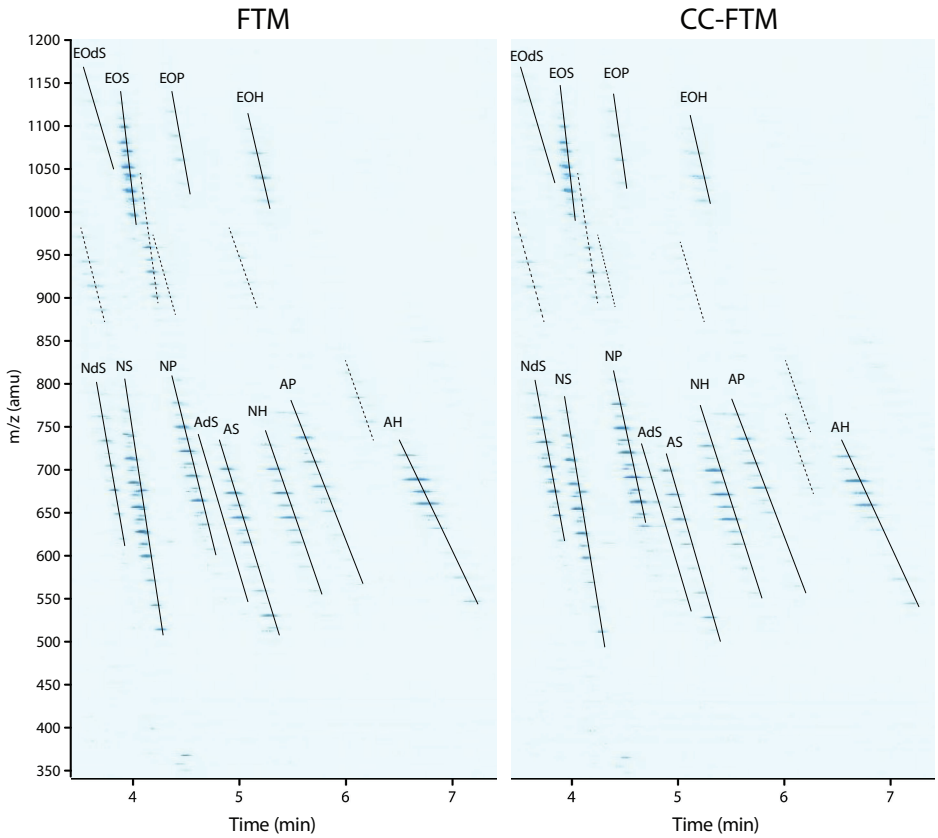
Supplementary table 1 (continued).

Immunofluorescence	Origin	Clone	Dilution	Secondary antibody	Manufacturer
Secondary antibody					
Cy3-conjugated anti-rabbit (B)	Goat		1:500		Jackson immunoresearch Laboratory, UK
Cy3-conjugated anti-mouse (C)	Goat		1:1000		Jackson immunoresearch Laboratory, UK
Rhodamine Red-X anti-rabbit (D)	Goat		1:300		Jackson immunoresearch Laboratory, UK

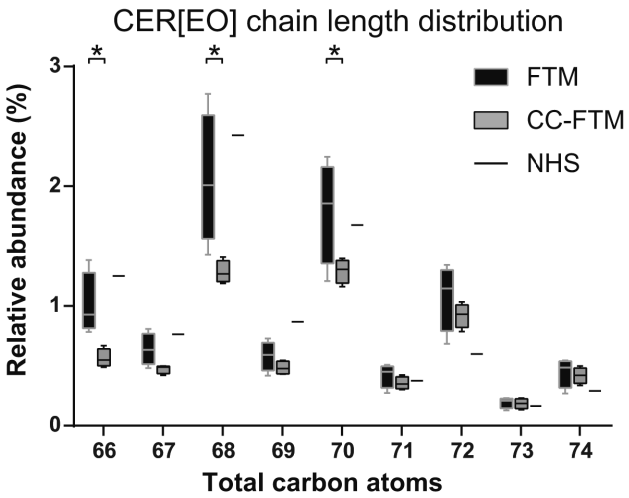


	Non-hydroxy fatty acid [N]	a-hydroxy fatty acid [A]	Esterified w-hydroxy fatty acid [EO]
Dihydrosphingosine [dS]	[NdS]	[AdS]	[EOdS]
Sphingosine [S]	[NS]	[AS]	[EOS]
Phytosphingosine [P]	[NP]	[AP]	[EOP]
6-hydroxy sphingosine [H]	[NH]	[AH]	[EOH]

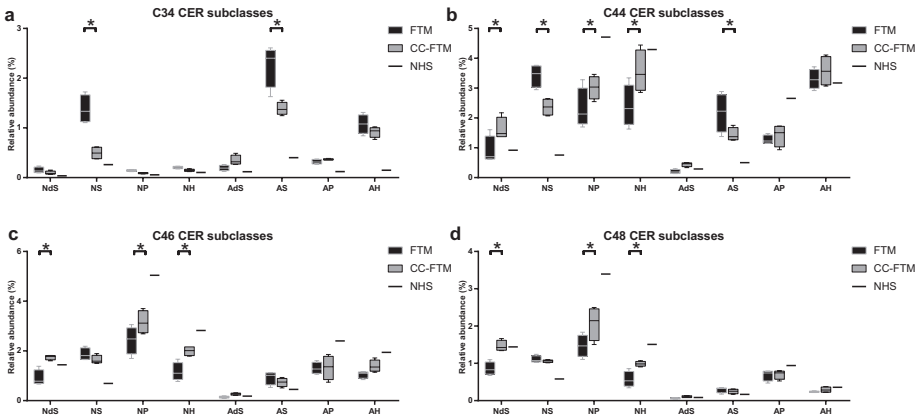
Supplementary figure 1. Overview of molecular structure of general ceramides and twelve ceramide subclasses. Ceramides contain a fatty acid chain (grey) amide linked to a sphingosine chain (blue). Red parts indicate positions with variable architectures. Red arrows indicate chain length variability. Nomenclature and structure of the twelve well-known ceramide subclasses is provided in the table. Reprinted from Janssens and Smeden *et al.* [45] under a CC BY license, with permission from JLR/ASBMB, original copyright 2012.



Supplementary figure 2. Two dimensional LC-MS plot of the ceramides isolated from the stratum corneum. The location and nomenclature of the twelve well-known ceramide subclasses are provided in two representative plots. Dashed lines indicate unknown lipid entities. Data is obtained from four independent experiments.

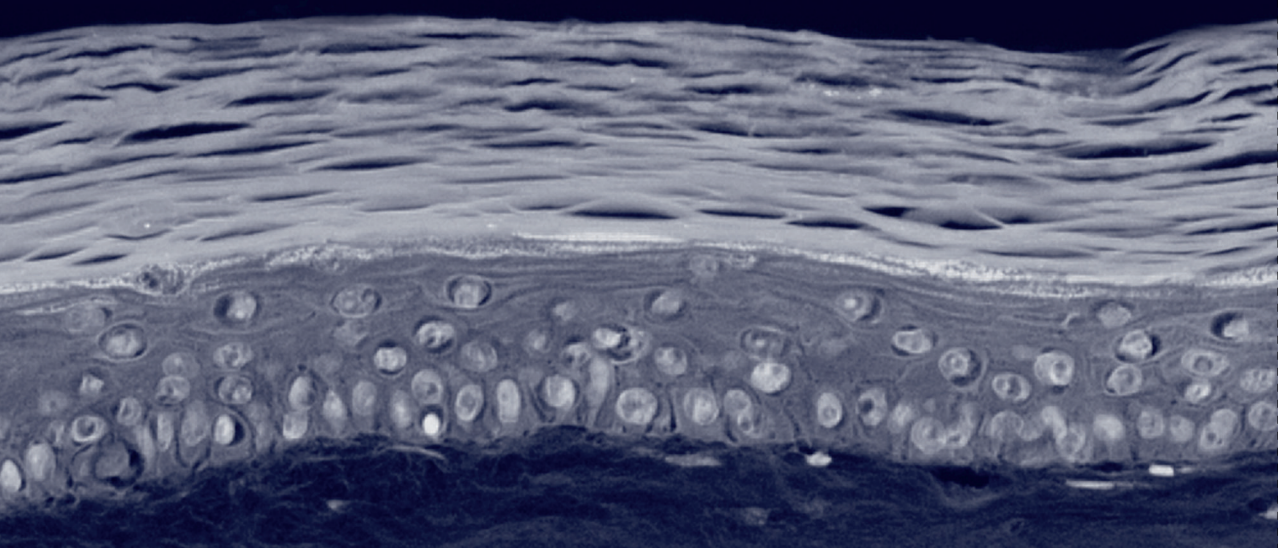


Supplementary figure 3. Relative abundance of CER[EO] with specific carbon chain length in FTMs and CC-FTMs. Box and whisker plot of CER[EO] with different number of C-atoms and indicated benchmark values of NHS. In CC-FTMs, a decrease of C66, C68 and C70 CER[EO] is detected. Whiskers indicate the 95% confidence interval. Data is obtained from four independent experiments.



Supplementary figure 4. Relative abundance of C34 and C44-48 CERs per subclass. Box and whisker plots of CER subclasses from only the **(a)** C34 CERs, **(b)** C44 CERs, **(c)** C46 CERs and **(d)** C48 CERs. Benchmark values of NHS are indicated for each subclass. The alteration in relative abundance of these groups is described to only some CER subclasses. These are NS and AS in C34 CERs, NdS, NS, NP, NH and AS in C44 CERs, NdS, NP and NH in C46 CERs and NdS, NP and NH in C48 CERs. Whiskers indicate the 95% confidence interval, *indicates $p<0.05$. Data is obtained from four independent experiments.

Part II



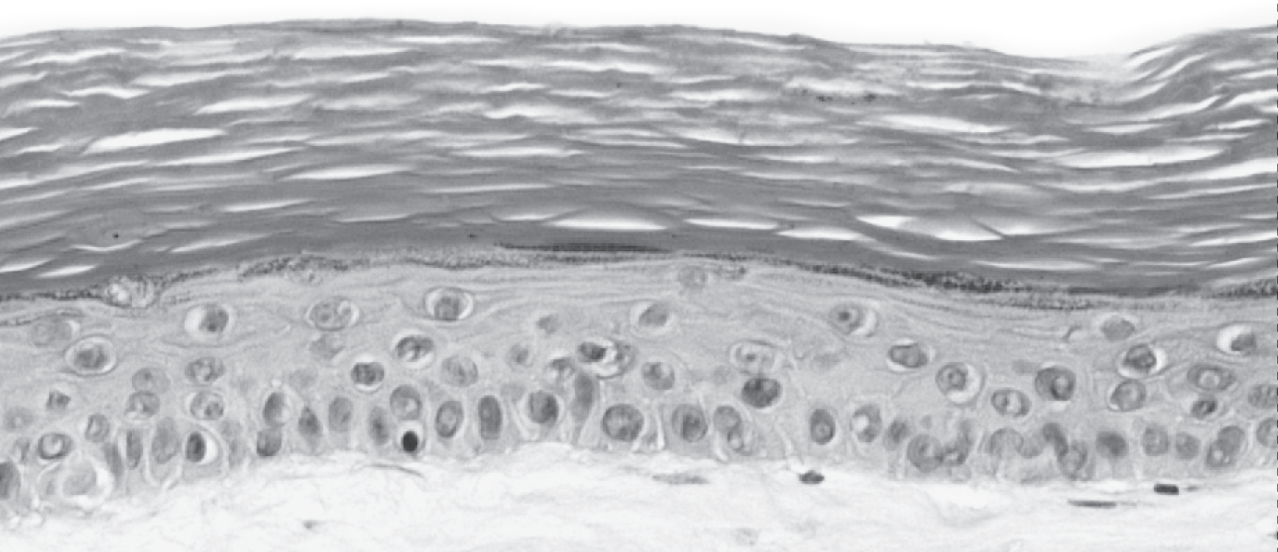
4

Characterization of human skin equivalents developed at body's core and surface temperatures

Arnout Mieremet
Rianne van Dijk
Walter Boiten
Gert Gooris
Joke A. Bouwstra[+]
Abdoelwaheb El Ghalbzouri[+]

[+] Joint senior authorship

Journal of Tissue Engineering and Regenerative Medicine 13(7): 1122-1133 (2019)



Abstract

Human skin equivalents (HSEs) are *in vitro* developed three-dimensional models resembling native human skin (NHS) to a high extent. However, the epidermal lipid biosynthesis, barrier lipid composition and organization are altered, leading to an elevated diffusion rate of therapeutic molecules. The altered lipid barrier formation in HSEs may be induced by standardized culture conditions, including a culture temperature of 37°C, which is dissimilar to skin surface temperature. Therefore, we aim to determine the influence of culture temperature during the generation of full thickness models (FTMs) on epidermal morphogenesis and lipid barrier formation. For this purpose, FTMs were developed at conventional core temperature (37°C) or lower temperatures (35°C and 33°C) and evaluated over a time period of four weeks. The stratum corneum (SC) lipid composition was analysed using advanced liquid chromatography coupled to mass spectrometry analysis. Our results show that SC layers accumulated at a similar rate irrespective of culture temperature. At reduced culture temperature an increased epidermal thickness, a disorganization of the lower epidermal cell layers, a delayed early differentiation, and an enlargement of granular cells were detected. Interestingly, melanogenesis was reduced at lower temperature. The ceramide subclass profile, chain length distribution and level of monounsaturated ceramides were similar in FTMs generated at 37°C and 35°C, but changed when generated at 33°C, reducing the resemblance to NHS. Herein, we report that culture temperature affects epidermal morphogenesis substantially and to a lesser extent the lipid barrier formation, highlighting the importance of optimized external parameters during reconstruction of skin.

Keywords: Tissue Engineering; Cell Culture Techniques; Artificial skin; Skin Temperature; Morphogenesis; Lipids; Ceramides.

1. Introduction

Tissue engineered human skin equivalents (HSEs) mimic many properties of native human skin (NHS). However, several aspects of *in vitro* tissue reconstruction need to be studied and optimised to further increase the resemblance to NHS, to understand the underlying biology, and to improve *in vitro – in vivo* correlations [1-4]. The main barrier of the skin resides in the uppermost layer of the epidermis, which is termed the stratum corneum (SC) [5]. This layer is made of corneocytes embedded in a lipid matrix. The composition of the lipid matrix affects the lamellar and lateral organization. The lipid organization has a profound impact on the rate of penetration of therapeutic compounds through the intercellular route when applied topically [6, 7]. Compared to NHS, the barrier formation of HSEs is altered, leading to an elevated *in vitro* diffusion rate and uncertainty in *in vitro - in vivo* correlations [8-11].

The most abundant lipid classes within the SC matrix are cholesterol, free fatty acids and ceramides. The latter can vary in headgroup architecture and carbon chain length and are crucial for the formation of lipid lamellae in the SC lipid matrix [12, 13]. In this study we specified these as total ceramides (CERs), which covers both the ω-esterified ceramide subclasses (CER[EO]) and the (non-ω-esterified) ceramide subclasses (CER[non-EO]). Several studies reported the differences in lipid composition between HSEs and NHS, which encompasses an altered CER subclass profile and CER carbon chain length distribution [11, 14]. Additionally, the level of monounsaturated CERs within the SC of HSEs is higher as compared to NHS. These compositional differences directly affect the organization and functionality of the lipid matrix [15].

To form the lipid barrier matrix, many precursor lipid entities are synthesized by keratinocytes [16]. To attain the proper amounts and classes of barrier lipids, the proliferation/differentiation processes of keratinocytes need to be in homeostasis. Many factors can influence the proliferation/differentiation balance *in vitro*, including level of nutrients and/or waste products in the culture medium and external environmental factors [17-19]. The first studies on modulating environmental factors *in vitro* were reported in 1997 [20, 21]. Key hypothesis in these studies was that the proliferation/differentiation balance of *in vitro* HSE cultures is altered due to the difference in temperature between *in vivo* (28-32°C) [22] and *in vitro* (37°C). In fact, these studies have reported that incubation of primary keratinocytes at reduced temperature (from 37°C to 33°C) affected epidermal morphogenesis directly. Recently this has been confirmed by using monocultures and an *ex vivo* skin barrier repair model [23-27]. However, there is still considerable uncertainty to what extent the culture temperature affects the

development of three-dimensional (3D) HSEs and whether or to what extent this affects the CER composition.

In this study, we aim to determine the influence of culture temperature on epidermal morphogenesis and lipid barrier formation. For this purpose, full thickness models (FTMs) were developed at conventional body's core temperature (37°C) and at reduced temperatures (35°C and 33°C), better approaching that of skin surface temperature.

2. Materials and Methods

2.1. Primary cell isolation

Primary human fibroblasts and keratinocytes were isolated from female adult surplus human breast skin, aged between 23 to 63 years old and Fitzpatrick skin photo-type classification I to III. Obtainment of healthy tissue was performed following the Declaration of Helsinki principles, as described before [28]. The dermis and epidermis were split after overnight incubation in 2.4 U/mL dispase II (Roche, Almere, The Netherlands). The epidermis was incubated in 0.05% (w/v) trypsin (BD Falcon, Breda, The Netherlands) and primary keratinocytes were isolated and cultured in Dulbecco's Modified Eagle's Medium (DMEM) diluted 3:1 in Ham's F12 (Gibco, Paisley, Scotland) supplemented with 5% foetal bovine serum (FBS) (Hyclone, Logan, UT, USA), 100 µg/mL penicillin/streptomycin, 1 µM hydrocortisone, 1 µM isoproterenol, and 0.087 µM insulin (Sigma, Zwijndrecht, The Netherlands) [29]. The dermis was incubated in a 3:1 (w/w) mixture of collagenase (ThermoFischer, Bleiswijk, The Netherlands) and dispase II for 2 hr at 37°C and primary fibroblasts were isolated and cultured in DMEM supplemented with 5% FBS, and 100 µg/mL penicillin/streptomycin [29, 30]. All primary cell cultures were tested negative for mycoplasma contamination.

2.2. Generation of full thickness models

Full thickness models (FTMs) were produced using a transwell system on filter inserts (Corning Transwell cell culture inserts, membrane diameter 24 mm, pore size 3 µm; Corning Life Sciences, The Netherlands). To form the 3D dermal equivalent, a suspension of rat tail tendon collagen (4 mg/mL) was mixed with Hank's Balanced Salt Solution, 0.1% acetic acid, pH corrected to neutral with NaOH, and enriched with 10% foetal bovine serum. With this suspension, a 1 mL cell free bottom layer and a 3 mL fibroblast containing top layer (1.2×10^5 cells/dermal equivalent) were formed. After one week, primary keratinocytes (2.5×10^5/model) in their first passage were seeded onto each dermal equivalent and cultured as described extensively before [11]. Reduction in temperature occurred at once on day 4 after air-exposure using the Memmert INC153med CO_2 incubator

(Memmert, Schwabach, Germany). At least three biological replicates of FTMs were generated and were harvested 7, 14, 21 and 28 days after air-exposure.

2.3. Morphology and protein expression

2.3.1. Fixation of the tissue

FTMs were snap frozen in liquid nitrogen using gelatin capsules filled with Tissue-Tek® O.C.T.™ Compound (Sakura Finetek Europe B.V., Alphen aan den Rijn, The Netherlands) or fixated with 4% formaldehyde (Added Pharma, Oss, The Netherlands), dehydrated and paraffin embedded [31].

2.3.2. Immunohistochemical analyses

Immunohistochemical analyses were performed on 5 µm sliced formalin fixed paraffin embedded (FFPE) tissue sections. These were stained with haematoxylin and eosin (Klinipath, Duiven, The Netherlands) according to manufacturer's instructions. For protein expression by immunohistochemistry, tissue sections were deparaffinised and rehydrated to perform heat-mediated antigen retrieval in citrate buffer (pH 6). Thereafter, sections were blocked with 2% normal human serum (Sanquin, Leiden, The Netherlands) followed by application of the primary and sequentially the secondary antibody, as described earlier [32]. Details of utilized primary and secondary antibody are described in **supplementary table 1**. No primary antibody was applied on sections for negative control. Images were post-processed by cropping and equally colour matched using Adobe Photoshop (CS6 version 13.0) to reduce inter-batch variability. No immunoreactivity of the secondary antibodies was detected in all stainings (**Supplementary fig. 1 a**).

2.3.3. Immunofluorescence analyses

For protein expression by immunofluorescence, 5 µm FFPE sections were deparaffinized and rehydrated to perform heat-mediated antigen retrieval in citrate buffer (pH 6) as described earlier [32]. Antigen retrieval for collagen type IV staining occurred using FFPE sections treated for 40 min with a 0.025% protease solution (Sigma). Laminin 332 staining was performed on 5 µm frozen sections, dried overnight and fixed in acetone for 10 min. Visualization of the sections occurred using a fluorescence microscope (Leica CTR5000, Leica, Wetzlar, Germany). Images were equally post-processed by cropping using Adobe Photoshop for better presentation.

2.3.4. Determination of the amount of corneocytes layers

Frozen sections were sliced 5 µm using a cryotome (Leica CM3050S), dried overnight and fixed in acetone for 10 min. Sections were stained for 1 min with a 1% (w/v) safranin O (Sigma) solution dissolved in Millipore water. After Millipore water washout, a 2% (w/v) KOH solution was applied for 10-15 min to swell the

corneocytes. Slides were sealed with a cover glass and imaged immediately. Per sample, four technical replicates were examined.

2.3.5. Estimation of epidermal thickness and proliferation index

The epidermal thickness was determined through quantification of six to eight images per sample of various regions. The outline of the viable epidermis area was measured with Adobe Photoshop (CS6 version 13.0) in pixels and transformed to squared micrometres. The proliferation index was determined through counting the number of Ki67 positive nuclei in the basal and suprabasal layer in a region of 100 basal cells. The resulting proliferation index is the percentage of Ki67 positive nuclei in at least three different regions per sample.

2.3.6. Melanin content

Fontana-Masson silver staining was performed on 5 µm FFPE sections after deparaffinization and rehydratation. Ammoniacal silver solution was prepared by adding ammonia solution to 5% (w/v) silver nitrate (Sigma) until the solution was clear. Slides were incubated for 20 min with this ammoniacal silver solution at 60°C followed by Millipore water washout and 90 sec incubation in 0.1% gold chloride solution (Sigma). Afterwards, incubation for 2 min in 2% (w/v) sodium thiosulfate and counterstaining with nuclear Fast Red (Sigma) was performed. Images were obtained using the light microscope. At least three technical replicates for a minimum of two biological replicates were analysed with Image J Software (NIH, Bethesda, MD).

2.4. Stratum corneum isolation and small angle X-ray diffraction analysis

SC was isolated from the skin, air-dried and stored under Argon gas over silica until further use as described before [31, 33]. Small-angle x-ray diffraction measurements were performed at the European Synchrotron Radiation Facility (ESRF, Grenoble, France) at station BM26B for a period of 2 x 150 sec as described elsewhere [15, 31]. From the positions of a series of equidistant diffraction peaks (located at q_n), the repeat distance (d) of a lamellar phase was calculated using the equation $d = n \cdot 2\pi / q_n$, where n is the order number of the diffraction peak.

2.5. Lipid extraction and liquid chromatography - mass spectrometry analysis

Extraction of total lipids from isolated SC of FTMs after 14 and 28 days cultured and NHS was performed with an adjusted Bligh and Dyer method as described by Boiten *et al.* [34]. To determine the weight percentage of lipids in the SC, dry SC weight was measured before and after extraction. The lipids were analysed and quantified using normal phase liquid chromatography - mass spectrometry (LC-MS) according to the method described by Boiten *et al.* [34]. The sample concentration of SC extracts was set at 0.3 mg/ml and 5 µl was injected. SC lipid

extracts were separated on a PVA-Sil column (5 µm particles, 100 x 2.1 mm i.d.) (YMC, Kyoto, Japan) and CERs were detected with an Acquity UPLC H-class (Waters, Milford, MA, USA) coupled to an XEVO TQ-S mass spectrometer (Waters). Measurements were performed in full scan mode from 1.25–8.00 min between m/z 350–1350 and from 8.0-12.5 min between m/z 500-1350. Ceramide N(24deuterated)S(18) was used as internal standard (ISTD). Predicted response factors for quantification were calculated using the response over mass (**Supplementary fig. 2**). For ceramides AS, NP and NS, the signal was corrected for overlap of monounsaturated ceramides containing two naturally abundant ^{13}C. Nomenclature of the CER subclasses is followed according to Motta *et al.* [35].

2.6. Statistics

Statistical analyses were conducted using GraphPad Prism version 7.00 for Windows (GraphPad Software, La Jolla, CA, USA). In general, statistical testing was performed after D'Agostino and Pearson normality testing with 1-way or 2-way ANOVA with Tukey's multiple comparisons post-testing, otherwise indicated. Significance is shown for comparison between FTMs (with lines and asterisk) and for comparison of FTMs to NHS (by NHS), otherwise indicated. Statistical differences are noted as *, ** or ***, corresponding to $P<0.05$, <0.01, <0.001.

3. Results

3.1. Epidermal development at various temperatures over time

The developed FTMs were cultured at different temperatures (37°C, 35°C and 33°C) and examined 7, 14, 21 and 28 days after air-exposure macroscopically (**Fig. 1 a**). We observed increased skin colouring in FTMs cultured at 37°C, strongest after 21-28 days. Surprisingly, this colouring was reduced or absent in FTMs generated at lower temperature. Assessment of general morphology revealed that the basal and lower spinous layers were less organized at reduced culture temperature, as the transition between columnar shaped keratinocytes in the basal layer and polygonal to flattened shaped keratinocytes in the spinous layer was less clear (**Fig. 1 b**). At 37°C the granular cells flatten over time, resulting in a higher resemblance to the morphology of granular cells in NHS between 21 and 28 days after air-exposure. This is less evident in FTMs developed at reduced temperatures, in which the granular cells remained enlarged. The thickness of the viable epidermis was increased at lower culture temperature, most pronounced at 33°C (**Fig. 1 c**). Although the epidermal thickness decreased over time, eventually to levels comparable to NHS, at reduced temperature the viable epidermis remained thicker during the entire culture period. The SC thickness was determined by quantification of the number of corneocyte layers after safranin red staining (**Supplementary fig. 1 b**). The number of corneocyte layers increased over time

and mimics that of NHS between 12-20 days after air-exposure (**Fig. 1 d**). Between the different temperatures, no significant differences were observed in the linear rate of accumulation in corneocyte layers. Extrapolation of the data revealed that the first SC layers were formed on 4-5 days after air-exposure, which is also the time point of temperature reduction during development of FTMs.

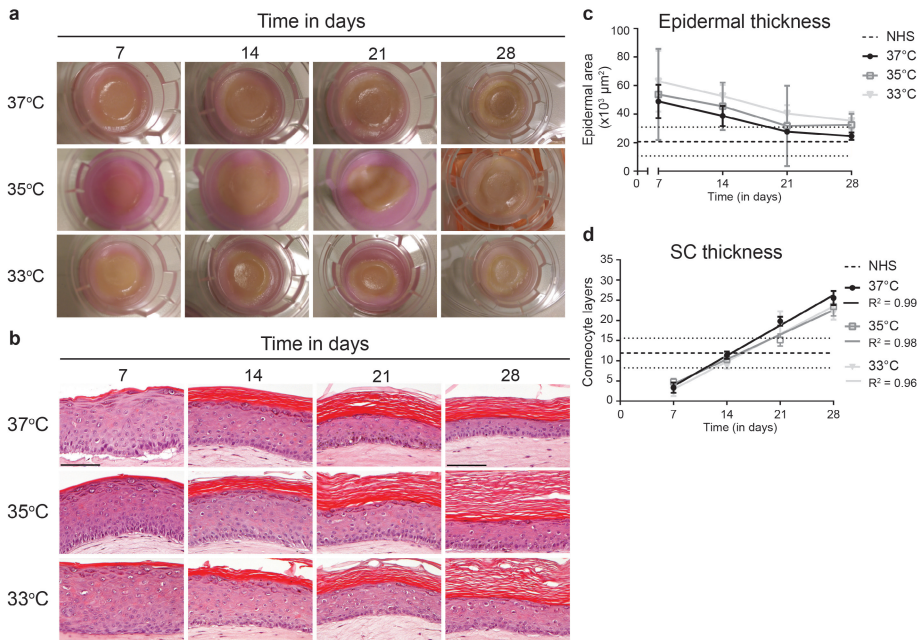


Figure 1. Generation of FTMs at different temperatures over time. (a) Macroscopic images of FTMs in the culture system with support cotton pad. **(b)** Hematoxylin and eosin stained cross sections of FTMs developed over a four week time period. Scale bar indicates 100 µm. **(c)** Viable epidermal thickness in FTMs. Data presented with connection line and indicated range for NHS (not as function of time). **(d)** The number of corneocyte layers in the SC. Data fitted by a linear regression line. Range indication for NHS between dotted lines (not as function of time). Linear trend line formulas are $Y_{37°C}$ = 1,07X - 3,75, $Y_{35°C}$ = 0,87X - 1,81, $Y_{33°C}$ = 0,98X - 3,89. All data represent mean ± 95% confidence interval (CI), n≥3.

3.2. Morphogenesis at various temperatures over time

To gain more insights into the proliferation/differentiation balance of FTMs generated at reduced temperatures, the epidermal morphogenesis was evaluated from apical to basal side by immunohistochemical analyses (**Fig. 2 a**). The late and terminal differentiation programs were assessed by loricrin, involucrin and filaggrin expression. Both loricrin and filaggrin were located at the stratum granulosum (SG) similarly in FTMs and in NHS. Involucrin was expressed at lower layers in the epidermis of FTMs, contrary to NHS. These examinations confirmed the enlargement of granular cells in FTMs generated at reduced temperature.

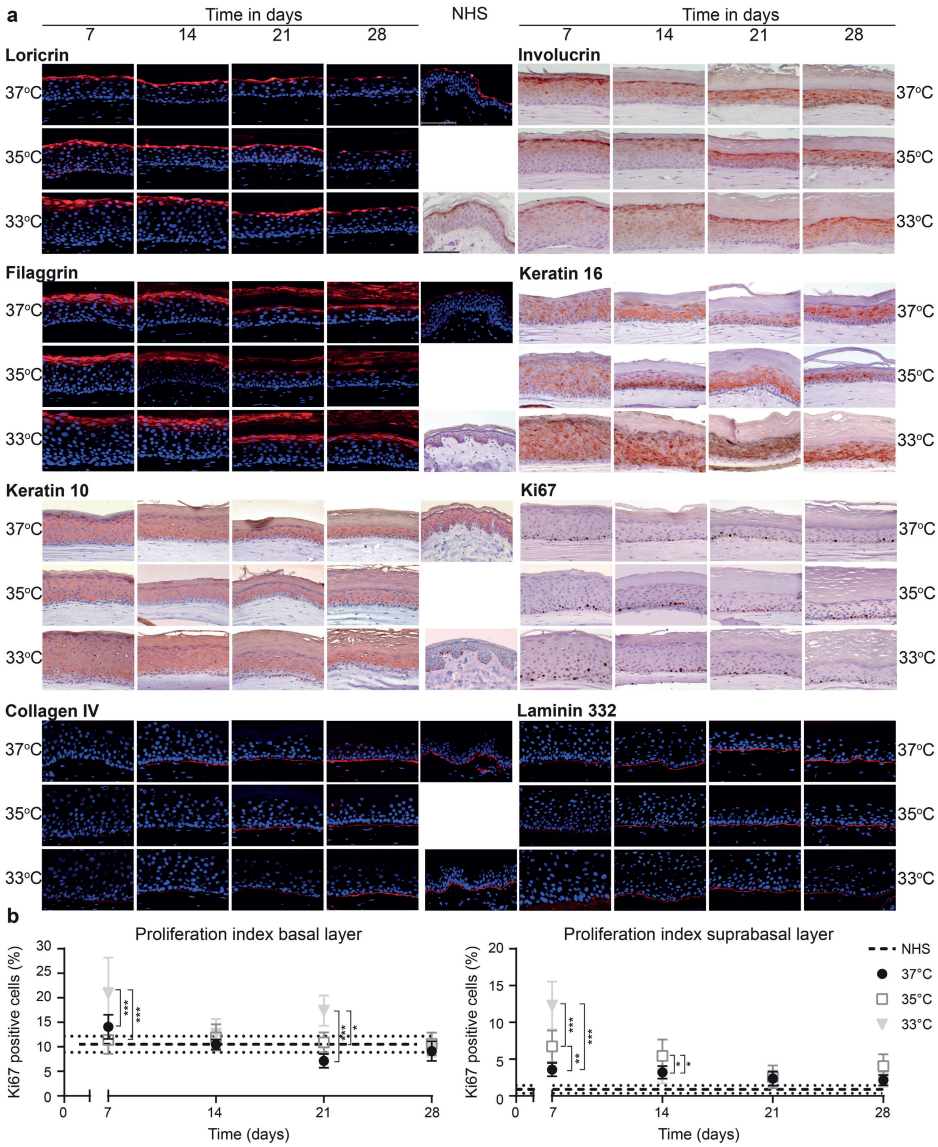


Figure 2. Epidermal morphogenesis in FTMs generated at different temperatures over time. **(a)** Expression of protein biomarkers for the late and terminal differentiation programs (loricrin, involucrin, filaggrin), epidermal activation (keratin 16), early differentiation (keratin 10), proliferation (Ki67) and basement membrane formation (collagen type IV and laminin 332). Protein expression is shown in FTMs developed at different temperatures over time and in NHS (middle section). Nuclei are stained blue using haematoxylin or DAPI. Scale bar indicates 100 µm. **(b)** The number of Ki67 positive cells in the basal and suprabasal layer. The proliferation index of NHS is indicated by the horizontal dotted lines (not as function of time). Data represent mean ± 95% CI, n≥3.

Epidermal cell activation was determined by the expression of keratin 16. This protein remained expressed in all conditions over time, in contrast to its absence in NHS. At reduced temperature the expression of the early differentiation marker keratin 10 is delayed. The proliferation index was determined for both the basal and suprabasal Ki67 positive cells (**Fig. 2 b**). At reduced temperature, the basal layer proliferation index was lower, while it was higher for suprabasal positive cells. Finally, we assessed the deposition of basement membrane proteins. Over time, an increased expression of collagen type IV and laminin 332 was observed. When comparing the FTMs developed at different temperatures, the deposition of collagen type IV is continuous but delayed at 35°C and 33°C.

3.3. Melanogenesis in the viable epidermis

Further investigation on the skin-coloring in FTMs generated at 37°C, 35°C and 33°C was performed by visualising the melanin content (**Fig. 3 a**). The melanin in the FTMs was less abundant at reduced temperature and more abundant at later time points, in line with the macroscopic observations (**Fig. 1 a**). Quantification of the melanin content in the viable epidermis revealed a significant reduction of melanin in FTMs generated at 33°C after 21 and 28 days in culture (**Fig. 3 b**). At FTMs developed at 35°C, there was no significant difference in the melanin content, irrespective of time compared to 37°C.

3.4. Stratum corneum lipid matrix composition

Epidermal barrier formation was investigated by examination of the SC lipid matrix composition. The twelve most abundant CER subclasses of the intercorneocyte space were evaluated (**Fig. 4 a**). The CERs from the lipid extract were detected as shown in the ion maps of FTMs generated at 14 days of culture (**Supplementary fig. 3**), which were highly similar as those of FTMs 28 days air-exposed (*data not shown*). Each subclass represents a series of CER entities due to the variation in chain length. In the ion maps of FTMs, we detected a high number of CER entities with a mass below 600 amu, indicative for the presence of CERs with a short total carbon chain length. The ratio between lipids to extracted SC weight was unchanged after reducing the culture temperature and is comparable to that of NHS (**Fig. 4 b**). To characterize the ceramide composition thoroughly, the CER composition was quantified into absolute amounts. The cumulative amounts of CERs of FTMs and NHS were compared, which revealed a high similarity in total CER content (**Fig. 4 c**). Due to the presence of lower mass CERs on the ion maps of FTMs, we determined the average carbon chain length of CER[non-EO] and CER[EO] separately (**Fig. 4 d,e**). The average carbon chain length of CER[non-EO] was similar in most FTMs, but was significantly reduced compared to that in NHS. In FTMs generated at 33°C, the shortest average chain length was observed of CER[non-EO] and CER[EO]. The average chain length of CER[EO] resembled that of NHS to a high extent. When focusing on carbon chain length distribution,

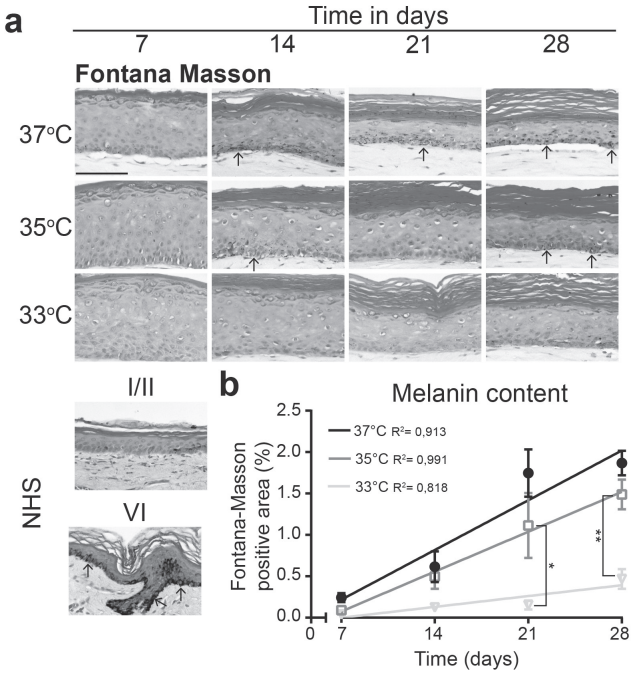


Figure 3. Melanogenesis in FTMs generated at different temperatures over time. (a) Fontana-Masson silver staining of melanin in FTMs developed at different temperatures over time and in NHS phototype I/II and phototype VI. Epidermis is counterstained with nuclear fast red. Arrowheads indicate melanin position. Scale bar indicates 100 µm. **(b)** Quantified melanin content in the viable epidermis plotted as Fontana-Masson positive area as percentage of the total area. Data represent mean ± SEM n≥2, and is fitted with a linear regression line.

a higher level of C34-C42 CER[non-EO] and a lower level of C42-C52 CER[non-EO] was observed in FTMs compared to that in NHS, while in FTMs generated at 33°C the C34-C42 CER[non-EO] were higher and the C42-C52 CER[non-EO] were lower than in FTMs generated at the two other temperatures (**Supplementary fig. 4 a**). In most conditions no differences were detected between FTMs and NHS regarding the CER[EO] chain length distribution, except in FTMs generated at the lowest temperature the distribution deviated significantly from those generated at the other two temperatures (**Supplementary fig. 4 b**).

Then, the CER subclass profiles of all FTMs and NHS were analysed, revealing comparability between the various culture temperatures in contrast to more substantial difference from that of NHS (**Fig. 4 f,g**). In FTMs generated at 33°C the CER subclass profile deviated from FTMs generated at 37°C, as subclasses NS, AS and EOS were significantly higher at 14 days culture deviating more from the subclass profile of NHS. Then, additional characteristics of CERs were examined, starting with the level of monounsaturated CERs. This is indicated by

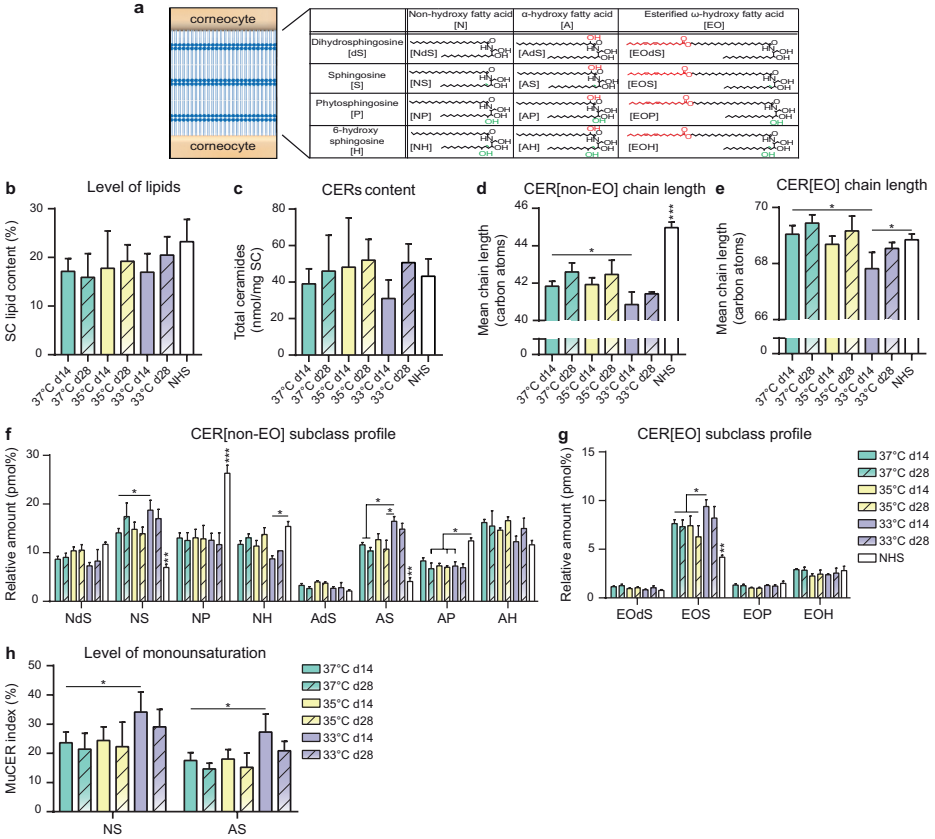


Figure 4. Barrier lipid composition in FTMs generated at different temperatures over time. **(a)** Schematic overview of the intercorneocyte lipid matrix with a table of the twelve most abundant ceramide subclasses, modified from Janssens *et al.* [36] with nomenclature of Motta *et al.* [35]. In the structure formulas, red parts indicate fatty acid based variations and green parts indicate sphingosine based variations. **(b)** Level of total lipids in the SC of indicated FTMs harvested at day 14 (d14) and day 28 (d28) after air-exposure and of NHS. **(c)** Total amount of CERs per mg SC in indicated FTMs and of NHS. **(d)** Bar diagram plot compares the average CER[non-EO] carbon chain lengths of saturated CERs of indicated FTMs and NHS. **(e)** Bar diagram plot compares the average CER[EO] carbon chain lengths of saturated CERs of indicated FTMs and NHS. **(f)** Saturated CER[non-EO] subclass profile of indicated FTMs and NHS. The total amount of saturated CERs has been set to 100%. **(g)** Saturated CER[EO] subclass profile of indicated FTMs and NHS. **(h)** Bar diagram plot compares the level of monounsaturation per ceramide subclass NS and AS of indicated FTMs. All data represent mean + SD, n≥3 (except in 33°C d28 where n=2). Significance is shown for comparison between FTMs (with lines and asterisk) horizontally and for comparison of FTMs to NHS (vertically by NHS), otherwise indicated. Statistical differences are noted as *, ** or ***, corresponding to P<0.05, <0.01, <0.001.

the percentage of monounsaturated as compared to the saturated CER; i.e. the unsaturation index. Changes in the unsaturation index of CER AS and NS provide a good indication for differences in the level of monounsaturated CERs in the total CER composition (*unpublished data*). In NHS, no monounsaturated CERs were analysed due to their low abundance, but these are substantially present in FTMs. The unsaturation index is significantly higher in FTMs developed at 33°C after 14 days (**Fig. 4 h**). Over time, small changes in the unsaturation index were observed, albeit not significantly. Finally, the presence of glucosylceramides (GlcCERs) as an important CER precursor was determined. The level of GlcCERs is indicated by the ratio in area of GlcCER to its CER analogue; i.e. the GlcCER index. This was determined for CERs EOS and EOH, as their GlcCER subclasses are processed exclusively by β-glucocerebrosidase (GBA). Furthermore, the CER[EO] are very relevant for a proper SC lipid matrix structure. The GlcCERs were detected in the ion plots of FTMs and NHS (**Supplementary fig. 5 a**). Most GlcCERs were present in FTMs generated at the lowest temperature, which were also elevated as compared to NHS (**Supplementary fig. 5 b**). When comparing the GlcCER indexes of FTMs over time, the GlcCERs index decreases after a longer culture period.

3.5. Lipid organization

As a result of the composition, the lipids in the intercorneocyte space form a highly structured organization. To evaluate the effect of culture temperature on the lamellar organization, small-angle X-ray diffraction studies were performed. In the obtained diffraction peak profile, various orders of diffraction were identified (**Fig. 5 a**). The obtained diffraction patterns of the FTMs indicate only the presence of the long periodicity phase (LPP), whereas in NHS both the LPP and short periodicity phase (SPP) have been detected [33]. No major differences were observed in the diffraction pattern of the FTMs developed at reduced temperatures, indicating similar phase behaviour. The peak position of the first, second and third order of diffraction was used to calculate the repeat distance of the lipid lamellae in FTMs (**Fig. 5 b**). This revealed an equal repeat distance of the LPP in all tested conditions.

4. Discussion

The main objective of this study was to investigate the influence of culture temperature on epidermal morphogenesis and barrier formation in HSEs. Our results demonstrate that reduction in culture temperature in FTMs augmented hyperplasia and leads to disorganization of the lower epidermal layers, indicated by the increased suprabasal proliferation and delayed early differentiation. In contrast, the late and terminal differentiation programs are weakly affected by culture temperature and the corneocyte layers are formed at similar rate. In line

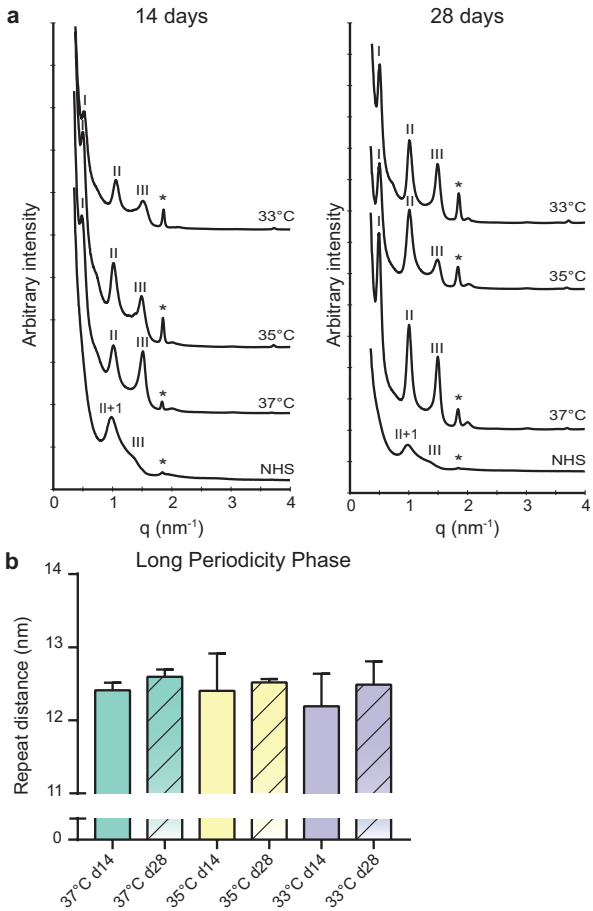


Figure 5. Lamellar organization within the lipid matrix. **(a)** Small angle X-ray diffraction patterns of FTMs developed at different temperatures during 14 (d14) and 28 (d28) days air-exposure combined with an identical NHS diffraction pattern. LPP diffraction orders are indicated by roman numbers, SPP diffraction orders by Arabic numbers (NHS only) and the diffraction peak of phase separated cholesterol is indicated by the asterisk (*). **(b)** Bar diagram plot compares the repeat distance of the long periodicity phase. Data represent mean ± 95% CI, n≥3 (except in 33°C d28 where n=2).

with terminal differentiation, the CER composition minimally differs at 35°C from that at 37°C, but deviates in some aspects significantly at 33°C. Although in NHS the skin surface temperature (28-32°C) is lower than the temperatures we tested *in vitro* (35°C and 33°C), closer approximation of *in vivo* temperatures used to generate FTMs is discouraged due to the higher disorganization of the lower epidermal layers at reduced culture temperature. This suggests that the lower epidermal layers are supported by temperatures closer to 37°C, indicating that the temperature gradient encountered in NHS plays an important role in the well-orchestrated epidermal morphogenesis.

Our findings are consistent with earlier results of keratinocytes grown on fibroblast-free de-epidermized dermis, at which the viable epidermis is thicker at 33°C compared to 37°C [20]. Furthermore, our data is in agreement with previous findings from our group observed in HSEs and skin barrier repair explant model cultured at reduced temperature (32/33°C) regarding the delayed

early differentiation [21, 27]. As in one of these models the basement membrane (BM) is already established, the dermal and BM structure are unlikely to induce the observed disorganization in the lower region [27]. Although our data differs to some extent from reports on the anti-proliferating and pro-differentiating effect induced by lower culture temperature [23, 24], it could be argued that the monolayer cultures of human keratinocytes which demonstrated these effects on proliferation/differentiation lack the epidermal calcium gradient and 3D epidermal structures, both important for epidermal homeostasis [37]. Advantage of our approach is the use of 3D co-culture models, which adds another aspect of complexity on how temperature reduction affects epidermal morphogenesis.

The main physical barrier of NHS and HSEs is formed by corneocytes, corneodesmosomes, tight junctions, and the lipid matrix [4, 38, 39]. However, in this study the lipid matrix was characterized, which is the only continuous pathway through the SC, thereby regarded pivotal for the outside-in permeability barrier. The formation of the lipid barrier remains comparable at earlier and later time points, which is important for the performance of FTMs during long-term *in vitro* testing. At this detailed level, this has not been reported before. In our compositional analysis, the relative abundance of CER[EO] is underestimated, since no unsaturated CER[EO] with a linoleic acyl chain (contributing ~17-19% to FTM and NHS (*unpublished data*)) and saturated CER[EO] with an oleic acyl chain (contributing ~23% to FTM (*unpublished data*)) were analysed. Nonetheless, the interpretation of the data is not affected by this. The increment in the level of CER subclasses AS and NS which are observed in FTMs generated at 33°C are also observed in regenerated SC of *ex vivo* skin and in *in vivo* diseased skin conditions [27, 40, 41]. Hence, these specific subclass alterations in several skin conditions could be linked to epidermal homeostatic imbalance, additionally emphasized by an upregulated keratin 16 expression. Furthermore, the ceramide composition contributes to the barrier functionality, as demonstrated in *in vivo* (diseased) skin conditions [36, 42], in HSEs [11, 31] and in pure lipid model membranes [43-45], suggesting a similar or reduced barrier functionality at lowered culture temperature. The CER precursors GlcCER was less abundant at a later time point, possibly ascribed to more activity of GBA over time or to the maturation of the SG-SC interface over time indicated by the flattening of the granular cells [46]. The normalization in GlcCER content over time could also improve the barrier functionality, since impairment in the formation and conversion negatively affects the barrier functionality [47-49].

In line with the result of the lipid composition, the lamellar organization is unaltered irrespective of the culture temperature and time. In the SC of FTMs, only LPP and no SPP was observed, which is attributed especially to an increased level of CER[EO], but other factors may also play a role [14]. As compared to the

reported 13.4 nm repeat distance of the LPP in NHS, the repeat distance of the LPP in FTMs is shorter [33].

An interesting, and not yet reported observation is the pigmentation in the epidermis of FTMs over time. In FTMs generated at reduced temperature the pigmentation was reduced and/or delayed. Although melanocytes were not added to the FTM intentionally, during isolation of primary keratinocytes and subsequent culturing of these in keratinocyte culture medium, a small subset of melanocyte cells survived and induced pigmentation in FTMs. The Fontana-Masson silver positive staining in parts of the SC is most likely caused by non-specific staining silver deposition in the SC as suggested earlier [50]. Our results are consistent with previous work by Kim *et al.* [51], who suggested that temperature may affect the activity of key melanogenic enzyme tyrosinase. However, further research is required to gain more insights on the possible association between fibroblast-melanocyte cross-talk in HSEs [52], lower epidermal region disorganization, culture temperature and pigmentation.

In conclusion, our results show that culture temperature strongly affects epidermal morphogenesis and melanogenesis but the barrier formation to a lesser extent. External conditions during *in vitro* tissue engineering play an important role and should be optimal to enhance the resemblance of human skin equivalents to native skin tissue.

5. Acknowledgements

This research was financially supported by Dutch Technology Foundation STW (grant no. 13151), which is part of the Netherlands Organisation for Scientific Research (NWO), and which is partly funded by the Ministry of Economic Affairs. The authors would like to thank the personnel at the DUBBLE beam line (BM26) at the ESRF for their support with the X-ray measurements. We thank the company Evonik (Essen, Germany) for their generous provision of ceramides.

6. Author Disclosure Statement

The authors declare no conflict of interest.

7. References

1. Boyce, S.T., Cultured skin substitutes: a review. Tissue engineering, 1996. 2(4): p. 255-266.
2. Planz, V., C.-M. Lehr, and M. Windbergs, In vitro models for evaluating safety and efficacy of novel technologies for skin drug delivery. Journal of Controlled Release, 2016. 242: p. 89-104.
3. Gordon, S., et al., Non-animal models of epithelial barriers (skin, intestine and lung) in research, industrial applications and regulatory toxicology. Alternatives to Animal Experimentation: ALTEX, 2015. 32(4): p. 327-378.
4. Niehues, H., et al., 3D skin models for 3R research: the potential of 3D reconstructed skin models to study skin barrier function. Experimental dermatology, 2018.
5. Proksch, E., J.M. Brandner, and J.-M. Jensen, The skin: an indispensable barrier. Experimental Dermatology, 2008. 17(12): p. 1063-1072.
6. Bouwstra, J.A., et al., Structure of the skin barrier and its modulation by vesicular formulations. Progress in Lipid Research, 2003. 42(1): p. 1-36.
7. Boncheva, M., The physical chemistry of the stratum corneum lipids. International journal of cosmetic science, 2014. 36(6): p. 505-515.
8. Regnier, M., et al., Barrier Function of Human Skin and Human Reconstructed Epidermis. Journal of Pharmaceutical Sciences, 1993. 82(4): p. 404-407.
9. Schmook, F.P., J.G. Meingassner, and A. Billich, Comparison of human skin or epidermis models with human and animal skin in in-vitro percutaneous absorption. International Journal of Pharmaceutics, 2001. 215(1): p. 51-56.
10. Schreiber, S., et al., Reconstructed epidermis versus human and animal skin in skin absorption studies. Toxicology in Vitro, 2005. 19(6): p. 813-822.
11. Thakoersing, V.S., et al., Unraveling barrier properties of three different in-house human skin equivalents. Tissue Engineering Part C: Methods, 2011. 18(1): p. 1-11.
12. Mojumdar, E.H., et al., Stratum corneum lipid matrix: Location of acyl ceramide and cholesterol in the unit cell of the long periodicity phase. Biochimica et Biophysica Acta (BBA) - Biomembranes, 2016. 1858(8): p. 1926-1934.
13. Eichner, A., et al., Localization of methyl-branched ceramide [EOS] species within the long-periodicity phase in stratum corneum lipid model membranes: A neutron diffraction study. Biochimica et Biophysica Acta (BBA) - Biomembranes, 2016. 1858(11): p. 2911-2922.
14. Thakoersing, V.S., et al., Increased Presence of Monounsaturated Fatty Acids in the Stratum Corneum of Human Skin Equivalents. Journal of Investigative Dermatology, 2013. 133(1): p. 59-67.
15. Mojumdar, E.H., et al., Monounsaturated fatty acids reduce the barrier of stratum corneum lipid membranes by enhancing the formation of a hexagonal lateral packing. Langmuir, 2014. 30(22): p. 6534-6543.
16. Feingold, K.R. and P.M. Elias, Role of lipids in the formation and maintenance of the cutaneous permeability barrier. Biochimica et Biophysica Acta (BBA) - Molecular and Cell Biology of Lipids, 2014. 1841(3): p. 280-294.
17. Ponec, M., et al., Lipid composition of cultured human keratinocytes in relation to their differentiation. Journal of lipid research, 1988. 29(7): p. 949-961.
18. Stark, H.-J., et al., Organotypic Keratinocyte Cocultures in Defined Medium with Regular Epidermal Morphogenesis and Differentiation. Journal of Investigative Dermatology, 1999. 112(5): p. 681-691.
19. Ponec, M., et al., The formation of competent barrier lipids in reconstructed human epidermis requires the presence of vitamin C. Journal of investigative dermatology, 1997. 109(3): p. 348-355.
20. Gibbs, S., et al., Culture of reconstructed epidermis in a defined medium at 33 C shows a delayed epidermal maturation, prolonged lifespan and improved stratum corneum. Archives of dermatological research, 1997. 289(10): p. 585-595.
21. Ponec, M., et al., Epidermal growth factor and temperature regulate keratinocyte differentiation. Archives of dermatological research, 1997. 289(6): p. 317-326.
22. Pinnagoda, J., et al., Guidelines for transepidermal water loss (TEWL) measurement. Contact dermatitis, 1990. 22(3): p. 164-178.
23. Borowiec, A.-S., et al., Optimal differentiation of in vitro keratinocytes requires multifactorial external control. PloS one, 2013. 8(10): p. e77507.
24. Viano, M., et al., A thermal gradient modulates the oxidative metabolism and growth of human keratinocytes. FEBS Open Bio, 2017: p. 1843–1853.
25. Bidaux, G., et al., Epidermal TRPM8 channel isoform controls the balance between keratinocyte proliferation and differentiation in a cold-dependent manner. Proceedings of the National Academy of Sciences, 2015. 112(26): p. E3345-E3354.

26. Bidaux, G., et al., Fine-tuning of eTRPM8 expression and activity conditions keratinocyte fate. Channels, 2016. 10(4): p. 320-331.
27. Danso, M.O., et al., An ex vivo human skin model for studying skin barrier repair. Experimental Dermatology, 2015. 24(1): p. 48-54.
28. Haisma, E.M., et al., Inflammatory and antimicrobial responses to methicillin-resistant Staphylococcus aureus in an in vitro wound infection model. PloS one, 2013. 8(12): p. e82800.
29. El Ghalbzouri, A., et al., Replacement of animal-derived collagen matrix by human fibroblast-derived dermal matrix for human skin equivalent products. Biomaterials, 2009. 30(1): p. 71-78.
30. van Drongelen, V., et al., Barrier properties of an N/TERT-based human skin equivalent. Tissue Engineering Part A, 2014. 20(21-22): p. 3041-3049.
31. Mieremet, A., et al., Improved epidermal barrier formation in human skin models by chitosan modulated dermal matrices. PloS one, 2017. 12(3): p. e0174478.
32. Mieremet, A., et al., Recapitulation of Native Dermal Tissue in a Full-Thickness Human Skin Model Using Human Collagens. Tissue Engineering Part A, 2017.
33. Bouwstra, J.A., et al., Structural Investigations of Human Stratum Corneum by Small-Angle X-Ray Scattering. Journal of Investigative Dermatology, 1991. 97(6): p. 1005-1012.
34. Boiten, W., et al., Quantitative analysis of ceramides using a novel lipidomics approach with three dimensional response modelling. Biochimica et Biophysica Acta (BBA)-Molecular and Cell Biology of Lipids, 2016. 1861(11): p. 1652-1661.
35. Motta, S., et al., Ceramide composition of the psoriatic scale. Biochimica et Biophysica Acta (BBA)-Molecular Basis of Disease, 1993. 1182(2): p. 147-151.
36. Janssens, M., et al., Increase in short-chain ceramides correlates with an altered lipid organization and decreased barrier function in atopic eczema patients. Journal of lipid research, 2012. 53(12): p. 2755-2766.
37. Elias, P.M., et al., Modulations in Epidermal Calcium Regulate the Expression of Differentiation-Specific Markers. Journal of Investigative Dermatology, 2002. 119(5): p. 1128-1136.
38. Basler, K., et al., The role of tight junctions in skin barrier function and dermal absorption. J Control Release, 2016. 242: p. 105-118.
39. Haftek, M., Epidermal barrier disorders and corneodesmosome defects. Cell and tissue research, 2015. 360(3): p. 483-490.
40. Boiten, W.A., et al., Applying a vernix caseosa based formulation accelerates skin barrier repair by modulating lipid biosynthesis. Journal of lipid research, 2018. 59(2): p. 250-260.
41. Van Smeden, J., et al., Intercellular skin barrier lipid composition and organization in Netherton syndrome patients. Journal of Investigative Dermatology, 2014. 134(5): p. 1238-1245.
42. Coderch, L., et al., Ceramides and Skin Function. American Journal of Clinical Dermatology, 2003. 4(2): p. 107-129.
43. Groen, D., et al., Investigating the barrier function of skin lipid models with varying compositions. European Journal of Pharmaceutics and Biopharmaceutics, 2011. 79(2): p. 334-342.
44. Mojumdar, E., et al., The role of ceramide chain length distribution on the barrier properties of the skin lipid membranes. Biochimica et Biophysica Acta (BBA)-Biomembranes, 2014. 1838(10): p. 2473-2483.
45. Školová, B., et al., Ceramides in the Skin Lipid Membranes: Length Matters. Langmuir, 2013. 29(50): p. 15624-15633.
46. Takagi, Y., et al., β-Glucocerebrosidase activity in mammalian stratum corneum. Journal of lipid research, 1999. 40(5): p. 861-869.
47. Sochorová, M., et al., Permeability Barrier and Microstructure of Skin Lipid Membrane Models of Impaired Glucosylceramide Processing. Scientific Reports, 2017. 7.
48. Holleran, W.M., et al., Consequences of beta-glucocerebrosidase deficiency in epidermis. Ultrastructure and permeability barrier alterations in Gaucher disease. Journal of Clinical Investigation, 1994. 93(4): p. 1756-1764.
49. Jennemann, R., et al., Integrity and barrier function of the epidermis critically depend on glucosylceramide synthesis. Journal of Biological Chemistry, 2007. 282(5): p. 3083-3094.
50. Joly-Tonetti, N., et al., Melanin fate in the human epidermis: a reassessment of how best to detect and analyse histologically. Experimental Dermatology, 2016. 25(7): p. 501-504.
51. Kim, D.-S., et al., Temperature regulates melanin synthesis in melanocytes. Archives of Pharmacal Research, 2003. 26(10): p. 840.
52. Wang, Y., et al., Precise role of dermal fibroblasts on melanocyte pigmentation. Journal of Dermatological Science, 2017. 88(2): p. 159-166.
53. van Smeden, J., et al., In situ visualization of glucocerebrosidase in human skin tissue: zymography versus activity-based probe labeling. Journal of lipid research, 2017. 58(12): p. 2299-2309.

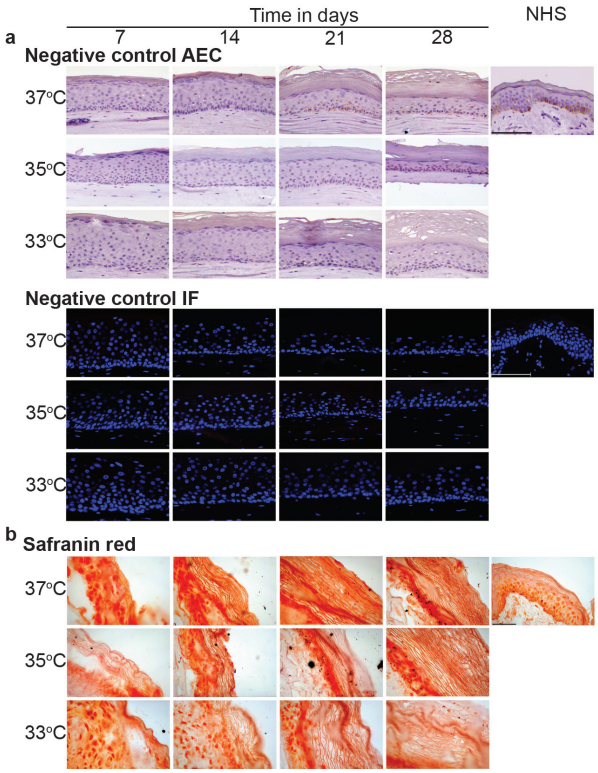
8. Supplementary information

Supplementary table 1. Specification of antibodies used for immunohistochemical and immunofluorescence staining.

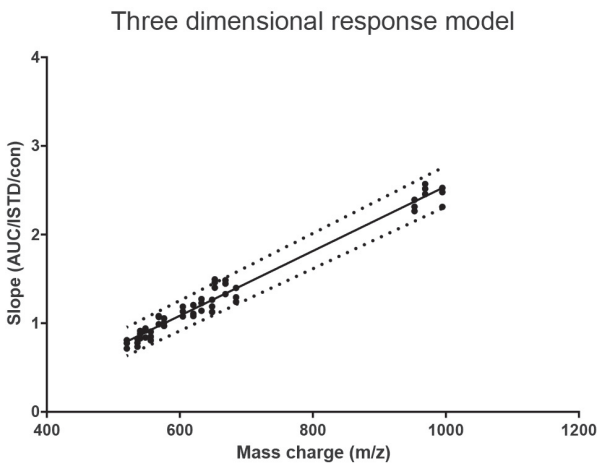
Immunohistochemistry	Origin	Clone	Dilution	Secondary antibody	Manufacturer
Primary antibody					
Ki67	Mouse	MIB1	1:100	A	DAKO, Denmark
Cytokeratin 10	Mouse	DE-K10	1:50	A	Labvision/Neomarkers, USA
Involucrin	Mouse	SY5	1:1200	A	Sanbio, The Netherlands
Cytokeratin 16	Mouse	LL025	1:100	A	Serotec, UK
Secondary antibody					
A) Biotinylated goat anti-mouse	Goat		1:200		Southern Biotechnology, USA
Immunofluorescence	**Origin**	**Clone**	**Dilution**	**Secondary antibody**	**Manufacturer**
Primary antibody					
Loricrin	Rabbit	AF62	1:1000	B	Covance, The Netherlands
Filaggrin	Rabbit	PRB417	1:1000	C	Covance, The Netherlands
Collagen type IV	Mouse	24.12.8 (PHM-12)	1:75	D	Chemicon, Australia
Laminin 332	Mouse	BM165	1:150	D	Provided by Dr. M. Aumailley, Germany
Secondary antibody					
B) Cy3-conjugated anti-rabbit	Goat		1:500		Jackson immunoresearch Laboratory, USA

Supplementary table 1 (continued)

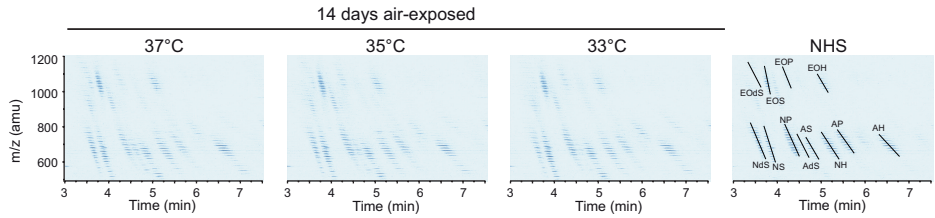
Immunofluorescence	Origin	Clone	Dilution	Secondary antibody	Manufacturer
C) Rodamine-conjugated anti-rabbit	Goat		1:300		Jackson immunoresearch Laboratory, USA
D) Cy3-conjugated anti-mouse	Goat		1:1000		Jackson immunoresearch Laboratory, USA



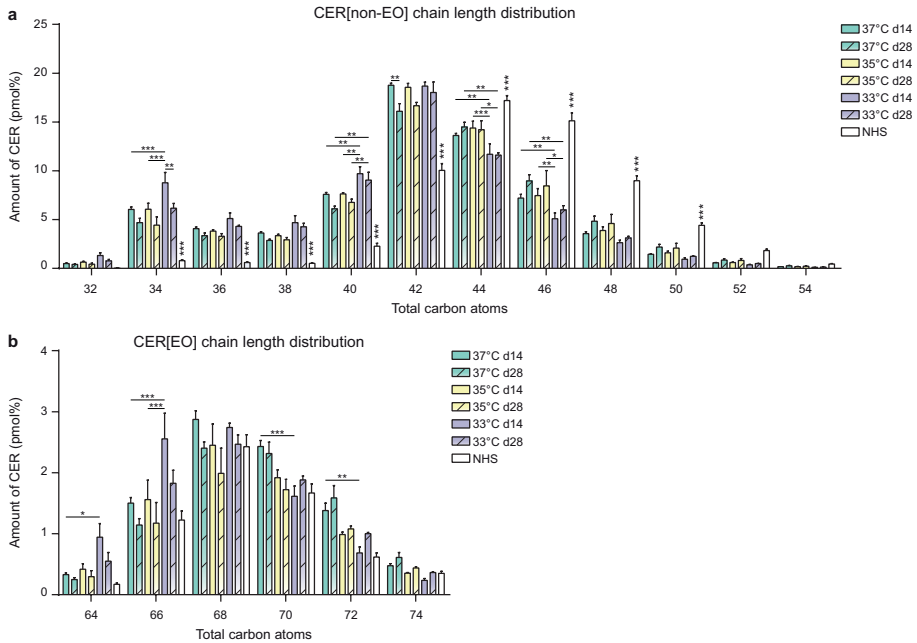
Supplementary figure 1. Negative controls of immunohistochemistry and safranin red staining of stratum corneum. **(a)** Experimental negative controls of immunohistochemistry and immunofluorescence stainings. Nuclei are stained blue using haematoxylin or DAPI. **(b)** Representative cross sections of FTMs and NHS stained with safranin red followed by alkali induced expansion of the stratum corneum used for quantification of the amount of corneocyte layers. Scale bar indicates 100 µm.



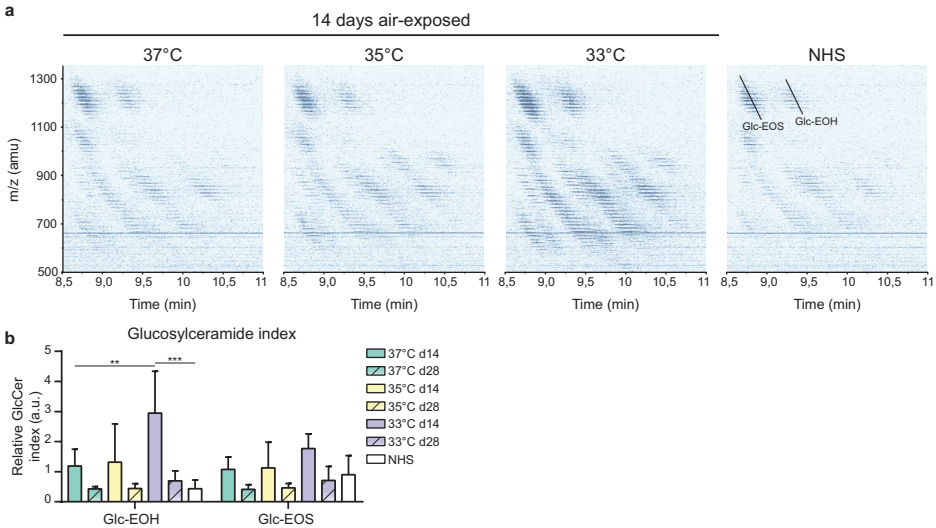
Supplementary figure 2. Three-dimensional response model for quantification of CERs. This 3D response model is used for quantification of the CER composition. Model is based on mass spectrometry settings, compound properties and a calibration curve from a limited number of synthetic ceramides, as described by Boiten *et al.* [34].



Supplementary figure 3. Ion maps of FTMs developed at different temperatures after 14 days air-exposed and of NHS. Positions and names of ceramide subclasses are indicated in the ion map of NHS.



Supplementary figure 4. Ceramide carbon chain length distribution of FTMs and NHS. (a) Bar diagram plot of CER[non-EO] with an even number of carbon atoms of FTMs generated at different temperatures during 14 and 28 days air-exposure and of NHS. **(b)** Bar diagram plot of even numbered CER[EO] of FTMs generated at different temperatures during 14 and 28 days air-exposure and of NHS. The saturated CERs has been set to 100%. Data represent mean + SEM, n≥3 (except 33°C d28 where n=2). Significance is shown for comparison between FTMs (with lines and asterisk) horizontally and for comparison of FTMs to NHS (vertically by NHS), otherwise indicated. Statistical differences are noted as *, ** or ***, corresponding to P<0.05, <0.01, <0.001.



Supplementary figure 5. Glucosylceramides in the lipid matrix of FTMs and NHS. (a) Ion plots of glucosylceramides as detected by LC-MS in FTMs developed for 14 days at 3 different temperatures and of NHS. Position and name of glucosyl-EOS and glucosyl-EOH (Glc-EOS and Glc-EOH) are indicated in the ion plot of NHS. **(b)** Bar diagram plot compares the glucosylceramide index of indicated FTMs and NHS based on the ratio of CERs EOS and EOH to their glucosylated analogues Glc-EOS and Glc-EOH, as described earlier [53]. Data represent mean + SD, n≥3 (except 33°C d28 where n=2).

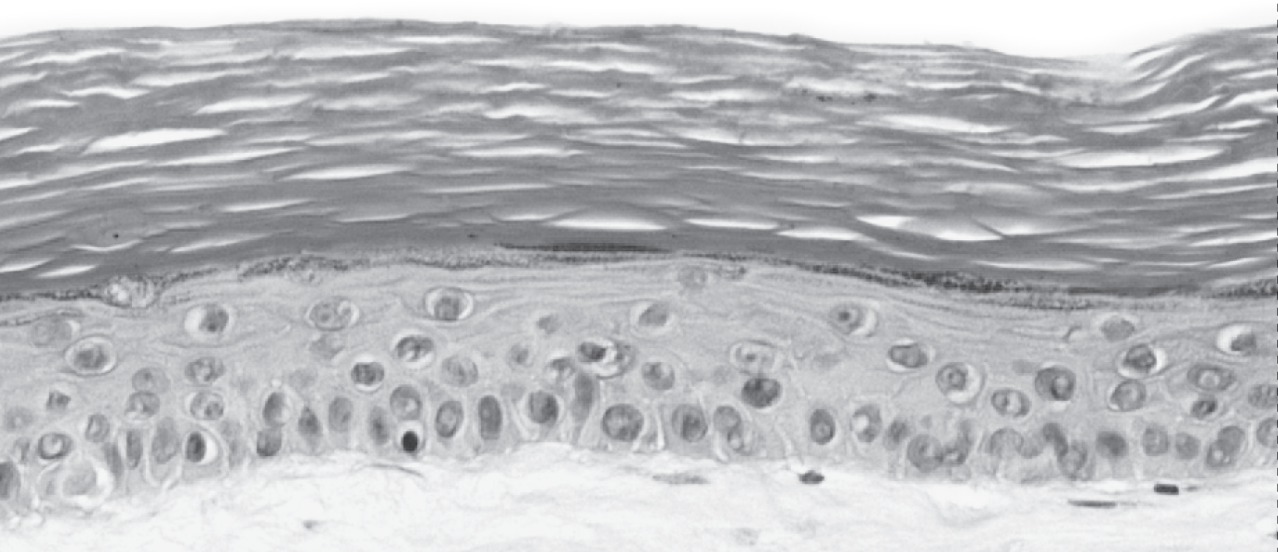
5

Human skin equivalents cultured under hypoxia display enhanced epidermal morphogenesis and lipid barrier formation

Arnout Mieremet
Adela Vázquez García
Walter Boiten
Rianne van Dijk
Gert Gooris
Joke A. Bouwstra[+]
Abdoelwaheb El Ghalbzouri[+]

[+] Joint senior authorship

Scientific Reports 9: 7811
(2019)



Abstract

Human skin equivalents (HSEs) are three-dimensional cell models mimicking characteristics of native human skin (NHS) to a high extent. However, a limitation of HSEs is the altered *in vitro* morphogenesis and barrier formation. These differences between *in vitro* and *in vivo* skin could have been induced by suboptimal cell culture conditions, of which the level of oxygen *in vitro* (20%) is much higher than *in vivo* (0.5-8%). Our aim is to study how external oxygen levels affect epidermal morphogenesis and barrier formation in HSEs. In the present study, fibroblast and keratinocyte monocultures, and HSEs were generated under 20% (normoxia) and 3% (hypoxia) oxygen level. In all cultures under hypoxia, expression of hypoxia-inducible factor target genes was increased. Characterization of HSEs generated under hypoxia using immunohistochemical analyses of morphogenesis biomarkers revealed a reduction in epidermal thickness, reduced proliferation, similar early differentiation, and an attenuated terminal differentiation program compared to normoxia, better mimicking NHS. The stratum corneum ceramide composition was studied with liquid chromatography coupled to mass spectrometry. Under hypoxia, HSEs exhibited a ceramide composition that more closely resembles that of NHS. Consequently, the lipid organization was improved. In conclusion, epidermal morphogenesis and barrier formation in HSEs reconstructed under hypoxia better mimics that of NHS.

1. Introduction

Three-dimensional (3D) human skin equivalents (HSEs) are mainly used for toxicology screenings and for research purposes to increase the knowledge on skin biology, or particularly the skin barrier formation. Various types of 3D skin models are currently available, including epidermal skin models, full thickness skin models (FTMs) (**Supplementary fig. 1 a,b**), explant models, and skin-on-a-chip models, listed by increased complexity and physiological relevance [1-7]. As reviewed recently by Niehues *et al.* [8], while all of these models have advantages and limitations, a known limitation of the *in vitro* developed skin models is the altered barrier formation and resulting reduced functionality when compared to native human skin (NHS) [9-11]. This could lead to inadequate *in vitro – in vivo* correlations regarding pharmacokinetics and permeability testing of compounds or misinterpretation of adverse outcome pathways [12].

The permeability barrier of the epidermis resides mainly in the uppermost layer, the stratum corneum (SC). In this layer of dead cells, corneocytes are keratinized and cross-linked to form impermeable structures [13, 14]. In between the corneocytes, the lipids form the only continuous pathway through the SC (**Supplementary fig. 1 c,d**). The lipids form a highly structured matrix organized in densely packed crystalline lamellar phases [15] (**Supplementary fig. 1 e,f**). This lipid matrix contributes substantially to the barrier functions of the skin, which are protecting from external substance or allergen entry and restricting water loss [15, 16]. The most abundant lipid classes within the SC are cholesterol, free fatty acids (FFAs) and ceramides [17]. Several ceramide subclasses exist, categorized based on their head group architecture [18-21]. When considering the total ceramides (CERs) subclasses analyzed in this study, these consist of (non ω-esterified) ceramides (CER[non-EO]) and ω-esterified ceramides (CER[EO]) (**Supplementary fig. 2**). Alterations in lipid composition most probably lead to an altered organization and can thereby reduce the permeability barrier functionality. This is encountered in HSEs and diseased skin conditions [22, 23]. In detail, the alterations in the lipid composition of HSEs as compared to NHS include an altered CER subclass profile, reduction of CER carbon chain length, and a higher level of monounsaturated CERs. These alterations directly affect the lipid organization, including the reduction in lamellar phase repeat distance and the conversion in lateral packing from a predominant orthorhombic to a hexagonal packing [22, 24].

Normalization of the barrier formation of HSEs is a complex procedure, as many external factors differ between *in vivo* and *in vitro* culture conditions. Besides a nutrient imbalance, several external factor differences are encountered, such as the constant high temperature (37°C) *in vitro*, the lack of sunlight, a high

environmental humidity, and a high oxygen level. Since the epidermis is not directly supplied with blood, the oxygen levels in the epidermis are regarded as low, ranging from 0.5% to 8% *in vivo* [25, 26]. In contrast, during culturing of HSEs the oxygen saturation is corresponding to the atmospheric oxygen pressure of the incubator (±20%) [27].

Oxygen levels affect cellular metabolism, as these are sensed continuously and can activate a signaling cascade mediated by Hypoxia-Inducible Factors (HIFs) [28]. HIFs are highly conserved transcriptional complexes comprising an oxygen labile subunit (HIF-1α, HIF-2α or HIF-3α) and a constitutively nuclear expressed HIF-1β subunit which can bind after heterodimerization to hypoxia response elements (HREs) [29]. As reported by Seleit *et al.* [30], in normal conditions HIF-1α is expressed in the basal and suprabasal layers in 90% of normal skin biopsies. During low or mild oxygen, nuclear translocation of HIF-α occurs, leading to transcriptional activation of HIF target genes [31]. More than 200 genes are involved in this pathway, of which many are involved in processes such as glycolysis, angiogenesis, apoptosis, adhesion, migration, and metastasis [26, 28]. Previous *in vivo* murine studies have already revealed that the HIF pathway is a crucial determinant of skin homeostasis [32, 33]. Because of the broad repercussion of HIFs in cellular gene expression, also of those involved in terminal differentiation and barrier properties of keratinocytes, it is of importance to obtain detailed insights on the effect of oxygen levels during the development of HSEs.

Therefore, we aim to study whether a reduction from a normoxic (20%) to a hypoxic (3%) oxygen level leads to higher resemblance to native epidermal morphogenesis and barrier formation in HSEs. Herein, we show that reduction from normoxia to hypoxia improved epidermal morphogenesis and SC barrier lipid composition mediated by activated HIF signaling pathway in HSEs.

2. Materials and methods

2.1. Isolation and culturing of primary fibroblasts and keratinocytes

Declaration of Helsinki principles are followed during obtainment of primary cells from human skin tissue originating from surplus breast tissue of healthy donors. Experiments were conducted in accordance with article 7:467 of the Dutch Law on Medical Treatment Agreement and the Code for proper Use of Human Tissue of the Dutch Federation of Biomedical Scientific Societies (https://www.federa.org/codes-conduct). As of this national legislation, coded surplus tissue can be used for scientific research purposes when no written objection in made by the informed donor, i.e. an informed opt-out system. Therefore, additional approval of an ethics committee regarding scientific use of surplus tissue was neither

requested nor required, as stated earlier [34]. Primary cells were isolated from surplus human mamma skin after separation of the epidermis and dermis by incubation in 2.4 U/mL dispase II (Roche, Almere, The Netherlands). Isolation and culturing of primary cell suspensions was performed as described before [35-37]. All isolated primary cells were tested and found negative for mycoplasma contamination. Amount of viable proliferating primary cells was determined by trypan blue exclusion assay using a Bio-Rad TC20™ automatic cell counter (Bio-Rad, Hercules, USA) according to manufacturer's instructions.

2.2. Generation of full thickness models

Full thickness models (FTMs) were generated in two steps and cultured on inert membranes using a transwell system (Corning Transwell cell culture inserts, membrane diameter 24 mm, pore size 3 µm; Corning Life Sciences, The Netherlands) as described before [9, 35]. In the first step, the dermal equivalents were generated using primary fibroblasts (1.2–1.5 x 10^5) in passage number 2-5, hydrated rat-tail tendon collagen (4 mg/mL), 1M NaOH, Hank's Balanced Salt Solution, and 5% fetal bovine serum (FBS; GE Healthcare, Logan, USA). After polymerization at 37°C, the dermal equivalents were cultured 7 days as described elsewhere [9, 35]. In the second step, the epidermal equivalents were generated by seeding primary keratinocytes (2.5 x 10^5/model) in passage number 1 directly onto each dermal equivalent as reported before [9, 37]. The FTMs were kept submerged for total of four days. Hereafter, the FTMs were lifted to the air-liquid interface and cultured for 14–15 days under normoxia (20%) in the Memmert INC153med CO_2 incubator (Memmert, Schwabach, Germany) or under hypoxia (3%) in the Heracell™ 240 CO_2 incubator (ThermoFisher). FTM batches were generated with 5 different primary cell donors.

2.3. Gene expression

2.3.1. RNA isolation

Isolation of RNA from 2D and 3D cell cultures was performed according to instructions provided by the manufacturer using a FavorPrep Tissue Total RNA Mini Kit (Favorgen, Ping-Tung, Taiwan). A single exception was the addition of a DNA digestion step, which was performed during 15 min after the initial washing steps using an RNAse-free DNAse solution (Qiagen, Hilden, Germany). Subsequently, the isolated RNA was eluted and the concentration of the nucleic acid content was determined using a NanoDrop™ UV-Vis Spectrophotometer (ThermoFisher).

2.3.2. Quantitative real-time polymerase chain reaction

A total of 500 ng isolated RNA was used to synthesize complementary DNA with an iScript™ cDNA Synthesis Kit (Bio-Rad, Hercules, USA). Then, quantitative real-time polymerase chain reactions were performed with the SYBR Green Supermix

(Bio-Rad) using the CFX384 Touch™ real-time PCR detection system (Bio-Rad). Used settings were described previously by Mieremet *et al.* [38]. Details on primer sequences used in this study are described in **Supplementary table 1**.

2.4. Tissue morphology

2.4.1. Tissue fixation

Sections of FTMs or NHS were fixated with formaldehyde for paraffin embedding or snap frozen for cryofixation. For paraffin embedding, the tissue was fixated overnight in 4% (w/v) formaldehyde (Added Pharma, Oss, The Netherlands), dehydrated and embedded in paraffin. For cryofixation, the tissue was placed in a gelatin capsule containing Tissue-Tek® O.C.T.™ Compound (Sakura Finetek Europe, Alphen aan den Rijn, The Netherlands), snap frozen in liquid nitrogen and stored at -80°C.

2.4.2. Protein expression

General morphological assessments were performed on 5 µm paraffin embedded tissue sections after staining with hematoxylin and eosin (HE; Klinipath, Duiven, The Netherlands). Immunohistochemical and immunofluorescence analyses of protein expression were performed on 5 µm sections. FFPE material was deparaffinized and rehydration, whereas frozen material was dried overnight and fixed in acetone for 10 minutes. For FFPE material, heat-mediated antigen retrieval in citrate buffer was performed, followed by blocking with normal human serum (Sanquin, Leiden, The Netherlands). Stainings were performed using the streptavidin-biotin-peroxidase system (GE Healthcare, Buckinghamshire, United Kingdom) according to the manufacturer's instructions or using indirect immunofluorescence, as described elsewhere. Exceptions were the ASMA and collagen type IV staining, for which no or protease-mediated antigen retrieval was performed respectively [35]. Visualization of the sections occurred using a light microscope (Zeiss Axioplan 2, Carl Zeiss BV, Breda, The Netherlands) or a fluorescence microscope (Leica CTR5000, Leica, Wetzlar, Germany). Application of solely secondary antibodies revealed no interfering background or unspecific staining (**Supplementary fig. 4 a**). Specifications of the materials are provided in **supplementary table 2**.

2.4.3. Determination of the number of corneocytes layers

Frozen sections were sliced 5 µm using a Leica CM3050S cryostat, placed on a Superfrost® Plus Micro Slide (VWR, Radnor, USA), air-dried overnight and fixed in ice-cold acetone for at least 10 min. Sections were stained for 1 min with a 1% (w/v) safranin O (Sigma) solution dissolved in Millipore water. After washout, a 2% (w/v) KOH solution was applied for 10-15 min to induce swelling of the corneocytes. Slides were sealed with a cover glass and imaged directly (**Supplementary fig. 4 b**).

2.4.4. Estimation of epidermal thickness and proliferation index

The epidermal thickness was determined by quantification of eight images of various tissue regions per sample. The outline of the nucleated epidermis area was measured with Adobe Photoshop (CS6 version 13.0) in pixels and transformed to squared micrometers. The proliferation index was estimated by counting the number of Ki67 positive nuclei of the basal layer in a region of minimally 100 cells. The resulting proliferation index is the percentage of Ki67 positive nuclei in at least three different regions.

2.5. Stratum corneum lipid composition

2.5.1. Stratum corneum isolation

Isolation of the stratum corneum occurred after overnight incubation in a 0.1% (w/v) trypsin/PBS solution at 4°C followed by incubation at 37°C for 1 hr. The SC was peeled off the epidermis and was washed with 0.1% trypsin inhibitor (Sigma) and Millipore water. The isolates were air-dried and stored at dry conditions.

2.5.2. Lipid extraction and liquid chromatography – mass spectrometry

Extraction of barrier lipids from the SC occurred using a modified Bligh and Dyer procedure [39], which was described by Boiten *et al.* [39]. To determine the amount of material extracted from the SC, the SC was dried and weighed before as well as after the extraction procedure. The obtained lipid extract was dissolved in a suitable volume of heptane:chloroform:methanol (95:2.5:2.5 v:v:v). The lipids were analyzed and quantified using normal phase liquid chromatography - mass spectrometry (LC-MS) analysis, as stated in the method described in Boiten *et al.* [40]. In brief, SC lipid extracts were separated on a PVA-Sil column (5 µm particles, 100 x 2.1 mm ID; YMC, Kyoto, Japan) with an Acquity UPLC H-class (Waters, Milford, MA, USA). CERs were detected by an XEVO TQ-S mass spectrometer (Waters). LC-MS measurements occurred in full scan mode with settings for time between 1.25 – 8.00 min at m/z 350–1350 and for time between 8.0-12.5 min at m/z 500-1350.

2.5.3. Data quantification

The area under the curve (AUC) of a chromatogram from the mono-isotopic mass of the main fragment was integrated. For a selected number of CERs, the relative abundance of the corresponding unsaturated CER containing two ^{13}C was more than 10%. When this occurred, the AUC of the two ^{13}C containing CER was calculated using its natural isotope distribution. This AUC was subtracted from the one of with which it overlapped. Quantification of the molar amount of ceramides occurred using the AUC of the chromatogram of any specific ceramide, the internal standard (INST) of CER N(24deuterated)S(18) and a three-dimensional response model based on compound properties and a calibration curve from a limited number of synthetic ceramides according to the method described by

Boiten *et al.* [40] (**Supplementary fig. 5**). Nomenclature of the CER subclasses is followed according to Motta *et al.* [41] and is shown in **supplementary figure 2**.

2.6. Stratum corneum lipid organization

2.6.1. Small-angle X-ray diffraction

Small-angle x-ray diffraction analyses occurred at station BM26B of the European Synchrotron Radiation Facility using methods specified before by Mojumdar *et al.* [42]. The detector was first calibrated with silver behenate and cholesterol followed by sample measurements, which occurred twice for 90 sec. Distance of the sample to the pilatus1M detector was approximately 2.1 meter. Profiles were obtained by converting the detector image from Cartesian (x, y) to polar (r, θ) coordinates by integrating over scattering angle θ. The scattering intensity was determined as a function of the scattering vector q, which was defined as $q = \frac{4 \cdot \pi \cdot \sin\theta}{\lambda}$, in which λ indicated the wavelength. Based on the positions of the peaks, the repeat distance was calculated according to the equation $d = \frac{2n \cdot \pi}{qn}$, where n indicates the order of the diffraction peak. Determination of the repeat distance of each lamellar phase was performed using combined data from the three main diffraction peaks.

2.6.2. Fourier Transform Infrared Spectrometry

Fourier transform infrared spectroscopy (FTIR) spectra were obtained using a Varian 670-IR spectrometer (Agilent Technologies, Santa Clara, CA, USA). The system was equipped with a broad-band mercury cadmium telluride detector, cooled with liquid nitrogen, and connected to an external controlled heating device. Before measurements, the SC was sandwiched by two AgBr cells in parallel to their surface. A constant stream of dry air was applied for 30 min to prevent signal interference by water condensations. The FTIR settings are described by Mieremet *et al.* [38]. Spectra were analyzed and deconvolved using Varian Resolutions Pro 5.2.0 software (Agilent Technologies).

2.7. Statistics

Statistical examinations were performed with GraphPad Prism v7.00 (GraphPad Software, La Jolla, CA, USA). In general, statistical testing was performed with 1-way or 2-way ANOVA with Tukey's multiple comparisons post-test, otherwise indicated. Significance is shown for comparison between normoxia and hypoxia (with lines) and for comparison between FTMs and NHS (above NHS), otherwise indicated. Significant differences were indicated by *, ** or ***, which correspond to P values <0.05, <0.01, <0.001, respectively.

3. Results

3.1. Fibroblast and keratinocyte monocultures under hypoxia

To fully understand the effects of oxygen levels on skin cell cultures, we initially characterized monocultures of fibroblasts or keratinocytes developed at 20% O_2 for normoxia or at 3% O_2 for hypoxia. The spindle shaped morphology of fibroblast monocultures was unaffected after 6 days in culture under hypoxia when compared to normoxia (**Fig. 1 a**). Next, we performed gene expression analysis on pre-selected HIF target genes involved in metabolic reprogramming (glucose transporter 1 (GLUT1) and pyruvate dehydrogenase lipoamide kinase isozyme 1 (PDK1)) and the angiogenic molecule vascular endothelial growth factor A (VEGFA). Significant upregulation of these HIF target genes was detected in fibroblasts when cultured under hypoxia (**Fig. 1 b**). To investigate the effect of oxygen levels on keratinocyte growth and differentiation, these were cultured in low (proliferating) and high (differentiating) calcium (Ca^{2+}) medium for several days in normoxia and hypoxia (**Fig. 1 c**). Similar to fibroblasts, keratinocyte morphology was not altered when cultured under hypoxia. However, keratinocytes showed a significant decrease in cell proliferation rate under hypoxia from 3 days in monoculture (**Fig. 1 d**). Furthermore, gene expression analysis of subconfluent proliferating and confluent differentiating keratinocytes also showed upregulation of the pre-selected HIF target genes under hypoxia (**Fig. 1 e**). This indicates that reduction from 20% to 3% oxygen level is sufficient to induce adaptation and metabolic reprogramming of fibroblasts and keratinocytes to hypoxic conditions.

3.2. Human skin equivalents generated under hypoxia

Next, evaluation of the effect of oxygen level in 3D co-cultures of fibroblasts and keratinocytes was performed by generation of full thickness models (FTMs) under normoxia or hypoxia. In both conditions, FTMs have a similar appearance based on macroscopic observations and the detection of four distinguishable epidermal layers (i.e. the stratum basale, stratum spinosum, stratum granulosum and SC) in hematoxylin and eosin (HE) stained cross sections (**Fig. 2 a**). The epidermis remained well-ordered under hypoxia and the thickness of the viable epidermis was significantly reduced, better resembling that of NHS (**Fig. 2 b**). The number of corneocyte layers in the SC of FTMs in hypoxia was significantly reduced as compared to normoxia and was similar to NHS (**Fig. 2 c**). Likewise as in monocultures, upregulation of HIF target genes VEGFA, PDK1 and GLUT1 was observed in the epidermis of FTMs generated under hypoxia (**Fig. 2 d**).

3.3. Morphogenesis of FTMs generated under hypoxia

To obtain further information on the influence of oxygen levels on FTMs, the expression of specific biomarkers for dermal and epidermal morphogenesis was examined in the various FTMs generated under normoxia and hypoxia and these

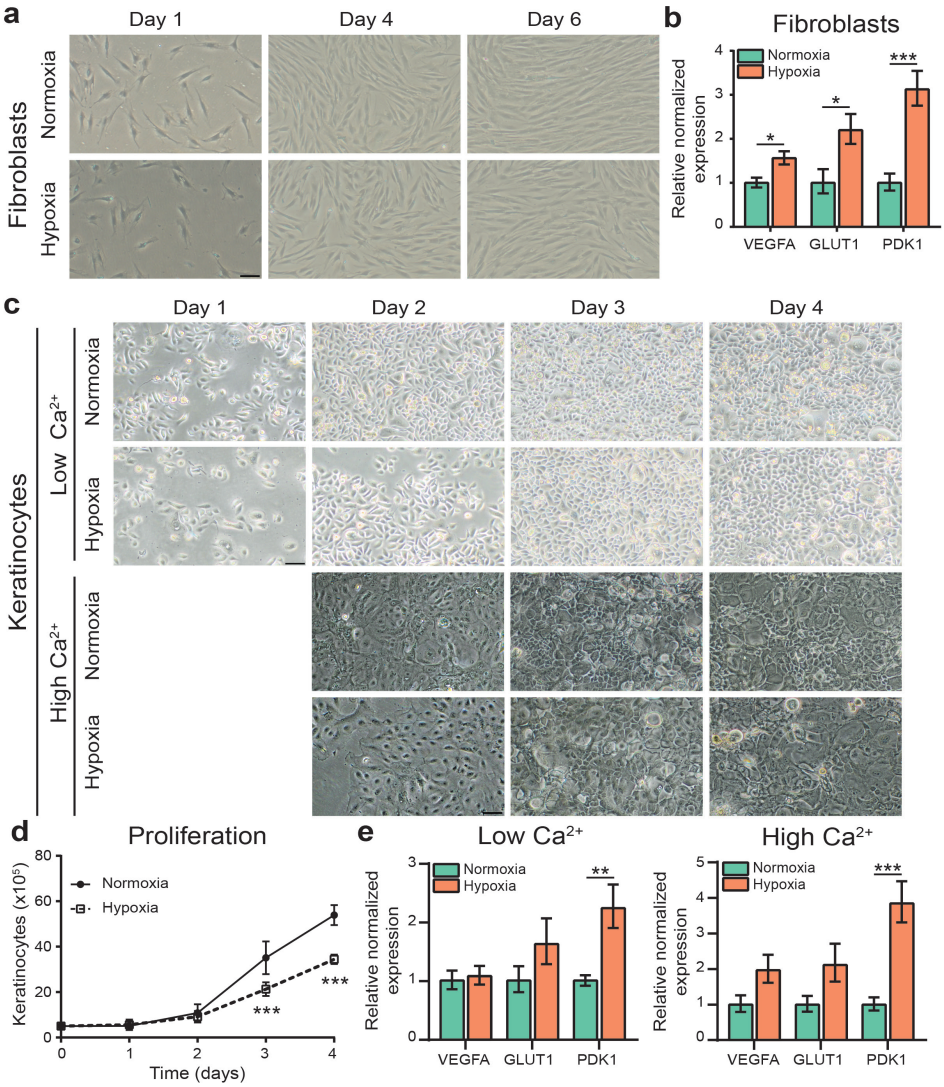


Figure 1. Fibroblast and keratinocyte monocultures under hypoxia. (a) Phase contrast images of fibroblasts under normoxia (20%) and hypoxia (3%) at indicated period. **(b)** Gene expression of HIF target genes in fibroblasts cultured under hypoxia and normoxia, indicated by mean ± s.e.m., n=4. **(c)** Phase contrast images of keratinocytes cultured for 4 days in low (proliferating) calcium medium and of keratinocytes cultured for 1 day in low calcium medium and 3 days in high (differentiating) calcium medium under normoxia or hypoxia. **(d)** Proliferation of keratinocytes in low calcium culture medium under hypoxia, indicated by mean ± 95% confidence interval. **(e)** Expression of HIF target genes in keratinocytes cultured in low or high calcium medium in hypoxia as compared to normoxia, indicated by mean ± s.e.m., n=4. Statistical differences are noted as *, ** or ***, corresponding to P<0.05, <0.01, <0.001. Scale bar indicates 50 µm.

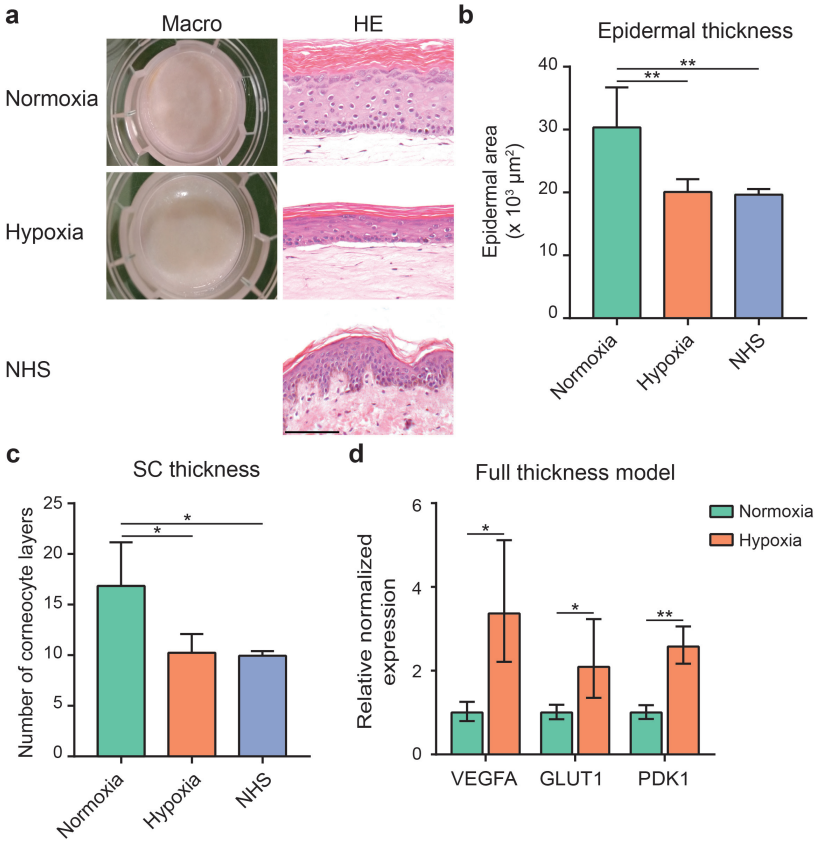


Figure 2. Full thickness models generated under hypoxia. (**a**) Macroscopic images of FTMs generated under normoxia or hypoxia. General morphology assessed through hematoxylin and eosin (HE) stained cross sections of FTMs generated under normoxia or hypoxia and NHS. Scale bar indicates 100 µm. (**b**) Epidermal thickness of FTMs generated under normoxia or hypoxia and NHS, indicated by mean + s.d. (**c**) Stratum corneum thickness of FTMs generated under normoxia or hypoxia and NHS. Data indicates mean + s.d. (**d**) HIF target gene expression in the epidermis of FTMs cultured under hypoxia as compared to normoxia, indicated by mean ± s.e.m., n=4. Statistical differences are noted as *, ** or ***, corresponding to P<0.05, <0.01, <0.001.

were compared to NHS (**Fig. 3**). The expression of the cell proliferation biomarker Ki67 remained restricted to the basal cell layer in all conditions. The proliferation was considerably higher in FTMs generated under normoxia as compared to NHS. However, the proliferation index of FTMs generated under hypoxia was lower than in normoxia, thereby mimicking that of NHS better. The early differentiation program was executed correctly in all conditions as indicated by suprabasal keratin 10 (K10) expression. The late and terminal differentiation programs were attenuated, as the keratinocytes in the granular layer appeared more flattened based on the expression of involucrin (INV), loricrin (LOR) and filaggrin (FLG).

Epidermal cell activation was determined by expression of biomarkers K16 and K17. In FTMs generated in hypoxia, increased expression of K16 was observed as compared to normoxia, whereas K17 remained unexpressed. Both cell activation biomarkers were absent in NHS. Next, we determined the deposition of the basement membrane (BM) proteins collagen type IV (COL IV) and laminin 332 (L332). These were more continuously present in NHS and had a patchier similar appearance in both FTMs. The distribution of fibroblasts was studied by the expression of the mesenchymal biomarker vimentin (VIM). In FTMs generated under normoxia or hypoxia, the distribution was continuous and comparable, whereas in NHS there was a clear distinction between papillary and reticular dermis. Finally, the fibroblasts differentiation was determined by assessment of expressed alpha smooth muscle actin (ASMA), specific for myofibroblasts. No differences for this fibroblast characteristic were found in the FTMs generated

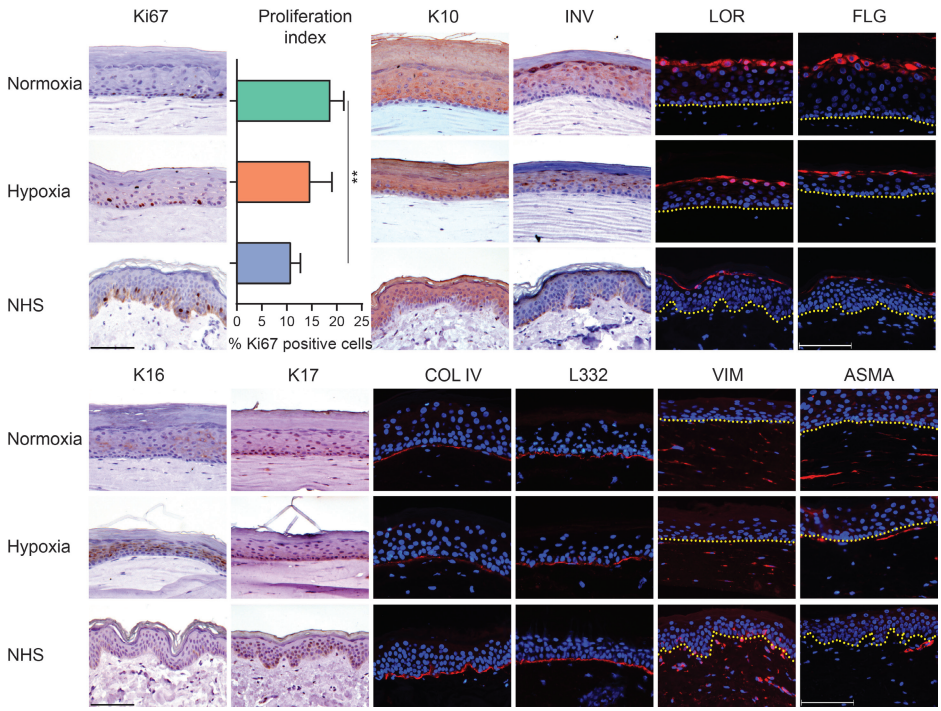


Figure 3. Morphogenesis of the epidermis and dermis in FTMs under hypoxia. Expression of protein biomarkers of proliferation (Ki67), early differentiation (K10), late and terminal differentiation (loricrin, involucrin, filaggrin), epidermal cell activation (K16 and K17), deposition of basement membrane (collagen type IV and laminin 332), fibroblasts distribution (vimentin) and fibroblasts stress signaling (alpha smooth muscle actin). Protein expression is shown in FTMs developed under normoxia or hypoxia and in NHS. Nuclei are counterstained blue using hematoxylin or DAPI, yellow dotted line indicates dermal-epidermal junction. Scale bar indicates 100 µm. Proliferation index is indicated by mean + s.d.

under normoxia or hypoxia. In NHS, ASMA expression was also observed in dermal regions surrounding the capillaries, which were absent in FTMs.

3.4. Stratum corneum lipid composition of FTMs under hypoxia

Thereafter, the lipid barrier formation was studied in FTMs generated under normoxia or hypoxia and compared to NHS. To this end, lipids were extracted from the SC, which revealed an equal total lipid content in the SC of FTMs in both conditions and NHS (**Fig. 4 a**). Next, we determined the CER composition within the lipid extract using a liquid chromatography coupled to mass spectrometry analysis. In FTMs generated under normoxia and hypoxia, all twelve major CER subclasses were detected (**Fig. 4 b**). As compared to the ion map of NHS, in that of FTMs there was an increased presence of CERs with a mass below 600, indicative for increased presence of CERs with a shorter carbon chain length.

Quantification of the CERs in absolute molar values revealed a similar cumulative amount of CERs per mg of SC in FTMs and NHS (**Fig. 4 c**). Subsequently, the CER[non-EO] and CER[EO] subclass profiles were analyzed (**Fig. 4 d**). An altered CER[non-EO] subclass profile in hypoxic FTMs was detected with significant higher abundance of subclass NP. This also improved the CER subclass ratio defined by $\frac{(dS+P+H)}{S}$, which mimics more closely that of NHS. The CER[EO] subclass profile of the FTMs did not differ, although the composition of CER[EO] in FTMs deviated from that in NHS. Next, the mean chain length (MCL) of the CER[non-EO] and CER[EO] was determined (**Fig. 4 e, f**). High similarity was observed between the FTMs for the MCL of the CER[non-EO] and of the CER[EO]. As compared to that of NHS, there is a significant reduction observed in the MCL of the CER[non-EO], but not in that of the CER[EO]. In line with the MCL, no differences in the carbon chain length distribution of the CERs in the FTMs generated at both conditions were detected (**Supplementary fig. 3**). When comparing the carbon chain length distribution of FTMs to that of NHS, the main difference is the increased presence of CER[non-EO] with ≤42 carbon atoms and the reduced presence of CER[non-EO] with ≥44 carbon atoms in the lipid composition in FTMs as compared to that in NHS (**Supplementary fig. 3 a**). No major differences were observed in the carbon chain length distribution of CER[EO] of FTMs, although substantially altered as compared to that of NHS (**Supplementary fig. 3 b**). Hereafter, the level of monounsaturated CERs in the subclasses AS and NS was determined. These subclasses were selected, as changes in the level of monounsaturated CERs in these subclasses properly indicate differences in the level of monounsaturated CERs for all subclasses (Helder *et al.*, submitted). The unsaturation index was indicated by the percentage of monounsaturated CERs per subclasses. When comparing the unsaturation index between FTMs developed under normoxia to hypoxia, a similar unsaturation

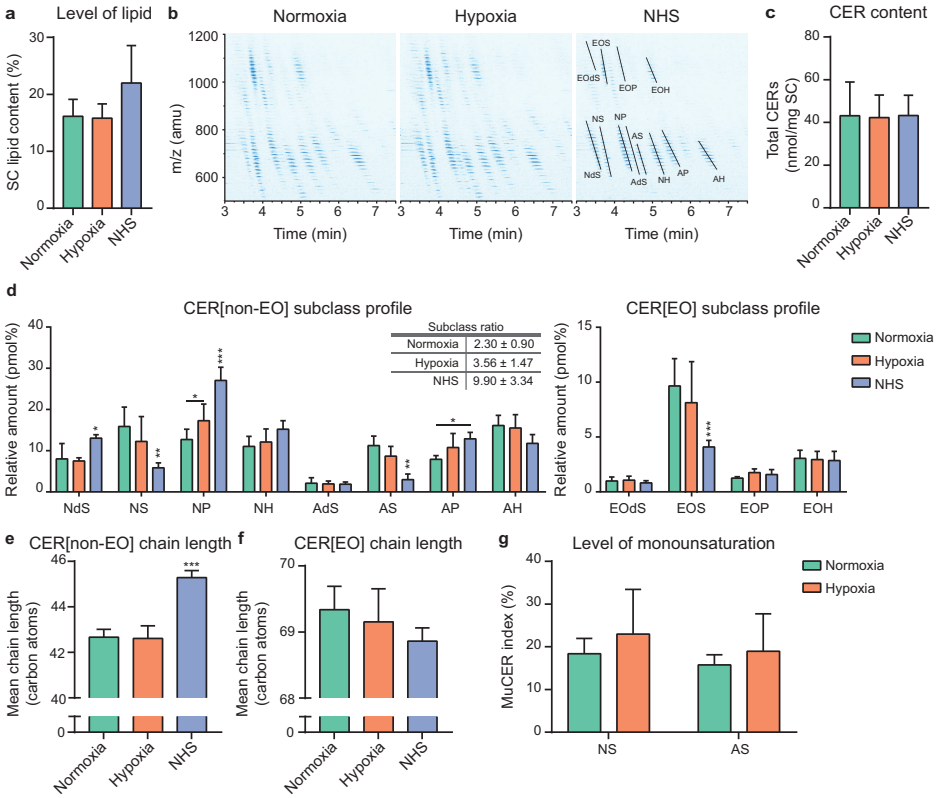


Figure 4. Stratum corneum ceramide composition of FTMs generated under hypoxia. (a) Level of total lipids in the SC of FTMs generated at indicated oxygen level and NHS. (b) Ion maps as detected by LC-MS of FTMs generated under normoxia or hypoxia and NHS. Twelve CER subclasses are identified. (c) Cumulative amount of quantified CERs per mg SC in FTMs and NHS. (d) CER[non-EO] and CER[EO] subclass profile of FTMs and NHS. Tabular inset provides subclass ratio defined by $\frac{(dS+P+H)}{S}$, as mean ± s.d. (e) Bar diagram plot compares the CER[non-EO] mean chain length in FTMs and NHS. (f) Bar diagram plot compares the CER[EO] mean chain length in FTMs and NHS. (g) Level of unsaturation in CER subclasses NS and AS in FTMs. All data represents mean + s.d. Significance is shown for comparison between normoxia and hypoxia (with lines) and for comparison between FTMs and NHS (above NHS), otherwise indicated. Statistical differences are noted as *, ** or ***, corresponding to P<0.05, <0.01, <0.001.

index was observed (**Fig. 4 g**). As monounsaturation in ceramides is naturally low in NHS, this was not further analyzed.

3.5. Stratum corneum lipid organization of FTMs under hypoxia

After assessment of the ceramide composition, the organization of the lipids in the intercorneocyte space was determined in FTMs generated under normoxia or hypoxia and compared to NHS. The lamellar organization was examined by small-angle X-ray diffraction. The diffraction profile with a first, second, and third

order of diffraction attributed to the long periodicity phase (LPP) were detected in FTMs, irrespective of oxygen level (**Fig. 5 a**). From the positions of the diffraction peaks, the repeat distance of the LPP in both FTMs was calculated. This revealed an increase in the repeat distance of the LPP in FTMs generated under hypoxia (**Fig. 5 b**). In NHS, by using recrystallization studies, the LPP repeat distance has been reported before to be around 13 nm [43]. Therefore, the LPP repeat distance in the FTMs generated in hypoxia better resembles the repeat distance in NHS. The lateral packing of FTMs generated under normoxia or hypoxia and NHS was evaluated by Fourier transformed infrared spectrometry (FTIR) measurements. Examination of the methylene rocking vibration in the 700-740 cm^{-1} region of the spectrum provides information about the lipid lateral packing; two peaks at 720 and 730 cm^{-1} indicate lipids assembled in the very dense orthorhombic packing, whereas a single peak at 720 cm^{-1} is visible when the lipids form a hexagonal packing [15]. In FTMs, a weak shoulder was visible at low temperatures (**Fig. 5 c**). This indicated that a small fraction of the lipids assembled in an orthorhombic lateral packing, but that most lipids form a hexagonal lateral packing. When increasing the temperature, the intensity of the 730 cm^{-1} shoulder gradually reduced. At 40°C, the lipids assembled only in a hexagonal packing, which was similar for normoxia and hypoxia. In NHS, the 730 cm^{-1} peak intensity was higher at low temperatures. This indicated that a higher fraction of lipids was organized in the orthorhombic lateral packing in NHS. When increasing the temperature, the intensity of the 730 cm^{-1} peak reduced, but a doublet was still present at 40°C, indicating a substantial level of lipids still adapted an orthorhombic packing. The conformational ordering of the lipids was examined to determine the ordered-disordered phase behavior of the lipid matrix. This could be obtained by assessment of the methylene symmetric stretching vibration peak position in the FTIR spectrum. When lipids chains adapt a higher conformational ordering, these are fully extended. This is indicated by methylene stretching vibration peaks positioned below a wavenumber of 2850 cm^{-1}. Vibration peaks shifted to a higher wavenumber (2852 cm^{-1}) when higher disordering of lipids is present. Peak positions of methylene symmetric stretching vibrations of FTMs and of NHS are plotted against temperature range of 0-40°C (**Fig. 5 d**). The conformational ordering of the lipids in FTMs generated at normoxia or hypoxia was comparable. In NHS, lowest vibrations were detected, indicative for highest conformational ordering of the lipid tails. In FTM and NHS, the lipids adopt a crystalline phase, as the observed frequency is below 2850 cm^{-1} at skin surface temperature of 32°C.

4. Discussion

The main objective of this study is to investigate the influence of oxygen level on dermal and epidermal morphogenesis and barrier formation in HSEs. Our results demonstrate that a reduced oxygen level i) activates HIF signaling *in vitro* leading

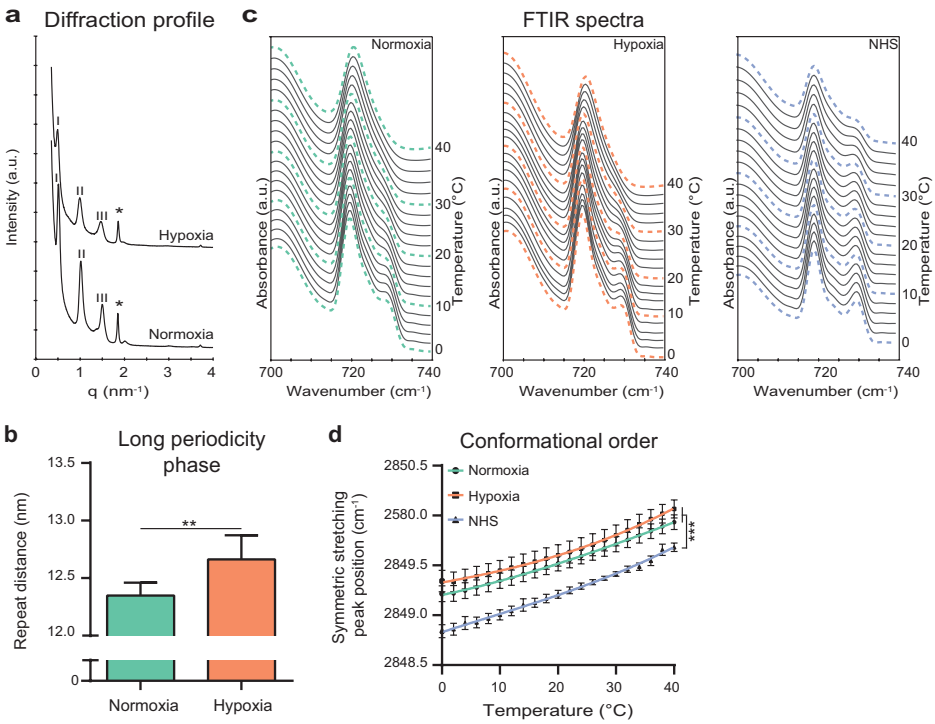


Figure 5. Lipid organization in FTMs generated under hypoxia. (**a**) Small angle X-ray diffraction patterns of FTMs developed under normoxia and hypoxia. Orders of diffraction of the LPP are indicated by roman numbers and phase separated crystalline cholesterol is indicated by the asterisk (*). (**b**) Bar diagram plot compares the repeat distance of the long periodicity. Data represent mean + s.d. Statistical testing is performed by paired t-test. (**c**) Representative rocking vibrations in a temperature range of 0-40°C in FTMs developed under normoxia, hypoxia and of NHS. (**d**) Conformational ordering of the lipids based on the symmetric stretching peak position over a temperature range of 0-40°C. Third order polynomial regression line connects the data points. Data represents mean ± s.e.m., n=4.

to metabolic reprogramming of primary human fibroblasts and keratinocytes in mono and 3D cultures, ii) decreases epidermal thickness in FTMs, iii) affects epidermal morphogenesis, and iv) alters the SC lipid composition and organization. These alterations led to better resemblance of HSEs to NHS.

The results obtained in this study are in line with previous studies, which demonstrated an altered expression of several barrier proteins including FLG, LOR and INV under hypoxia, indicative for a restructured barrier formation [33, 44]. Furthermore, silencing of HIF-α affected the terminal differentiation program in a human epidermal model that resulted in impaired stratification of the epidermis [32]. A similar observation was made *in vivo*, where it has been shown that the lack of HIF-α results in an impaired terminal differentiation

program and barrier formation in a murine model [33]. This emphasizes the importance of oxygen levels and HIF signaling in the formation of the SC barrier. An abnormal differentiation under hypoxia has also been reported, as determined by a reduced K1/K10 and FLG/LOR expression in HSEs after 24 hours at 1% oxygen [45]. However, the level of ROS scavenger molecules (vitamin C and E) and the duration and level of oxygen reduction (1% vs 3%) differ between that and our study, in part explaining the divergent outcomes. Complementary to our results, hyperbaric oxygen treatment (hyperoxia) of HSEs accelerated the formation of the epidermis, concomitantly with an increased proliferation rate and enlargement of the granular cell layer, which again emphasizes the critical role of oxygen during skin tissue engineering and regeneration [46, 47].

The lipid barrier formation is enhanced in FTMs generated under hypoxia, as it mimics that of NHS more closely than in FTMs generated under normoxia. Of interest is the significant improvement in CER subclass NP level and improved subclass ratio $\frac{(dS+P+H)}{S}$ under hypoxia. An increase in this subclass or in the subclass ratio is also one of the key alterations observed *in vivo* in diseased skin conditions [48, 49] and is shown to be directly correlated with the skin barrier function [50]. Lipid elongation or the level of monounsaturation in subclasses AS and NS is not affected by culturing under hypoxia, indicating that other regulatory pathways are involved in these processes. In this study, we thoroughly characterized the barrier formation in HSEs by full quantification of the ceramide composition. Due to the technical complexity of the data analysis, no unsaturated CER[EO] with a linoleic chain (contributing ~17-19% to FTM and NHS, Helder *et al.*, submitted) and saturated CER[EO] with an oleic chain (contributing ~23% to FTM, Helder *et al.*, submitted) were analyzed. However, the interpretation of the data is not affected by this. The ceramide composition affects the lipid organization as shown in this study and others [49, 51], but also for the barrier functionality, as demonstrated in *in vivo* (diseased) skin conditions [49, 52], in HSEs [9, 35], and in pure lipid model membranes [53, 54]. The influence of reduced oxygen level on the presence of other major lipid classes (free fatty acids, cholesterol) could be of interest in future studies.

Incorporation of the optimized oxygen micro-environment in future projects could open new possibilities to study different aspects of skin biology. One of these is a 3D co-culture with vascular endothelial cells. These are often supplemented with high concentrations of synthetic VEGF [55-57], whereas under hypoxia the production of endogenous VEGF is upregulated, potentially leading to a more supportive micro-environment. This facilitates studies on dermal angiogenesis, which is an important aspect in wound healing and tumorigenesis [58, 59]. Furthermore, a low oxygen micro-environment could also be applied in human skin organ culture (hSOC) [60]. This enables the determination of the

effect of hypoxia on other skin resident cell populations, which are currently missing in FTMs. Additionally, the interplay between oxygen levels in the skin micro-environment with the ability of the epidermis to induce anti-microbial responses during bacterial (*S. aureus*) infections was reported recently [61, 62]. Essentially, hypoxia lowers the threshold for induction of these protective responses, suggesting a role of oxygen level during the dynamic anti-microbial barrier [63], besides its role on the structural barrier formation.

In summary, we have shown in monocultures and in FTMs that external oxygen level directly affects cellular proliferation rate, epidermal morphogenesis and barrier formation. Importantly, we have shown that sub-optimized external conditions are in part responsible for altered *in vitro* skin tissue reconstruction.

5. Acknowledgements

This work was supported by the personnel at the ESRF in Grenoble, France stationed at the DUBBLE beam line (BM26), to whom the authors show appreciation for their assistance during SAXD measurements. We thank Samira Absalah for the support and assistance with the LC-MS analyses. Additionally, the authors are grateful for the received CERs by the company Evonik, located in Essen, Germany. Research funding was granted by the Dutch Technology Foundation STW (grant #13151), which is part of the Netherlands Organization for Scientific Research (NWO), and which is partly funded by the Ministry of Economic Affairs.

6. Conflict of interest

The authors declare no competing interests.

7. Author contributions

AM, JB and AEG designed the research study. AM, AVG, RvD, and GG performed the research. AM and WB performed the data analysis. AM drafted the manuscript, which was commented on by JB and AEG. All authors approved the submitted manuscript.

8. References

1. Gordon, S., et al., Non-animal models of epithelial barriers (skin, intestine and lung) in research, industrial applications and regulatory toxicology. Alternatives to Animal Experimentation: ALTEX, 2015. **32**(4): p. 327-378.
2. Sun, T., et al., Culture of skin cells in 3D rather than 2D improves their ability to survive exposure to cytotoxic agents. Journal of biotechnology, 2006. **122**(3): p. 372-381.
3. Helmedag, M.J., et al., The effects of constant flow bioreactor cultivation and keratinocyte seeding densities on prevascularized organotypic skin grafts based on a fibrin scaffold. Tissue Engineering Part A, 2014. **21**(1-2): p. 343-352.
4. van Drongelen, V., et al., Reduced filaggrin expression is accompanied by increased Staphylococcus aureus colonization of epidermal skin models. Clinical & Experimental Allergy, 2014. **44**(12): p. 1515-1524.
5. Mathes, S.H., H. Ruffner, and U. Graf-Hausner, The use of skin models in drug development. Advanced drug delivery reviews, 2014. **69**: p. 81-102.
6. van den Broek, L.J., et al., Progress and future prospectives in skin-on-chip development with emphasis on the use of different cell types and technical challenges. Stem Cell Reviews and Reports, 2017. **13**(3): p. 1-12.
7. Sriram, G., et al., Full-thickness human skin-on-chip with enhanced epidermal morphogenesis and barrier function. Materials Today, 2018. **21**(4): p. 326-340.
8. Niehues, H., et al., 3D skin models for 3R research: the potential of 3D reconstructed skin models to study skin barrier function. Experimental dermatology, 2018. **27**(5): p. 501-511.
9. Thakoersing, V.S., et al., Unraveling barrier properties of three different in-house human skin equivalents. Tissue Engineering Part C: Methods, 2011. **18**(1): p. 1-11.
10. Schreiber, S., et al., Reconstructed epidermis versus human and animal skin in skin absorption studies. Toxicology in vitro, 2005. **19**(6): p. 813-822.
11. Schmook, F.P., J.G. Meingassner, and A. Billich, Comparison of human skin or epidermis models with human and animal skin in in-vitro percutaneous absorption. International journal of pharmaceutics, 2001. **215**(1): p. 51-56.
12. Maxwell, G., et al., Applying the skin sensitisation adverse outcome pathway (AOP) to quantitative risk assessment. Toxicology in Vitro, 2014. **28**(1): p. 8-12.
13. Brandner, J., et al., Epidermal tight junctions in health and disease. Tissue barriers, 2015. **3**(1-2): p. e974451.
14. Yokouchi, M., et al., Epidermal cell turnover across tight junctions based on Kelvin's tetrakaidecahedron cell shape. Elife, 2016. **5**: p. e19593.
15. van Smeden, J., et al., The important role of stratum corneum lipids for the cutaneous barrier function. Biochimica et Biophysica Acta (BBA) - Molecular and Cell Biology of Lipids, 2014. **1841**(3): p. 295-313.
16. Feingold, K.R. and P.M. Elias, Role of lipids in the formation and maintenance of the cutaneous permeability barrier. Biochimica et Biophysica Acta (BBA)-Molecular and Cell Biology of Lipids, 2014. **1841**(3): p. 280-294.
17. Vávrová, K., A. Kováčik, and L. Opálka, Ceramides in the skin barrier. European Pharmaceutical Journal, 2017. **64**(2): p. 28-35.
18. Kihara, A., Synthesis and degradation pathways, functions, and pathology of ceramides and epidermal acylceramides. Progress in lipid research, 2016. **63**: p. 50-69.
19. van Smeden, J. and J.A. Bouwstra, Stratum corneum lipids: their role for the skin barrier function in healthy subjects and atopic dermatitis patients. Current Problems in Dermatology, 2016. **49**: p. 8-26.
20. Harayama, T. and H. Riezman, Understanding the diversity of membrane lipid composition. Nature Reviews Molecular Cell Biology, 2018. **19**: p. 281–296.
21. Rabionet, M., K. Gorgas, and R. Sandhoff, Ceramide synthesis in the epidermis. Biochimica et Biophysica Acta (BBA)-Molecular and Cell Biology of Lipids, 2014. **1841**(3): p. 422-434.
22. Thakoersing, V.S., et al., Increased presence of monounsaturated fatty acids in the stratum corneum of human skin equivalents. Journal of Investigative Dermatology, 2013. **133**(1): p. 59-67.
23. Tfayli, A., et al., Comparison of structure and organization of cutaneous lipids in a reconstructed skin model and human skin: spectroscopic imaging and chromatographic profiling. Experimental dermatology, 2014. **23**(6): p. 441-443.
24. Moore, T.C., et al., Effect of Ceramide Tail Length on the Structure of Model Stratum Corneum Lipid Bilayers. Biophysical Journal, 2018. **114**(1): p. 113-125.
25. Evans, S.M., et al., Oxygen Levels in Normal and Previously Irradiated Human Skin as Assessed by EF5 Binding. Journal of Investigative Dermatology, 2006. **126**(12): p. 2596-2606.

26. Rezvani, H.R., et al., HIF-1α in Epidermis: Oxygen Sensing, Cutaneous Angiogenesis, Cancer, and Non-Cancer Disorders. Journal of Investigative Dermatology, 2011. **131**(9): p. 1793-1805.
27. Place, T.L., F.E. Domann, and A.J. Case, Limitations of oxygen delivery to cells in culture: An underappreciated problem in basic and translational research. Free Radical Biology and Medicine, 2017. **113**: p. 311-322.
28. Weidemann, A. and R. Johnson, Biology of HIF-1α. Cell Death & Differentiation, 2008. **15**(4): p. 621-627.
29. Wu, D., et al., Structural integration in hypoxia-inducible factors. Nature, 2015. **524**(7565): p. 303-308.
30. Seleit, I., et al., Evaluation of Hypoxia Inducible Factor-1α and Glucose Transporter-1 Expression in Non Melanoma Skin Cancer: An Immunohistochemical Study. Journal of Clinical and Diagnostic Research, 2017. **11**(6): p. 9-16.
31. Maxwell, P.H., et al., The tumour suppressor protein VHL targets hypoxia-inducible factors for oxygen-dependent proteolysis. Nature, 1999. **399**(6733): p. 271-275.
32. Rezvani, H.R., et al., Loss of epidermal hypoxia-inducible factor-1α accelerates epidermal aging and affects re-epithelialization in human and mouse. Journal of Cell Science, 2011. **124**(24): p. 4172-4183.
33. Wong, W.J., et al., Hypoxia-inducible factors regulate filaggrin expression and epidermal barrier function. Journal of Investigative Dermatology, 2015. **135**(2): p. 454-461.
34. Haisma, E.M., et al., Inflammatory and antimicrobial responses to methicillin-resistant Staphylococcus aureus in an in vitro wound infection model. PloS one, 2013. **8**(12): p. e82800.
35. Mieremet, A., et al., Improved epidermal barrier formation in human skin models by chitosan modulated dermal matrices. PloS one, 2017. **12**(3): p. e0174478.
36. El Ghalbzouri, A., et al., Replacement of animal-derived collagen matrix by human fibroblast-derived dermal matrix for human skin equivalent products. Biomaterials, 2009. **30**(1): p. 71-78.
37. van Drongelen, V., et al., Barrier properties of an N/TERT-based human skin equivalent. Tissue Engineering Part A, 2014. **20**(21-22): p. 3041-3049.
38. Mieremet, A., et al., Shedding light on the effects of 1,25-dihydroxyvitamin D3 on epidermal lipid barrier formation in three-dimensional human skin equivalents. The Journal of Steroid Biochemistry and Molecular Biology, 2019. **189**: p. 19-27.
39. Bligh, E.G. and W.J. Dyer, A rapid method of total lipid extraction and purification. Canadian journal of biochemistry and physiology, 1959. **37**(8): p. 911-917.
40. Boiten, W., et al., Quantitative analysis of ceramides using a novel lipidomics approach with three dimensional response modelling. Biochimica et Biophysica Acta (BBA)-Molecular and Cell Biology of Lipids, 2016. **1861**(11): p. 1652-1661.
41. Motta, S., et al., Ceramide composition of the psoriatic scale. Biochimica et Biophysica Acta (BBA)-Molecular Basis of Disease, 1993. **1182**(2): p. 147-151.
42. Mojumdar, E.H., et al., Monounsaturated Fatty Acids Reduce the Barrier of Stratum Corneum Lipid Membranes by Enhancing the Formation of a Hexagonal Lateral Packing. Langmuir, 2014. **30**(22): p. 6534-6543.
43. Bouwstra, J.A., et al., Structural investigations of human stratum corneum by small-angle X-ray scattering. Journal of investigative dermatology, 1991. **97**(6): p. 1005-1012.
44. Li, H., L. Zhou, and J. Dai, Retinoic acid receptor-related orphan receptor RORα regulates differentiation and survival of keratinocytes during hypoxia. Journal of cellular physiology, 2018. **233**(1): p. 641-650.
45. Park, J.-y., et al., Hypoxia leads to abnormal epidermal differentiation via HIF-independent pathways. Biochemical and biophysical research communications, 2016. **469**(2): p. 251-256.
46. Kairuz, E., et al., Hyperbaric oxygen stimulates epidermal reconstruction in human skin equivalents. Wound Repair and Regeneration, 2007. **15**(2): p. 266-274.
47. Malda, J., T.J. Klein, and Z. Upton, The roles of hypoxia in the in vitro engineering of tissues. Tissue engineering, 2007. **13**(9): p. 2153-2162.
48. Farwanah, H., et al., Ceramide profiles of the uninvolved skin in atopic dermatitis and psoriasis are comparable to those of healthy skin. Archives of dermatological research, 2005. **296**(11): p. 514-521.
49. Janssens, M., et al., Increase in short-chain ceramides correlates with an altered lipid organization and decreased barrier function in atopic eczema patients. Journal of Lipid Research, 2012. **53**(12): p. 2755-2766.
50. Boiten, W.A., et al., Applying a vernix caseosa based formulation accelerates skin barrier repair by modulating lipid biosynthesis. J Lipid Res, 2018. **59**(2): p. 250-260.
51. Mieremet, A., et al., Recapitulation of Native Dermal Tissue in a Full-Thickness Human Skin Model Using Human Collagens. Tissue Engineering Part A, 2017. **24**(11): p. 873-881.
52. Coderch, L., et al., Ceramides and Skin Function. J American Journal of Clinical Dermatology, 2003. **4**(2): p. 107-129.

53. Školová, B., et al., Phytosphingosine, sphingosine and dihydrosphingosine ceramides in model skin lipid membranes: permeability and biophysics. Biochimica et Biophysica Acta (BBA) - Biomembranes, 2017. **1859**(5): p. 824-834.
54. Mojumdar, E.H., et al., The role of ceramide chain length distribution on the barrier properties of the skin lipid membranes. Biochimica et Biophysica Acta (BBA) - Biomembranes, 2014. **1838**(10): p. 2473-2483.
55. Ponec, M., et al., Endothelial network formed with human dermal microvascular endothelial cells in autologous multicellular skin substitutes. Angiogenesis, 2004. **7**(4): p. 295-305.
56. Auxenfans, C., et al., Adipose-derived stem cells (ASCs) as a source of endothelial cells in the reconstruction of endothelialized skin equivalents. Journal of tissue engineering and regenerative medicine, 2012. **6**(7): p. 512-518.
57. Monsuur, H.N., et al., Extensive Characterization and Comparison of Endothelial Cells Derived from Dermis and Adipose Tissue: Potential Use in Tissue Engineering. PLOS ONE, 2016. **11**(11): p. e0167056.
58. Chuan, T., et al., Hypoxia pretreatment of bone marrow—derived mesenchymal stem cells seeded in a collagen-chitosan sponge scaffold promotes skin wound healing in diabetic rats with hindlimb ischemia. Wound Repair and Regeneration, 2016. **24**(1): p. 45-56.
59. Kur-Piotrowska, A., et al., Foxn1 expression in keratinocytes is stimulated by hypoxia: further evidence of its role in skin wound healing. Sci Rep, 2018. **8**(1): p. 5425.
60. Zhou, L., et al., The renaissance of human skin organ culture: A critical reappraisal. Differentiation, 2018. **104**: p. 22-35.
61. Peyssonnaux, C., et al., Critical Role of HIF-1α in Keratinocyte Defense against Bacterial Infection. Journal of Investigative Dermatology, 2008. **128**(8): p. 1964-1968.
62. Wickersham, M., et al., Metabolic stress drives keratinocyte defenses against staphylococcus aureus infection. Cell reports, 2017. **18**(11): p. 2742-2751.
63. Rademacher, F., et al., Skin microbiota and human 3D skin models. Experimental dermatology, 2018. **27**(5): p. 489-494.

9. Supplementary information

Supplementary table 1. Specifications of primer used for quantitative real-time polymerase chain reaction.

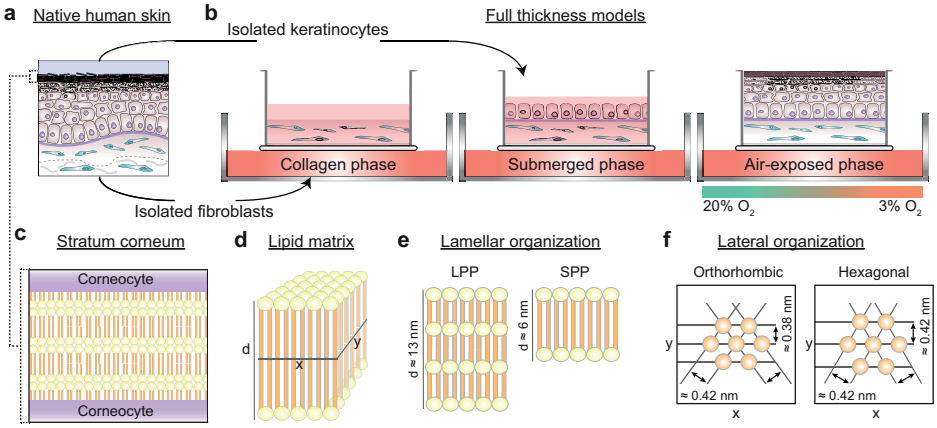
Target	Sequence Forward (5'-> 3')	Sequence Reverse (5'-> 3')	Amplicon size	Exonic location	Accession No.
SDHA	AACCAAACGCTGGGGAAGAA	GGAACACGGCAGCATGATTT	126	11,12	NM_004168.3
ZNF410	GCTGTGGTAAGCAGTTTACTACAG	CTTGGGCTTCACAAAGGAAAGG	90	6,7	NM_001242924.1
ARCP2	TCCGGGACTACCTGCACTAC	GGTTCAGCACCTTGAGGAAG	96	9,10	NM_152862.2
VEGFA	ACTGAGGAGTCCAACATCACC	CTGCATTCACATTTGTTGTGCTG	104	3,4	NM_001025366.2
PDK1	CACCAGGACAGCCAATACAA	AACACCTCTGTTGGCATGGT	116	7,8	NM_002610.4
GLUT1	GGCGGGTTGTGCCATACTCA	CAAAGAAGGCCACAAAGCCAA	107	8,9	NM_006516.2

Supplementary table 2. Specification of antibodies used for immunohistochemical and immunofluorescence staining.

Immunohistochemistry	Material	Origin	Clone	Dilution	2nd Ab	Manufacturer
Primary antibody						
Ki67	FFPE	Mouse	MIB1	1:100	A	DAKO, Denmark
Cytokeratin 10	FFPE	Mouse	DE-K10	1:50	A	Labvision/Neomarker, USA
Involucrin	FFPE	Mouse	SY5	1:1200	A	Sanbio, The Netherlands
Cytokeratin 16	FFPE	Mouse	LL025	1:100	A	Serotec, UK
Cytokeratin 17	FFPE	Mouse	E3	1:1500	A	EMD Millipore Corporation, USA
Secondary antibody						
A) Biotinylated goat anti-mouse		Goat		1:200		Southern Biotechnology, USA

Supplementary table 2 (continued).

Immunofluorescece		Origin	Clone	Dilution	2nd Ab	Manufacturer
Primary antibody						
Loricrin	FFPE	Rabbit	AF62	1:1000	B	Covance, The Netherlands
Filaggrin	FFPE	Rabbit	PRB417	1:1000	B	Covance, The Netherlands
Collagen type IV	FFPE	Mouse	24.12.8 (PHM-12)	1:75	C	Chemicon, Australia
Laminin 332	Frozen	Mouse	BM165	1:150	C	Provided by Dr. M. Aumailley, Germany
Vimentin	FFPE	Mouse	V9	1:250	C	Sigma-Aldrich, Germany
Alpha smooth muscle actin	FFPE	Mouse	1A4	1:500	C	Abcam, UK
Secondary antibody						
B) Cy3-conjugated anti-rabbit		Goat		1:500		Jackson immunoresearch Laboratory, USA
C) Cy3-conjugated anti-mouse		Goat		1:1000		Jackson immunoresearch Laboratory, USA

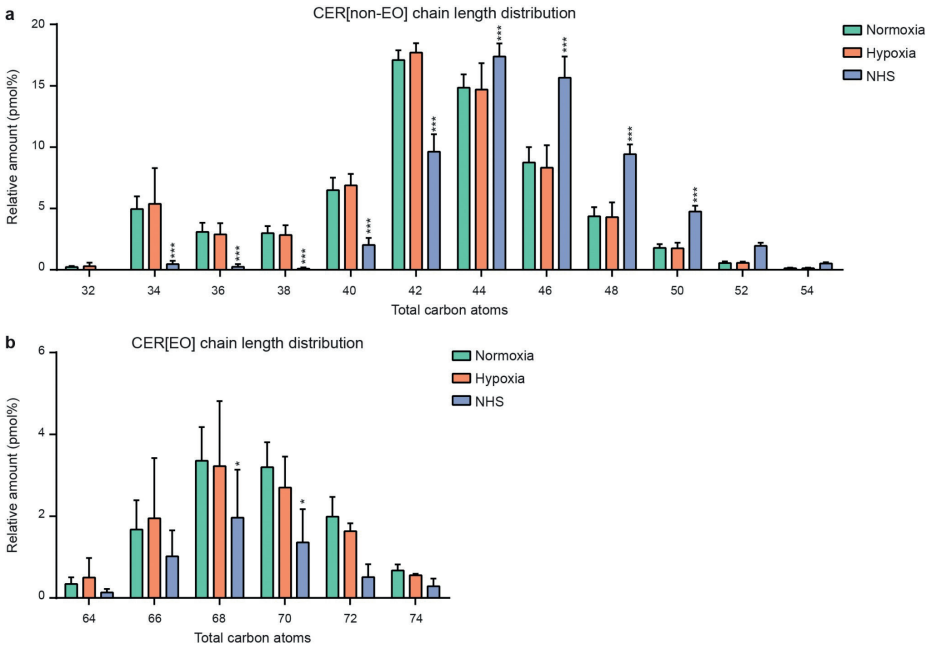


Supplementary figure 1. Lipid barrier in native human skin and human skin equivalents. (**a**) Schematic overview of the dermis and epidermis of native human skin. (**b**) Development of full thickness models occurred in three main phases. Isolated primary fibroblasts were seeded in and rearranged the extracellular matrix during the collagen phase. Isolated primary keratinocytes were seeded on top of the collagen and proliferated during the submerged phase. Stratification occurred during air-exposed phase, at which oxygen levels were modulated in this study. (**c**) Schematic overview of the intercorneocyte lipid matrix of the stratum corneum. (**d**) Illustration of the 3D lipid matrix. (**e**) Simplified overview of the lamellar organization. Long periodicity phase (LPP) and short periodicity phase (SPP) as shown by head group regions and hydrocarbon chain regions. Both LPP and SPP are characterized by a specific repeat distance [43]. (**f**) Lateral organization of the hydrocarbon chains of the lipids. The orthorhombic organization is a very dense ordered packing, whereas the hexagonal organization is less dense ordered.

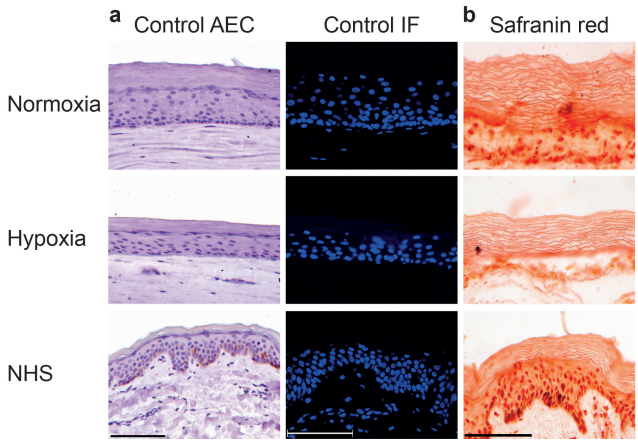
Ceramides

	CERs		
	CER[non-EO]		CER[EO]
	Non-hydroxy fatty acid [N]	α-hydroxy fatty acid [A]	Esterified ω-hydroxy fatty acid [EO]
Dihydrosphingosine [dS]	[NdS]	[AdS]	[EOdS]
Sphingosine [S]	[NS]	[AS]	[EOS]
Phytosphingosine [P]	[NP]	[AP]	[EOP]
6-hydroxy sphingosine [H]	[NH]	[AH]	[EOH]

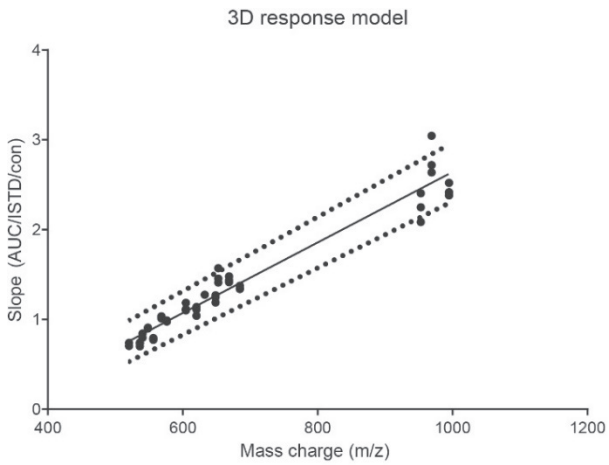
Supplementary figure 2. Ceramide subclasses of the lipid matrix. Tabular overview of the structural formulas of twelve major ceramide subclasses, which consist of a sphingoid base coupled to a fatty acid chain. Total ceramides (CERs) consist of CER[non-EO] and CER[EO]. The latter subclasses contain a characteristic esterified acyl chain. Ceramide nomenclature is followed according to Motta *et al.* [41].



Supplementary figure 3. Stratum corneum ceramide carbon chain length distribution. (**a**) Bar diagram plot of CER[non-EO] with an even number of carbon atoms of FTMs generated under normoxia or hypoxia and of NHS. (**b**) Bar diagram plot of CER[EO] with an even number of carbon atoms of FTMs generated under normoxia or hypoxia and of NHS. All data represents mean + s.d.



Supplementary figure 4. Safranin red staining and negative controls of immunohistochemistry. (**a**) Representative cross sections of FTMs and NHS stained with safranin red followed by alkali expansion of the SC used for quantification of the number of corneocyte layers. (**b**) Negative controls for immunohistochemical and immunofluorescence stainings. Nuclei are stained blue using hematoxylin or DAPI. Scale bar indicates 100 µm.



Supplementary figure 5. Three-dimensional response model used for quantification of the ceramide composition. This 3D response model is used for quantification of the CER composition. Model is based on mass spectrometry settings, compound properties and a calibration curve from a limited number of synthetic ceramides, as described by Boiten *et al.* [40].

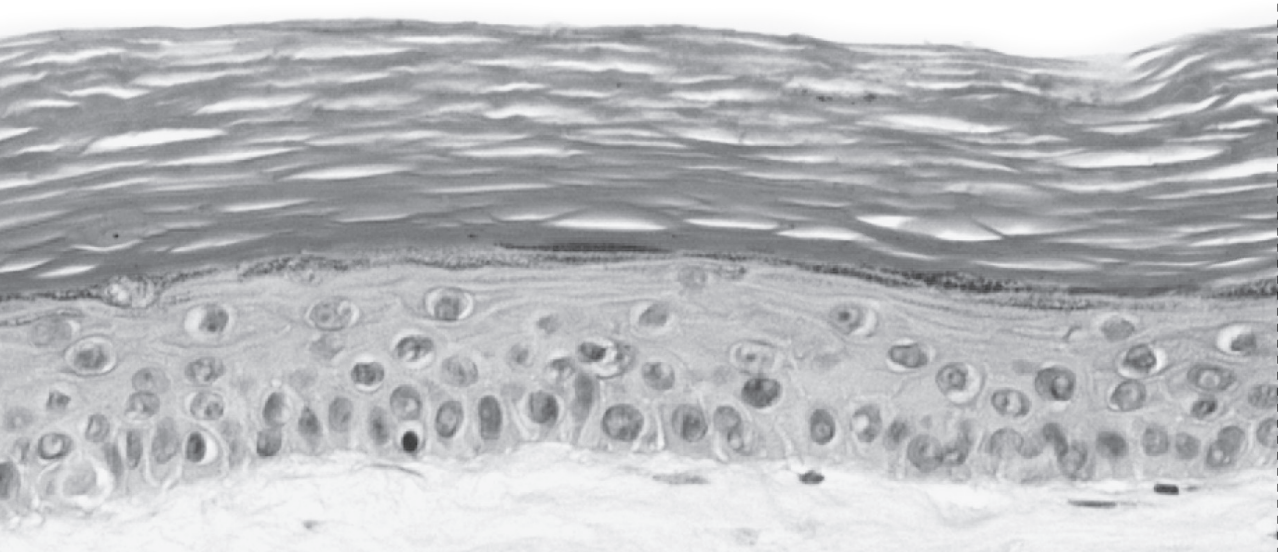
6

Unravelling effects of relative humidity on lipid barrier formation in human skin equivalents

Arnout Mieremet
Walter Boiten
Rianne van Dijk
Gert Gooris
Herman S. Overkleeft
Johannes M.F.G. Aerts
Joke A. Bouwstra[+]
Abdoelwaheb El Ghalbzouri[+]

[+] Joint senior authorship

Archives of Dermatological Research (*in press*)



Abstract

Relative humidity (RH) levels vary continuously *in vivo*, although during *in vitro* generation of three dimensional human skin equivalents (HSEs) these remain high (90-95%) to prevent evaporation of the cell culture medium. However, skin functionality is directly influenced by environmental RH. As the barrier formation in HSEs is different, there is a need to better understand the role of cell culture conditions during generation of HSEs. In this study, we aim to investigate the effects of RH on epidermal morphogenesis and lipid barrier formation in HSEs. Therefore, two types of HSEs were developed at 90% or at 60% RH. Assessments were performed to determine epidermal morphogenesis by immunohistochemical analyses, ceramide composition by lipidomic analysis, and lipid organization by Fourier transform infrared spectroscopy and small angle X-ray diffraction. We observed that reduction of RH mainly affected the uppermost viable epidermal layers in the HSEs, including an enlargement of the granular cells and induction of epidermal cell activation. Neither the composition nor the organization of the lipids in the intercorneocyte space were substantially altered at reduced RH. Additionally, lipid processing from glucosylceramides to ceramides was not affected by reduced RH in HSEs as shown by enzyme expression, enzyme activity, and substrate to product ratio. Our results demonstrate that RH directly influences epidermal morphogenesis, albeit the *in vitro* lipid barrier formation is comparable at 90% and 60% RH.

Keywords: Artificial Skin; Humidity; Cell Culture Techniques; Ceramides; Molecular Probes.

1. Introduction

Main functions of the skin are to protect the body from water loss and against exogenous factors, which is primarily performed by the stratum corneum (SC). Skin functionality is directly influenced by environmental relative humidity (RH) regarding susceptibility to mechanical stress and fracture, elasticity, protein organization, lipid conformation, and epidermal hydration [1-6]. *In vivo* studies revealed that high RH levels delayed epidermal barrier repair and reduced the level of natural moisturizing factor [2, 3]. Furthermore, switching from high to low RH affected total epidermal water loss (TEWL) values, indicating adaptation of skin barrier formation to fluctuating RH levels [7].

Despite the interactions between RH and the skin, during generation of three-dimensional human skin equivalents (HSEs) high RH levels (90-95%) are used as standard cell culture condition. This difference between *in vivo* and *in vitro* RH levels could contribute to the altered barrier formation of HSEs compared to that of native human skin (NHS) [8-11]. Only a limited amount of comparative studies addressed the influence of RH levels *in vitro* [12-16]. These showed that epidermal morphogenesis was affected by a reduction in RH, albeit not uniformly in all HSE types. Moreover, an improved skin hydration was observed, at which 60% RH was reported to be an optimal *in vitro* level [17]. Furthermore, the HSEs developed at reduced RH were shown to have enhanced barrier properties [15]. Nevertheless, it remains unresolved by which mechanism the epidermal barrier is reinforced.

The SC consists of fully keratinized corneocytes surrounded by a lipid matrix, which is the only continuous pathway through the SC [18, 19]. Therefore, the lipid matrix is highly important for the functionality of the epidermal barrier. It consists of a specific lipid composition (i.e. ceramides, cholesterol and free fatty acids), assembled in a characteristic lipid organization (i.e. lateral and lamellar). The twelve most common ceramide subclasses were analysed in this study, referred to as total ceramides (CERs). These were subcategorized in ω-esterified ceramide (CER[EO]) subclasses and in non- ω-esterified ceramide (CER[non-EO]) subclasses [20-22]. Previous studies revealed a different composition of CERs and an altered lipid composition indicative for the altered barrier formation in HSEs as compared to NHS [11, 23].

The interaction between RH and the lipid barrier formation in HSEs has been studied in submerged (>100% RH) and in reduced RH (<90% RH) conditions. When developed at submerged conditions (>100% RH), the level of ceramide precursor (acyl)glucosylceramide was elevated, leading to a lower level of ceramide EOS as compared to air-exposed cultures (93%) [24]. This could be a consequence of elevated pH values at submerged or occluded conditions [5], which may affect

the hydrolytic activities of β-glucocerebrosidase-1 (GBA) or acid sphingomyelinase (aSMASE). These enzymes convert glucosylceramide and sphingomyelin respectively to ceramide, at the stratum granulosum (SG) – SC interface [25, 26]. Opposite to submerged conditions, in HSEs generated at reduced RH (50%) the expression of glucosylceramide synthase was upregulated [15], indicating that RH is associated with biosynthesis and processing of glucosylceramides. Nevertheless, it remains to be determined whether RH levels directly affect lipid composition and organization in the SC of *in vitro* developed HSEs.

In this study, we aim to determine if RH levels affect epidermal morphogenesis and barrier lipid formation in HSEs. Therefore, full thickness models (FTMs) and collagen-chitosan full thickness models (CC-FTMs) were generated at 90% and 60% RH. Both HSE types encompass the epidermal and dermal equivalent, although the CC-FTM has a strengthened dermal extracellular matrix due to the added biopolymer chitosan and improved barrier formation [27]. Additionally, we examined the conversion of precursor glucosylceramide to ceramide at the SG-SC interface to obtain more detailed information on this process at various RH levels.

2. Materials and methods

2.1. Generation of FTMs and CC-FTM at reduced RH

Declaration of Helsinki principles are followed during obtainment of primary cells from surplus female adult mama skin tissue, as stated earlier [28]. Isolation of primary cells from the dermis and epidermis and cell culturing was performed as described before [29, 30]. All isolated primary cells were tested and found negative for mycoplasma contamination. FTMs and CC-FTMs were generated as described before [11, 27, 31]. The reduction in RH was performed from 90% gradually in steps of 7.5% each day initiated after 7 days air exposure to 60% using a Memmert INC153med CO_2 incubator with humidity module (Memmert, Schwabach, Germany). Medium was refreshed every other day after 7 days air-exposure. HSEs were developed for a total of 16 days air-exposed. HSE batches were generated with four unique primary cell donors.

2.2. Immunohistochemical analyses

Sections of HSEs or NHS were formaldehyde fixated and embedded in paraffin or snap frozen in liquid nitrogen [32]. Haematoxylin and eosin (HE) was performed according to manufacturer's instructions (Klinipath, Duiven, The Netherlands). Protein analyses by immunohistochemistry or indirect immunofluorescence were performed on 5 µm sliced paraffin embedded cross-sections. After deparaffinization and rehydration, heat mediated antigen retrieval in citrate buffer pH 6 occurred. Antigen retrieval for collagen type IV staining was mediated by protease incubation. Non-specific antibody binding was reduced

through blocking with normal human serum (Sanquin, Leiden, The Netherlands). Immunohistochemical analyses were performed using the streptavidin-biotin-peroxidase system (GE Healthcare, Buckinghamshire, United Kingdom) according to the manufacturer's instructions or using indirect immunofluorescence, as described before [27]. Specifications of the antibodies are provided in **supplementary table 1**. Control immunostainings revealed no unspecific binding or background staining of the secondary antibody **(Supplementary fig. 1 a)**. Number of corneocyte layers was determined by safranin red staining and potassium hydroxide expansion of the SC [33, 34]. Estimations of the epidermal thickness and the proliferation index were performed as reported earlier [27, 35]. Activity based probe assay using MDW941 was performed as reported earlier by van Smeden *et al.* [26].

2.3. Stratum corneum lipid composition

Extraction of SC lipids was performed based on an adjusted Bligh and Dyer method as described by Boiten *et al.* [36]. The dry SC was weighed before and after lipid extraction using a microbalance. The lipids were analysed by liquid chromatography coupled to mass spectrometry (LC-MS) according to the methods as described elsewhere [36]. Details of instrument settings and data quantification are described in supplementary materials and methods.

2.4. Stratum corneum lipid organization

Determination of lamellar organization was performed by small-angle X-ray diffraction and determination of lateral organization was performed by Fourier transform infrared spectroscopy (FTIR), according to methods described in supplementary materials and methods.

2.5. Statistics

Statistical analyses are conducted using GraphPad Prism version 7.00 for Windows (GraphPad Software, La Jolla, CA, USA). Statistical testing was performed with 1-way or 2-way ANOVA with Tukey's post-test. Significance is shown for comparison between high and low RH (with lines) within a HSE type and for comparison between all HSEs versus NHS (above NHS), otherwise specifically stated. No comparisons between FTMs and CC-FTMs were performed due to primary donor effect. Statistical differences are noted as *, ** or ***, corresponding to $P<0.05$, <0.01, <0.001.

3. Results

3.1. Epidermal morphogenesis in HSEs developed at reduced relative humidity

To thoroughly and robustly assess the effect of RH on HSEs, we generated FTMs and CC-FTMs at 90% and 60% RH. The reduction in RH was performed gradually after the first SC layers were formed to protect the viable epidermis from excessive desiccation [12]. Assessments of macroscopic appearance and general morphology were performed for CC-FTMs and NHS (**Fig. 1 a)** and for FTMs **(Supplementary fig. 2 a)**. The epidermis contained four distinguishable epidermal layers in both HSE types, irrespective of RH levels. Also, the thickness of the viable epidermis and number of corneocyte cell layers in the SC was similar at 90% and 60% RH in both HSE types (**Fig. 1 b,c**). In HSEs generated for 16 days, the number of corneocyte layers was slightly higher than that of NHS. Noteworthy, the corneocytes of both HSE types expanded more in the alkali environment that the corneocytes of NHS (**Supplementary fig. 1 b**).

The expression of protein biomarkers in HSEs and NHS was evaluated to assess the effect of RH on epidermal morphogenesis, basement membrane (BM) formation, and fibroblast distribution in CC-FTMs and NHS **(Fig. 1 d)**, and in FTMs **(Supplementary fig. 2 b)**. The epidermal terminal and late differentiation programs were examined by expression of loricrin, filaggrin, and involucrin. This revealed an increased thickness of the SG in CC-FTMs generated at 60% RH, but not in FTMs at 60% RH. Involucrin was also expressed in the spinous layer of HSEs, in contrast to its restricted expression in the SG of NHS. Similar execution of the early differentiation program was detected in all conditions based on the suprabasal keratin 10 expression. Epidermal activation was increased at reduced RH in CC-FTMs based on the expression of keratin 16 (**Fig. 1 d**). Elevated epidermal activation could not be detected in FTMs, due to the expression of keratin 16 at 90% RH. In all HSEs and NHS, the expression of keratin 17 was absent, indicating no severe epidermal activation induced by reduced RH (**Supplementary fig. 2 c**). The cell proliferation marker Ki67 remained located at the basal layer in all conditions, with comparable proliferation indexes at high and low RH. The expression of collagen type IV was unaffected by the reduced RH, indicating similar BM formation. Furthermore, the distribution of the fibroblasts was analysed by vimentin expression, which was similar at both RH levels. As compared to NHS, the deposition of the BM was reduced and the distribution of the fibroblasts was homogeneous. Altogether, these results indicate that reduction in RH mainly affected the uppermost layers of the epidermis.

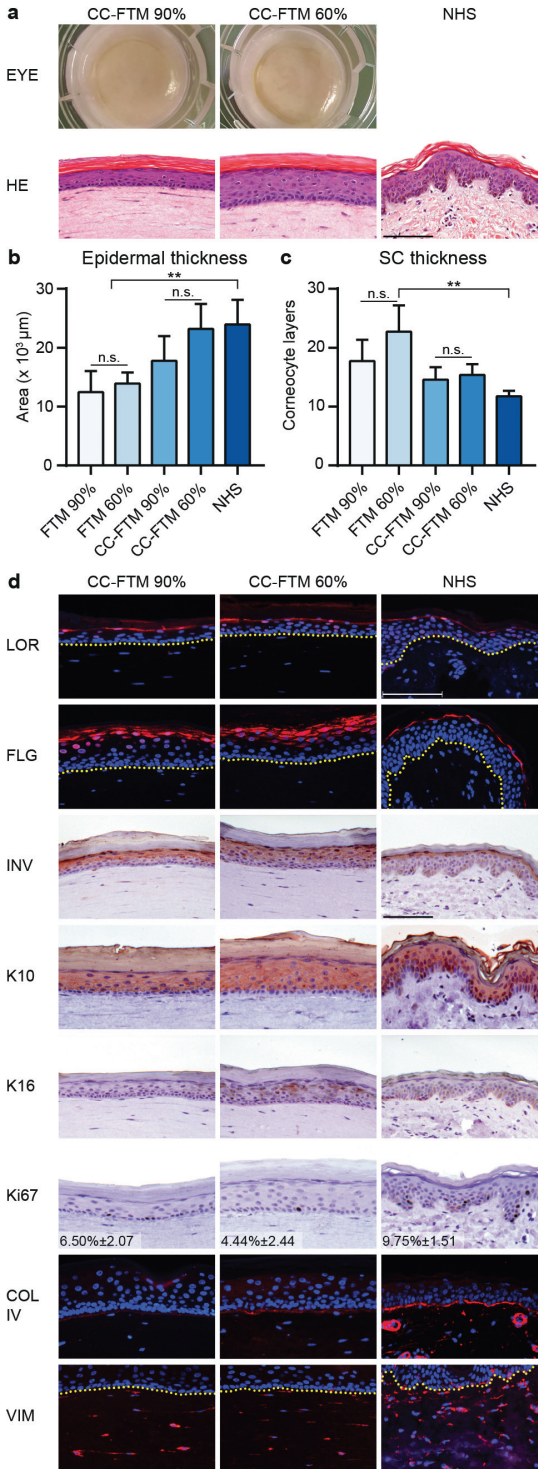


Figure 1. Generation of HSEs at reduced relative humidity. (a) General morphology of CC-FTMs generated at high (90%) and low (60%) RH, assessed by eye or after HE staining. **(b)** Epidermal thickness of HSEs and of NHS, indicated by mean + SD, N=4. **(c)** Number of corneocyte layers in HSEs and in NHS. Data indicates mean + SD, N=4. **(d)** Epidermal morphogenesis, basement membrane formation, and fibroblast distribution in CC-FTMs and NHS. Expression of loricrin (LOR), filaggrin (FLG), involucrin (INV), keratin 10 (K10), and keratin 16 (K16) indicate epidermal differentiation programs or activation. Proliferation was assessed by Ki67 (with indicated proliferation index as mean ± SD, N=4), basement membrane formation by collagen type IV (COL IV), and fibroblast distribution by vimentin (VIM) expression. Protein biomarkers are shown in red and nuclei in blue. Yellow dotted line indicates dermal-epidermal junction. Scale bar indicates 100 µm.

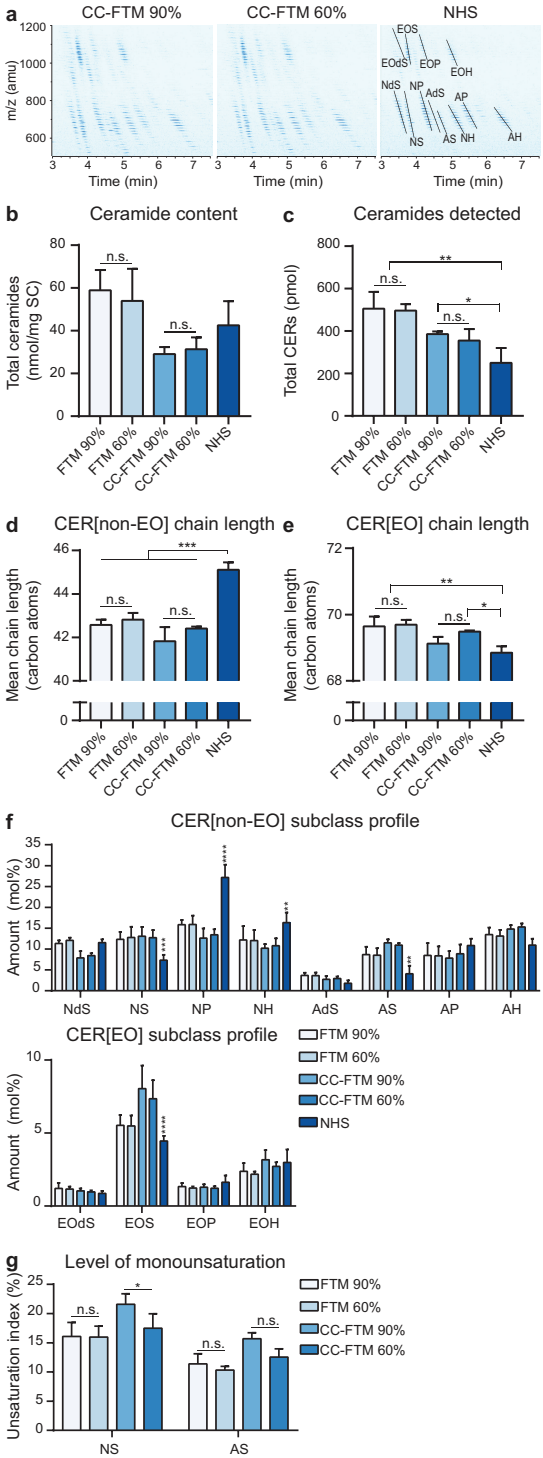


Figure 2. Stratum corneum ceramide composition of HSEs generated at reduced relative humidity. (a) Representative ion maps of CC-FTMs generated at 90% and 60% RH and of NHS. Twelve CER subclasses are indicated by position in the ion map of NHS and are named according to Motta *et al.* [37]. Ion maps are shown as time after elution on the x-axis and mass in atomic mass unit (amu) on the y-axis. **(b)** Level of CER in the SC per mg SC of indicated HSEs and of NHS. **(c)** Total amount of CERs in 1500 ng lipid extract as detected by LC-MS. **(d)** Bar diagram plot of the mean carbon chain length of CER[non-EO]. **(e)** Bar diagram plot showing the CER[EO] mean carbon chain length. **(f)** CER[non-EO] and CER[EO] subclass profiles in relative amount. **(g)** Bar diagram plot of the unsaturation index in CER subclasses NS and AS of indicated HSEs. All data represent mean + SD, N=4.

3.2. Lipidomic profiling of stratum corneum ceramides

To gain more information on the barrier formation, the ceramide composition was investigated using an advanced liquid chromatography coupled to mass spectrometry (LC-MS) analysis. All CER subclasses were detected in both HSE types and in NHS on the LC-MS ion maps (**Fig. 2 a**). An increased presence of low mass CERs was detected (below 600 atomic mass units) in HSEs compared to NHS. Quantification of the detected signal was performed to determine the level of CERs per mg SC. This revealed no significant change in the absolute amount of CERs after generating HSEs at reduced RH compared to high RH (**Fig. 2 b**). Also, a comparison between the cumulative detected CERs per injection in the LC-MS revealed similarity in HSEs generated at high and low RH (**Fig. 2 c**). The mean carbon chain length (MCL) of CERs was calculated, which revealed no significant difference for neither the MCL of CER[non-EO] nor for the MCL of CER[EO] between high and low RH (**Fig. 2 d,e**). The MCL of CER[non-EO] in NHS was significantly higher as compared to HSEs, whereas the MCL of CER[EO] in NHS was more comparable to that of HSEs. More detailed information on the chain length of CER[non-EO] and CER[EO] was obtained by plotting the distribution by carbon atom number, for even numbered CER[non-EO] ranging from C32 (32 carbon atoms) to C54 and for CER[EO] ranging from C64 to C74 (**Supplementary fig. 3 a-d**). This revealed no substantial differences between high and low RH levels, solely CER[EO] C68 in CC-FTMs was significantly reduced at 60% RH. Compared to NHS, the fraction of CER[non-EO] ≤C42 was increased and the fraction of CER[non-EO] ≥C44 was reduced in HSEs in relative amounts. Furthermore, the CER[EO] chain length distribution was generally similar in NHS and HSEs in relative and absolute values, except for FTMs as these contain a higher level of CER[EO] C70 and C72 per mg SC. Then, the CER subclass profiles were determined and compared in HSEs generated at varying RH levels for relative (**Fig. 2 f**) and for absolute amounts (**Supplementary fig. 4**). No differences were observed between high and low RH in both comparisons. As compared to NHS, alterations in the subclass profile (i.e. subclasses NS, NP, AS and EOS) were detected in both HSE types. Considering the absolute amounts, the CC-FTMs resembled NHS to a higher extent in subclass profile, although important deviations persisted. Composition assessment was continued by determination of the level of monounsaturated CERs in the subclasses AS and NS. Due to the low abundance of monounsaturated CER in NHS, these levels were not further analysed [36].

The percentage of monounsaturated CERs (i.e. unsaturation index) was determined in subclasses NS and AS. At 60% RH, a reduction in the unsaturation index was observed for subclass NS as compared to high RH in CC-FTM, whereas in FTMs no changes were observed due to altered RH. The unsaturation index

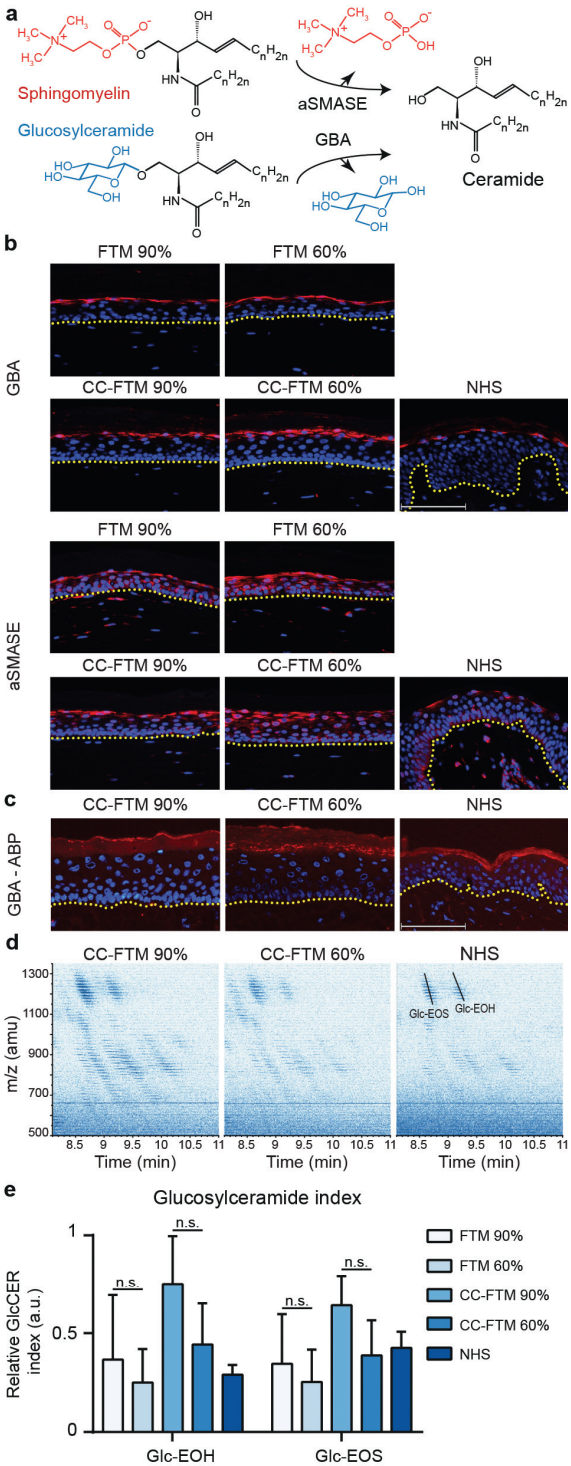


Figure 3. Precursor ceramide conversion in HSEs generated at reduced relative humidity. **(a)** Illustration of terminal ceramide processing mediated by β-glucocerebrosidase-1 (GBA) and acid sphingomyelinase (aSMASE) **(b)** Protein expression of GBA and aSMASE in HSEs and NHS. **(c)** Activity based probe (ABP) fluorescence signal of MDW941, which solely binds to the active GBA enzyme. Protein expression and ABP signal are shown in red and nuclei are shown in blue, and yellow dotted line indicates dermal-epidermal junction. Scale bar indicates 100 µm **(d)** Ion maps of the GlcCERs in CC-FTMs and NHS. **(e)** Relative values of the glucosylceramide index of subclasses EOS and EOH. Data represent mean + SD, N=4.

for these subclasses provides an indication on the change in level of unsaturation for the other CER subclasses.

3.3. Glucosylceramide processing at varying RH levels

We further studied the terminal ceramide processing which occurs at the SG-SC interface. The conversion of precursor ceramides into ceramides is mediated by the enzymes aSMASE and GBA (**Fig. 3 a**). To fully comprehend the effect of RH on this process, we analysed enzyme protein expression, enzyme activity, and substrate to product ratio. In both HSE types, GBA expression was detected in the SG and aSMASE expression was highest in the SG, similar as in NHS (**Fig. 3 b**). In CC-FTMs generated at 60% RH, GBA and aSMASE were present in more cell layers of the SG, in line with the results of epidermal morphogenesis. Active GBA was detected *in situ* using the activity-based probe MDW941, a fluorescent suicide inhibitor. Active GBA molecules resided at the SG-SC interface and this distribution was similar at both RH levels and in NHS (**Fig. 3 c**). The ratio between glucosylceramide (GlcCER) to ceramide was determined by LC-MS. The presence of the high molecular weight GlcCERs for most of the CER subclasses was detected on another part of the LC-MS ion map (**Fig. 3 d**).

We determined the relative GlcCER indexes for subclasses EOS and EOH, which are exclusively processed by GBA [26]. Also, this provides an indication for the GlcCER index in other CER subclasses. Comparing the GlcCER indexes between high and low RH and to NHS, no significant differences were observed in this dataset.

3.4. Organization of the stratum corneum barrier lipids

Analyses of the lipid organization provides additional information on the barrier formation at varying RH levels. The intercorneocyte lipid matrix contains repetitive lamellar stackings (**Fig. 4 a,b**), which were studied by small-angle X-ray diffraction. The diffraction profiles revealed the presence of the long periodicity phase (LPP) at 90% and 60% RH in both HSE types (**Fig. 4 c**). The repeat distance of the LPP was longer in the CC-FTMs generated at reduced RH, whereas in FTMs this remained equal. As compared to NHS, the LPP repeat distance is shorter and there is no SPP formed in both HSE types [38]. Within the lamellae, lipids are organized in either a very dense orthorhombic or in a dense hexagonal lateral packing (**Fig. 4 d**). The lateral packing was determined in HSEs generated at high and low RH and appeared to be hexagonal in the CC-FTMs (**Fig. 4 e**) as well as in the FTMs (*data not shown*), irrespective of RH level. In NHS, the lipids were predominantly ordered in the orthorhombic lateral packing.

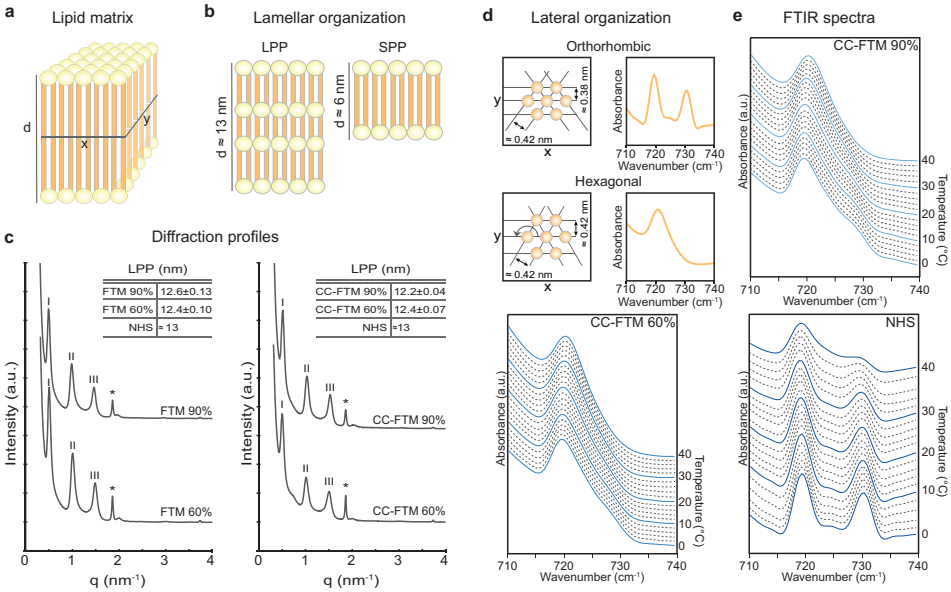


Figure 4. Lipid organization in HSEs generated at reduced relative humidity. (a) Schematic overview of the 3D lipid matrix in the SC. Lipids are shown with head group region in yellow and hydrocarbon chain region in orange. **(b)** Illustration of the lamellar phases. The long periodicity phase (LPP) has an approximate repetition distance (d) of around 13 nm and the short periodicity phase (SPP) has an approximate d of 6 nm [38]. **(c)** Representative X-ray diffraction profiles. Peaks attributed to the LPP are indicated by Roman numbers. The peak of crystalline cholesterol phase is indicated by the asterisk symbol (*). Inset shows the d of the LPP as mean ± SD, N=4, whereas for NHS d was derived from Bouwstra *et al.* [38]. **(d)** Schematic overview of lateral lipid organization. Hydrocarbon chains can adopt a very dense orthorhombic or a dense hexagonal packing. This is indicated by a double or single peak respectively in the methylene rocking vibration region after measurement by FTIR. **(e)** Representative FTIR spectra of the methylene rocking vibrational mode of lipids in CC-FTMs and NHS.

4. Discussion

The objectives of this study were to determine the effects of RH on epidermal morphogenesis and on lipid barrier formation during *in vitro* development of HSEs. In addition, whether RH affects the conversion of GlcCER into CER was tested. This study shows that reduction of RH mainly influenced the differentiation in the uppermost epidermal layers and that it resulted in epidermal activation, although variations between HSE types were observed. Strong alterations for neither SC ceramide composition nor lipid organization were observed. Also, the conversion of GlcCER into CER at the SG-SC interface remained unaffected by variations in RH.

Our data is in agreement with the diversity in adaptations after RH reduction in different HSE types. The FTMs data showed no effect on epidermal

morphogenesis, which also has been observed before [12]. The CC-FTM data showed an enlarged SG at reduced RH, in line with previous results in epidermal models [13, 15]. More research is required to explain this diversity, although the dermis is likely to play a contributing factor in adaptation to reduced RH. Another morphogenetic adaptation to lower RH was the higher epidermal cell activation, which has been aggravated at levels below 60% RH (J.A. Bouwstra, *unpublished results*). This could be due to an accelerated differentiation program and barrier formation as response to the lower external water level, inducing temporary but fierce signalling for barrier repair responses [39]. Also reduced RH levels affected the activation of dermal fibroblasts, which could contribute to more epidermal activation [40, 41]. As an activated epidermis is shown to undermine the lipid barrier formation *in vitro* and *in vivo* [42, 43], lower *in vitro* RH levels are not recommended.

The variance in lipid composition between high and low RH was small, leading to an unaltered SC lipid organization in HSEs. The differences in lipid composition between HSEs and NHS are related to the differences in lipid organization, which is in line with previous reports [11, 23]. Although the contribution of each lipid molecule to the matrix organization is not fully elucidated, it is known that major contributors to a reduced repeat distance of the LPP are the disbalanced CER subclass profile in combination with the reduced MCL of CERs [44]. The lack of formation of SPP is ascribed to the overabundance of CER[EO] subclasses [45, 46]. Moreover, formation of a hexagonal lateral packing in HSEs is associated with the increased presence of monounsaturated CERs, and the increased presence of CERs with a shorter chain length [23, 44]. These aspects remain important targets for future studies to better mimic the barrier formation of NHS in HSEs.

Novel insights on the effect of RH on the conversion of GlcCER into CERs were obtained. Earlier findings in dry (50% RH) HSEs revealed an upregulated expression of glucosylceramide synthase, indicating an upregulation of total CER synthesis [15]. On the other hand, in submerged (>100% RH) HSEs an accumulation of GlcCER in the lipid matrix was observed [24]. Our results show similarity in GlcCER indexes, absolute ceramide content, GBA enzyme expression and GBA activity at high and low RH level. These complementary findings indicate that ceramide biosynthesis is not affected by reduced RH levels. Although in submerged HSEs there was an accumulation of GlcCERs [24], mediated by increased synthesis or reduced conversion, after air-exposure the terminal ceramide processing is not impeded by high *in vitro* RH levels.

The expected epidermal hyperplasia in control FTMs was not observed in this study [11, 32], most probably caused by primary donor effects or increased rate of medium refreshments, but will not impair our conclusions [27, 32].

Furthermore, due to a high technical complexity in the data analysis, in this study no unsaturated CER[EO] with a linoleic chain (contributing ~17-19% to FTM and NHS; Helder *et al.*, submitted) and saturated CER[EO] with an oleic chain (contributing ~23% to FTM; Helder *et al.*, submitted) were quantified. This leads to underestimation of the abundance of CER[EO]. Although FTMs and CC-FTMs were generated with different primary cell donors limiting a direct comparison between both, it appears reasonable that the morphogenesis and barrier formation in CC-FTMs better resembles that of NHS in line with previous findings [27]. An overall limitation of both HSE types is the lack sweat and sebum production, of which the salt, glycerol, and lactate are known to affect the hydration status and barrier functionality of the SC [12, 47-49]. These factors should also be considered in future studies regarding the interplay between RH and HSEs.

This study revealed that reduction of external relative humidity levels during *in vitro* development of human skin equivalents does not lead to strong alterations in the epidermal lipid barrier formation. This study contributes with novel insights to better understand the influence of cell culture conditions on the lipid barrier formation in HSEs.

5. Acknowledgements

J. van Smeden is thanked for the support during the activity-based probe analyses. We also thank S. Absalah for the assistance during preparation and running of the lipidomics analyses. The authors are grateful for the support during the small angle X-ray diffraction measurements by the personnel of the DUBBLE beam line (BM26) at the ESRF. The company Evonik (Essen, Germany) is thanked for the provision of ceramides. The work was funded by grant no. 13151 of the Dutch Technology Foundation STW, which is part of the Netherlands Organisation for Scientific Research (NWO), and which is partly funded by the Ministry of Economic Affairs.

6. Conflict of interest

The authors have declared no conflicting interests.

7. Author contributions

AM, JAB and AEG designed the research study. AM, RvD, GG performed the research. AM and WB performed the data analysis. AM drafted the manuscript, which was commented on by HSO, JMFGA, JAB, AEG. All authors approved the submitted manuscript

8. References

1. Choe, C., et al., Keratin-water-NMF interaction as a three layer model in the human stratum corneum using in vivo confocal Raman microscopy. Scientific reports, 2017. **7**(1): p. 15900.
2. Engebretsen, K., et al., The effect of environmental humidity and temperature on skin barrier function and dermatitis. Journal of the European Academy of Dermatology and Venereology, 2016. **30**(2): p. 223-249.
3. Goad, N. and D. Gawkrodger, Ambient humidity and the skin: The impact of air humidity in healthy and diseased states. Journal of the European Academy of Dermatology and Venereology, 2016. **30**(8): p. 1285-1294.
4. Mojumdar, E.H., et al., Skin hydration: interplay between molecular dynamics, structure and water uptake in the stratum corneum. Scientific reports, 2017. **7**(1): p. 15712.
5. Rawlings, A.V. and C.R. Harding, Moisturization and skin barrier function. Dermatologic therapy, 2004. **17**(s1): p. 43-48.
6. Vyumvuhore, R., et al., Effects of atmospheric relative humidity on Stratum Corneum structure at the molecular level: ex vivo Raman spectroscopy analysis. Analyst, 2013. **138**(14): p. 4103-4111.
7. Sato, J., et al., Abrupt decreases in environmental humidity induce abnormalities in permeability barrier homeostasis. Journal of investigative dermatology, 2002. **119**(4): p. 900-904.
8. El Ghalbzouri, A., et al., Leiden reconstructed human epidermal model as a tool for the evaluation of the skin corrosion and irritation potential according to the ECVAM guidelines. Toxicology in Vitro, 2008. **22**(5): p. 1311-1320.
9. Niehues, H., et al., 3D skin models for 3R research: the potential of 3D reconstructed skin models to study skin barrier function. Experimental dermatology, 2018.
10. Ponec, M., et al., Lipid and ultrastructural characterization of reconstructed skin models. International journal of pharmaceutics, 2000. **203**(1-2): p. 211-225.
11. Thakoersing, V.S., et al., Unraveling barrier properties of three different in-house human skin equivalents. Tissue Engineering Part C: Methods, 2011. **18**(1): p. 1-11.
12. Bouwstra, J.A., et al., Water distribution and natural moisturizer factor content in human skin equivalents are regulated by environmental relative humidity. Journal of Investigative Dermatology, 2008. **128**(2): p. 378-388.
13. Cau, L., et al., Lowering relative humidity level increases epidermal protein deimination and drives human filaggrin breakdown. Journal of dermatological science, 2017. **86**(2): p. 106-113.
14. Mak, V.H.W., et al., Barrier Function of Human Keratinocyte Cultures Grown at the Air-Liquid Interface. Journal of Investigative Dermatology, 1991. **96**(3): p. 323-327.
15. Sun, R., et al., Lowered humidity produces human epidermal equivalents with enhanced barrier properties. Tissue Engineering Part C: Methods, 2014. **21**(1): p. 15-22.
16. Supp, A.P., et al., Incubation of cultured skin substitutes in reduced humidity promotes cornification in vitro and stable engraftment in athymic mice. Wound Repair and Regeneration, 1999. **7**(4): p. 226-37.
17. Bouwstra, J.A., et al., Water distribution and related morphology in human stratum corneum at different hydration levels. Journal of Investigative Dermatology, 2003. **120**(5): p. 750-758.
18. Elias, P.M., Structure and Function of the Stratum Corneum Extracellular Matrix. Journal of Investigative Dermatology, 2012. **132**(9): p. 2131-2133.
19. Proksch, E., J.M. Brandner, and J.M. Jensen, The skin: an indispensable barrier. Experimental Dermatology, 2008. **17**(12): p. 1063-1072.
20. Kihara, A., Synthesis and degradation pathways, functions, and pathology of ceramides and epidermal acylceramides. Progress in lipid research, 2016. **63**: p. 50-69.
21. van Smeden, J., et al., The important role of stratum corneum lipids for the cutaneous barrier function. Biochimica et Biophysica Acta - Molecular and Cell Biology of Lipids, 2014. **1841**(3): p. 295-313.
22. Vávrová, K., A. Kováčik, and L. Opálka, Ceramides in the skin barrier. European Pharmaceutical Journal, 2017. **64**(2): p. 28-35.
23. Thakoersing, V.S., et al., Increased Presence of Monounsaturated Fatty Acids in the Stratum Corneum of Human Skin Equivalents. Journal of Investigative Dermatology, 2013. **133**(1): p. 59-67.
24. Thakoersing, V.S., M. Ponec, and J.A. Bouwstra, Generation of human skin equivalents under submerged conditions—mimicking the in utero environment. Tissue Engineering Part A, 2010. **16**(4): p. 1433-1441.
25. Fluhr, J.W. and P.M. Elias, Stratum corneum pH: formation and function of the 'acid mantle'. Exogenous Dermatology, 2002. **1**(4): p. 163-175.

26. van Smeden, J., et al., In situ visualization of glucocerebrosidase in human skin tissue: zymography versus activity-based probe labeling. Journal of lipid research, 2017. **58**(12): p. 2299-2309.
27. Mieremet, A., et al., Improved epidermal barrier formation in human skin models by chitosan modulated dermal matrices. PloS one, 2017. **12**(3): p. e0174478.
28. Haisma, E.M., et al., Inflammatory and antimicrobial responses to methicillin-resistant Staphylococcus aureus in an in vitro wound infection model. PloS one, 2013. **8**(12): p. e82800.
29. El Ghalbzouri, A., et al., Replacement of animal-derived collagen matrix by human fibroblast-derived dermal matrix for human skin equivalent products. Biomaterials, 2009. **30**(1): p. 71-78.
30. van Drongelen, V., et al., Barrier properties of an N/TERT-based human skin equivalent. Tissue Engineering Part A, 2014. **20**(21-22): p. 3041-3049.
31. Ponec, M., et al., The formation of competent barrier lipids in reconstructed human epidermis requires the presence of vitamin C. Journal of investigative dermatology, 1997. **109**(3): p. 348-355.
32. Mieremet, A., et al., Recapitulation of Native Dermal Tissue in a Full-Thickness Human Skin Model Using Human Collagens. Tissue Engineering Part A, 2017.
33. Rissmann, R., et al., Skin barrier disruption by acetone: observations in a hairless mouse skin model. Archives of dermatological research, 2009. **301**(8): p. 609-613.
34. Sakai, S., et al., Characteristics of the Epidermis and Stratum Corneum of Hairless Mice with Experimentally Induced Diabetes Mellitus. Journal of Investigative Dermatology, 2003. **120**(1): p. 79-85.
35. Blair, C., Morphology and thickness of the human stratum corneum. British Journal of Dermatology, 1968. **80**(7): p. 430-436.
36. Boiten, W., et al., Quantitative analysis of ceramides using a novel lipidomics approach with three dimensional response modelling. Biochimica et Biophysica Acta (BBA) - Molecular and Cell Biology of Lipids, 2016. **1861**(11): p. 1652-1661.
37. Motta, S., et al., Ceramide composition of the psoriatic scale. Biochimica et Biophysica Acta - Molecular Basis of Disease, 1993. **1182**(2): p. 147-151.
38. Bouwstra, J.A., et al., Structural investigations of human stratum corneum by small-angle X-ray scattering. Journal of Investigative Dermatology, 1991. **97**(6): p. 1005-12.
39. Grubauer, G., P.M. Elias, and K.R. Feingold, Transepidermal water loss: the signal for recovery of barrier structure and function. Journal of Lipid Research, 1989. **30**(3): p. 323-333.
40. Zhao, J., et al., Epidermal HMGB1 activates dermal fibroblasts and causes hypertrophic scar formation in reduced hydration. Journal of Investigative Dermatology, 2018.
41. Zhao, J., et al., S100A12 Induced in the Epidermis by Reduced Hydration Activates Dermal Fibroblasts and Causes Dermal Fibrosis. J Invest Dermatol, 2017. **137**(3): p. 650-659.
42. Choi, M.J. and H.I. Maibach, Role of Ceramides in Barrier Function of Healthy and Diseased Skin. American Journal of Clinical Dermatology, 2005. **6**(4): p. 215-223.
43. Proksch, E., R. Fölster-Holst, and J.-M. Jensen, Skin barrier function, epidermal proliferation and differentiation in eczema. Journal of Dermatological Science, 2006. **43**(3): p. 159-169.
44. Janssens, M., et al., Increase in short-chain ceramides correlates with an altered lipid organization and decreased barrier function in atopic eczema patients. Journal of lipid research, 2012: p. jlr. P030338.
45. Boncheva, M., The physical chemistry of the stratum corneum lipids. International journal of cosmetic science, 2014. **36**(6): p. 505-515.
46. de Jager, M.W., et al., Novel lipid mixtures based on synthetic ceramides reproduce the unique stratum corneum lipid organization. Journal of lipid research, 2004. **45**(5): p. 923-932.
47. Fluhr, J.W., et al., Glycerol regulates stratum corneum hydration in sebaceous gland deficient (asebia) mice. Journal of Investigative Dermatology, 2003. **120**(5): p. 728-737.
48. Hara, M. and A. Verkman, Glycerol replacement corrects defective skin hydration, elasticity, and barrier function in aquaporin-3-deficient mice. Proceedings of the National Academy of Sciences, 2003. **100**(12): p. 7360-7365.
49. Lee, A.-R.C. and H.K. Moon, Gravimetric analysis and differential scanning calorimetric studies on glycerin-induced skin hydration. Archives of Pharmacal Research, 2007. **30**(11): p. 1489-1495.
50. Mojumdar, E.H., et al., Monounsaturated fatty acids reduce the barrier of stratum corneum lipid membranes by enhancing the formation of a hexagonal lateral packing. Langmuir, 2014. **30**(22): p. 6534-6543.
51. Groen, D., et al., Is an orthorhombic lateral packing and a proper lamellar organization important for the skin barrier function? Biochimica et Biophysica Acta (BBA)-Biomembranes, 2011. **1808**(6): p. 1529-1537.

52. Mieremet, A., et al., Shedding light on the effects of 1,25-dihydroxyvitamin D3 on epidermal lipid barrier formation in three-dimensional human skin equivalents. The Journal of Steroid Biochemistry and Molecular Biology, 2019. **189**: p. 19-27.

9. Supporting Information

9.1. Supplementary materials and methods

9.1.1. LC-MS settings and data quantification

The LC-MS methods were used as described before by Boiten *et al.* [36]. SC lipid extracts concentration was set at 0.3 mg/ml of which 5 µl was injected. Samples were separated on a PVA-Sil column (5 µm particles, 100 x 2.1 mm i.d.)(YMC, Kyoto, Japan) with an Acquity UPLC H-class (Waters, Milford, MA, USA). CERs were detected using a XEVO TQ-S mass spectrometer (Waters). Measurements were performed in full scan mode from 1.25-8.00 min between m/z 350–1200 and from 8.00-12.5 min between m/z 500-1350. The area under the curve (AUC) of a chromatogram from the mono-isotopic mass of the main fragment of each CER was integrated. For a selected number of CERs, the relative abundance overlap of the corresponding monounsaturated CERs containing two naturally abundant ^{13}C was more than 10%. When this occurred, the AUC of the monounsaturated CERs containing two naturally abundant ^{13}C was determined. Using its natural isotope distribution, the overlap was calculated and subtracted from the one of with which it overlapped for correction. Quantification to the molar amount of CERs occurred using the AUC of the chromatogram of any specific ceramide, the internal standard of CER N(24deuterated)S(18) and a 3D response model based on compound properties and a calibration curve from a limited number of synthetic ceramides (**Supplementary fig. 5**). Quantified values of the glucosylceramide index of subclasses EOS and EOH are determined by dividing the AUC values of total GlcCER signal by that of cumulative AUC values of corresponding CER[EO], as described by van Smeden *et al.* [26]. As this data is not quantified, it is presented as arbitrary amount.

9.1.2. Small angle X-ray diffraction

Measurements were performed at the European Synchrotron Radiation Facility at station BM26B as described in detail by Mojumdar *et al.* [50]. Measurements occurred twice during 90 sec to overcome a gap in signal detection, with a sample distance to pilatus1M detector of 2.1 meter. Calibration methods and data conversion from x,y coordinates to polar coordinates were performed as described by Groen *et al.* [51]. From the positions of a series of equidistant diffraction peaks, the repeat distance (d) of a lamellar phase was calculated using the equation $d = n \cdot 2\pi / q_n$, where q is the scattering vector and n is the order number of the diffraction peak.

9.1.3. Fourier transform infrared spectroscopy

Setting of the FTIR were described previously by Mieremet *et al.* [52]. In brief, the isolated SC was placed between two AgBr cells and put under continuous dry air for 30 min before the start of measurements. All spectra were acquired on a Varian

670-IR spectrometer equipped with a broad-band mercury cadmium telluride detector. The spectrometer was cooled with liquid nitrogen and connected to a controlled heating device. The spectrometer collected the data with a frequency range of 400-4000 cm^{-1}. The spectral parameters were speed 25 kHz, UDR 2, filter 6.4 and aperture 1 cm^{-1}. The measurements were performed with a 240 sec time resolution and a length of run equal to 164 min. The lateral packing behaviour was examined between 0°C and 40°C with a heating rate of 0.25°C/min, resulting in a 1°C temperature increase per measurement. FTIR spectra were analysed and deconvoluted with Varian Resolutions Pro software and finally processed with a custom designed XRAY plot program.

9.2. Supplementary table

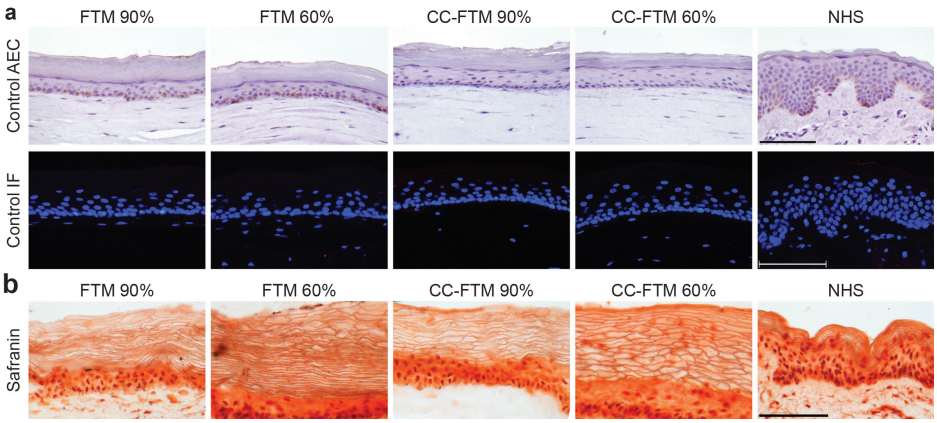
Supplementary table 1. Antibody specifications which are used during immunohistochemistry and immunofluorescence analyses.

Immunohistochemistry	Material	Origin	Clone	Dilution	2nd Ab	Manufacturer
Primary antibody						
Ki67	FFPE	Mouse	MIB1	1:100	A	DAKO, Denmark
Cytokeratin 10	FFPE	Mouse	DE-K10	1:50	A	Labvision/Neomarker, USA
Involucrin	FFPE	Mouse	SY5	1:1200	A	Sanbio, The Netherlands
Cytokeratin 16	FFPE	Mouse	LL025	1:100	A	Serotec, UK
Cytokeratin 17	FFPE	Mouse	E3	1:1500	A	EMD Millipore Corporation, USA
Secondary antibody						
A) Biotinylated goat anti-mouse		Goat		1:200		Southern Biotechnology, USA
Immunofluorescence		**Origin**	**Clone**	**Dilution**	**2nd Ab**	**Manufacturer**
Primary antibody						
Loricrin	FFPE	Rabbit	AF62	1:1000	B	Covance, The Netherlands
Filaggrin	FFPE	Rabbit	PRB417	1:1000	B	Covance, The Netherlands
Collagen type IV	FFPE	Mouse	24.12.8 (PHM-12)	1:75	C	Chemicon, Australia
Vimentin	FFPE	Mouse	V9	1:250	C	Sigma-Aldrich, Germany
GBA	FFPE	Rabbit	EPR5142	1:150	B	Abcam, UK
aSMASE	FFPE	Rabbit	polyclonal	1:1000	B	Abcam, UK

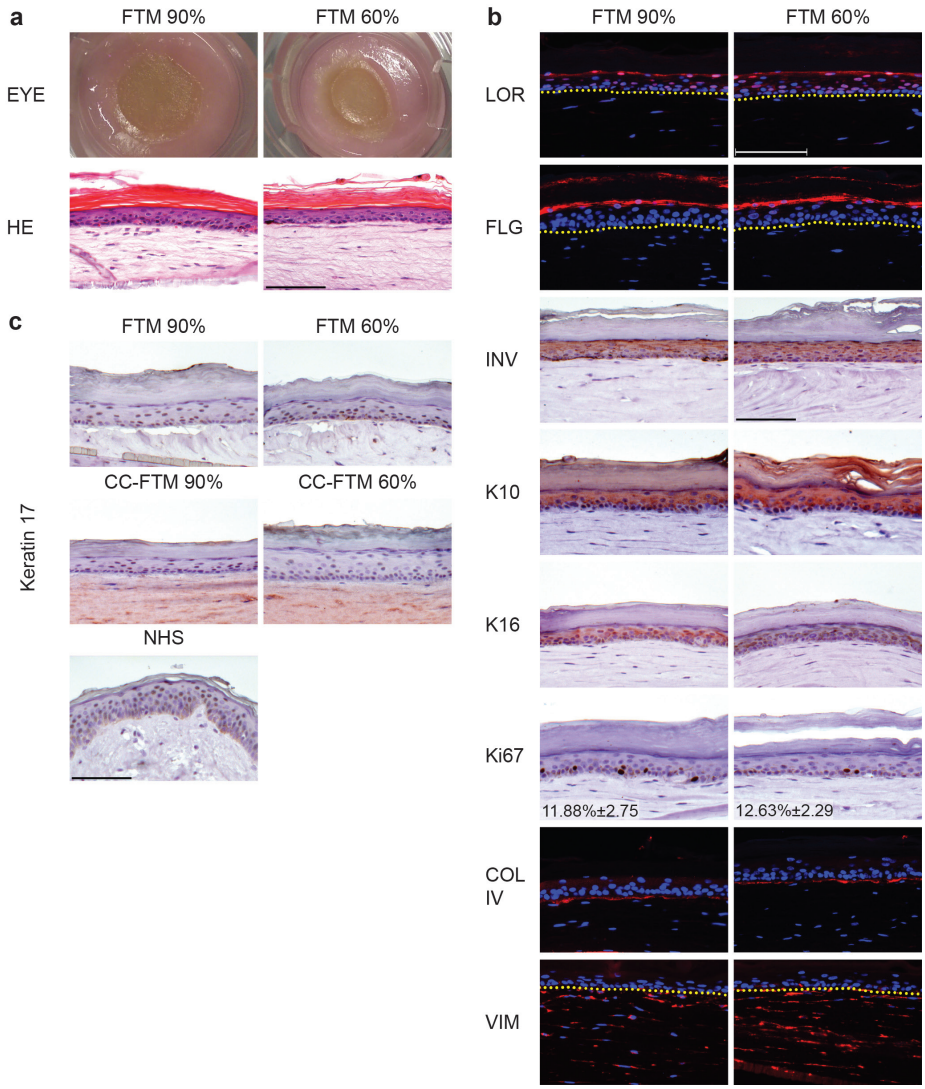
Supplementary table 1 (continued).

Immunofluorescence	Origin	Clone	Dilution	2nd Ab	Manufacturer
Secondary antibody					
B) Cy3-conjugated anti-rabbit	Goat		1:500		Jackson immunoresearch Laboratory, USA
C) Cy3-conjugated anti-mouse	Goat		1:1000		Jackson immunoresearch Laboratory, USA

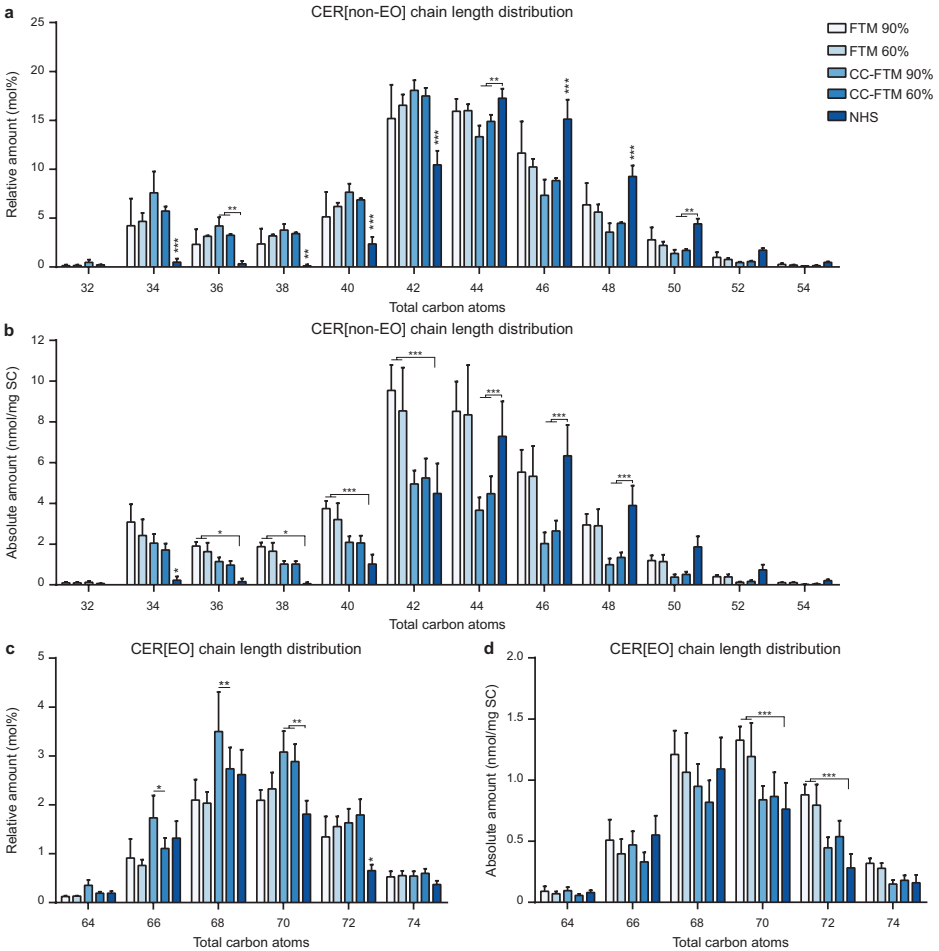
9.3.Supplementary figures



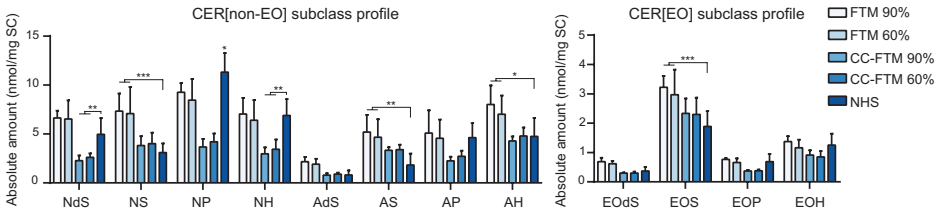
Supplementary figure 1. Epidermal morphogenesis protein biomarker controls and stratum corneum thickness analysis. (a) Immunohistochemical control sections for the 3-Amino-9-ethylcarbazole (AEC) method and immunofluorescence (IF) method. **(b)** Safranin red stained lipid matrix of the stratum corneum imaged after alkali expansion of the corneocyte layers. Scale bar indicates 100 µm.



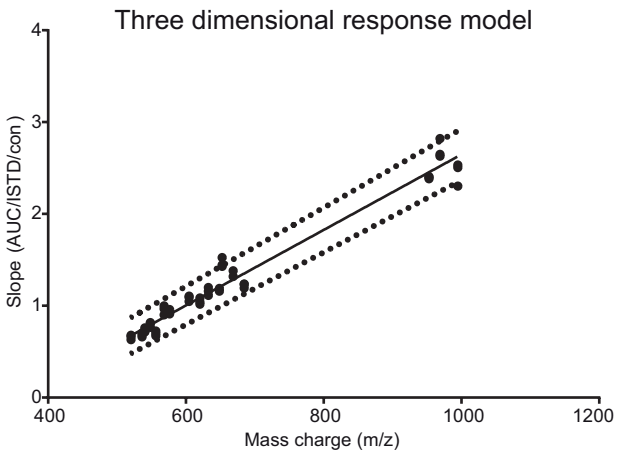
Supplementary figure 2. Generation of full thickness models at reduced relative humidity. **(a)** General morphology in high (90%) and low (60%) RH, assessed by eye and HE staining. **(b)** Expression of loricrin (LOR), filaggrin (FLG), involucrin (INV), keratin 10 (K10), keratin 16 (K16) indicating epidermal differentiation programs and activation respectively. Proliferation was assessed by Ki67 (with indicated proliferation index as mean ± SD, N=4), basement membrane by collagen type IV (COL IV), and fibroblast distribution by vimentin (VIM). **(c)** Keratin 17 expression in HSEs and in NHS. Protein biomarkers are shown in red and nuclei in blue. Yellow dotted line indicates dermal-epidermal junction. Scale bar indicates 100 µm.



Supplementary figure 3. CER carbon chain length distribution. Bar plot showing the carbon chain length distributions of even numbered CER[non-EO] between C32 and C54 and of even numbered CER[EO] between C64 and C74. Data is presented in relative amount **(a, c)** and in absolute amount per mg stratum corneum **(b, d)**. Data is shown for both HSE types developed at 90% and 60% RH and of NHS. Data represents mean + SD, N=4.



Supplementary figure 4. Quantitative CER subclass profile. Bar plot showing the CER[non-EO] and CER[EO] subclass profiles as absolute amounts per mg stratum corneum. Data is shown for both HSE types developed at 90% or 60% RH and for NHS, represented by mean + SD, N=4.



Supplementary figure 5. Three dimensional response model. The model is generated based on settings of the mass spectrometer, compound properties, and a limited number of synthetic ceramides according to Boiten *et al.* [36].

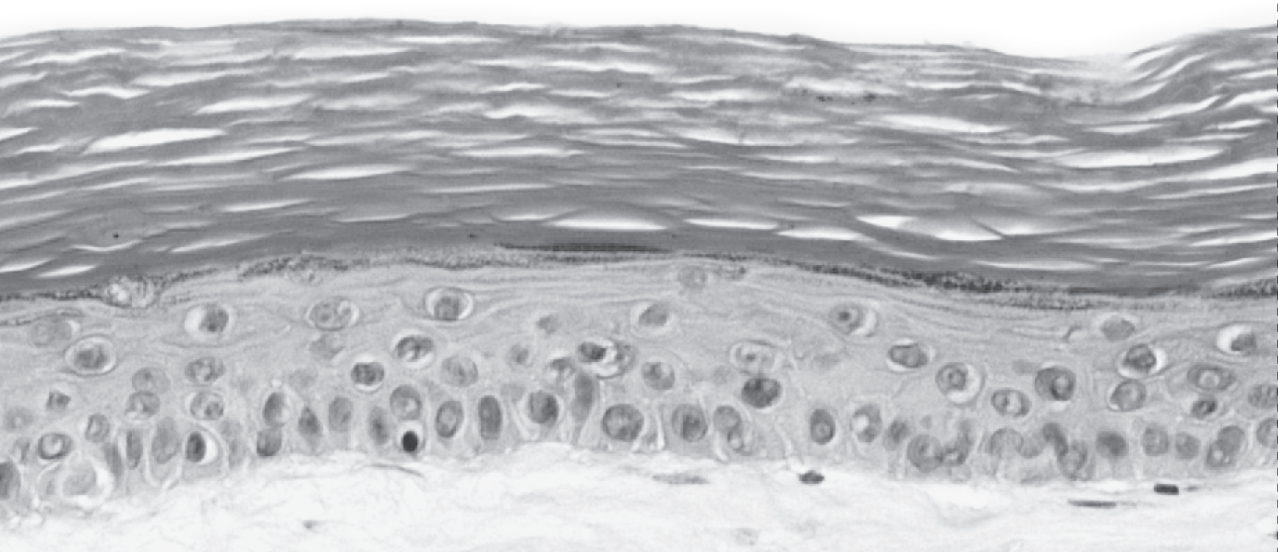
7

Shedding light on the effects of 1,25-dihydroxyvitamin D3 on epidermal lipid barrier formation in three-dimensional human skin equivalents

Arnout Mieremet
Rianne van Dijk
Gert Gooris
Joke A. Bouwstra[+]
Abdoelwaheb El Ghalbzouri[+]

[+] Joint senior authorship

The Journal of Steroid Biochemistry and Molecular Biology 189: 19-27 (2019)



Abstract

Human skin equivalents (HSEs) are three-dimensional models resembling native human skin (NHS) in many aspects. Despite the manifold similarities to NHS, a restriction in its applications is the altered *in vitro* lipid barrier formation, which compromises the barrier functionality. This could be induced by suboptimal cell culturing conditions, which amongst others is the diminished activation of the vitamin D receptor (VDR) signalling pathway. The active metabolite of this signalling pathway is 1,25-dihydroxyvitamin D_3 ($1,25(OH)_2D_3$). An interacting role in the formation of the skin barrier has been ascribed to this pathway, although it remains unresolved to which extent this pathway contributes to the (mal-) formation of the epidermal barrier in HSEs. Our aim is to study whether cell culture medium enriched with $1,25(OH)_2D_3$ affects epidermal morphogenesis and lipid barrier formation in HSEs. Addition of 20 nM $1,25(OH)_2D_3$ resulted in activation of the VDR signalling pathway by inducing transcription of VDR target genes (CYP24A and LL37) in keratinocyte monocultures and in HSEs. Characterization of HSEs supplemented with $1,25(OH)_2D_3$ using immunohistochemical analyses revealed a high similarity in epidermal morphogenesis and in expression of lipid processing enzymes. The barrier formation was assessed using state-of-the art techniques analysing lipid composition and organization. Addition of $1,25(OH)_2D_3$ did not alter the composition of ceramides. Additionally, the lateral and lamellar organization of the lipids was similar, irrespective of supplementation. In conclusion, epidermal morphogenesis and barrier formation in HSEs generated in presence or absence of $1,25(OH)_2D_3$ leads to a similar morphogenesis and comparable barrier formation *in vitro*.

Keywords: Primary Cell Culture; Artificial skin; Vitamin D; Calcitriol; Lipids; Ceramides; Tissue Engineering

1. Introduction

The native human skin (NHS) is the largest organ of the body with the principle function to protect the body's interior from the external environment. Multiple defence mechanisms are formed to exert various functions of the skin including the physical, chemical, immunological, and microbial barrier [1]. Where possible, these are regulated to maintain local homeostasis, which is mediated by interactions of the cutaneous endocrine and neuroendocrine systems [2]. These are also integrated into central regulators by a continuous exchange of endocrine and neuroendocrine mediators between skin and other organs to preserve systemic homeostasis when adaptation to external stimuli is required [2]. The skin is directly exposed to ultraviolet (UV) radiation, acting as stressor for tissue homeostasis thereby inducing elements of the stress response [3]. Importantly, UV exposure is also driving the activation of vitamin D pathway in the skin. The active metabolite of the vitamin D pathway is 1α,25-dihydroxyvitamin D_3 ($1,25(OH)_2D_3$), which can bind to the vitamin D receptor (VDR). Upon activation, heterodimerization of VDR and retinoid-X receptor occurs, followed by binding to vitamin D response elements (VDREs) resulting in transcription of VDR target genes. These genes are involved in cellular proliferation, differentiation, and barrier formation of the skin [4-7]. The skin represents an autonomous vitamin D system due to the local synthesis of ligand $1,25(OH)_2D_3$ as well as expression of VDR in the various cell types of the skin [8].

The main physical barrier of the human skin resides in the uppermost layer of the epidermis. The stratum corneum (SC) consists of corneocytes embedded in a lipid matrix. Corneocytes are terminally differentiated keratinocytes, containing a thick cornified envelope [9-13]. Due to the cross-linked proteins, corneocytes are regarded to be impermeable for most substances. Consequently, diffusion of topical applied molecules mainly occurs through the intercorneocyte lipid matrix [14, 15]. This matrix is connected to the corneocytes by the cornified lipid envelope. In the intercorneocyte space, the lipids are highly structured in the lateral and the lamellar organization [16]. The type of lipid organization influences the rate of compound penetration [17-19]. The main lipid classes in the SC lipid matrix are ceramides, free fatty acids (FFAs), and cholesterol [20]. The diversity in lipid composition is a result of numerous biosynthesis steps occurring in the epidermis. Various lipid processing enzymes or enzyme families are involved herein, as reviewed elsewhere [15, 21-24]. Specifically, the diversity in carbon chain length is a result of regulated enzymatic lipid processing by the elongation of very long fatty acids (ELOVL) family.

The NHS is recapitulated *in vitro* by human skin equivalents (HSEs), which are the most sophisticated three-dimensional (3D) model systems. These exhibit

the stratum basale, stratum spinosum, stratum granulosum and SC [25, 26]. Consequently, HSEs form a physiological relevant *in vitro* model and are therefore widely applied in *in vitro* screenings of therapeutics and in toxicology assessments [27]. However, HSEs show dissimilar barrier properties as compared to NHS, potentially leading to altered *in vitro - in vivo* correlations or misclassifications of toxicology profiles [1, 26]. Differences in composition and organization of the lipid matrix in the SC of HSEs as compared to NHS include but are not limited to the i) altered ceramide subclass profile, ii) reduced carbon chain length of FFAs and ceramides, iii) higher level of unsaturated lipids, iv) reduced repeat distance of lamellar phases, and v) increase in hexagonal lateral packing at the expense of the orthorhombic lateral packing [26, 28]. Contributing factors to the aberrant barrier formation could be suboptimal culture medium composition or external culture conditions which are different from *in vivo*. HSEs are generated without exposure to sunlight or nutritional supplementation of $1,25(OH)_2D_3$, waning the activation of the vitamin D signalling pathway, which is in contrast to *in vivo* conditions.

A supporting role in the formation of the skin barrier has been ascribed to the vitamin D signalling pathway. The several roles that vitamin D plays during proliferation and differentiation of the keratinocytes in the epidermis is mediated by various coregulators [29, 30]. Basically, $1,25(OH)_2D_3$ reduces cell proliferation, and promotes differentiation and cornified envelope formation [31]. Moreover, $1,25(OH)_2D_3$ is suggested to modulate the formation of the lipid barrier, mediated by altered expression of lipid processing enzymes ELOVL3, ELOVL4, and ceramide glucosyltransferase (UGCG) [4]. The interplay between the vitamin D signalling pathway and calcium signalling pathway regarding promotion of differentiation is captivating, as both induce differentiation, although these effects do not always seem to be in synergy [31, 32]. Until today, it is unknown whether the vitamin D signalling pathway can contribute to normalization of cell proliferation, differentiation, and formation of the lipid barrier in 3D HSEs. Furthermore, to which extent the lack of $1,25(OH)_2D_3$ and/or sunlight exposure contributes to a compromised epidermal barrier in HSEs remains unresolved [26].

In this study, we aim to determine whether *in vitro* activation of the vitamin D signalling pathway affects epidermal morphogenesis and lipid barrier formation in HSEs. Addition of $1,25(OH)_2D_3$ in the cell culture medium during the generation of HSEs and subsequent analyses of the lipid barrier formation provides additional insights in the development of HSEs and formation of its barrier.

2. Materials and Methods

2.1. Primary cell isolation and generation of skin models

Isolation of primary cells from the dermis and epidermis and cell culturing was performed as described before [33-35]. Full thickness models (FTMs) were generated as described before in a Memmert INC153med CO_2 incubator (Memmert, Schwabach, Germany) (**Supplementary fig. 1**) [35]. The supplementation with 20 nM 1α,25$(OH)_2D_3$ (Sigma-Aldrich) or ethanol vehicle occurred twice a week for four times in total using serum-free high calcium medium (DMEM 3:1 (v/v) mixed with Ham's F12 (Gibco)), supplemented as described before [36]. Four different batches of FTMs were developed using unique primary cells and 3D models were generated for a total of 14 days at the air-liquid interface. Keratinocyte monocultures of three biological replicates were developed in 6-wells plates, in which 100.000 cells were plated per well. Cells reached 80% confluence in 3 days in low calcium medium (Dermalife medium (Lifeline Cell Technology) enriched with penicillin (10,000 U) and streptomycin (10 mg/ml). Subsequently, the medium was supplemented with 20 nM 1,25$(OH)_2D_3$ or ethanol vehicle for 24 hr. For high calcium medium condition, after reaching 80% confluence the keratinocytes were pre-incubated 24 hr in serum high calcium medium (DMEM mixed 3:1 (v/v) with Ham's F12 supplemented with 5% fetal bovine serum (Hyclone, Logan, UT, USA) and additives as described before [36]) to induce differentiation. Afterwards, supplementation for 24 hr with 1,25$(OH)_2D_3$ in high calcium medium occurred. Culture medium of all isolated primary cells was tested for mycoplasma contamination by qPCR and found negative.

2.2. Tissue imaging

Parts of NHS or FTM were 4% formaldehyde fixated and embedded in paraffin or snap frozen in liquid nitrogen. Haematoxylin and eosin (HE) staining was performed according to manufacturer's instructions (Klinipath, Duiven, The Netherlands). Protein analyses by immunohistochemistry or immunofluorescence were performed on 5 µm sections of both formalin fixed paraffin embedded (FFPE) or snap frozen material, as described earlier [35]. Specifications of the primary and secondary antibodies are provided in **supplementary table 1**. Estimations of the thickness of the viable epidermis was performed on four different regions per sample using Adobe Photoshop software measuring the circumference of the viable epidermis. The amount of corneocyte layers was determined by safranin red staining and potassium hydroxide expansion of the SC following methods described earlier [37, 38].

2.3. Gene expression

Total RNA was extracted from monocultures or from the viable epidermis of FTMs using the FavorPrep Tissue Total RNA Mini Kit (Favorgen, Ping-Tung,

Taiwan) according to manufacturer's instruction. A DNA digestion step was added on-column using RNAse-free DNAse set (Qiagen, Hilden, Germany) for 15 min. Nucleic acid concentration was determined using a NanoDrop™ UV-Vis Spectrophotometer (ThermoFisher). Complementary DNA was synthesized using 500 ng total RNA using the iScript™ cDNA Synthesis Kit (Bio-Rad, Hercules, USA) according to manufacturer's instructions. Quantitative real-time polymerase chain reaction was performed using the SYBR Green Supermix (Bio-Rad) on the CFX384™ real-time PCR detection system (Bio-Rad). Following settings were used: polymerase activation for 5 min at 95°C, denaturation for 20 sec at 95°C, annealing for 20 sec at 60°C and extension for 20 sec at 72°C for 40 cycles followed by the generation of a melt curve. Data was normalized against the 2-3 most stable reference genes using the delta delta Ct method. Primers sequences are listed in **supplementary table 2**.

2.4. Stratum corneum isolation and small angle X-ray diffraction analysis

SC was isolated after trypsin digestion, air-dried and stored under Argon gas over silica until further use as described before [35]. Small-angle X-ray diffraction (SAXD) measurements were performed at the European synchrotron radiation facility (Grenoble, France) at station BM26B for a period of 2 x 150 sec as described elsewhere [18]. The scattering intensity I was measured as a function of the scattering vector q. The latter is defined as $q = \frac{4 \cdot \pi \cdot \sin\theta}{\lambda}$, in which θ is the scattering angle and λ is the wavelength. From the positions of the peaks (q_n), the repeat distance can be calculated using the equation $d = \frac{2n \cdot \pi}{qn}$, where n is the order of diffraction peak [39].

2.5. Fourier transform infrared spectroscopy

The isolated SC was placed between two AgBr cells and put under continuous dry air for 30 min before the start of measurements. All spectra were acquired on a Varian 670-IR spectrometer equipped with a broad-band mercury cadmium telluride detector. The spectrometer was cooled with liquid nitrogen and connected to a controlled heating device. The spectrometer collected the data with a frequency range of 400-4000 cm^{-1}. The spectral resolution was 1 cm^{-1}. The measurements were performed with a 240 sec time resolution. The lateral packing behaviour was examined between 0°C and 40°C with a heating rate of 0.25°C/min, resulting in a 1°C temperature increase per measurement. The software used to obtain and analyse spectra was Varian Resolutions Pro 5.2.0. Spectra were deconvoluted and finally processed with XRAY Plot program.

2.6. Liquid chromatography coupled to mass spectrometry analysis

Extraction of total lipids from isolated SC of FTMs was performed with an adjusted Bligh and Dyer method as described by Boiten *et al.* [40]. To determine the weight percentage of lipids in the SC, dry SC weight was measured before and after

extraction. The lipids were analysed using normal phase liquid chromatography - mass spectrometry (LC-MS) according to the method described by Boiten *et al.* [40], with exception of the quantification to molar amounts. A total of 1500 ng lipids were separated on a PVA-Sil column (5 µm particles, 100 x 2.1 mm i.d.) (YMC, Kyoto, Japan) using an Acquity UPLC H-class (Waters, Milford, MA, USA) and detection occurred by a XEVO TQ-S mass spectrometer (Waters, Milford, MA, USA). Measurements were performed in full scan mode from 1.25–8.00 min between m/z 350–1350 for ceramides and from 8.0-12.5 min between m/z 500-1350 for glucosylceramides. Area under curve (AUC) were determined and corrected by ceramide N(24deuterated)S(18) as internal standard (ISTD).

2.7. Statistics

Statistical analyses are conducted using GraphPad Prism version 7.00 for Windows (GraphPad Software, La Jolla, CA, USA). Statistical testing was performed with 1-way or 2-way ANOVA with Tukey's post-test, otherwise specifically stated. Statistical differences are noted as *, ** or ***, corresponding to $P<0.05$, <0.01, <0.001.

3. Results

3.1. Morphogenesis of HSEs supplemented with $1,25(OH)_2D_3$

To determine the effect of vitamin D signalling pathway activation on epidermal morphogenesis and barrier formation, full thickness models (FTMs) were generated with cell culture medium which was enriched with 1α,25-dihydroxyvitamin D_3 (FTM-$1,25(OH)_2D_3$) or vehicle (FTM-control). Macroscopic examination revealed similarities in pigmentation, shape, and structure of FTMs in both conditions **(Fig. 1 a)**. Examination by haematoxylin and eosin (HE) showed the presence of all four epidermal layers in FTMs similar to NHS **(Fig. 1 a)**, indicating that supplementation with $1,25(OH)_2D_3$ leads to a similar epidermal organization. The effects of $1,25(OH)_2D_3$ supplementation was evaluated for the expression of VDR and of selected VDR target genes (LL-37 and CYP24A). Similar gene expression of VDR was observed after supplementation with $1,25(OH)_2D_3$, whereas expression of both target genes was upregulated **(Fig. 1 b)**. This demonstrated that the delivery of $1,25(OH)_2D_3$ was successful to the epidermis of the FTMs, despite its poor solubility and presence of albumin in the culture medium. In addition, the vast fold change indicated that the utilized concentration was adequate. To further assess epidermal characteristics, the thickness of the viable epidermis was quantified and compared **(Fig. 1 c)**. This revealed that supplementation with $1,25(OH)_2D_3$ did not alter epidermal thickness, whereas the epidermis of NHS was significantly thinner as compared to FTMs. The number of corneocyte layers in the SC was equal in all conditions and comparable to NHS **(Fig. 1 d)**. The epidermal morphogenesis was further studied using expression of specific

morphogenesis biomarkers for epidermal differentiation, cell activation, and basal layer proliferation **(Fig. 1 e)**. For validation, the expression of these biomarkers was also studied in NHS. From apical to basal side, examination of late (loricrin, filaggrin and involucrin) and early epidermal differentiation (keratin (K)10) revealed no effect of activated vitamin D signalling pathway on the execution of the differentiation programs. Comparison with the differentiation programs in NHS revealed a similar early, but distinct late epidermal differentiation program, as the granular layer in FTMs was enlarged and expression of involucrin initiated in the spinous layer. The equal expression of biomarker K16 indicated an activated state of FTMs, instead of no K16 expression and full homeostasis observed in NHS. The expression of Ki67 positive cells in the basal layer (proliferation) was similar irrespective the conditions tested. The proliferation indexes were: 17.7±3.9 (FTM-control), 20.6±8.7 (FTM-1,25$(OH)_2D_3$), and 12.1±0.4 (NHS).

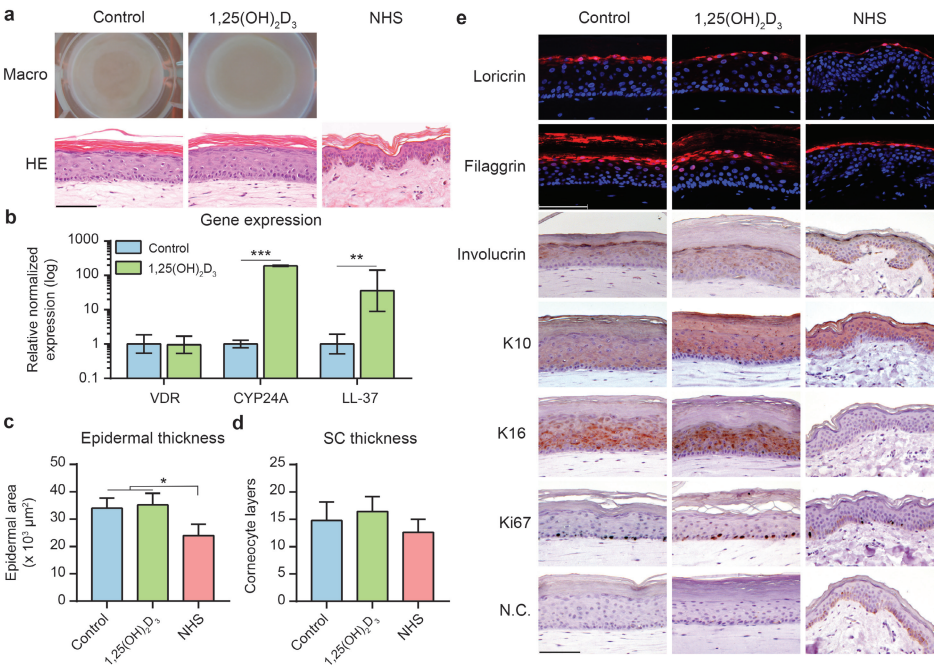


Figure 1. General morphology of full thickness models after addition of 20 nM 1,25$(OH)_2D_3$. **(a)** Assessment of macro- and microanatomy, the latter after haematoxylin and eosin (HE) staining. **(b)** Epidermal gene expression of vitamin D receptor (VDR) and its target genes (CYP24A and LL-37) in FTM-control and FTM-1,25$(OH)_2D_3$. Data indicates mean ± SD, N=3. **(c)** Epidermal thickness of FTMs and of NHS. Data indicates mean + SD, N=4. **(d)** Stratum corneum thickness of FTMs and of NHS, determined after safranin red staining and alkali expansion. Data indicates mean + SD, N=4. **(e)** Expression of loricrin, filaggrin, involucrin, keratin 10 (K10), keratin 16 (K16), and Ki67 indicating epidermal differentiation programs, activation, and proliferation respectively. No non-specific binding of the secondary antibody was detected (negative control (N.C.)). Protein biomarkers are shown in red and nuclei in blue, scale bars indicate 100 µm.

3.2. Lipid processing after supplementation with 1,25(OH)$_2$D$_3$

The expression of lipid processing enzymes which play an important role in the barrier formation was evaluated on protein level in FTM-control, FTM-1,25(OH)$_2$D$_3$, and NHS (**Fig. 2 a**). Similar expression of ELOVL family members 1, 3, 4, and 6 was detected, irrespective of supplementation with 1,25(OH)$_2$D$_3$. Protein expression of stearoyl-CoA desaturase-1 (SCD1) was detected comparably in both FTMs. As compared to NHS, an increased expression of ELOVL1 and SCD1 was detected in FTMs. Additionally, expression of these lipid processing enzymes was also assessed in UV light (UVA and UVB) irradiated FTMs, which compensates for the diminished sunlight exposure in another way than supplementation with 1,25(OH)$_2$D$_3$ does (**Supplementary fig. 2**). Evaluation of the expression of lipid processing enzymes in these FTMs showed a similar expression profile as non-irradiated FTMs. However, high dose UV (≥90 mJ/cm^2) exposure did lead to apoptosis, while in low dose UV (<90 mJ/cm^2) irradiation this was undetected. In case of apoptosis, the lipid processing enzyme expression reduced, possibly linked to reduced viability.

To obtain more insights on the equal expression of lipid processing enzymes after 1,25(OH)$_2$D$_3$ supplementation, the contribution of extracellular calcium was determined in primary proliferating and differentiating keratinocyte monocultures. Examination of gene expression of VDR and its downstream targets revealed a similar expression of VDR and upregulated expression of CYP24B and LL-37, indicative for an effective delivery of 1,25(OH)$_2$D$_3$ (**Fig. 2 b**). Expression of ELOVL family members 1, 4 and 6 was unchanged after 1,25(OH)$_2$D$_3$ supplementation (**Fig. 2 c**). Solely an increased expression of ELOVL4 was detected due to the elevated external calcium levels. Furthermore, the protein barrier formation was promoted due to the calcium concentration indicated by elevated involucrin expression, but was similar regardless of supplementation with 1,25(OH)$_2$D$_3$ (**Fig. 2 d**). These complementary findings indicate that the lipid processing is similar, irrespective of 1,25(OH)$_2$D$_3$ supplementation or UV light exposure.

3.3. Ceramide composition of the intercorneocyte lipid matrix

To obtain more insights on the epidermal barrier formation, the ceramide composition in the SC was studied. The total lipid content within the SC was similar in all conditions tested (**Supplementary fig. 3 a**). Although three main classes of lipids are present in the SC, the ceramides are very characteristic in the SC composition and are crucial for the lipid organization. Therefore, we focused on the twelve most abundant ceramide subclasses in the SC lipid matrix (**Fig. 3 a**). After separation by polarity and detection per mass using the in-house developed liquid chromatography coupled to mass spectrometry (LC-MS) approach [40], the ceramide subclasses were analysed (**Supplementary fig. 3 b**). Comparisons were

made for the profiles of the total ceramide (CERs) subclasses of FTM-control and FTM-1,25(OH)$_2$D$_3$, which showed a high similarity for ceramides of subclasses N and A (CER[non-EO]) and for ceramides of subclasses EO (CER[EO]) in both conditions (**Fig. 3 b, c**). The ceramide composition was examined in more detail by analysing the carbon chain length distribution. A wide distribution in the carbon chain length of the CER[non-EO] was observed, from CER[non-EO] with 32 carbon atoms to CER[non-EO] with 54 carbon atoms (**Fig. 3 d**). The broad distribution in carbon chain length was also detected for the CER[EO], ranging between 64 and 74 total carbon atoms (**Fig. 3 e**). The carbon chain length distribution for all CER[non-EO] and CER[EO] was similar in both conditions tested. Next, the level of monounsaturated CERs in four CER[non-EO] subclasses was studied, serving as an indication for the level of monounsaturated CERs in all subclasses (Helder *et al.*, submitted). This revealed that these CER[non-EO] in both FTMs have a similar percentage of monounsaturated CERs (**Supplementary fig. 3 c**). In addition, the levels of glucosylceramides (Glc-CERs) were investigated, as these are important CER precursors. These showed a variability in their presence based on the two-dimensional ion plot (**Supplementary fig. 3 d**). Calculation of the

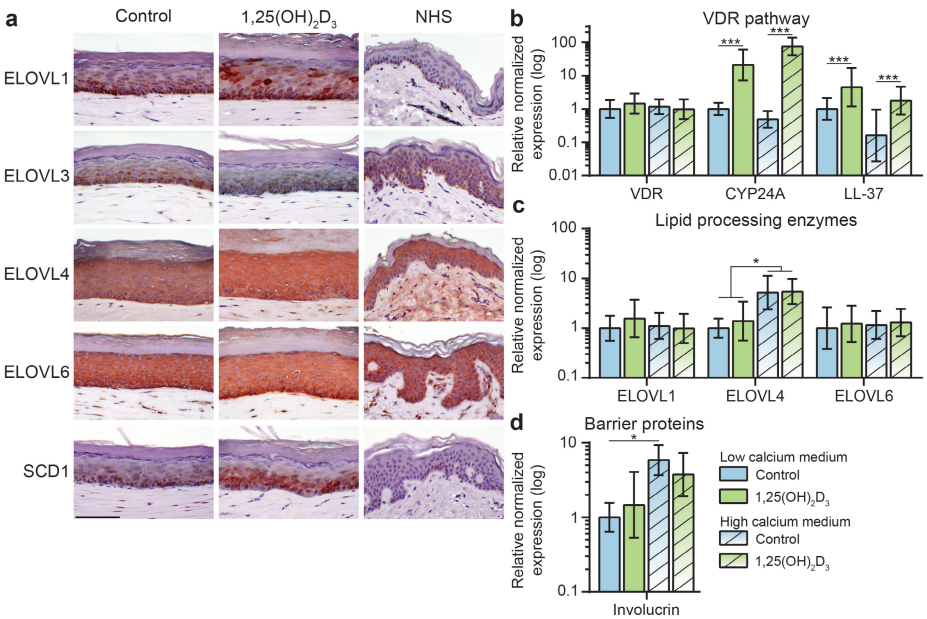


Figure 2. Lipid processing enzyme expression after addition of 20 nM 1,25(OH)$_2$D$_3$. (a) Representative images show the expression and localization of lipid processing enzyme which are involved in elongation (ELOVL1, 3, 4, 6) or desaturation (SCD1) of SC barrier lipids in FTMs and NHS. Enzymes are shown in red and nuclei in blue, scale bar indicates 100 µm. **(b-d)** Expression profiles of **(b)** genes involved in the VDR pathway, **(c)** lipid processing enzymes, and **(d)** skin barrier proteins in keratinocyte monocultures. Gene expression was determined after supplementation with 1,25(OH)$_2$D$_3$ or vehicle in low or high calcium medium. Data represents mean ± SD, N=3.

glucosylceramide index revealed that $1,25(OH)_2D_3$ supplementation did lead to reduction in the amount of Glc-CERs, showing a difference in the lipid precursors of the SC lipid matrix barrier formation after $1,25(OH)_2D_3$ supplementation (**Supplementary fig. 3 e**).

3.4. Intercorneocyte lipid organization

Analysis of the barrier formation in FTM-control and FTM-$1,25(OH)_2D_3$ continued with assessment of the lipid organization in the SC (**Fig. 4 a, b**). The lipid lamellae in the SC can be organized in either the long periodicity phase (LPP) or the short periodicity phase (SPP) (**Fig. 4 c**). In the direction perpendicular to the lamellar stacking within the lipid matrix, the lipids are arranged in a lateral

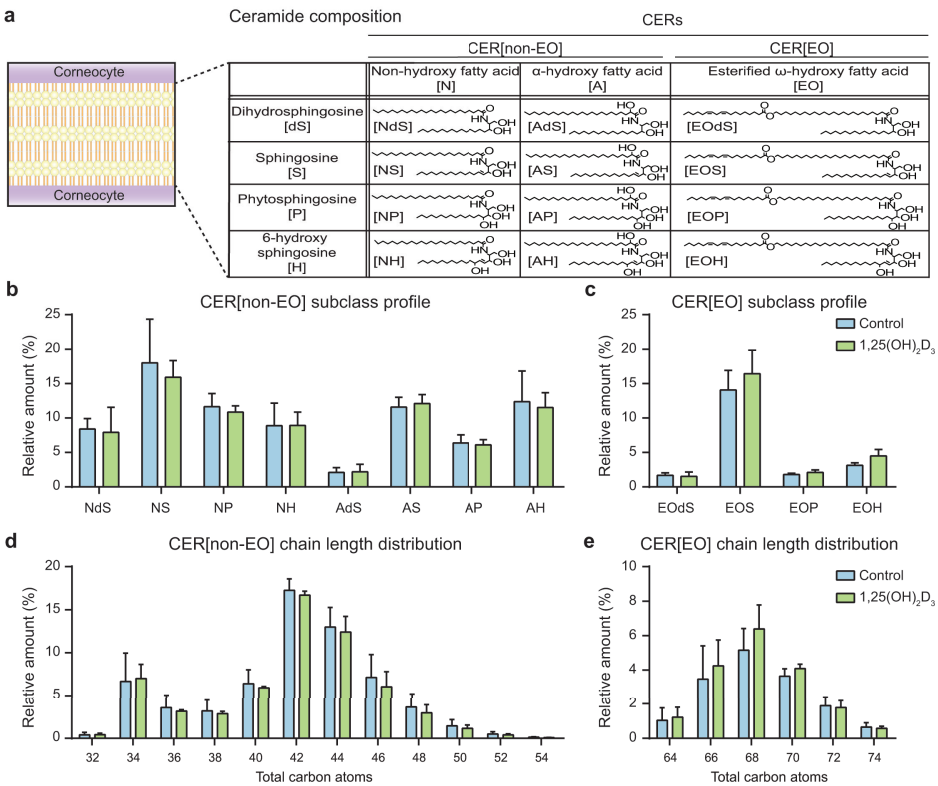


Figure 3. Ceramide composition in the lipid matrix of the stratum corneum in FTM-control and FTM-$1,25(OH)_2D_3$. (a) Schematic overview of the lipids in the intercorneocyte space. Tabular overview provides structural formulas of the twelve most abundant ceramide subclasses with nomenclature according to Motta *et al.* [41]. **(b)** Bar plot showing CER[non-EO] subclass profiles. **(c)** Bar plot showing CER[EO] subclass profiles. Subclass profiles are shown in relative abundance as percentage of total AUC/ISTD of CERs. **(d)** Bar plot of CER[non-EO] carbon chain length distributions. **(e)** Bar plot of CER[EO] carbon chain length distributions. Carbon chain length distributions are presented in relative abundance as percentage of total AUC/ISTD of CERs. A concentration of 20 nM $1,25(OH)_2D_3$ was added. All data indicates mean + SD, N=4.

organization **(Fig. 4 d)**. In the orthorhombic lateral packing, the hydrocarbon chains of the lipids form the most dense packing. The hexagonal lateral packing is characterized by a less dense packing, enabling lipid rotation along their axis. SAXD was utilized to determine the repeat distance of the lamellar phases **(Fig. 4 e)**. In the diffraction pattern of FTM-control and FTM-1,25$(OH)_2D_3$ a series of peaks were observed demonstrating the presence of the LPP with similar repeat distances, although this distance is shorter than that observed in NHS [39] **(Fig. 4 g)**. An additional phase was observed in the representative profiles, although inconsistently throughout the batches for both the FTM-control and FTM-1,25$(OH)_2D_3$, indicating no induction or aggravation of aberrant phase formation by 1,25$(OH)_2D_3$. As compared to NHS, no diffraction peaks attributed to the SPP were observed. The lateral organization was examined using Fourier transform infrared spectroscopy (FTIR). Methylene rocking vibrations are detected which consists of two peaks at 720 cm^{-1} and 730 cm^{-1} when lipids adopt an orthorhombic packing, whereas only a single peak at 720 cm^{-1} is detected when lipids adopt a hexagonal packing **(Fig. 4 f)**. The predominant hexagonal lateral packing was observed in all FTMs, irrespective supplementation with 1,25$(OH)_2D_3$ **(Fig. 4 h)**. In NHS, the lipids were arranged predominantly in the orthorhombic lateral organization, which remained present even at 40°C.

4. Discussion

In this study, we aimed to unravel the effects of 1,25$(OH)_2D_3$ on epidermal morphogenesis and lipid barrier formation during *in vitro* development of human skin equivalents. In the present report, we showed that addition of 1,25$(OH)_2D_3$ in the cell culture medium activated the vitamin D signalling pathway, although this did not affect epidermal morphogenesis in FTMs. Moreover, the lipid barrier formation remained comparable for the ceramide composition and lipid organization.

The similar proliferation rate and the unaltered expression of involucrin in FTM-1,25$(OH)_2D_3$ as compared to FTM-control are of specific interest. A similar proliferation rate was not observed in monocultures of keratinocytes [44]. However, anti-proliferative effects were reported in 2D keratinocyte cultures, whereas in this study 3D models with a supportive viable dermal equivalent were used. Furthermore, additional explanations on the diverge results on proliferation could be either the high calcium concentration in the FTM culture medium (±1.43 mM) [45] or the occurrence of 1,25$(OH)_2D_3$ catabolism over time mediated by increased CYP24A gene expression [46, 47]. The expression of the structural protein involucrin, with a VDRE in the promoter region, was shown to be upregulated after 1,25$(OH)_2D_3$ supplementation before in monocultures of keratinocytes [48] [49]. Our keratinocyte monocultures showed upregulated

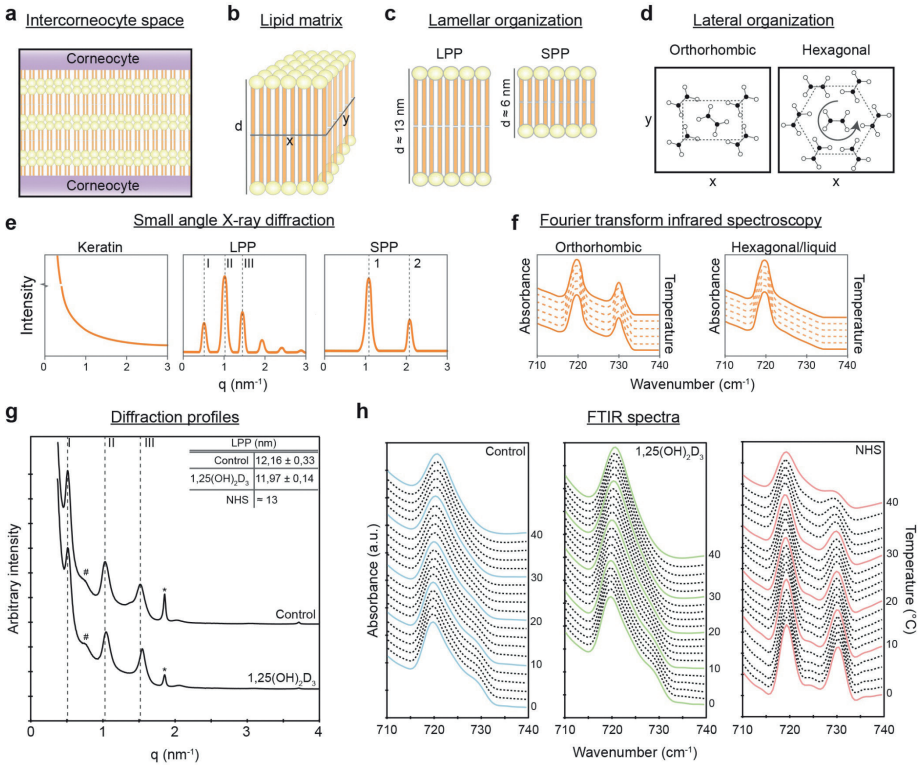


Figure 4. Intercorneocyte lipid matrix organization. (a) Schematic overview of the intercorneocyte space in the stratum corneum. **(b)** Three-dimensional schematic overview of the lipid matrix in the intercorneocyte space. Lipids are drawn in hairpin conformation, although lipids could also adapt the extended conformation [42, 43]. **(c)** Schematic simplified overview of the lamellar organization of the lipid matrix. The long periodicity phase (LPP) has an approximate repetition distance (d) of 13 nm and the short periodicity phase (SPP) has an approximate d of 6 nm [39]. **(d)** Schematic presentation of hydrocarbon chains in the lateral organization. In the orthorhombic organization, lipids form the most dense packing. The hexagonal organization is characterized by a dense packing, with equal density in plane perpendicular to the hydrocarbon chains enabling lipids to rotate along their axis [16]. **(e)** Concepts of Small Angle X-ray Diffraction (SAXD) plots of isolated keratin, LPP and SPP. Diffraction profiles are generated by plotting the scattering intensity (arbitrary unit) as a function of the scattering vector q (in nm-1). **(f)** Principles of Fourier Transform Infrared Spectroscopy (FTIR) profiles in the methylene rocking vibration spectrum. In the orthorhombic lateral packing, the spectrum in the rocking vibration region consists of two peaks located at 720 and 730 cm^{-1}. In contrast, in the hexagonal lateral packing the spectrum in the rocking vibration regions consist of one peak at 720 cm^{-1}. **(g)** SAXD profiles of FTM-control and of FTM-1,25$(OH)_2D_3$. Representative diffraction pattern in which the first, second and third diffraction order of the long periodicity phase (LPP) are indicated by the dotted line with Roman numbers (I, II, and III). Phase separated crystalline cholesterol is indicated by the asterisk (*), whereas phase separated lipids of unknown origin are indicated by the number sign (#). Inset provides tabular overview of repeat distances of the LPP, indicated for FTMs and for NHS by mean ± SD, N=4 [39]. **(h)** Representative FTIR spectra of the methylene rocking vibrational mode of lipids. Spectra are shown for FTM-control, FTM-1,25$(OH)_2D_3$ and of NHS. In the rocking vibration region of the spectrum in both FTMs a single peak at 720 cm^{-1} was detected , whereas in NHS two peaks were detected. A concentration of 20 nM 1,25$(OH)_2D_3$ was added.

involucrin gene expression after high calcium treatment, but no additional effect was observed after 1,25$(OH)_2D_3$ supplementation. Furthermore, no altered involucrin protein expression was detected in FTM-1,25$(OH)_2D_3$ as compared to FTM-control. This partial discrepancy to literature could be explained by lack of synergic effects of high calcium and 1,25$(OH)_2D_3$ supplementation during longer incubation periods, as reported before [48, 50, 51]. Besides, involucrin is expressed in FTMs in the stratum granulosum and stratum spinosum, which contrasts with the restricted expression in the stratum granulosum in NHS, contributing to high level of complexity interpreting the result for this protein. Other interactions between calcium and vitamin D signalling pathways are discussed elsewhere [32, 52]. Based on these interactions and similar effects, the calcium pathway is suggested as the major factor minimizing the effectiveness of 1,25$(OH)_2D_3$ supplementation in 3D models. Alternatively, activation of distinct signalling transduction pathways by 1,25$(OH)_2D_3$ involving other nuclear receptors expressed by keratinocytes and fibroblasts could occur [53, 54]. Additionally, the activation of vitamin D by alternative pathways forming structurally different but potent metabolites have been suggested [55-57]. Phenotypic characteristics of proliferation and differentiation are often difficult to link to a single signalling pathway or metabolite due to the myriad overlapping and intercommunication pathways. Further preclinical studies using a phenotypic relevant model need to be performed to disentangle this.

The barrier formation was studied before by Oda *et al.* [4] in submerged monocultures of keratinocytes, in which the ELOVL3, ELOVL4, and UGCG expression and/or activity was altered after VDR or VDR co-activator knockdown. However, supportive effects on ELOVL expression were not observed in this study after activation of VDR signalling pathway or UV exposure in 3D HSEs. The comparable epidermal location of ELOVL 3, 4 and 6 proteins was observed in HSEs, irrespective of supplementation. Furthermore, the equal ceramide chain length distribution profiles of FTM-1,25$(OH)_2D_3$ and FTM-control supports similar ELOVL functionality after VDR activation *in vitro*. As compared to NHS, ELOVL1 is more expressed in HSEs. This is ascribed to its role in elongation of monounsaturated lipids, which are more present in HSEs and are associated with the elevated expression of SCD1 [21].

The reduced presence of Glc-CERs in the SC of FTM-1,25$(OH)_2D_3$ is linked to the modified Glc-CER content observed after VDR knockdown [4]. This suggests an important role of VDR in the regulation of Glc-CER formation and adds another layer of significance on the interplay between 1,25$(OH)_2D_3$ and the epidermal barrier formation. However, the barrier lipid organization remained equal in both conditions, in line with the similar CERs composition. A limitation of the ceramide composition analysis is the lack of quantification of the LC-MS data, due

to a high technical complexity in the data analysis, concomitant with analysis of the various CER[EO] esterified entities (Helder *et al.*, submitted). This leads to underestimation of the abundance of CER[EO], although the interpretations and conclusions drawn from the data are not affected by this.

Recent observations reported the upregulation of the antimicrobial defence mechanism after vitamin D culture medium supplementation in HSEs [34]. Besides, there is accumulating evidence that the activation of the vitamin D signalling pathway influences the anti-inflammatory pathway [58, 59], making the vitamin D signalling pathway of high interest regarding the immune barrier function of the skin. In this study, the increased expression of LL-37 as part of the antimicrobial defence mechanism was observed. Akiyama *et al.* [60] described that this peptide upregulates tight junction-related proteins and thereby reinforces the epidermal barrier function on protein barrier level. Various studies reported the beneficial effect of $1,25(OH)_2D_3$ supplementation of skin-resident immune cells, including dermal dendritic cells and Langerhans cells [59]. However, as the current FTMs are immune incompetent and do not contain vascular and nerve structures, the behaviour of these cell types and the link to systemic effects could not be studied. Notably, $1,25(OH)_2D_3$ addition to immune competent HSEs should therefore not be overlooked [61, 62]. This could lead to higher preclinical relevance, as vitamin D and its analogues are used in the treatment of skin diseases [8]. However, we determined the effects of $1,25(OH)_2D_3$ in co-culture of solely keratinocytes and fibroblasts, yielding novel insights in the barrier formation based on these cell types, thereby excluding effects based on immune cell (de-)activation.

In conclusion, the effect of vitamin D signalling pathway activation on the epidermal morphogenesis and barrier formation was characterized in detail based on the expression of morphogenesis biomarkers and lipid processing enzymes and extensive profiling of the lipid composition and organization. This revealed no major differences after addition of $1,25(OH)_2D_3$ to the cell culture medium of FTMs, mainly ascribed to high calcium levels in the culture medium. These novel insights provide valuable information about the influence of culture medium and environmental factors on the barrier formation in HSEs, which are important in the reconstruction of skin models mimicking physiological or pathophysiological conditions.

5. Acknowledgements

This research was financially supported by Dutch Technology Foundation STW (grant no. 13151), which is part of the Netherlands Organisation for Scientific Research (NWO), and is partly funded by the Dutch Ministry of Economic Affairs. The authors would like to thank the personnel at the DUBBLE beam line (BM26) at the European synchrotron radiation facility for their support with the SAXD measurements. Samira Absalah is thanked for her support with the lipid extraction and the liquid chromatography coupled to mass spectrometry run. Pieter Voskamp is thanked for his contribution with UV irradiation of HSEs. We thank the company Evonik (Essen, Germany) for their generous provision of CERs.

6. Conflict of interest

The authors have declared no conflicting interests.

7. References

1. Niehues, H., et al., 3D skin models for 3R research: The potential of 3D reconstructed skin models to study skin barrier function. Experimental Dermatology, 2018. **27**(5): p. 501-511.
2. Slominski, A.T., et al., Sensing the environment: regulation of local and global homeostasis by the skin's neuroendocrine system. Advances in anatomy, embryology, and cell biology, 2012. **212**: p. v-115.
3. Slominski, A.T., et al., How UV Light Touches the Brain and Endocrine System Through Skin, and Why. Endocrinology, 2018. **159**(5): p. 1992-2007.
4. Oda, Y., et al., Vitamin D receptor and coactivators SRC2 and 3 regulate epidermis-specific sphingolipid production and permeability barrier formation. J Invest Dermatol, 2009. **129**(6): p. 1367-78.
5. Hill, N., et al., 1α, 25-Dihydroxyvitamin D 3 and the vitamin D receptor regulates ΔNp63α levels and keratinocyte proliferation. Cell death & disease, 2015. **6**(6): p. e1781.
6. Lehmann, B., K. Querings, and J. Reichrath, Vitamin D and skin: new aspects for dermatology. Experimental Dermatology, 2004. **13**(s4): p. 11-15.
7. Bikle, D.D., Vitamin D and the skin: Physiology and pathophysiology. Reviews in endocrine & metabolic disorders, 2012. **13**(1): p. 3-19.
8. Reichrath, J., et al., Targeting the vitamin D endocrine system (VDES) for the management of inflammatory and malignant skin diseases: An historical view and outlook. Reviews in Endocrine and Metabolic Disorders, 2016. **17**(3): p. 405-417.
9. Candi, E., R. Schmidt, and G. Melino, The cornified envelope: a model of cell death in the skin. Nat Rev Mol Cell Biol, 2005. **6**(4): p. 328-340.
10. Jackson, B., et al., Late cornified envelope family in differentiating epithelia—response to calcium and ultraviolet irradiation. Journal of Investigative Dermatology, 2005. **124**(5): p. 1062-1070.
11. Brandner, J.M., M. Haftek, and C.M. Niessen, Adherens junctions, desmosomes and tight junctions in epidermal barrier function. Open Dermatol J, 2010. **4**: p. 14-20.
12. Haftek, M., et al., Compartmentalization of the human stratum corneum by persistent tight junction-like structures. Experimental dermatology, 2011. **20**(8): p. 617-621.
13. Yokouchi, M., et al., Epidermal cell turnover across tight junctions based on Kelvin's tetrakaidecahedron cell shape. eLife, 2016. **5**: p. e19593.
14. Trommer, H. and R. Neubert, Overcoming the stratum corneum: the modulation of skin penetration. Skin pharmacology and physiology, 2006. **19**(2): p. 106-121.
15. Van Smeden, J., et al., The important role of stratum corneum lipids for the cutaneous barrier function. Biochimica et Biophysica Acta (BBA)-Molecular and Cell Biology of Lipids, 2014. **1841**(3): p. 295-313.
16. Boncheva, M., F. Damien, and V. Normand, Molecular organization of the lipid matrix in intact Stratum corneum using ATR-FTIR spectroscopy. Biochimica et Biophysica Acta (BBA) - Biomembranes, 2008. **1778**(5): p. 1344-1355.
17. Groen, D., et al., Is an orthorhombic lateral packing and a proper lamellar organization important for the skin barrier function? Biochimica et Biophysica Acta (BBA) - Biomembranes, 2011. **1808**(6): p. 1529-1537.
18. Mojumdar, E.H., et al., Monounsaturated fatty acids reduce the barrier of stratum corneum lipid membranes by enhancing the formation of a hexagonal lateral packing. Langmuir, 2014. **30**(22): p. 6534-6543.
19. Damien, F. and M. Boncheva, The Extent of Orthorhombic Lipid Phases in the Stratum Corneum Determines the Barrier Efficiency of Human Skin In Vivo. Journal of Investigative Dermatology, 2010. **130**(2): p. 611-614.
20. Wertz, P.W. and B. van den Bergh, The physical, chemical and functional properties of lipids in the skin and other biological barriers. Chemistry and Physics of Lipids, 1998. **91**(2): p. 85-96.
21. Kihara, A., Synthesis and degradation pathways, functions, and pathology of ceramides and epidermal acylceramides. Prog Lipid Res, 2016. **63**: p. 50-69.
22. Breiden, B. and K. Sandhoff, The role of sphingolipid metabolism in cutaneous permeability barrier formation. Biochim Biophys Acta, 2014. **1841**(3): p. 441-52.
23. Feingold, K.R. and P.M. Elias, Role of lipids in the formation and maintenance of the cutaneous permeability barrier. Biochim Biophys Acta, 2014. **1841**(3): p. 280-94.
24. Rabionet, M., K. Gorgas, and R. Sandhoff, Ceramide synthesis in the epidermis. Biochim Biophys Acta, 2014. **1841**(3): p. 422-34.

25. El Ghalbzouri, A., et al., Fibroblasts facilitate re-epithelialization in wounded human skin equivalents. Laboratory investigation, 2004. **84**(1): p. 102-112.
26. Thakoersing, V.S., et al., Unraveling Barrier Properties of Three Different In-House Human Skin Equivalents. Tissue Engineering Part C: Methods, 2011. **18**(1): p. 1-11.
27. Mathes, S.H., H. Ruffner, and U. Graf-Hausner, The use of skin models in drug development. Advanced Drug Delivery Reviews, 2014. **69-70**: p. 81-102.
28. Thakoersing, V.S., et al., Increased Presence of Monounsaturated Fatty Acids in the Stratum Corneum of Human Skin Equivalents. J Invest Dermatol, 2013. **133**(1): p. 59-67.
29. Oda, Y., et al., Differential role of two VDR coactivators, DRIP205 and SRC-3, in keratinocyte proliferation and differentiation. J Steroid Biochem Mol Biol, 2007. **103**(3-5): p. 776-80.
30. Oda, Y., et al., Two distinct coactivators, DRIP/mediator and SRC/p160, are differentially involved in vitamin D receptor transactivation during keratinocyte differentiation. Mol Endocrinol, 2003. **17**(11): p. 2329-39.
31. Bikle, D.D. and S. Pillai, Vitamin D, Calcium, and Epidermal Differentiation*. Endocrine Reviews, 1993. **14**(1): p. 3-19.
32. Bikle, D.D., Vitamin D Metabolism and Function in the Skin. Molecular and cellular endocrinology, 2011. **347**(1-2): p. 80-89.
33. El Ghalbzouri, A., et al., Replacement of animal-derived collagen matrix by human fibroblast-derived dermal matrix for human skin equivalent products. Biomaterials, 2009. **30**(1): p. 71-78.
34. Haisma, E.M., et al., Inflammatory and Antimicrobial Responses to Methicillin-Resistant Staphylococcus aureus in an In Vitro Wound Infection Model. PLoS ONE, 2013. **8**(12): p. e82800.
35. Mieremet, A., et al., Improved epidermal barrier formation in human skin models by chitosan modulated dermal matrices. PLOS ONE, 2017. **12**(3): p. e0174478.
36. Voskamp, P., et al., Rapamycin impairs UV induction of mutant-p53 overexpressing cell clusters without affecting tumor onset. International Journal of Cancer, 2012. **131**(6): p. 1267-1276.
37. Mieremet, A., et al., Recapitulation of Native Dermal Tissue in a Full-Thickness Human Skin Model Using Human Collagens. Tissue Engineering Part A, 2018. **24**(11-12): p. 873-881.
38. Sakai, S., et al., Characteristics of the epidermis and stratum corneum of hairless mice with experimentally induced diabetes mellitus. Journal of investigative dermatology, 2003. **120**(1): p. 79-85.
39. Bouwstra, J.A., et al., Structural Investigations of Human Stratum Corneum by Small-Angle X-Ray Scattering. Journal of Investigative Dermatology, 1991. **97**(6): p. 1005-1012.
40. Boiten, W., et al., Quantitative analysis of ceramides using a novel lipidomics approach with three dimensional response modelling. Biochimica et Biophysica Acta (BBA) - Molecular and Cell Biology of Lipids, 2016. **1861**(11): p. 1652-1661.
41. Motta, S., et al., Ceramide composition of the psoriatic scale. Biochimica et Biophysica Acta (BBA)-Molecular Basis of Disease, 1993. **1182**(2): p. 147-151.
42. Vávrová, K., A. Kováčik, and L. Opálka, Ceramides in the skin barrier. Acta Facultatis Pharmaceuticae Universitatis Comenianae, 2017. **64**(2): p. 28-35.
43. Iwai, I., et al., The human skin barrier is organized as stacked bilayers of fully extended ceramides with cholesterol molecules associated with the ceramide sphingoid moiety. Journal of Investigative Dermatology, 2012. **132**(9): p. 2215-2225.
44. Smith, E.L., N.C. Walworth, and M.F. Holick, Effect of 1α,25-Dihydroxyvitamin D3 on the Morphologic and Biochemical Differentiation of Cultured Human Epidermal Keratinocytes Grown in Serum-Free Conditions. Journal of Investigative Dermatology, 1986. **86**(6): p. 709-714.
45. Gniadecki, R., Stimulation versus Inhibition of Keratinocyte Growth by 1,25-Dihydroxyvitamin D3: Dependence on Cell Culture Conditions. Journal of Investigative Dermatology, 1996. **106**(3): p. 510-516.
46. Xie, Z., et al., The Mechanism of 1, 25-Dihydroxyvitamin D3 Autoregulation in Keratinocytes. 2002. **277**(40): p. 36987-36990.
47. Moll, P.R., et al., Expression profiling of vitamin D treated primary human keratinocytes. Journal of cellular biochemistry, 2007. **100**(3): p. 574-592.
48. Bikle, D.D., et al., The Vitamin D Response Element of the Involucrin Gene Mediates its Regulation by 1,25-Dihydroxyvitamin D3. Journal of Investigative Dermatology, 2002. **119**(5): p. 1109-1113.
49. Su, M.J., et al., 1,25-Dihydroxyvitamin D3 potentiates the keratinocyte response to calcium. J Biol Chem, 1994. **269**(20): p. 14723-9.
50. Bikle, D., Vitamin D: Production, metabolism, and mechanisms of action, in Endotext [Internet]. 2017, MDText. com, Inc.
51. Bikle, D.D., Vitamin D regulated keratinocyte differentiation. Journal of cellular biochemistry, 2004. **92**(3): p. 436-444.

52. Bikle, D.D., Y. Oda, and Z. Xie, Calcium and 1,25(OH)2D: interacting drivers of epidermal differentiation. The Journal of Steroid Biochemistry and Molecular Biology, 2004. **89-90**: p. 355-360.
53. Slominski, A., et al., Differential and Overlapping Effects of 20,23(OH)2D3 and 1,25(OH)2D3 on Gene Expression in Human Epidermal Keratinocytes: Identification of AhR as an Alternative Receptor for 20,23(OH)2D3. Int. J. Mol. Sci., 2018. **19**(10): p. 3072.
54. Slominski, A.T., et al., Endogenously produced nonclassical vitamin D hydroxy-metabolites act as "biased" agonists on VDR and inverse agonists on RORalpha and RORgamma. J Steroid Biochem Mol Biol, 2017. **173**: p. 42-56.
55. Slominski, A.T., et al., In vivo evidence for a novel pathway of vitamin D_3 metabolism initiated by P450scc and modified by CYP27B1. FASEB journal, 2012. **26**(9): p. 3901-3915.
56. Slominski, A.T., et al., Novel activities of CYP11A1 and their potential physiological significance. The Journal of steroid biochemistry and molecular biology, 2015. **151**: p. 25-37.
57. Slominski, A.T., et al., Detection of novel CYP11A1-derived secosteroids in the human epidermis and serum and pig adrenal gland. Scientific Reports, 2015. **5**: p. 14875.
58. Bakdash, G., et al., Intradermal application of vitamin D3 increases migration of CD14+ dermal dendritic cells and promotes the development of Foxp3+ regulatory T cells. Human vaccines & immunotherapeutics, 2013. **9**(2): p. 250-258.
59. van der Aar, A.M.G., et al., Vitamin D3 targets epidermal and dermal dendritic cells for induction of distinct regulatory T cells. Journal of Allergy and Clinical Immunology, 2011. **127**(6): p. 1532-1540.e7.
60. Akiyama, T., et al., The human cathelicidin LL-37 host defense peptide upregulates tight junction-related proteins and increases human epidermal keratinocyte barrier function. Journal of innate immunity, 2014. **6**(6): p. 739-753.
61. Kosten, I.J., et al., MUTZ-3 derived Langerhans cells in human skin equivalents show differential migration and phenotypic plasticity after allergen or irritant exposure. Toxicology and applied pharmacology, 2015. **287**(1): p. 35-42.
62. Vidal, S.E.L., et al., 3D biomaterial matrix to support long term, full thickness, immuno-competent human skin equivalents with nervous system components. Biomaterials, 2018.
63. van Smeden, J., et al., In-situ visualization of glucocerebrosidase in human skin tissue: Zymography vs activity-based probe labeling. Journal of lipid research, 2017: p. jlr. M079376.
64. Drongelen, V., et al., Reduced filaggrin expression is accompanied by increased Staphylococcus aureus colonization of epidermal skin models. Clinical & Experimental Allergy, 2014. **44**(12): p. 1515-1524.

8. Supporting Information

8.1. Supplementary material and methods

8.1.1. Irradiation of human skin equivalents

HSEs were exposed to UV irradiation from TL-12/20W tubes (Philips, Eindhoven, The Netherlands; UVB (280–315 nm) and UVA (315–400 nm) at 0.28 mJ/cm²/sec, as described by Voskamp *et al.* [36]. Dosages ranged from 0 to 150 mJ/cm² depending on total exposure time.

8.1.2. Analysis of additional characteristics of ceramide composition

Two-dimensional ion plots were generated using the 3D plot program. The glucosylceramide index of subclasses EOS and EOH are determined by dividing the AUC values of total Glc-CER signal by that of cumulative AUC values of corresponding CER[EO], as described by van Smeden *et al.* [63]. The percentage of monounsaturated CERs for subclasses NS, NP, AS, AP was determined by calculating the cumulative AUC of each monounsaturated subclass. Then, the percentage of monounsaturated CERs was determined by division of it through the cumulative AUC value of monounsaturated and saturated ceramide subclass.

8.2. Supplementary Tables

Supplementary table 1. Specification of antibodies used for immunohistochemical and immunofluorescence staining.

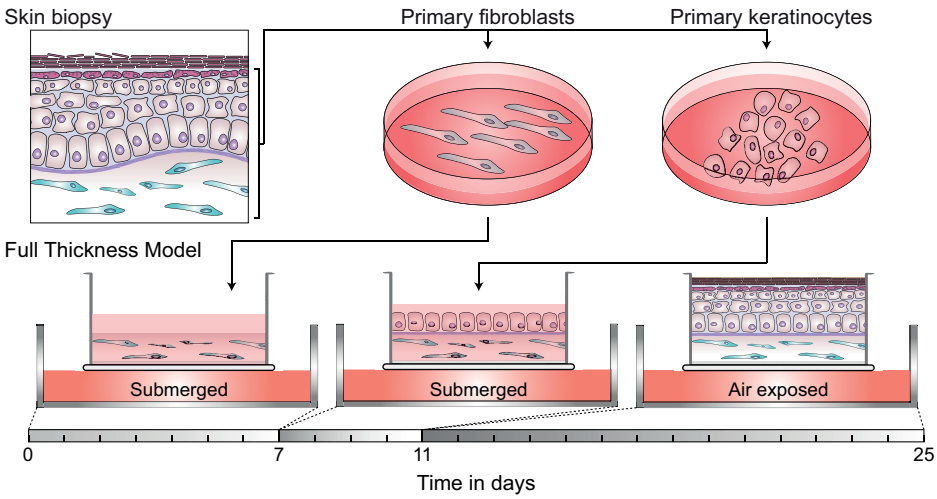
Immunohistochemistry	Material	Origin	Clone	Dilution	2nd Ab	Manufacturer
Primary antibody						
Ki67	FFPE	Mouse	MIB1	1:100	A	DAKO, Denmark
Cytokeratin 10	FFPE	Mouse	DE-K10	1:50	A	Labvision/Neomarker, USA
Involucrin	FFPE	Mouse	SY5	1:1200	A	Sanbio, The Netherlands
Cytokeratin 16	FFPE	Mouse	LL025	1:100	A	Serotec, UK
ELOVL1	FFPE	Rabbit	Poly	1:200	B	Abcam, UK
ELOVL3	FFPE	Mouse	V61 P2B3*D10	1:500	A	Novus Biologicals, USA
ELOVL4	FFPE	Rabbit	Poly	1:100	B	Abcam, UK
ELOVL6	FFPE	Rabbit	Poly	1:500	B	Abcam, UK
SCD1	FFPE	Mouse	CD.E10	1:300	A	Abcam, UK
Secondary antibody						
A) Biotinylated goat anti-mouse		Goat		1:200		Southern Biotechnology, USA
B) Biotinylated swine anti-rabbit		Swine		1:200		Southern Biotechnology, USA

Immunofluorescence		Origin	Clone	Dilution	2nd Ab	Manufacturer
Primary antibody						
Loricrin	FFPE	Rabbit	AF62	1:1000	C	Covance, The Netherlands
Filaggrin	FFPE	Rabbit	PRB417	1:1000	C	Covance, The Netherlands
Secondary antibody						
C) Cy3-conjugated anti-rabbit		Goat		1:500		Jackson immunoresearch Laboratory, USA

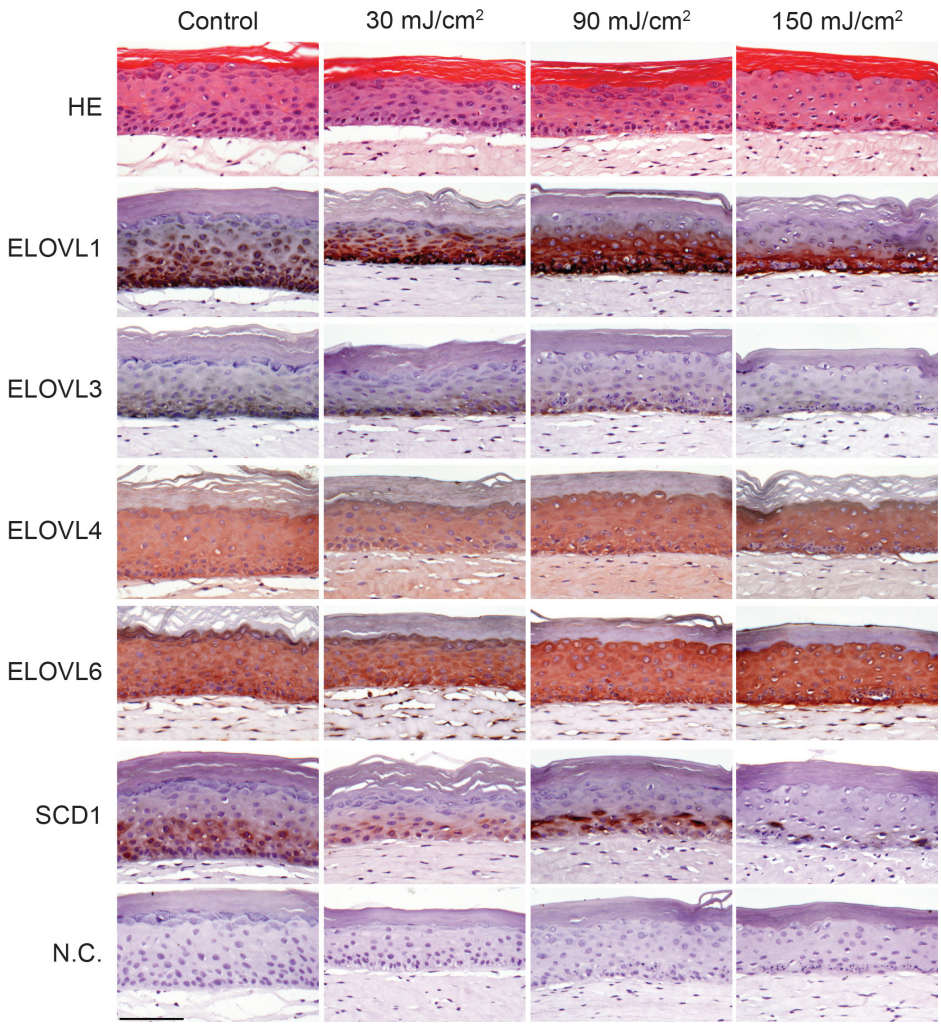
Supplementary table 2. Specifications of primer used for quantitative real-time polymerase chain reaction.

	Sequence Forward (5'à 3')	Sequence Reverse (5'à 3')	Amplicon size	Accession No.	Ref.
SDHA	AACCAAACGCTGGGGAAGAA	GGAACACGGCAGCATGATTT	126	NM_004168.3	
ZNF410	GCTGTGGTAAGCAGTTTACTACAG	CTTGGGCTTCACAAAGGAAAGG	90	NM_001242924.1	
ARCP2	TCCGGGACTACCTGCACTAC	GGTTCAGCACCTTGAGGAAG	96	NM_152862.2	
VDR	GCTCAGATCACTGTATCACCTC	AGGGTCACAGAAGGGTCATC	100	NM_000376.2	
CYP24A1	CAAGGCAACAGTTCTGGGTGA	GTCTTCACTGGATCCCAACAC	85	NM_000782.4	
LL-37	ATTTCTCAGAGCCCAGAAGC	CGGAATCTTGTACCCAGGAC	72	NM_004345.4	[34]
ELOVL1	GGAGCTCCAGGTATTGCCAAGG	AGCCGTGGTCCCTGTAGAGCA	203	NM_001256402.1	[64]
ELOVL4	TTTGGTGGAAACGATACCTGA	TTAGAGCCCAGTGCATCCAT	120	NM_022726.3	
ELOVL6	TCGGTGCTCTTCGAACTGGTGC	GTATCTCCTAGTTCGGGTGCTTTGC	154	NM_024090.2	[64]
INV	GGCCCGTCTCATCTGTGAAC	TGCTCACCTACCTGAGGTTGGGAT	132	NM_005547.3	

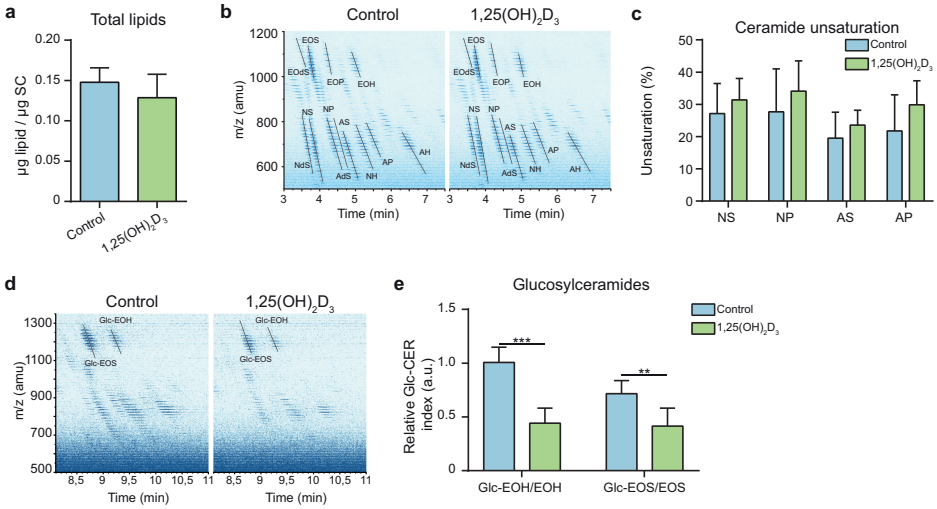
8.3. Supplementary figures



Supplementary figure 1. Generation of full thickness models. Primary cells are isolated from a skin biopsy and cultured in Petri dishes. Full thickness models are generated by seeding fibroblast in a collagen matrix, after which keratinocytes are seeded onto the dermal equivalents in submerged culture, and subsequently lifted to air exposure to induce full epidermal stratification.

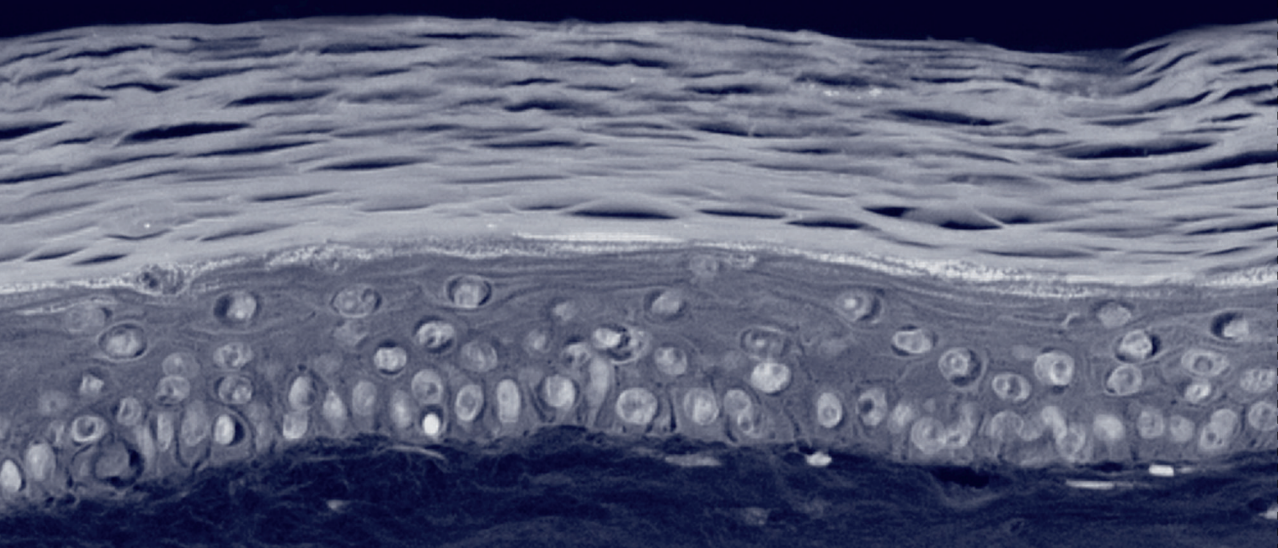


Supplementary figure 2. Lipid processing enzyme expression in FTMs irradiated with UV-B. Expression of lipid processing enzymes which are involved in elongation (ELOVL1, 3, 4, 6) or desaturation (SCD1) of epidermal barrier lipids. Models were fixated 24 hr after irradiation with indicated UV-B dosage. Enzymes are shown in red and nuclei in blue. HE stained cross-sections are also provided. No non-specific binding of the secondary antibody was detected (negative control (N.C.)). Scale bar indicates 100 µm.



Supplementary figure 3. Additional characteristics of the lipid matrix composition. (a) Amount of total lipids present in the SC of FTM-control and FTM-1,25$(OH)_2D_3$. (b) Two-dimensional ion maps of the CER composition, as separated and detected by LC-MS. Each subclass is indicated by a line which covers all compounds. (c) Level of monounsaturated CER in the subclasses NS, NP, AS and AP. Data is shown as total AUC of monounsaturated CERs divided by total AUC of saturated and monounsaturated CERs and indicated by mean + SD, N=4. (d) Two-dimensional ion maps of the Glc-CERs after separation and detection by LC-MS. The analysed Glc-CER subclasses Glc-EOS and Glc-EOH are indicated by a line which covers all compounds. (e) Quantified values of the glucosylceramide index for subclasses Glc-EOH and Glc-EOS. Total AUC of Glc-CER is divided by the total AUC of corresponding CER subclass. Data is presented as arbitrary amount and represent mean + SD, N=4.

Part III



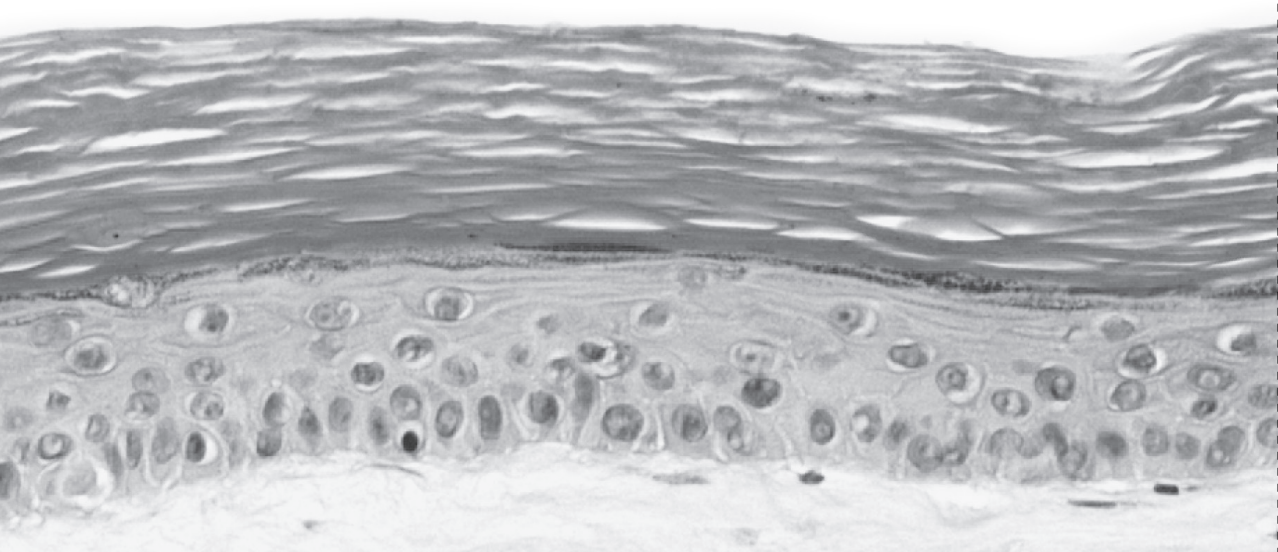
8

Contribution of palmitic acid to epidermal morphogenesis and lipid barrier formation in human skin equivalents

Arnout Mieremet[‡]
Richard Helder[‡]
Andreea Nadaban
Gert Gooris
Walter Boiten
Abdoelwaheb El Ghalbzouri[+]
Joke A. Bouwstra[+]

[‡] Authors contributed equally
[+] Joint senior authorship

Submitted



Abstract

The outermost layer of the human skin is the stratum corneum (SC), which consists of corneocytes embedded in a lipid matrix. Biosynthesis of barrier lipids occurs *de novo* in the epidermis or is performed with external derived lipids. Hence, *in vitro* developed human skin equivalents (HSEs) are supplemented with a mixture of free fatty acids (FFAs). Nevertheless, the lipid barrier formation in HSEs remains altered as compared to that of native human skin (NHS). The aim of this study is to decipher the role of medium supplemented saturated FFA palmitic acid (PA) on morphogenesis and lipid barrier formation in HSEs. Therefore, HSEs were developed with 100% (25 µM), 10%, or 1% PA in the culture medium. Morphogenesis was characterized by gene and protein analyses, SC lipid matrix composition by lipidomics analysis, and SC lipid organization by various biophysical techniques. In HSEs supplemented with reduced level of PA, the early differentiation was delayed and epidermal activation was increased. Nevertheless, similar lipid composition in the SC of HSEs was detected. Additionally, the lipid organization was comparable for lamellar and lateral organization, irrespective of PA medium concentration. As compared to NHS, the level of monounsaturated lipids was increased and the FFA tot ceramide ratio was drastically reduced in HSEs. This study describes the crucial role of PA in epidermal morphogenesis and elucidates the role of medium added PA in lipid barrier formation of HSEs, thereby expanding our knowledge on the role of supplemented lipids during generation of HSEs and providing additional insight in the differences in lipid composition between HSEs and NHS.

Keywords: Primary Cell Culture; Artificial Skin; Bioengineering; Palmitic Acid; Free Fatty Acid; Ceramide; Lipid Metabolism; Mass Spectrometry.

1. Introduction

The human skin protects the body from desiccation and environmental challenges through the establishment of a multi-layered barrier system. The main physical barrier is formed by the outermost layer of the epidermis, which is the stratum corneum (SC). This SC consists of corneocytes embedded in a lipid matrix (**Supplementary fig. 1 a-c**). The lipid matrix forms the only continuous penetration pathway through the SC. Therefore, it is crucial for the functionality of the barrier.

Sophisticated *in vitro* tools which resemble native human skin (NHS) to a high extent are three-dimensional human skin equivalents (HSEs). Therefore, these are widely applied in preclinical screenings and for research purposes to increase understanding of skin biology and epidermal barrier formation in healthy and diseased phenotypes [1-6]. HSEs mimic NHS in morphologic appearance, including the presence of distinguishable epidermal layers and formation of the SC [7, 8]. Characterization of the barrier formation in HSEs revealed similarities as well as differences compared to the barrier formation of NHS. Similarities in the SC lipid matrix between HSEs and NHS include the presence of the main lipid classes and subclasses thereof, and the presence of distinctive lipid lamellae in the intercorneocyte space [7-9]. However, differences were reported regarding the lipid composition, such as an increased level of monounsaturated lipids, a reduced chain length of free fatty acids (FFAs) and ceramides (CERs), and a different CER subclass profile [9, 10]. Changes in lipid composition coincides with a reduction in the length of the repeat distance of the long periodicity phase (LPP), as well as a lack in the formation of the short periodicity phase (SPP) (**Supplementary fig. 1 d,e**) [7, 11]. Also, the formation of a predominant hexagonal lateral organization was observed in HSEs, in contrast to a predominant orthorhombic lateral organization in NHS (**Supplementary fig. 1 f**) [8]. These compositional and organizational differences directly contribute to an impaired skin barrier, as compound penetration occurs at an elevated rate [4, 5, 7]. Although the altered composition of CERs in the SC of HSE is relatively well described [7, 9, 10, 12], there is still a need for more detailed characterization of the composition of FFA in the SC of HSEs.

For the formation of the epidermal barrier, FFAs are essential for numerous processes. Most prominent are to serve as building blocks for more complex lipids (e.g. CERs) of the lipid barrier and to contribute to the structure of the lipid matrix [13, 14]. FFAs are mainly synthesized *de novo* in the skin, although these could also be taken up from the systemic circulation originating from dietary resources [13, 15]. Both are important, since the epidermis can switch between local to systemic sources for lipid barrier repair [15, 16]. To improve the barrier

formation, it is essential to better comprehend lipid biosynthesis pathways within the HSEs.

To mimic the systemic availability of lipids, the culture medium of HSEs is supplemented with a mixture of FFAs during submerged and air-exposed phases. This mixture consists of the essential FFA linoleic acid (LA; 18:2(ω-6)), the conditionally essential FFA arachidonic acid (AA; 20:4(ω-6)), and the saturated FFA palmitic acid (PA; 16:0). These exogenous FFAs are shown to be taken up and processed in the epidermis of HSEs to become part of the SC lipid barrier [17-19]. Several studies have been performed to optimize the timepoint of supplementation, concentration, and ratio of FFAs during the development of HSEs [17, 18, 20]. These showed that supplementation with FFAs was crucial to induce the formation of lamellar bodies [20], although a fourfold increase in either PA level or in total FFA mixture in the medium during generation of HSEs did not modulate the FFA composition in SC [17]. However, too high concentrations of supplemented saturated lipids could lead to lipotoxicity, followed by induced expression of enzymes to prevent lipotoxicity and ER stress response [21, 22]. This would result in elevated stearoyl-CoA desaturase-1 (SCD-1) expression and a higher level of monounsaturated lipids [23], which is also observed in HSEs [10]. However, LA and AA are not involved in a saturated FFA lipotoxic response, which is mediated by increased expression of SCD-1 [24].

In this study, we aim to decipher the effect of PA on the epidermal morphogenesis and barrier formation of HSEs and to obtain more insights in the presence of FFAs in the SC of HSEs. To this end, we supplemented the medium with various concentrations of PA and studied the dermal and epidermal morphogenesis and lipid barrier formation of full thickness models (FTMs) and NHS. Herein, we report that the original PA supplementation concentration is most optimal for the formation of a well-ordered epidermal morphogenesis and biosynthesis of barrier lipids is similar at all levels of supplemented PA in the FTMs. Additionally, we observed a considerable reduction in the absolute amount of FFAs in the SC of FTMs as compared to that of NHS, irrespective of the PA concentration.

2. Materials and Methods

2.1. Generation of full thickness models

Surplus female breast skin tissues were obtained after mamma reduction surgeries according to declaration of Helsinki principles and are regarded in this study as NHS. Epidermis and dermis were separated after removal of adipose tissue followed by enzymatic digestion and primary cell suspensions were obtained and cultured as described before [3, 25]. Isolated primary keratinocytes and fibroblasts were tested for mycoplasma contamination using polymerase chain reaction

(PCR) analysis before further use. Generation of full thickness models occurred as described before [9]. Except for the PA content, this was reduced to 10% and 1% of the original 100% level (25 µM). FFA mixtures were coupled to the carrier molecule bovine serum albumin before supplementation to the medium. FTMs were grown for 14 days at the air-liquid interface in a Memmert INC153med CO_2 incubator (Memmert, Germany) at 37°C, 90% RH, 7.3% CO_2, atmospheric oxygen levels. HSE batches were generated from four different primary cell donors.

2.2. Immunohistochemical analyses

Sections of NHS or FTM were 24 hr fixated in 4% formaldehyde before rehydration and paraffin embedding or snap frozen for cryopreservation. Histological assessment with haematoxylin and eosin was performed according to instructions provided by the manufacturer (VWR, Breda, The Netherlands). Immunohistochemistry or indirect immunofluorescence was performed on 5 µm sliced formalin fixed paraffin embedded (FFPE) sections. After deparaffinization of the sections and rehydration, heat mediated antigen retrieval in citrate buffer (pH 6) was performed. The retrieval of collagen type IV antigen was performed by incubation with a protease solution. Non-specific antibody binding was reduced by incubation with normal human serum (Sanquin, Leiden, The Netherlands) prior to application of primary antibodies **(Supplementary table 1)**. Antigen visualisation occurred using a streptavidin-biotin-peroxidase system (GE Healthcare, Buckinghamshire, United Kingdom) according to the manufacturer's instructions, or using an indirect immunofluorescence approach as described before [9]. Imaging of the stainings was performed using a Zeiss Axioplan 2 light microscope (Carl Zeiss BV, Breda, The Netherlands) or a Leica CTR5000 fluorescence microscope (Leica, Wetzlar, Germany). Neither non-specific nor background staining of secondary antibodies were detected **(Supplementary fig. 2 a)**. Number of corneocyte layers was determined by safranin red staining and KOH expansion of the SC as described before [9, 26] **(Supplementary fig. 2 b)**. Estimations of the epidermal thickness and proliferation index were performed as reported earlier [9].

2.3. Gene expression analyses

Total RNA was extracted from the viable epidermis of FTMs or epidermis and partially attached dermis of NHS using the FavorPrep Tissue Total RNA Mini Kit (Favorgen, Ping-Tung, Taiwan) according to manufacturer's instruction. After loading of the RNA on the provided column, an additional 15 min DNA digestion step was performed by means of a RNAse-free DNAse set (Qiagen, Hilden, Germany). After RNA elution, the nucleic acid concentration was determined using a NanoDrop™ UV-Vis Spectrophotometer (ThermoFisher). Complementary DNA was synthesized from 500 ng total RNA using the iScript™ cDNA Synthesis Kit (Bio-Rad, Hercules, USA), followed by performance of quantitative real-time

polymerase chain reactions. Amplification solutions were mixed with SYBR Green Supermix (Bio-Rad), enabling signal detection on the CFX384 Touch™ (Bio-Rad). Following settings were used: polymerase activation for 5 min at 95°C, denaturation for 20 sec at 95°C, annealing for 20 sec at 60°C, and extension for 20 sec at 72°C for 40 cycles followed by the generation of a melt curve. Data was normalized against the 2-3 most stable reference genes using the ΔΔCt method. Primers sequences are listed in **supplementary table 2**.

2.4. Lipidomic analysis by LC-MS

2.4.1. Lipid extraction

The stratum corneum was isolated using trypsin digestion steps and stored until use in an inert environment as described before [27]. The lipid extraction was performed using an adapted Bligh and Dyer extraction procedure as reported by Boiten *et al.* [12]. After extraction, samples were stored under argon gas at 4°C until FFA and CER analyses were performed. Dry weight of SC was determined before and after lipid extraction using a microbalance.

2.4.2. FFA analysis

Compositional analysis by liquid chromatography-mass spectrometry (LC-MS) FFA analysis occurred as described before [27]. In short, 2 µl of 0.75 mg/ml lipid extract was injected into a Waters Acquity UPLC H-class system (Waters, Milford, MA, USA) for lipid separation using a Purospher Star LiChroCART reverse phase column (3 µm particle size, 55 x 2 mm i.d.) (Merck, Darmstadt, Germany). Detection occurred by a XEVO TQ-S mass spectrometer (Waters) measuring in negative ion mode between m/z 200 and 550 atomic mass units (amu). Data analysis was performed by Waters Masslynx 4.1. Several FFA entities were selected for analysis, including saturated FFAs (C20:0, C22:0, C24:0, C26:0, C28:0, and C30:0), monounsaturated FFAs (C16:1, C18:1, C20:1, C22:1, and C24:1), and polyunsaturated FFAs (C18:2). Quantification occurred using the areas under the curves (AUCs) by correction for the deuterated C24 as internal standard (Cambridge Isotope Laboratories, Andover, MA, USA) and for response using the calibration curves of the FFA standards (C16:1, C18:1, C18:2, C20:0, C20:1, C22:0, C22:1, C24:0, C24:1, C26:0, C28:0, and C30:0) (Sigma). Due to manufacturer's contamination of C16:0 and C18:0 in the solvents and the lack of available long chain muFFA standards, no additional FFAs were quantified.

2.4.3. CER analysis

The extracted samples were evaporated under a stream of nitrogen at 40°C and reconstituted in 95:2½:2½ (v/v/v) heptane:chloroform:methanol to a concentration of 0.3 mg/mL. After addition of the internal standard (ISTD) N(24deuterated)S(18) (Evonik industries, Essen, Germany), 5 µL of the sample was injected into the UPLC. The UPLC-MS setup consisted of an Acquity UPLC H-class coupled to an

XEVO TQ-S mass spectrometer (Waters) with an atmospheric pressure chemical ionization chamber. Detection occurred in positive ion mode measuring full scan m/z between 350 and 1200 amu. Separation of the CERs was performed on a PVA-Sil column (5 µm particles size, 100x2.1 mm i.d.) (YMC, Kyoto, Japan) as described in before [12]. Data analysis was performed with Masslynx 4.1 software. For the composition analysis, 12 CER subclasses were included (**Supplementary fig. 1 g**). For the CER[non-EO], both saturated and monounsaturated entities were included for [NdS], [NS], [NP], [NH], [AdS], [AS], [AP], and [AH]. For the CER[EO], both saturated and monounsaturated entities were included for [EOdS], [EOS], [EOP], and [EOH]. In addition, besides the linoleic acid residue (18:2) also the oleic acid residue (18:1) in CER[EO] were included as described by Helder *et al.* (submitted). Quantification of the AUCs was performed using a three dimensional response model according to the processing method described by Boiten *et al.* [12]. Corrections for the isotope overlap of the CER entities containing two ^{13}C atoms to those which only contain ^{12}C (resulting in equal mass) were performed. After the data corrections, the quantities were converted to absolute amount per mg SC.

2.5. Small angle X-ray diffraction

Small angle X-ray diffraction (SAXD) measurements were performed at the European Synchrotron Radiation Facility at station BM26B as described extensively by Mojumdar *et al.* [28]. The scattering intensity I was measured as a function of the scattering vector q. The latter is defined as $q = \frac{4 \cdot \pi \cdot \sin\theta}{\lambda}$, where θ is the scattering angle and where λ is the wavelength. From the positions of the peaks (q_n), the repeat distance was calculated using the equation $\overline{d = \frac{2n \cdot \pi}{qn}}$, where n is the order of diffraction peak. The length of the repeat unit of the lipid lamellae was determined based on the peak position of the first, second and third order of diffraction peak.

2.6. Fourier transform infrared spectroscopy

The isolated SC of NHS, $FTM_{100\%PA}$ $FTM_{10\%PA}$, and $FTM_{1\%PA}$ were hydrated during 24 hr before placement between two AgBr cells. All spectra were acquired on a Varian 670-IR spectrometer (Agilent Technologies, Santa Clara, CA, USA) equipped with a broad-band mercury cadmium telluride detector. The Fourier transform infrared spectroscopy (FTIR) spectrometer was cooled with liquid nitrogen and connected to a temperature regulating device. The spectrometer collected the data with a frequency range of 400-4000 cm^{-1}. The spectral parameters were speed 25 kHz, UDR 2, filter 6.4 and aperture 1 cm^{-1}. The measurements were performed with a 240 sec time resolution and a length of run equal to 164 min, resulting in a 1°C temperature increase per measurement between 0°C and 40°C. The spectra were analysed and deconvoluted with Varian Resolutions Pro 5.2.0. software.

2.7. Statistics

Statistical analyses were conducted using GraphPad Prism version 7.00 for Windows (GraphPad Software, La Jolla, CA, USA). Statistical testing was performed with 1-way or 2-way ANOVA with Holm-Sidak post-test tests for the effects of within FTMs. NHS versus $FTM_{100\%PA}$ was tested using unpaired student's t-test. Statistical differences are noted as *, ** or *** with lines between bars for the former and vertically above NHS for the latter comparison, corresponding to $P<0.05$, <0.01, <0.001.

3. Results

3.1. Morphological similar FTMs are generated with reduced PA levels

Full thickness models (FTMs) were developed with 100% ($FTM_{100\%PA}$), 10% ($FTM_{10\%PA}$), or 1% ($FTM_{1\%PA}$) of the original medium PA concentration (25 µM) and were compared to NHS (**Fig. 1 a**). This revealed a similar appearance in all conditions. Quantification of the thickness of the viable epidermis and number of corneocyte layers showed equal thickness of the viable epidermis and similar number of corneocyte layers in FTMs, irrespective of PA level (**Fig. 1 b,c**). As compared to NHS, the FTMs lack the epidermal rete ridges and have a thicker viable epidermis. The number of corneocyte layers was similar, despite the lack in exfoliation in FTMs. This indicates that FTMs supplemented with reduced level of PA contain a well-ordered viable epidermis.

3.2. Strong reduction in PA level leads to compromised epidermal morphogenesis

Assessments of epidermal and dermal morphogenesis were performed using protein biomarkers. The late differentiation program was unaffected by reduction in PA (loricrin, filaggrin, involucrin) (**Fig. 2 a**). As compared to NHS, involucrin was more expressed in the spinous layer, while filaggrin and loricrin were equally localized. Early differentiation was delayed in FTMs developed with reduced PA levels, most severe at 1% indicated by keratin 10 (K10) expression. Epidermal activation of the viable epidermis was found to be directly affected by PA supplementation levels (**Fig. 2 b**). Moderate K16 expression was detected in $FTM_{10\%PA}$, whereas strong K16 expression was detected in $FTM_{1\%PA}$. Nevertheless, K17 remained absent in all conditions. As compared to NHS, epidermal activation was only present *in vitro*. Another characteristic of epidermal morphogenesis is the proliferation of the viable epidermis. Biomarker Ki67 remained expressed only in the basal layer and the proliferation index was comparable in all conditions (**Fig. 2 c**). The viable epidermis is connected to the dermis via the basement membrane (BM), which was reconstructed *in vitro* in a similar proportion at all exogenous PA levels (**Fig. 2 d**). As PA is a lipid which is also bioactive in the dermis [14, 29], dermal morphogenesis was examined for fibroblast distribution

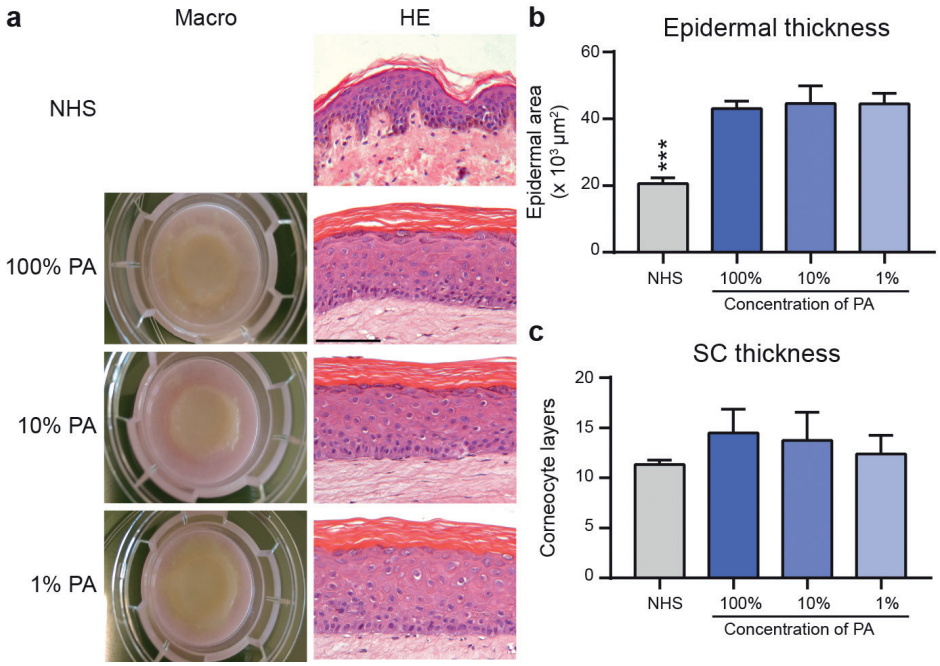


Figure 1. Generation of FTMs supplemented with reduced palmitic acid levels. (a) Macro and micro anatomy of FTMs and NHS. Histology examined after haematoxylin and eosin (HE) staining. **(b)** Quantified epidermal thickness of NHS and indicated FTMs. **(c)** Number of corneocyte layers reflects the thickness of the SC. Data represents mean + SD, N=4.

and fibroblasts subpopulations with focus on myofibroblasts (**Fig. 2 e**). Both were similar regardless of PA levels, although fibroblast distribution in FTMs was more continuous and not divided in a papillary and reticular dermal zone as in NHS.

3.3. Considerable reduction of the FFA abundance in the SC of FTMs remained similar at various PA levels

We then evaluated the lipid barrier formation in the FTMs by examination of the SC lipid composition. A similar amount of extracted lipids was observed in all FTMs and NHS (**Fig. 3 a**). The composition of free fatty acids (FFAs) was determined using the LC-MS FFA analysis (**Supplementary fig. 3 a**). The absolute amount of FFAs remained similar despite the reduction in supplemented PA (**Fig. 3 b**). As compared to NHS, a substantial reduction in level of FFAs was observed. The reduction in absolute amount of FFAs is mainly ascribed to the reduced presence of saturated FFAs (saFFAs) with a carbon (C) chain length of ≥C23:0 (**Fig. 3 c**). The absolute amount of short chain monounsaturated FFA (muFFA) C16:1 and C18:1 was similar in FTMs and NHS, whereas the long chain muFFAs ≥C22:1 were more abundant in FTMs (**Fig. 3 d**). The polyunsaturated FFA C18:2 was substantially reduced in FTMs as compared to NHS (**Fig. 3 e**).

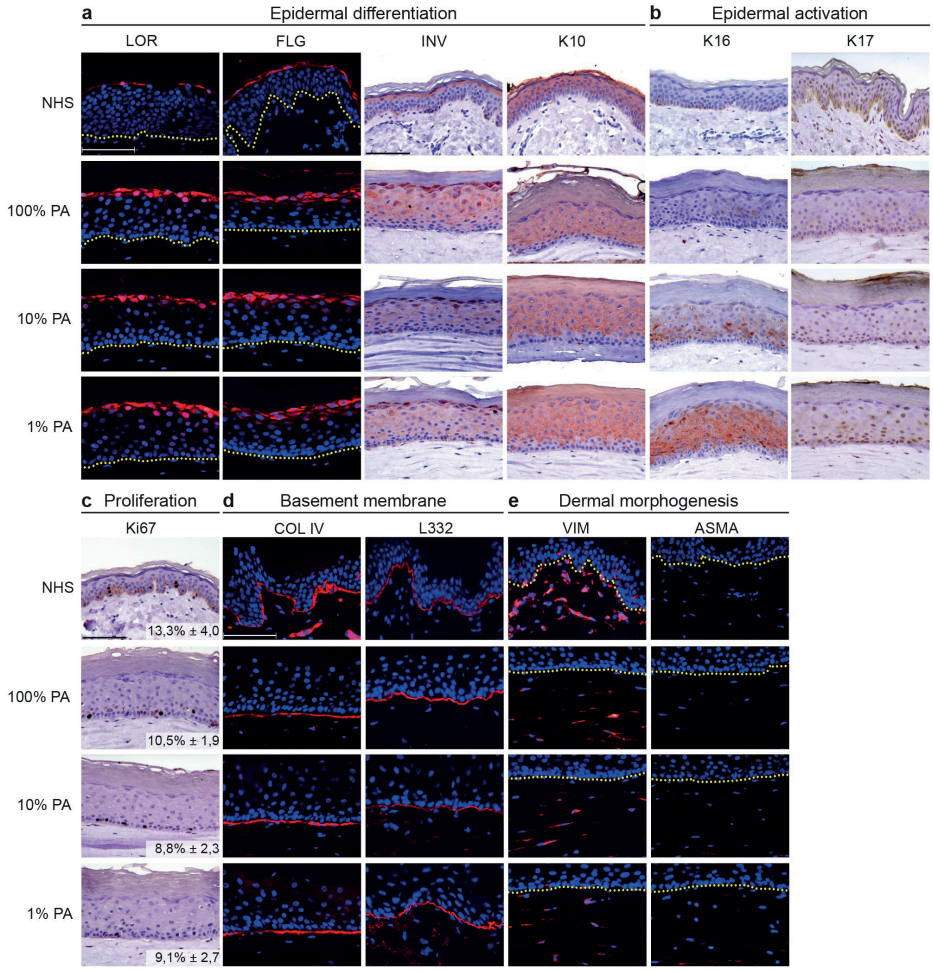


Figure 2. Morphogenesis of FTMs supplemented with various PA levels. Expression of protein biomarkers in NHS and FTMs of **(a)** late or terminal (loricrin, involucrin, filaggrin) and early differentiation (keratin 10), **(b)** epidermal activation (keratin 16 and keratin 17), **(c)** proliferation (Ki67) with indicated proliferation index (mean ± SD, N=4), **(d)** dermal-epidermal junction (collagen type IV and laminin 332), and **(e)** fibroblasts distribution (vimentin) and fibroblasts stress signalling (alpha smooth muscle actin). Nuclei are counterstained blue using haematoxylin or DAPI, yellow dotted line indicates dermal-epidermal junction. Scale bar indicates 100 µm.

The absolute quantities were used to calculate the relative amount of FFAs. No difference in the relative saFFA and muFFA composition was observed between the $FTM_{100\%PA}$, $FTM_{10\%PA}$, and $FTM_{1\%PA}$. When comparing the FTMs with NHS, differences in saFFA and muFFA composition were observed (**Fig. 3 f, g**). In contrast to NHS, in the SC of FTMs there was a higher relative level of FFA C20:0 and C22:0, which was counterbalanced by a reduced relative abundance of FFA with chain length ≥C25:0. The FFA C24:0 remained the most abundant FFA in the

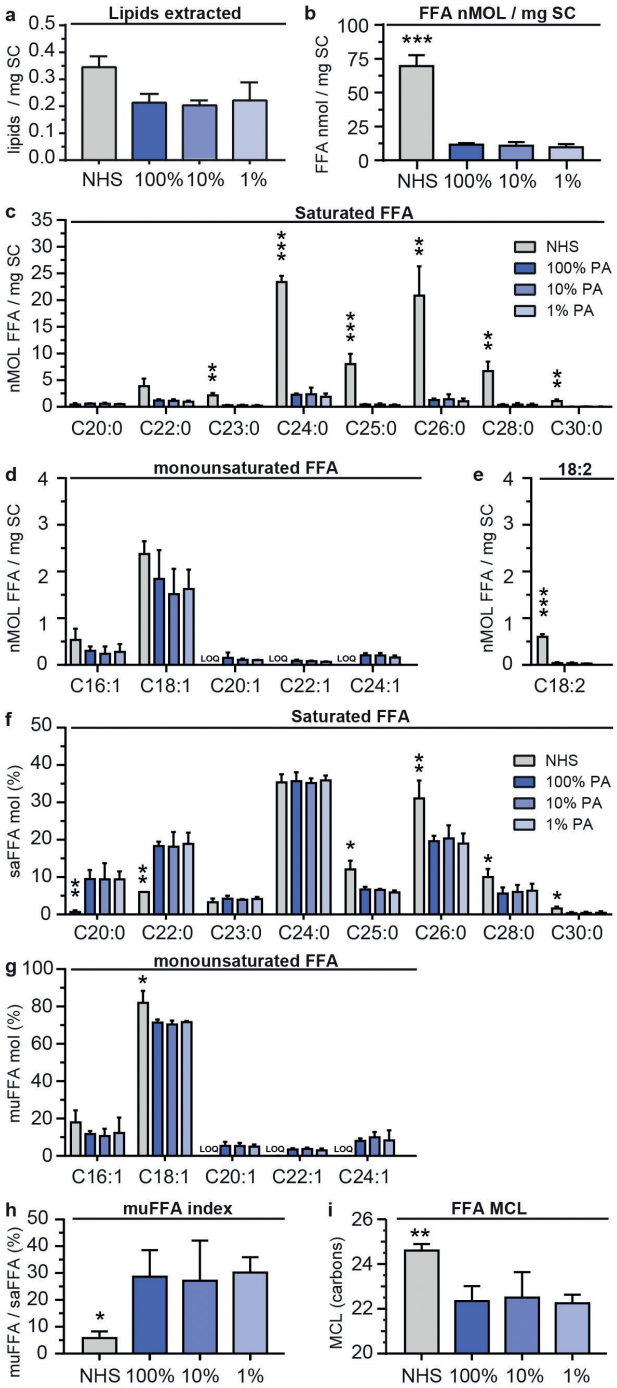


Figure 3. FFA composition in the SC of NHS and in FTM supplemented with different PA levels. **(a)** Extracted lipids were plotted per mg SC of NHS and the FTMs supplemented with 100%, 10% or 1% PA. **(b)** Absolute amount of FFAs in the SC of NHS and of indicated FTMs. **(c)** Bar diagram of the saturated FFA profile as presented in absolute amount. **(d)** Bar diagram of the monounsaturated FFA profile as presented as absolute amount. **(e)** Bar diagram of the polyunsaturated FFA C18:2 per mg SC. **(f)** Relative amount of saturated FFAs in the SC of NHS and FTMs. **(g)** Relative amount of monounsaturated FFAs in the SC of NHS and FTMs. **(h)** The level of monounsaturated FFAs as percentage of total FFAs. All data for NHS, FTM$_{100\%PA}$, FTM$_{10\%PA}$, and FTM$_{1\%PA}$. **(i)** Bar diagram of the mean carbon chain length of FFAs. Data represents mean + SD, N=3. LOQ indicates below limit of quantification. Significance indicated by * = P<0.05, ** P<0.01, *** = P<0.001.

SC of both FTMs and of NHS. Regarding the relative abundance of muFFAs, in the SC of FTMs there was a higher level of C20:1, C22:1, and C24:1, which reduced the relative abundance of C18:1, in agreement with the observations of the absolute level of muFFAs (**Fig. 3 g**).

The differences between the FFA composition of NHS and FTMs were also reflected in the muFFA index. This index displays the level of monounsaturated FFAs as percentage of all FFAs. A considerable increase in muFFA content in the SC was detected in FTMs as compared to NHS (**Fig. 3 h**). In addition, the mean carbon chain length (MCL) of the FFAs was also reduced in FTMs as compared to NHS (**Fig. 3 i**).

Our quantified LC-MS FFA analysis did not include FFA C16:0 and C18:0 due to manufacturer's contamination of C16:0 and C18:0 in the solvents, and very long chain muFFAs C26:1 and C28:1 due to the absence of these FFA standards. To still provide an indication on the presence of these FFAs, we analysed the AUC and corrected these for the internal standard (ISTD) and contamination, followed by plotting the relative amount. First, we observed FFA C16:0 and C18:0 at a similar (C16:0) and higher (C18:0) level in the FTMs as compared to NHS (**Supplementary fig. 4 a**). Second, we observed that the muFFAs C26:1 and C28:1 are present in higher quantities in the SC of FTMs as compared to that of NHS (**Supplementary fig. 4 b**), in line with previous observations [10]. This indicates that there are more short chain FFAs present in FTMs and it implies that the muFFA index obtained with the quantified FFA data is understating the fraction of muFFAs in the SC of FTMs.

These results indicate that variations in supplemented PA lead to a similar FFA composition, although there are substantial differences between the FFA profiles of NHS and FTMs.

3.4. Variations in supplemented PA does not alter the composition of ceramides in the stratum corneum

As FFAs serve as building blocks for CERs, we assessed whether reduction in PA could affect the composition of CERs. The CER lipidomic analysis revealed the presence of all major subclasses in NHS and the FTMs on the LC-MS ion maps (**Supplementary fig. 3 b**). In FTMs, an increased presence of CERs with a mass lower than 600 atomic mass units was detected, which is a premature indication for an altered CER composition. The CER data was quantified to absolute amounts per mg of SC. This revealed a similar absolute amount of CERs in all FTMs, although the level of CER per mg of SC in NHS was significantly lower (**Fig. 4 a**). Since the absolute amount of FFA per mg of SC was also calculated (**Fig.3 b**), this provided an unique opportunity to calculate the ratio between FFAs and

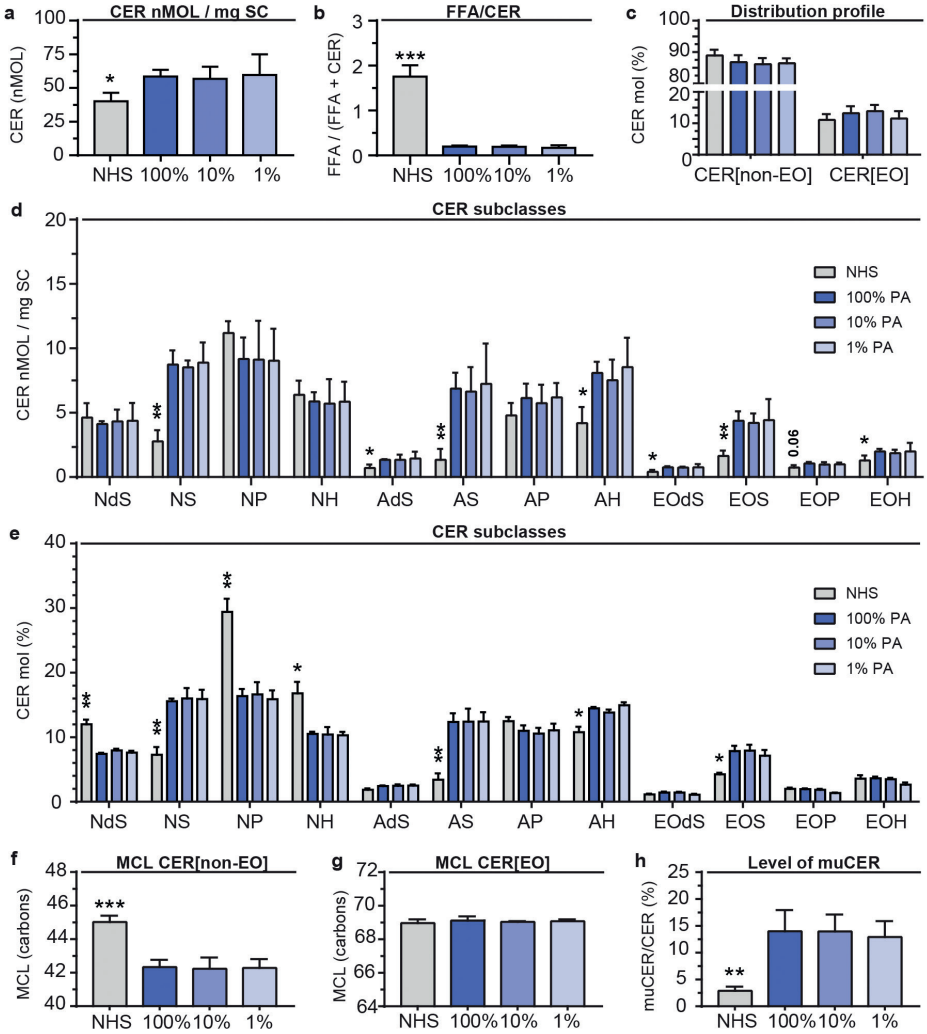


Figure 4. CER composition in the SC of NHS and in FTM supplemented with different PA levels. (a) Absolute amount of CERs in the SC of NHS and of FTMs. **(b)** Ratio of FFAs and CERs present in the SC. **(c)** Distribution profile of total CER[non-EO] and CER[EO] in the SC presented as relative amount. **(d)** Absolute subclass profile of CERs plotted as nMOL per mg of SC. **(e)** Subclass profile of CERs plotted as relative amount per CER subclass in percentage of the total CER quantity. **(f)** The mean chain length (MCL) of the CER[non-EO] subclasses. **(g)** The MCL of the CER[EO] subclasses. **(h)** The level of muCER in the CER[non-EO] subclasses, presented as percentage of muCER[non-EO] in the total CER[non-EO] quantity. All data for NHS, $FTM_{100\%PA}$, $FTM_{10\%PA}$, and $FTM_{1\%PA}$ represents mean + SD, N=3. Significance indicated by * = P<0.05, ** P<0.01, *** = P<0.001.

CERs at this detailed level. The obtained ratio was drastically reduced in FTMs as compared to NHS, irrespective of PA level (**Fig. 4 b**).

Then, the composition of the CER subclasses was evaluated by comparing the distribution profile of CER[non-EO] versus CER[EO], which revealed a high level of similarity in all FTMs and NHS (**Fig. 4 c**). Next, the absolute amount of each CER subclass was determined for $FTM_{100\%PA}$, $FTM_{10\%PA}$, $FTM_{1\%PA}$, and NHS (**Fig. 4 d**). The data for CER[non-EO] represents the saturated ceramide (saCER) and the monounsaturated CER (muCER). The bars of CER[EO] subclasses represent a combination of 4 different subgroups, which are muCER[EO-18:2], saCER[EO-18:2] + muCER[EO-18:1], and saCER[EO-18:1]. The CER subclass profiles of FTMs generated with different PA levels showed a high level of similarity. Considerable differences were observed comparing the subclass profiles of NHS and FTMs, which included an increased quantity of CER[NS], CER [AS], CER [AH], and most of the CER[EO] subclasses. This resulted in a relative abundance of the CER subclasses with a strong reduced fraction of CER [NP], while most other CER subclasses changed in abundancy, but to a lesser extent (**Fig. 4 e**). The data strongly indicate that biosynthesis pathways generating CER subclasses [NS], [AS], and [EOS] are most altered *in vitro*, whereas this is not influenced by PA supplementation.

The CER[EO] subclasses are composed of four different subgroups, as shown in **supplementary figure 6**. In the FTMs, no differences were observed upon reduced PA supplementation in the CER[EO] subgroups. Comparing FTMs to NHS, a difference for the CER[EO] subgroups is the presence of saCER[EO-18:1] in contrast to its absence in NHS.

Subsequently, we addressed the mean carbon chain length (MCL) of CER[non-EO] and CER[EO] (**Figure 4 f,g**). The MCL of CER[non-EO] in NHS was higher than that of FTMs, but no differences were observed regarding PA levels. **Figure 4 g** shows a similar MCL of CER[EO] in NHS and FTMs with different PA conditions. The carbon chain length distributions for the CER[non-EO] and CER[EO] deviated significantly from that of NHS, but were similar for the various levels of PA (**Supplementary fig. 6**). Importantly, the increased presence of C34 (CER with 34 carbon atoms), C36, C38, C40, and C42 CER[non-EO] in both absolute and relative level in FTMs as compared to NHS is a major difference.

As a final point, the level of muCERs was calculated as percentage of the total CERs (**Fig. 4 h**). The level of muCERs[non-EO] in the SC of FTMs was not influenced after reduction of the PA concentration, although this was considerably increased as compared to NHS.

3.5. FTMs supplemented with reduced PA exhibit a similar lipid organization

After addressing the lipid composition, the barrier formation was examined for lamellar organization by SAXD and for lateral organization by FTIR. The obtained SAXD diffraction profiles were indicative for the presence of the long periodicity phase (LPP) in FTMs (**Fig. 5 a**). The repeat distance of the LPP was determined, based on indicated orders of diffraction, which revealed a high similarity between $FTM_{100\%PA}$, $FTM_{10\%PA}$, and $FTM_{1\%PA}$ (**Fig. 5 b**). The repeat distance of the LPP in FTMs was considerably reduced as compared to that of NHS [30]. For the lateral organization, the FTIR spectrum at the methylene rocking vibration region is indicative for the orthorhombic lateral packing when there were two peaks present, whereas the hexagonal lateral packing is indicated by a single peak [7]. In $FTM_{100\%PA}$, $FTM_{10\%PA}$, and $FTM_{1\%PA}$ the hexagonal lateral packing was observed (**Fig. 5 c**). In contrast, the lipids were predominantly arranged in the orthorhombic lateral packing in NHS. At higher temperatures, the intensity of the peak at 730

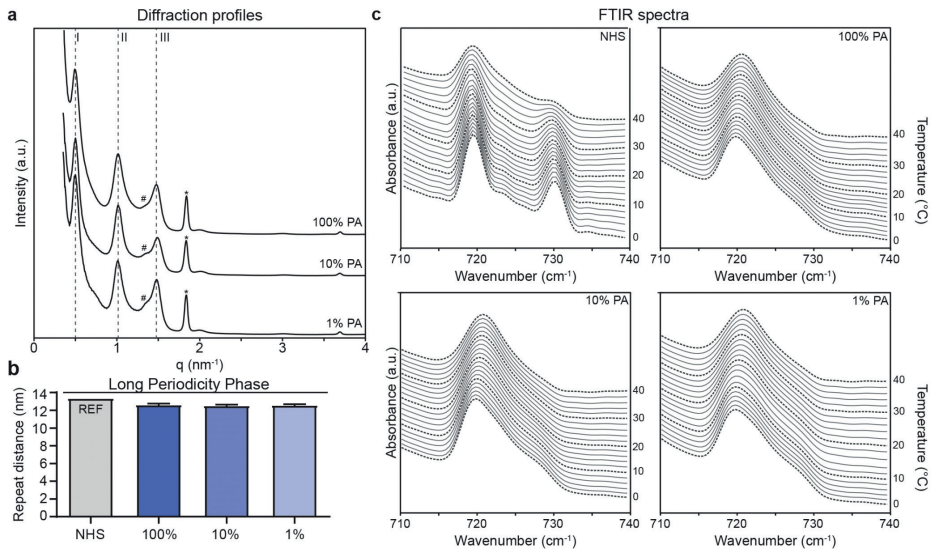


Figure 5. Lipid matrix organization in FTMs supplemented with different PA levels. (a) SAXD profiles of FTMs plotted as intensity in arbitrary units (a.u.) over the scattering vector q. The orders of diffraction (I, II and III) are indicated by dashed lines, phase separated cholesterol is indicated by the asterisk (*) symbol. Unknown phases are indicated by the number sign (#). **(b)** Bar plot showing the repeat distance of the LPP in NHS and FTMs based on the indicated orders of diffraction. Data for NHS was obtained from Bouwstra *et al.* [30], data represents mean + SD, N=3. **(c)** Fourier transform infrared spectroscopy spectra plotted as absorbance over the wavenumber in the methylene rocking vibrational region. On the right y-axis the temperature is shown at which the measurement occurred. Representative FTIR spectra were plotted for NHS and for FTMs with indicated level of supplemented PA.

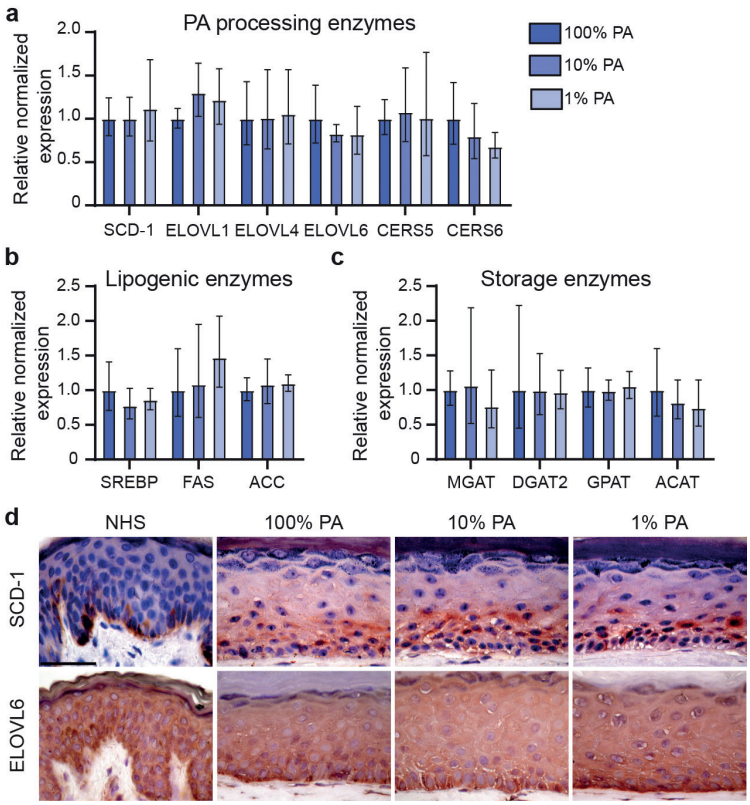


Figure 6. Lipid processing enzyme expression in FTMs supplemented with different PA levels. **(a)** Gene expression of direct and indirect PA processing enzymes SCD-1, ELOVL1, ELOVL4, ELOVL6, CERS5, and CERS6 in FTMs supplemented with indicated PA levels. **(b)** Gene expression of lipogenic mediators SREBP-1c, FAS, and ACC in FTMs. **(c)** Gene expression of lipid storage enzymes MGAT, DGAT2, GPAT, and ACAT in FTMs. Data represents mean ± SD, N=4. **(d)** Protein expression of PA processing enzymes SCD-1 and ELOVL6 in NHS and indicated FTMs. Proteins are shown in red and nuclei in blue. Scale bar represent 50 µm.

cm^{-1} reduced in NHS, indicative for a transition from orthorhombic to hexagonal packing.

3.6. Reduction of supplemented PA leads to similar expression of lipid processing enzymes

To obtain more information on the lipid biosynthesis pathway in $FTM_{100\%PA}$, $FTM_{10\%PA}$, and $FTM_{1\%PA}$, we assessed the expression of various lipid processing enzymes related to the barrier formation in the SC. The enzymes SCD-1, ELVOL6, CERS5 and CERS6 are able to process PA by desaturation to form 16:1, elongation to produce 18:0, or synthesis of CERs with a C16 acyl-chain, respectively [31-33]. The level of gene expression for these enzymes was similar in $FTM_{100\%PA}$, $FTM_{10\%PA}$,

and $FTM_{1\%PA}$ (**Fig. 6 a**). Also, expression of ELVOL1 and ELOVL4 remained similar. Furthermore, gene expression of lipogenic mediators (i.e. SREBP-1c, FAS, ACC) remained unaffected (**Fig. 6 b**). Lipid storage pathways were unaffected in all conditions tested based on the similar expression of enzymes involved in mono-, di-, and triglyceride synthesis (i.e. MGAT, DGAT2, GPAT) and biosynthesis of cholesterol esters (ACAT) (**Fig. 6 c**). Additionally, there was no evidence of a change in the amount of diglycerides based on the LC-MS CER ion maps (*data not shown*). On protein level, the expression of lipid processing enzymes SCD-1 and ELOVL6 was similar irrespective of PA level supplemented into the medium (**Fig.6 d**). As compared to NHS, the expression of SCD-1 was upregulated in FTMs, whereas the expression of ELOVL6 was similar. Together, these results show that lipid biosynthesis in FTMs remained similar after reduction of supplemented PA.

4. Discussion

In this study, we deciphered that addition of the bioactive lipid palmitic acid to the culture medium of HSEs is essential for a well-orchestrated epidermal morphogenesis. Irrespective of PA level in the culture medium, the SC lipid barrier composition and organization were similar. This indicates that the original level of PA was adequate and that the aberrant lipid barrier formation in HSEs is not associated with the overabundance of this saFFA in the culture medium. Furthermore, we showed that the level of FFAs in the SC of FTMs is substantially reduced as compared to NHS, which emerged as target for future barrier optimization approaches.

Supplementation of a mixture of essential and non-essential lipids to cultured skin substitutes was for the first time implemented by Boyce and Williams [20], who showed that it induced the formation of lamellar bodies and presence of acyl-glucosylceramides to mimic the lipid processing of NHS more closely. Importantly, the medium supplemented FFAs were found to be processed by the epidermis and incorporated into the SC of HSEs [17, 34]. Histological assessment revealed similar appearance of the FTMs with varying levels of PA, in line with results by Spiekstra *et al.* [35]. However, in this study we showed that PA has a direct effect on the epidermal morphogenesis by promoting the proper execution of the early differentiation and reducing the epidermal activation. Especially the latter is considered important for a proper barrier formation, as HSEs which display an activated phenotype generally contain a reduced barrier function [7, 9]. Furthermore, *in vivo* data also suggests that an activated epidermis is associated with a reduced formation and function of the human skin barrier [36, 37].

Although the morphogenesis clearly benefits from a sufficient level of supplemented PA, the gene/protein expression of lipid processing enzymes

(i.e. elongases, desaturases, or ceramide synthases) was not affected by ten to hundredfold reduction of PA. Furthermore, there is no evidence obtained that lipogenic pathways (mediated by SREBP-1c, FAS, and ACC) and lipid storage pathways (mediated by MGAT, DGAT2, GPAT, and ACAT) were altered after reduced supplementation of PA. Therefore, it remains of interest to obtain mechanistic insight in the metabolism of external derived FFAs and in *de novo* lipid biosynthesis of FFAs. Other attempts to modulate the *in vitro* biosynthesis of barrier lipids by changing supplementation of FFAs were performed by Thakoersing *et al.* [17]. After a fourfold increase in PA supplementation in epidermal models, no strong differences were observed in the composition of barrier lipids. In this study, we presented effects on the morphogenesis after reduction of PA concentration, although the lipid barrier composition remained similar. These results suggest that biosynthesis of barrier lipids is difficult to fine-tune by external supplementation of FFAs, although a basal supplementation level is crucial to support the proper development of FTMs. Reasonably, *de novo* lipid biosynthesis plays a dominant role in this, although determination of the interactions between *de novo* synthesis and uptake of lipids *in vitro* remains highly complex [38]. This is reflected by the *in vivo* situation, where systemic essential and non-essential lipids can be actively taken up and further processed by the skin [39-42]. Alternatively, addition of other classes of bioactive lipids besides FFAs in the culture medium is a promising approach to improve the lipid barrier formation [43, 44].

The altered composition of the major lipids in the SC of HSEs highly contributes to the aberrant formation of the lipid organization, which are in line with previous reports [7, 10]. The reduced repeat distance of the LPP could be ascribed to a disbalance in the CER subclass profile in combination with the reduced MCL of both FFAs and CERs. The absence of the SPP is also ascribed to the increased presence of the CER[EO] subclasses, which play a crucial role in the formation of the LPP [45, 46]. The lateral organization in HSEs is hexagonal, which is caused by the increased presence of muFFAs and muCERs, the drastic reduction in ratio of FFAs to CERs, and the reduced MCL of both FFAs and CERs [28, 47]. Analyses in lipid membrane models showed that these compositional alterations induced the formation of the hexagonal packing instead of the orthorhombic packing [28, 47]. Importantly, these alterations in lipid organization are associated with reduced barrier functionality, which has been confirmed to be much elevated based on inside-out as well as outside-in evaluations in HSEs as compared to NHS [7, 9].

Based on the combination of the LC-MS FFA with the LC-MS CER analysis, we were able to calculate the ratio of FFA to CER in the SC of NHS and FTMs. Limiting factor in the FFA analysis was the contamination of the solvents, which forced the excluding of C16:0, C18:0. However, after correcting for the impurities,

it was indicated that the short chain FFA C18:0 is relatively more present in FTMs than in NHS. Furthermore, the C26:1 and C28:1 were excluded due to a lack of corresponding FFA standards. However, we obtained indications that these muFFAs are more present in FTMs than in NHS. These factors partially contributed to the reduced abundance of FFAs in FTMs. Nonetheless, the absolute quantity as well as the FFA profile in the SC of FTMs came up as highly interesting and crucial targets for future studies.

Due to the high resolution of our LC-MS CER analysis, increased presence of saCER[EO-18:1] was monitored in the FTMs, which are not present in NHS [48]. The esterification of oleic acid (18:1) instead of linoleic acid (18:2) could be a result of reduced availability of the essential FFA C18:2, reduced release from triglycerides, or an excessive rapidity of biosynthesis of CER[EO] during *in vitro* biosynthesis [18]. As Vičanová *et al.* [18] reported that the addition of 30 µg/ml LA resulted in normalization of the LA content of the SC barrier. Optimization of the concentration of LA in our culture system (8.42 µg/ml) is therefore an interesting strategy to reduce the content of saCER[EO-18:1] and increase the level of FFA C18:2. On the other hand, LA is a potent ligand for the peroxisome proliferator-activated receptor alpha (PPAR-α) [49]. Activation of this nuclear receptor induced a substantial increase in the presence of CERs in a skin equivalent model [50]. As this will further reduce the FFA/CER ratio, this could be unbeneficial for the lipid organization and barrier functionality. Alternatively, kinetic studies of the essential FFAs added to keratinocyte cultures show that the conversion of LA to AA is extremely rapid [51], emphasizing the dynamic FFA metabolism in keratinocytes.

Interestingly, PA is also present in the sebum secreted by sebaceous glands [52]. Major roles of PA present in the sebum is to serve as antimicrobial agent by its physicochemical properties directly, or indirectly by inducing the expression of anti-microbial peptides [53]. Furthermore, sebum interacts with the lipid matrix on the superficial part of the skin, creating the skin surface lipid film [54]. As sebum lipid are not present until this day in HSEs, this alternative source of PA could be a major interfering factor increasing the relative and absolute amounts of PA and more interestingly PA-derived FFAs in NHS.

With this study, we unravelled that supplementation with adequate levels of PA during *in vitro* reconstruction of human skin is crucial for a correct epidermal morphogenesis, although the lipid barrier formation is similar after a ten to hundredfold reduction in external PA levels. Moreover, there is a substantial reduction in the quantitative presence of FFAs in the SC of HSEs. These findings broaden our understanding on the mechanisms underlying *in vitro* epidermal

morphogenesis and barrier formation and provide leads to further mimic the native skin tissue by HSEs.

5. Acknowledgments

This research was financially supported by Dutch Technology Foundation STW (grant no. 13151), which is part of the Netherlands Organisation for Scientific Research (NWO), and which is partly funded by the Ministry of Economic Affairs. The authors appreciate the support of the personnel at the DUBBLE beam line (BM26) at the ESRF during the SAXD measurements. The company Evonik (Essen, Germany) is acknowledged for the provision of ceramides.

6. Competing interests

The authors have declared no conflicting interests.

7. Author contributions

A.M., R.H., J.B., and A.E.G. designed the research study. A.M., R.H., A.N., and G.G. performed the research. A.M., R.H., A.N., and W.B. performed the data analysis. A.M. and R.H. drafted the manuscript, which was commented on by J.B and A.E.G. All authors approved the submitted manuscript.

8. References

1. Lilienblum, W., et al., Alternative methods to safety studies in experimental animals: role in the risk assessment of chemicals under the new European Chemicals Legislation (REACH). Archives of Toxicology, 2008. **82**(4): p. 211-236.
2. EU Directive, Directive 2003/15/EC of the European Parliament and of the Council of 27 February 2003 amending Council Directive 76/768/EEC on the approximation of the laws of the Member States relating to cosmetic products. Official Journal of the European Union, 2003. **66**: p. 26-35.
3. Hogervorst, M., et al., A shift from papillary to reticular fibroblasts enables tumour–stroma interaction and invasion. British journal of cancer, 2018: p. 1.
4. Schreiber, S., et al., Reconstructed epidermis versus human and animal skin in skin absorption studies. Toxicology in vitro, 2005. **19**(6): p. 813-822.
5. Schäfer-Korting, M., et al., The use of reconstructed human epidermis for skin absorption testing: Results of the validation study. Alternatives to laboratory animals: ATLA, 2008. **36**(2): p. 161-187.
6. Niehues, H., et al., 3D skin models for 3R research: the potential of 3D reconstructed skin models to study skin barrier function. Experimental dermatology, 2018.
7. Thakoersing, V.S., et al., Unraveling barrier properties of three different in-house human skin equivalents. Tissue Engineering Part C: Methods, 2011. **18**(1): p. 1-11.
8. Ponec, M., et al., Characterization of reconstructed skin models. Skin Pharmacology and Physiology, 2002. **15**(Suppl. 1): p. 4-17.
9. Mieremet, A., et al., Improved epidermal barrier formation in human skin models by chitosan modulated dermal matrices. PloS one, 2017. **12**(3): p. e0174478.
10. Thakoersing, V.S., et al., Increased presence of monounsaturated fatty acids in the stratum corneum of human skin equivalents. Journal of Investigative Dermatology, 2013. **133**(1): p. 59-67.
11. Ponec, M., et al., Barrier Function in Reconstructed Epidermis and Its Resemblance to Native Human Skin. Skin Pharmacology and Physiology, 2001. **14(suppl 1)**(Suppl. 1): p. 63-71.
12. Boiten, W., et al., Quantitative analysis of ceramides using a novel lipidomics approach with three dimensional response modelling. Biochimica et Biophysica Acta (BBA) - Molecular and Cell Biology of Lipids, 2016. **1861**(11): p. 1652-1661.
13. Lin, M.-H. and D. Khnykin, Fatty acid transporters in skin development, function and disease. Biochimica et Biophysica Acta (BBA) - Molecular and Cell Biology of Lipids, 2014. **1841**(3): p. 362-368.
14. Kendall, A.C., et al., Distribution of Bioactive Lipid Mediators in Human Skin. Journal of Investigative Dermatology, 2015. **135**(6): p. 1510-1520.
15. Feingold, K.R. and P.M. Elias, Role of lipids in the formation and maintenance of the cutaneous permeability barrier. Biochimica et Biophysica Acta (BBA) - Molecular and Cell Biology of Lipids, 2014. **1841**(3): p. 280-294.
16. Mao-Qiang, M., P.M. Elias, and K.R. Feingold, Fatty acids are required for epidermal permeability barrier function. J Clin Invest, 1993. **92**(2): p. 791-8.
17. Thakoersing, V.S., et al., Modulation of stratum corneum lipid composition and organization of human skin equivalents by specific medium supplements. Experimental dermatology, 2015. **24**(9): p. 669-674.
18. Vičanová, J., et al., Incorporation of linoleic acid by cultured human keratinocytes. Archives of Dermatological Research, 1999. **291**(7): p. 405-412.
19. Schürer, N., V. Schliep, and M.L. Williams, Differential Utilization of Linoleic and Arachidonic Acid by Cultured Human Keratinocytes. Skin Pharmacology and Physiology, 1995. **8**(1-2): p. 30-40.
20. Boyce, S.T. and M.L. Williams, Lipid Supplemented Medium Induces Lamellar Bodies and Precursors of Barrier Lipids in Cultured Analogues of Human Skin. Journal of Investigative Dermatology, 1993. **101**(2): p. 180-184.
21. Peter, A., et al., Individual stearoyl-coa desaturase 1 expression modulates endoplasmic reticulum stress and inflammation in human myotubes and is associated with skeletal muscle lipid storage and insulin sensitivity in vivo. Diabetes, 2009. **58**(8): p. 1757-1765.
22. Hall, E., et al., Effects of palmitate on genome-wide mRNA expression and DNA methylation patterns in human pancreatic islets. BMC medicine, 2014. **12**(1): p. 103.
23. Listenberger, L.L., et al., Triglyceride accumulation protects against fatty acid-induced lipotoxicity. Proceedings of the National Academy of Sciences, 2003. **100**(6): p. 3077-3082.

24. Zouboulis, C., S. Angres, and H. Seltmann, Regulation of stearoyl-coenzyme A desaturase and fatty acid delta-6 desaturase-2 expression by linoleic acid and arachidonic acid in human sebocytes leads to enhancement of proinflammatory activity but does not affect lipogenesis. British Journal of Dermatology, 2011. **165**(2): p. 269-276.
25. El Ghalbzouri, A., et al., Replacement of animal-derived collagen matrix by human fibroblast-derived dermal matrix for human skin equivalent products. Biomaterials, 2009. **30**(1): p. 71-78.
26. Sakai, S., et al., Characteristics of the epidermis and stratum corneum of hairless mice with experimentally induced diabetes mellitus. Journal of investigative dermatology, 2003. **120**(1): p. 79-85.
27. Berkers, T., et al., Topically applied fatty acids are elongated before incorporation in the stratum corneum lipid matrix in compromised skin. Experimental Dermatology, 2017. **26**(1): p. 36-43.
28. Mojumdar, E.H., et al., Monounsaturated Fatty Acids Reduce the Barrier of Stratum Corneum Lipid Membranes by Enhancing the Formation of a Hexagonal Lateral Packing. Langmuir, 2014. **30**(22): p. 6534-6543.
29. Ezure, T. and S. Amano, Negative Regulation of Dermal Fibroblasts by Enlarged Adipocytes through Release of Free Fatty Acids. Journal of Investigative Dermatology, 2011. **131**(10): p. 2004-2009.
30. Bouwstra, J.A., et al., Structural Investigations of Human Stratum Corneum by Small-Angle X-Ray Scattering. Journal of Investigative Dermatology, 1991. **97**(6): p. 1005-1012.
31. Kihara, A., Very long-chain fatty acids: elongation, physiology and related disorders. J Biochem, 2012. **152**(5): p. 387-95.
32. Frigolet, M.E. and R. Gutiérrez-Aguilar, The Role of the Novel Lipokine Palmitoleic Acid in Health and Disease–. Advances in Nutrition, 2017. **8**(1): p. 173S-181S.
33. Mizutani, Y., et al., Ceramide biosynthesis in keratinocyte and its role in skin function. Biochimie, 2009. **91**(6): p. 784-790.
34. Schürer, N.Y., et al., Fatty acid metabolism in human keratinocytes cultivated at an air-medium interface. Journal of Investigative Dermatology, 1989. **92**(2): p. 196-202.
35. Spiekstra, S.W., et al., Potential method to determine irritant potency in vitro – Comparison of two reconstructed epidermal culture models with different barrier competency. Toxicology in Vitro, 2009. **23**(2): p. 349-355.
36. Janssens, M., et al., Increase in short-chain ceramides correlates with an altered lipid organization and decreased barrier function in atopic eczema patients. Journal of lipid research, 2012: p. jlr. P030338.
37. Ishikawa, J., et al., Changes in the Ceramide Profile of Atopic Dermatitis Patients. Journal of Investigative Dermatology, 2010. **130**(10): p. 2511-2514.
38. Strable, M.S. and J.M. Ntambi, Genetic control of de novo lipogenesis: role in diet-induced obesity. Critical Reviews in Biochemistry and Molecular Biology, 2010. **45**(3): p. 199-214.
39. Grubauer, G., K.R. Feingold, and P.M. Elias, Relationship of epidermal lipogenesis to cutaneous barrier function. J Lipid Res, 1987. **28**(6): p. 746-52.
40. Man, M.-Q., K.R. Feingold, and P.M. Elias, Exogenous lipids influence permeability barrier recovery in acetone-treated murine skin. Archives of dermatology, 1993. **129**(6): p. 728-738.
41. Schmuth, M., et al., Differential expression of fatty acid transport proteins in epidermis and skin appendages. J Invest Dermatol, 2005. **125**(6): p. 1174-81.
42. Popa, I., et al., Linoleate-enriched diet increases both linoleic acid esterified to omega hydroxy very long chain fatty acids and free ceramides of canine stratum corneum without effect on protein-bound ceramides and skin barrier function. 2018. **310**(7): p. 579-589.
43. Kim, S., et al., Phytosphingosine stimulates the differentiation of human keratinocytes and inhibits TPA-induced inflammatory epidermal hyperplasia in hairless mouse skin. Molecular medicine, 2006. **12**(1-3): p. 17-24.
44. Choi, H.K., et al., Phytosphingosine Increases Biosynthesis of Phytoceramide by Uniquely Stimulating the Expression of Dihydroceramide C4-desaturase (DES2) in Cultured Human Keratinocytes. Lipids, 2018. **53**(9): p. 909-918.
45. de Jager, M.W., et al., Novel lipid mixtures based on synthetic ceramides reproduce the unique stratum corneum lipid organization. Journal of lipid research, 2004. **45**(5): p. 923-932.
46. Mojumdar, E.H., et al., Stratum corneum lipid matrix: Location of acyl ceramide and cholesterol in the unit cell of the long periodicity phase. Biochimica et Biophysica Acta (BBA) - Biomembranes, 2016. **1858**(8): p. 1926-1934.
47. Uchiyama, M., et al., Free fatty acids chain length distribution affects the permeability of skin lipid model membranes. Biochimica et Biophysica Acta (BBA) - Biomembranes, 2016. **1858**(9): p. 2050-2059.
48. t'Kindt, R., et al., Profiling and Characterizing Skin Ceramides Using Reversed-Phase Liquid Chromatography–Quadrupole Time-of-Flight Mass Spectrometry. Analytical Chemistry, 2012. **84**(1): p. 403-411.

49. Forman, B.M., J. Chen, and R.M. Evans, Hypolipidemic drugs, polyunsaturated fatty acids, and eicosanoids are ligands for peroxisome proliferator-activated receptors α and δ. Proceedings of the National Academy of Sciences of the United States of America, 1997. **94**(9): p. 4312-4317.
50. Rivier, M., et al., Peroxisome Proliferator-Activated Receptor-α Enhances Lipid Metabolism in a Skin Equivalent Model. Journal of Investigative Dermatology, 2000. **114**(4): p. 681-687.
51. Marcelo, C.L. and W.R. Dunham, Fatty acid metabolism studies of human epidermal cell cultures. 1993. **34**(12): p. 2077-90.
52. Camera, E., et al., Comprehensive analysis of the major lipid classes in sebum by rapid resolution-high performance liquid chromatography and electrospray mass spectrometry. Journal of lipid research, 2010.
53. Nakatsuji, T., et al., Sebum Free Fatty Acids Enhance the Innate Immune Defense of Human Sebocytes by Upregulating β-Defensin-2 Expression. Journal of Investigative Dermatology, 2010. **130**(4): p. 985-994.
54. Sheu, H.M., et al., Human skin surface lipid film: an ultrastructural study and interaction with corneocytes and intercellular lipid lamellae of the stratum corneum. British Journal of Dermatology, 1999. **140**(3): p. 385-391.
55. Motta, S., et al., Ceramide composition of the psoriatic scale. Biochimica et Biophysica Acta (BBA)-Molecular Basis of Disease, 1993. **1182**(2): p. 147-151.

9. Supporting information

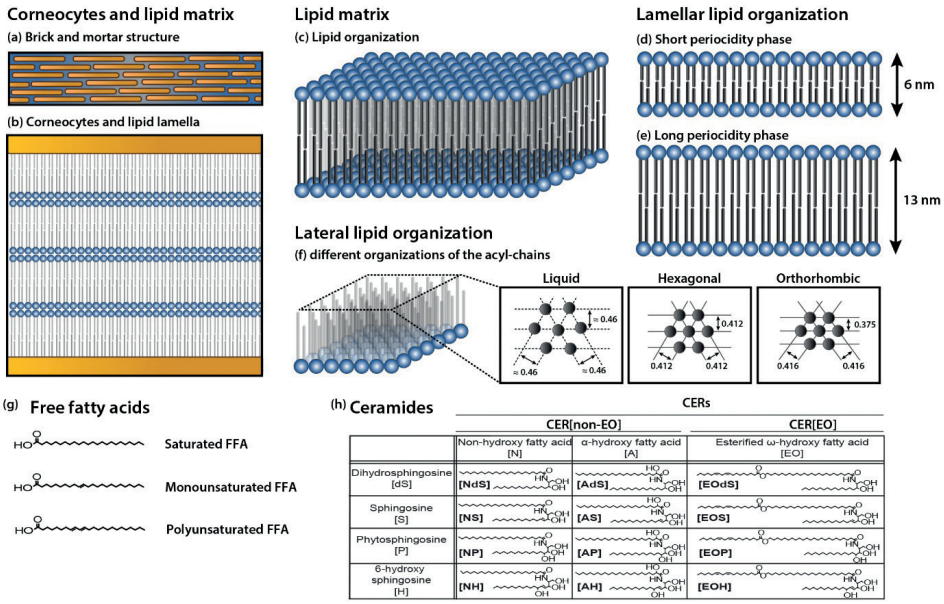
Supplementary table 1. Antibodies utilized during immunohistochemical or immunofluorescence analyses.

Target	Material	Host	Clone	Dilution	Supplier
Ki67	FFPE	Mouse	MIB1	1:100	DAKO, Denmark
Cytokeratin 10	FFPE	Mouse	DE-K10	1:50	Labvision/Neomarker, USA
Involucrin	FFPE	Mouse	SY5	1:1200	Sanbio, The Netherlands
Cytokeratin 16	FFPE	Mouse	LL025	1:100	Serotec, UK
Cytokeratin 17	FFPE	Mouse	E3	1:1500	EMD Millipore Corporation, USA
Loricrin	FFPE	Rabbit	AF62	1:1000	Covance, The Netherlands
Filaggrin	FFPE	Rabbit	PRB417	1:1000	Covance, The Netherlands
Collagen type IV	FFPE	Mouse	24.12.8 (PHM-12)	1:75	Chemicon, Australia
Laminin 332	Frozen	Mouse	BM165	1:150	Provided by Dr. M. Aumailley, Germany
Vimentin	FFPE	Mouse	V9	1:250	Sigma-Aldrich, Germany
Alpha smooth muscle actin	FFPE	Mouse	1A4	1:500	Abcam, UK
SCD-1	FFPE	Mouse	CD.E10	1:300	Abcam, UK
ELOVL6	FFPE	Rabbit	Poly	1:500	Abcam, UK

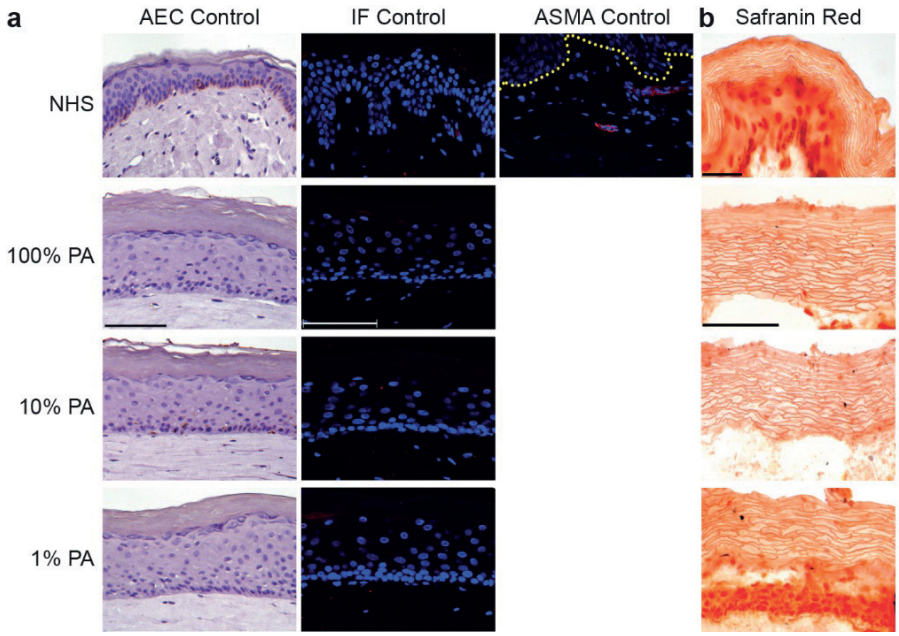
Supplementary table 2. Primer sequences utilized during qPCR analyses.

Target	Sequence Forward (5'-> 3')	Sequence Reverse (5'-> 3')	Amplicon size
SDHA*	AACCAAACGCTGGGGAAGAA	GGAACACGGCAGCATGATTT	126
ZNF410*	GCTGTGGTAAGCAGTTTACTACAG	CTTGGGCTTCACAAAGGAAAGG	90
ARCP2*	TCCGGGACTACCTGCACTAC	GGTTCAGCACCTTGAGGAAG	96
SCD-1	ACAGTGCTGCCCACCTCTTCG	CCCTCACCCACAGCTCCAAGTG	94
ELOVL1	GGAGCTCCAGGTATTGCCAAGG	AGCCGTGGTCCCTGTAGAGCA	203
ELOVL4	TTTGGTGGAAACGATACCTGA	TTAGAGCCCAGTGCATCCAT	120
ELOVL6	TCGGTGCTCTTCGAACTGGTGC	GTATCTCCTAGTTCGGGTGCTTTGC	154
CERS5	CGGCTCTGTGACACCCTTT	TCTCAAAGAGGGTCGTGTTCA	100
CERS6	TGTTTGTTATGTTTGCCGTGGT	CCAACGATCTCCCAGCTTTCA	100
SREBP	GGAGGGGTAGGGCCAACGGCCT	CATGTCTTCGAAAGTGCAATCC	80
FAS	CATCCCCACCTATGGCCTGC	GCCTGATGCAGTCGATGTAGTA	89
ACC	CATATCCAGTCCATGCTGCGT	GTTCCAGCCACTGCACAACC	100
MGAT	GCAGAGAGCAGGTGTGTGAT	GCCTCCTCTGGACTATGGGA	71
DGAT2	GCAAGGGCTTTGTGAAACTGG	CCTCGAAGATCACCTGCTTGTA	99
GPAT	ATGAAACACCAGATGGACGGA	TCCTAGAACGTGTGCCTTCC	120
ACAT	TGCTTCAGGAATGAAAGCCATC	CATCCCACCTGCCACCATC	82

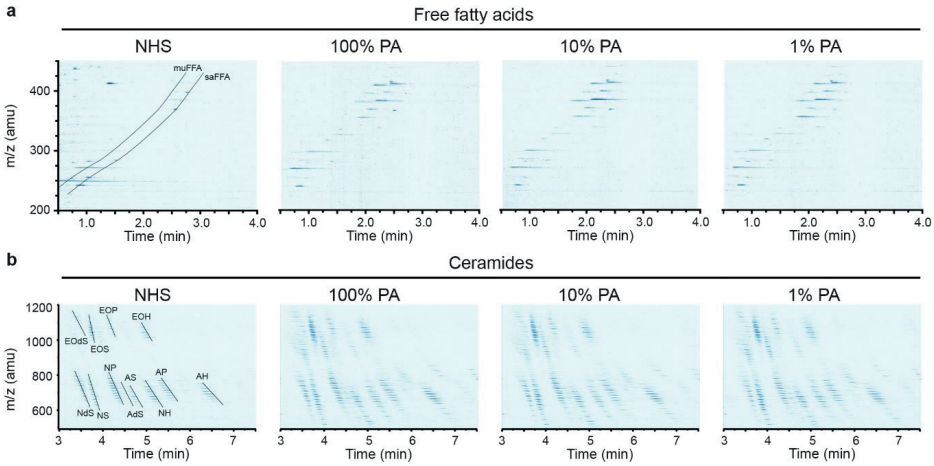
* Reference genes



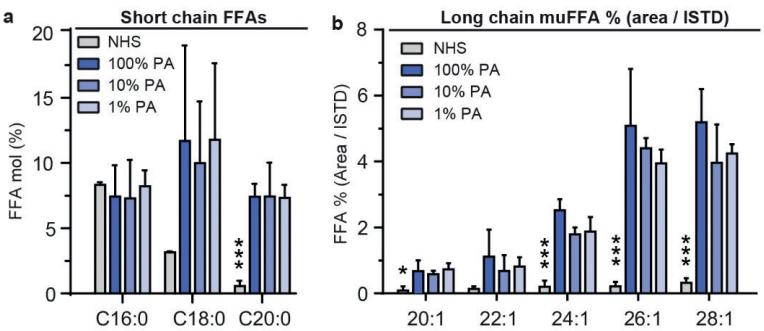
Supplementary figure 1. Intercorneocyte lipid matrix of the SC with main lipid organizations and constituents. (a) Simplified schematic overview of the SC which figuratively considered as brick and mortar structure. **(b)** Isolated elements of the lipid matrix with repetitive pattern as detected in the intercorneocyte space. **(c)** Schematic overview of the lipid molecular arrangement, with head groups as dark blue spheres and hydrocarbon chains in dark grey. **(d)** Lipids in the lamellar organization shown in the short periodicity phase with a repeat distance of approximately 6 nm [30]. **(e)** Lipids in the lamellar organization shown in the long periodicity phase with a repeat distance of approximately 13 nm [30]. **(f)** Lateral organization of the hydrocarbon chains, which adopt the liquid, hexagonal, or orthorhombic organization. Approximations of the intermolecular space for each organization is indicated. **(g)** Schematic overview of the FFA subgroups analysed in this study. **(h)** Tabular overview of the 12 CER subclasses analysed in this study with nomenclature according to Motta *et al.* [55]. Illustrations adapted from Helder *et al.* (submitted).



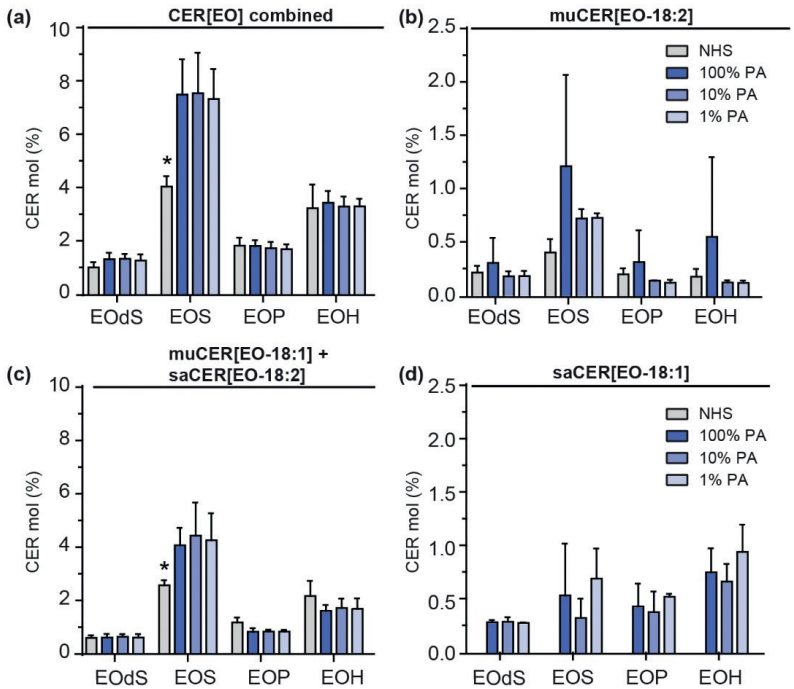
Supplementary figure 2. Controls of immunohistochemistry and safranin red staining. (a) Negative controls for immunohistochemical and immunofluorescence stainings. Positive control for ASMA staining showing fibroblasts stress signalling in NHS. Nuclei are stained blue using haematoxylin or DAPI, yellow dotted line indicates dermal-epidermal junction. **(b)** Representative cross sections of FTMs and NHS stained with safranin red followed by alkali expansion of the SC used for quantification of the amount of corneocyte layers. Scale bar indicates 100 µm.



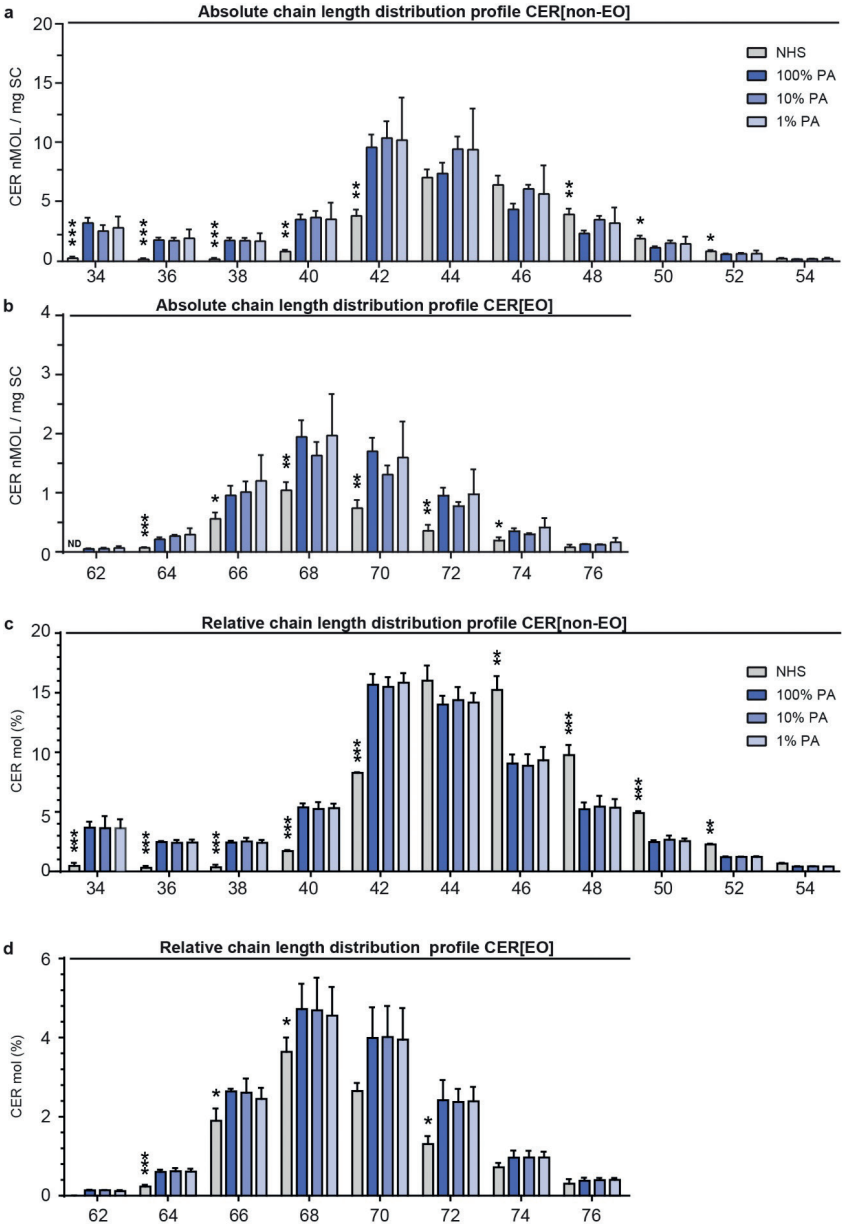
Supplementary figure 3. LC-MS ion maps of detected free fatty acids and ceramides present in the SC of FTMs generated with various PA levels and of NHS. **(a)** LC-MS FFA ion maps with indicated position of saturated (saFFA) and monounsaturated (muFFA) FFA are indicated in the plot of NHS. **(b)** LC-MS CER ion maps with indicated position and names of 12 CER subclasses according to Motta *et al.* [55] in the plot of NHS.



Supplementary figure 4. Non-quantified data for the composition of free fatty acids. **(a)** Relative level of saturated short chain FFAs. The C16:0 and C18:0 FFAs are calculated after additional corrections for the solvent impurities. **(b)** Relative level in of long chain muFFAs calculated as area under curve divided by internal standard presented in arbitrary units, which were not quantified due to lack of standard. The relative data is calculated with the signal of FFA C20:0 - C28:0. All data is provided for FTMs with indicated level of supplemented PA and for NHS, data indicates mean + SD, N=3. Statistical differences are noted as *, ** or ***, corresponding to P<0.05, <0.01, <0.001.



Supplementary figure 5. Compositional analysis of CER[EO] subgroups in the SC of FTMs generated with various PA levels and of NHS. (a) Relative level in of total CER[EO] plotted per subclass, which is the cumulative amount of muCER[EO-18:2], saCER[EO-18:2] + muCER[EO-18:1], and saCER[EO-18:1]. **(b)** Relative level of muCER[EO-18:2] plotted per subclass. **(c)** Relative level of saCER[EO-18:2] + muCER[EO-18:1]. **(d)** Relative level of saCER[EO-18:1]. All data is provided for FTMs with indicated level of supplemented PA and for NHS, data indicates mean + SD, N=3. Statistical differences are noted as *, ** or ***, corresponding to P<0.05, <0.01, <0.001.



Supplementary figure 6. Carbon chain length distribution of CERs in the SC of FTMs generated with varying PA levels and of NHS. (a) Bar diagram plot of absolute level of CER[non-EO] with an even number of carbon atoms. **(b)** The absolute level of CER[EO] with an even number of carbon atoms. **(c)** Bar diagram plot of relative level of CER[non-EO] with an even number of carbon atoms. **(d)** The relative level CER[EO] with an even number of carbon atoms. Data is shown for NHS, $FTM_{100\%PA}$, $FTM_{10\%PA}$, and $FTM_{1\%PA}$ and represents mean + SD, N=3. Statistical differences are noted as *, ** or ***, corresponding to P<0.05, <0.01, <0.001.

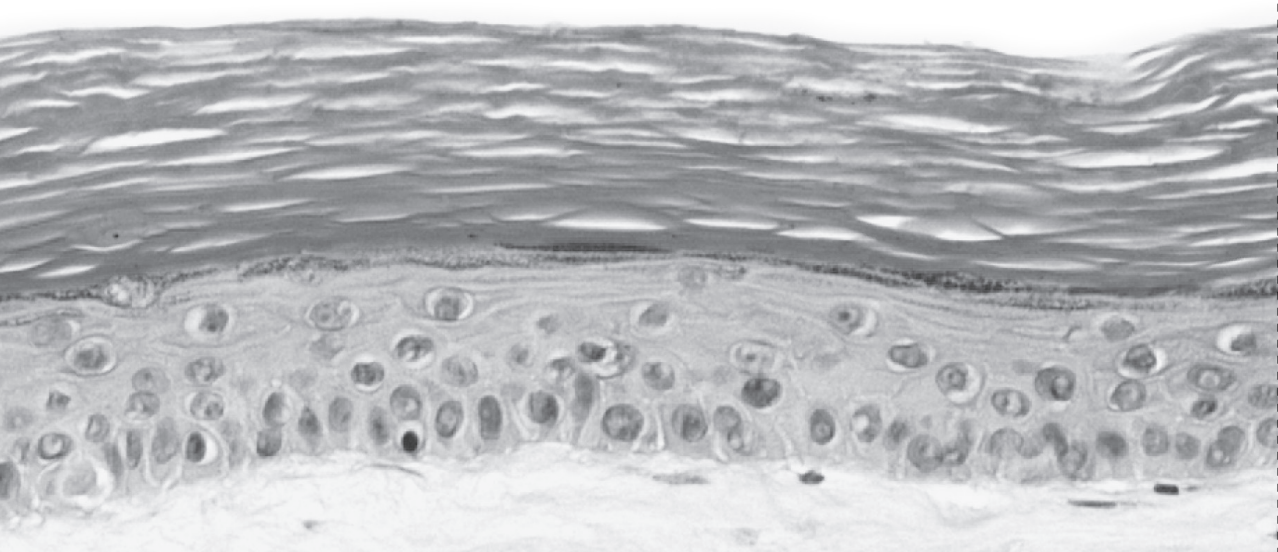
9

Multitargeted approach for the optimization of morphogenesis and barrier formation in human skin equivalents

Arnout Mieremet[‡]
Richard Helder[‡]
Andreea Nadaban
Walter Boiten
Gert Gooris
Abdoelwaheb El Ghalbzouri[+]
Joke A. Bouwstra[+]

[‡]Authors contributed equally
[+] Joint senior authorship

In preparation



Abstract

In vitro skin tissue engineering is challenging due to the manifold differences between the *in vivo* and *in vitro* conditions. Yet, three-dimensional (3D) human skin equivalents (HSEs) are able to mimic the native human skin (NHS) in many aspects. However, the epidermal lipid barrier formation, which is essential for the functionality of the skin barrier, remains compromised. Recently, we generated HSEs with an improved lipid barrier formation by i) incorporating chitosan in the dermal collagen matrix, ii) reducing external oxygen level to 3%, and iii) inhibiting the liver-X-receptor (LXR). In this study, we aim to determine synergic effects of these factors during generation of HSEs. Therefore, we developed full thickness models (FTMs) with combinations of these as single, double, and triple targeted optimization approaches. The collagen-chitosan FTM combined with LXR inhibition showed an improved epidermal morphogenesis, an enhanced lipid composition, and a better lipid organization. Functionality analyses also revealed improved barrier performance in the corresponding approach. In conclusion, our lead optimization approach substantially improved the epidermal morphogenesis, barrier formation, and functionality in the FTM, which therefore better mimics NHS.

1. Introduction

In vitro developed human skin equivalents (HSEs) replicate multiple critical aspects of *in vivo* skin biology due to the presence of the nourishing culture medium as well as the supportive micro-environment [1-3]. Numerous types of three-dimensional (3D) HSEs exist, ranging from epidermal models to skin-on-a-chip models [4-7]. Nevertheless, a shared restriction in all models is the reduced barrier formation [8-11]. This affects the resemblance to the native human skin (NHS) tissue and limits the applicability in pharmacokinetics and toxicological screenings [12]. Therefore, there is an urgent need to improve epidermal morphogenesis and barrier formation in HSEs.

The stratum corneum (SC) is the main component of the physical epidermal barrier [13]. This outermost epidermal layer consists of corneocytes embedded in a lipid matrix. The corneocytes contain a cornified envelope consisting of highly crosslinked proteins, resulting in almost impermeable objects [13]. The lipid matrix is the only continuous pathway through the SC, thereby crucial for the functionality of the skin barrier [14, 15]. Within the lipid matrix, the lipids are organized in lipid lamellae. Two major repetitive lamellar phases can be distinguished, which are termed the short periodicity phase (SPP) and the long periodicity phase (LPP) [16, 17]. Perpendicular to the plane of the lamellae, the lipids are organized in the lateral packing. From very dense to less dense, lipids can adopt the orthorhombic, hexagonal, or liquid lateral organization [16, 17]. The lipid organization is principally a result of the lipid composition. Main SC lipid classes are ceramides (CERs), free fatty acids (FFAs), and cholesterol [15]. The CERs contribute 50% by mass to the lipid composition and are a key player in the formation of structured lamellae [14, 15]. CERs vary in headgroup architecture, resulting in the presence of at least 16 subclasses [18-20]. Furthermore, both CERs and FFAs can differ in the number of carbons in the acyl chains and the degree of unsaturation, yielding a high diversity of lipid entities within the SC matrix. Variations in the lipid composition can induce changes in the lipid organization and functionality [21-23].

The lipid barrier formation is usually characterized based on the expression of lipid biosynthesis enzymes, lipid composition, lipid organization, and/or barrier functionality. Characterization of the lipid barrier formation in HSEs revealed similar features as compared to that of NHS. These similarities include the biosynthesis of all lipid classes, extrusion of lamellar bodies at the stratum granulosum (SG) – SC interface, presence of all CER subclasses with a wide distribution in carbon chain length, and formation of organized lipid lamellae anchored to the lipid envelope [8, 24]. Differences were observed for the lipid composition. These cover the altered CER subclass profile, the increased presence

of CERs with a low number of carbon atoms (<40 carbon atoms), and a higher level of monounsaturated CERs (muCERs) and monounsaturated FFAs (muFFAs). This is linked to an elevated expression of the lipid desaturase enzyme stearoyl-CoA desaturase-1 (SCD-1) in HSEs [8, 24-26].

As the *in vitro* barrier formation of HSEs is a result of complex interactions, it is currently not fully understood. Therefore, we investigated the barrier formation of HSEs by an innovative multitargeted strategy. The targets were identified based on results obtained in studies which aimed to optimize single aspects of 3D skin tissue engineering, which are the extracellular matrix (ECM) composition, external culture conditions, and the medium composition [27] (Mieremet *et al.* (chapter 5), Helder *et al.*, submitted). For the latter, it was revealed that inhibition of the liver-X-receptor (LXR), as a key regulator of SCD-1, was a successful approach to reduce the level of monounsaturated lipids in the SC of HSEs.

In this study, we aim to evaluate the synergic effects of improved dermal ECM, external factors, and medium composition on epidermal morphogenesis and lipid barrier formation in HSEs (**Supplementary fig. 1 a-g**). Therefore, full thickness models (FTMs) and collagen-chitosan FTMs (CC-FTMs) were generated under normoxic or hypoxic conditions with or without inhibition of LXR. Herein, we report that our lead optimization approaches resulted in a well-structured epidermal morphogenesis with enhanced barrier formation contributing to an improved barrier functionality in HSEs.

2. Materials and Methods

2.1. Generation of human skin equivalents

Declaration of Helsinki principles were followed during obtainment of primary cells from human skin originating from surplus breast tissue of healthy female donors aged between 18 - 45. Experiments were conducted in accordance with article 7:467 of the Dutch Law on Medical Treatment Agreement and the Code for proper Use of Human Tissue of the Dutch Federation of Biomedical Scientific Societies (https://www.federa.org/codes-conduct). As of this national legislation, coded surplus tissue can be used for scientific research purposes when no written objection in made by the informed donor. Therefore, additional approval of an ethics committee regarding scientific use of surplus tissue was not obligatory, as reported before [28]. Isolation and cell culturing of primary cells isolated from the dermis and epidermis was performed as described before [28]. Culture medium of all isolated primary cells was tested for mycoplasma contamination by qPCR and found negative. FTMs and CC-FTMs were generated as described before [8, 27, 29]. Reduction to hypoxic conditions (3% O_2) was performed in a Heracell™ 240 CO_2 incubator (ThermoFisher, Waltham, MT, United States). Supplementation with

500 nM LXR inhibitor GSK2033 (Merck KGaA, Darmstadt, Germany) occurred twice a week for four times in total during the air-exposed phase. Treatment with vehicle (dimethyl sulfoxide) did not induce additional effects for all analyses performed, and was therefore excluded from the results. Four different batches of HSEs were developed using different primary cell donors and were generated for a total of 14 days at the air-liquid interface. A tabular overview of the approaches is shown in **table 1**.

Table 1. Overview of single, double, and triple targeted optimization approaches.

	HSE TYPE	O_2	GSK2033	APPROACH	ACRONYM
1	FTM	20%	(-)	Control	FTM(20-)
2	FTM	20%	(+)	Single	FTM(20+)
3	FTM	3%	(-)	Single	FTM(3-)
4	FTM	3%	(+)	Double	FTM(3+)
5	CC-FTM	20%	(-)	Single	CC-FTM(20-)
6	CC-FTM	20%	(+)	Double	CC-FTM(20+)
7	CC-FTM	3%	(-)	Double	CC-FTM(3-)
8	CC-FTM	3%	(+)	Triple	CC-FTM(3+)

2.2. Immunohistochemical analyses

Tissue fixation occurred in 4% formaldehyde for 24 hr before rehydration and paraffin embedment. Tissue was cut in 5 µm thickness for haematoxylin and eosin (HE) staining and immunohistochemical analyses. HE staining was performed according to instructions provided by the manufacturer (VWR, Breda, The Netherlands). Immunohistochemical analyses were performed as described before using the following antibodies: Ki67 (1:100, clone MIB, DAKO, Denmark), involucrin (1:1200, clone SY5, Sanbio, The Netherlands), and keratin 16 (1:100, clone LL025, Serotec, United Kingdom) [27]. Estimations of the epidermal thickness were performed on at least six regions per sample according to methods reported before [27]. Proliferation index was determined on two different central regions per sample by counting the Ki67 positive cells in a region of at least 100 basal cells.

2.3. Liquid chromatography coupled to mass spectrometry analyses

Stratum corneum was isolated using trypsin digestion steps and stored until use in an inert environment as described before [30]. Lipids were extracted using a modified Bligh and Dyer extraction procedure as reported before [19, 31]. Dry weight of SC was determined before and after lipid extraction using a microbalance. Extracted lipids were evaporated and reconstituted in appropriate volume of heptane/chloroform/methanol (95/2.5/2.5 v/v/v) to obtain a 0.3 mg/ml concentration. Ceramide N(24deuterated)S(18) (Evonik industries, Essen,

Germany) was added as internal standard (ISTD). Liquid chromatography coupled to mass spectrometry (LC-MS) analyses were performed as described by Boiten *et al.* [19]. In brief, 5 µl sample volume was injected into the ultra-pressure liquid chromatograph (UPLC) (Waters, Milford, MA, USA) equipped with a PVA-Sil column (5 µm particles size, 100 x 2.1 mm i.d., YMC, Kyoto, Japan). Detection occurred by a XEVO TQ-S mass spectrometer (Waters), measuring full scan m/z between 350 and 1200 atomic mass units. Data was analysed with Masslynx software (version 4.1, Waters), corrected for ISTD and quantified using a 3D response model according to methods as described before [19].

2.4. Small angle X-ray diffraction

Small-angle X-ray diffraction (SAXD) measurements were performed at the European Synchrotron Radiation Facility (ESRF, Grenoble, France) at station BM26B for a period of 2 x 90 sec as described elsewhere [21]. The scattering intensity I was measured as a function of the scattering vector q. The latter is defined as $q = \frac{4 \cdot \pi \cdot \sin\theta}{\lambda}$, in which θ is the scattering angle and λ is the wavelength of the X-rays. From the positions of the peaks, the repeat distance of a lamellar phase was calculated using the equation $d = \frac{2n \cdot \pi}{qn}$, where n is the order of diffraction peak of this phase and q_n the position of the n-order peak.

2.5. Fourier transform infrared spectroscopy

The isolated SC was rehydrated for 12 hr in a desiccator containing deuterated H_2O. After rehydration, the SC was placed between two AgBr windows prior to measurements. Spectra were acquired on a Varian 670-IR spectrometer (Varian, Palo Alto, CA, USA) equipped with a broad-band mercury cadmium telluride detector. The Fourier transform infrared spectroscopy (FTIR) spectrometer was connected to a customized temperature regulator to facilitate measurements at temperatures ranging from 0 to 40°C. The spectrometer collected the data with a frequency range of 400-4000 cm^{-1} with spectral resolution of 1 cm^{-1}. Measurements were performed in 240 sec during a total run of 164 min. Varian resolution pro software (Varian) was used to analyse and deconvolute the FTIR spectra.

2.6. Barrier functionality assays

The permeation study was performed using isolated SC placed on a supporting dialysis membrane (Diachema, Munich, Germany) mounted into Permegear inline diffusion cell (Bethlehem, PA, USA) using settings as described before [21, 32]. The donor compartment consisted of a saturated solution of benzocaine (165.189 g/mol) in acetate buffer (pH 5.0). The acceptor compartment consisted of phosphate-buffered saline solution (pH 7.4), which was stirred and perfused at a flow rate of about 2 mL/hr. The diffusing area between donor and acceptor compartment was 0.282 cm^2. Each experiment was performed under occlusive conditions at a temperature of 32°C. Analysis of the amount of diffused benzocaine

was performed using a UPLC system. Flux of benzocaine through each sample was calculated using Fick's first law of diffusion, as described earlier [21]. Measurement of transepidermal water loss (TEWL) were performed at controlled ambient conditions. The isolated SC was supported by a dialysis membrane and placed in the diffusion cell, which was filled with Millipore water. After a 15 min equilibration period, the closed chamber evaporimeter (Aqua Flux AF200, Biox Systems Ltd, London, UK) was connected with an adapter to the apical side of the diffusion cell for 30 min. Subsequently, measurements were performed every 20 sec during at least 6 min [27].

2.7. Statistics

Statistical analyses were conducted using GraphPad Prism version 7.0 for Windows (GraphPad Software, La Jolla, CA, USA). Statistical testing was performed between single- and multitargeted FTMs using 1-way or 2-way ANOVA with Holm-Sidak post-tests. The NHS versus control FTM (FTM(20-)) comparison was statistically tested using unpaired student's t-test. Statistical differences are noted with lines for the former and vertically above NHS for the latter comparison, otherwise indicated. Significance is indicated by *, ** or *** corresponding to $P<0.05$, <0.01, or <0.001.

3. Results

3.1. Multitargeted optimization approach improves epidermal morphogenesis

The single, double, and triple targeted FTMs were evaluated for histological appearance, which revealed a well-orchestrated epidermal stratification in all conditions (**Fig. 1 a**). However, in some approaches a reduction in thickness of the viable epidermis was observed as compared to control FTM(20-) (**Fig. 1 b**). The FTM(3-), FTM(3+), CC-FTM(20-), and CC-FTM(20+) displayed highest resemblance to the epidermal thickness of NHS. Furthermore, the shape of granular cells was more flattened in these four models. Evaluation of epidermal morphogenesis using protein biomarkers confirmed these observations on late differentiation using involucrin expression (**Fig. 1 c**). The FTM(3-), FTM(3+), CC-FTM(20-), and CC-FTM(20+) most closely mimicked the late differentiation program of NHS, although involucrin remained overexpressed in the stratum spinosum of all FTMs. Epidermal activation was determined by keratin 16 expression, which was expressed in control FTM(20-) in contrast to no expression in NHS. Although K16 remained expressed in the majority of FTMs, K16 expression was reduced in CC-FTM(20-) and CC-FTM(20+), thereby better resembling the homeostasis of NHS. Proliferation was evaluated by Ki67 expression, revealing restriction to the basal cell layer in all conditions. However, a high proliferation index was observed in FTM(20-) and FTM(20+), which was reduced in 3% hypoxia and in CC-FTMs,

with additional reduction after combination of these in CC-FTM(20-) and CC-FTM(20+). Together, these results indicate that the epidermal morphogenesis was improved using our strategy, mainly ascribed to the modification of the dermal ECM by chitosan.

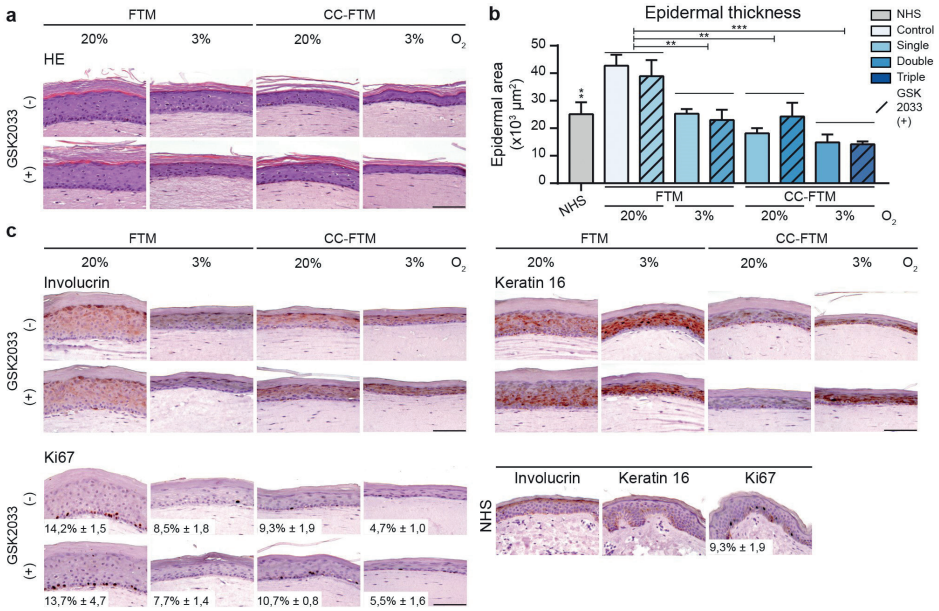


Figure 1. Epidermal morphogenesis of single, double, and triple targeted FTMs. (a) Histology of FTMs generated with single, double, and triple targeted approaches. Single targets were the dermal matrix composition (FTM or CC-FTM), oxygen level (20% or 3%), or inhibition of LXR by 500 nM GSK2033 (- or +). Double and triple targeted FTMs were generated by a combination of these. **(b)** Thickness of the viable epidermis of NHS and of indicated FTMs. **(c)** Epidermal morphogenesis examined by expression of protein biomarkers for late differentiation (involucrin), activation (keratin 16), and proliferation (Ki67). Representative images are shown with biomarkers in red and nuclei in blue, scale bar indicates 100 µm. All data represents mean + s.d., n=3.

3.2. Multitargeted optimization approach in FTMs leads to enhanced ceramide composition

Examination of the barrier formation in FTMs initiated by characterization of the SC lipid composition. To show the results efficiently, we present the data for NHS, control FTM(20-), and the FTMs which exhibited most promising results regarding epidermal morphogenesis and lipid composition. These lead optimization approaches are the CC-FTM(20-) and the CC-FTM(20+). Nonetheless, complete datasets are presented as **supplementary figures 2-6**. Within the SC of selected FTMs, a comparable level of total lipids was detected, although this was lower as compared to that of NHS (**Fig. 2 a**). The composition of CERs was

examined for the most prevalent CER subclasses [19] (**Supplementary fig. 1 g**). The LC-MS ion maps indicated deviations in CER composition of FTMs compared to NHS, including the presence of CERs with a m/z below 600 (**Supplementary fig. 7**).

Then, the lipidomics data was quantified to determine the CER composition in detail. This revealed a similar level of detected CERs within the extracted lipids derived from FTMs and NHS (**Fig. 2 b**). Quantification into absolute amounts per mg of SC also showed that the level of CERs in all FTMs was comparable to NHS (**Fig. 2 c**). The CER[non-EO] and CER[EO] subclass profiles were plotted in relative amount as percentage of the total quantified amount of CERs. The relative amounts were provided as these are directly related to the lipid phase behaviour within the SC. Comparisons of the CER[non-EO] subclass profiles between FTMs showed no differences, except for increased amounts of CER [NdS] and [AdS] between FTM(20-) and CC-FTM(20+) (**Fig. 2 d**). However, as compared to NHS in the CER[non-EO] subclass profile differences were detected for the presence of subclasses [NdS], [NS], [NP], [NH], [AS], and [AP]. The CER[EO] subclass profiles showed minor but significant changes between FTMs for [EOdS], [EOP], and [EOH] (**Fig. 2 e**). As compared to NHS, the CER[EO] subclass profile revealed substantial differences in the presence of subclasses [EOS] and [EOP].

The absolute amount of each CER[non-EO] and CER[EO] subclass per mg of SC was provided as **supplementary figure 4** for all single, double, and triple targeted FTMs. This quantitative data did not show major differences between the various FTMs, including the lead approaches. As compared to NHS, there is a deficiency in the absolute presence of [NP], [NH], [EOP], [EOH], whereas there is an overabundance in the absolute amount of subclass [AS], again indicating an imbalanced sphingolipid biosynthesis in the FTM as compared to that of NHS.

We next addressed the effects of the targeting approaches on the CER carbon chain length. Therefore, the mean carbon chain length (MCL) of CER[non-EO] and of CER[EO] was determined (**Fig. 2 g**). A drastic reduction in the MCL of CER[non-EO] was observed in FTM(20-) as compared to that of NHS. Excitingly, the MCL of CER[non-EO] in the CC-FTM(20+) was increased as a result of inhibition of LXR, thereby better mimicking that of NHS. A comparable MCL of CER[EO] in NHS, FTM(20-), and CC-FTM(20-) was observed, while the MCL of CER[EO] in CC-FTM(20+) was increased. To further evaluate the carbon chain length of CER[non-EO] and CER[EO], a distribution profile was plotted for the relative and absolute amount of CERs per number of carbons (**Supplementary fig. 8**). The carbon chain length distributions in the CER[non-EO] and CER[EO] in the various FTMs deviated substantially from that of NHS. An increased presence of CER[non-EO] ≤40 carbon atoms and a reduced presence of CER[non-EO] ≥46 carbon atoms

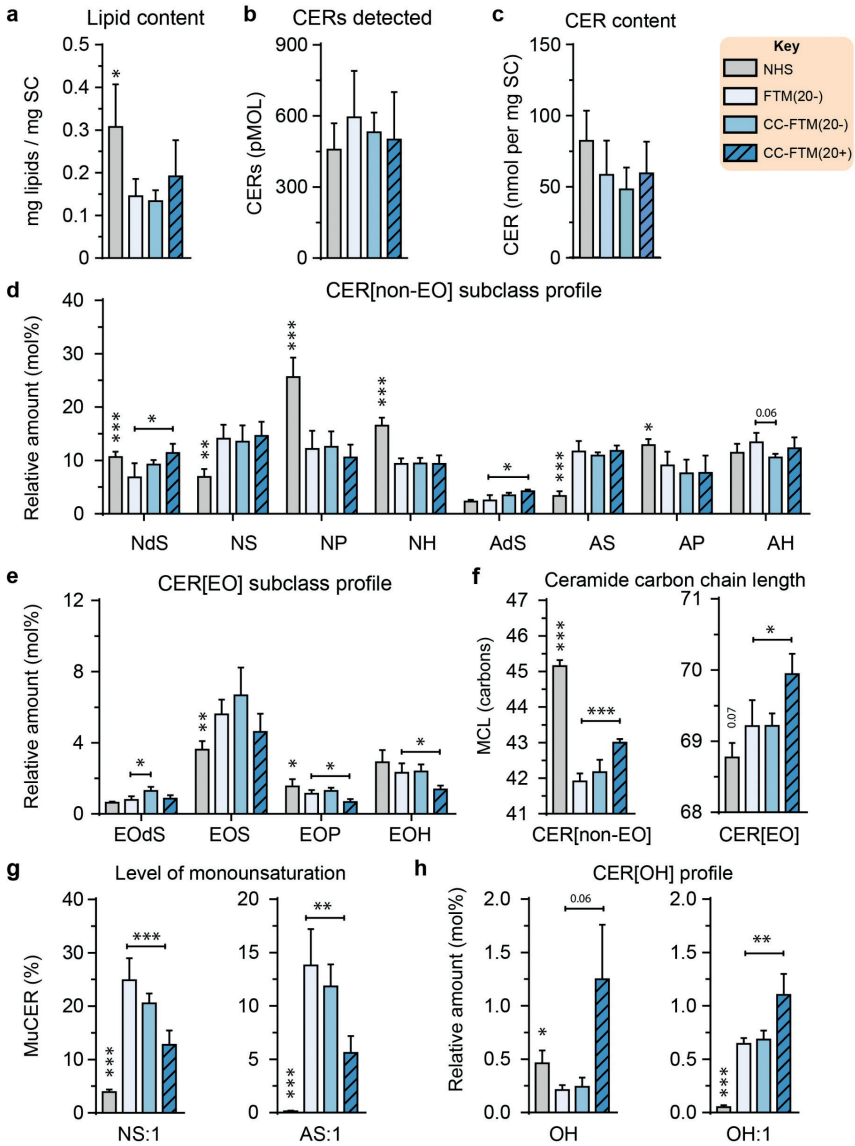


Figure 2. Ceramide composition profile in lead optimization approaches. **(a)** Total lipids in the SC of a selection of single and double targeted FTMs. **(b)** The level of total detected CERs by LC-MS in 1500 ng lipid extract of NHS and of indicated FTMs. **(c)** Absolute amount of CER in the SC as shown per mg SC of NHS and of indicated FTMs. **(d)** CER[non-EO] subclass profile in NHS and indicated FTMs, shown in relative amounts. Data is shown for saturated CERs and is indicated by mean + s.d., n≥4. **(e)** CER[EO] subclass profile in NHS and indicated FTMs, shown in relative amounts. Data is shown for saturated CERs and is indicated by mean + s.d., n≥4. **(f)** Mean carbon chain length of CER[non-EO] and CER[EO] in indicated FTMs. **(g)** Level of monounsaturated CERs for subclasses [AS] and [NS]. Level of monounsaturation is indicated by the percentage of muCERs within each subclass. **(h)** The relative amount of saturated and monounsaturated CER[OH]. Data is shown for NHS, single and double targeted FTMs. Data represents mean + s.d., n≥4.

in the control FTM(20-) in relative and absolute amount was observed. This contributed to the considerable lower MCL in the FTM(20-) as compared to NHS. Interestingly, the relative carbon chain length distribution profile of CC-FTM(20+) better resembled that of NHS due to a lower level CER[non-EO] ≤40 carbon atoms and a higher level of CER[non-EO] ≥46 carbon atoms. This explains the higher MCL of CER[non-EO] in the CC-FTM(20+) as compared to the control.

Subsequently, the level of muCERs was determined, which was indicated by the percentage of muCERs within the subclasses [NS] and [AS]. This provides an indication for the fraction of muCERs for all subclasses (**Fig. 2 g**). In FTMs, the level of muCERs was substantially increased as compared to that in NHS. Interestingly, the percentage of muCERs was significantly reduced after inhibition of LXR in all conditions (**Supplementary fig. 5**), better resembling the level of muCERs in the CER[non-EO] composition of NHS. The level of muCERs in the CER[EO] composition of the SC was also determined, although due to a higher number of subgroups within the CER[EO] subclasses this was more complex. Four different subgroups can be distinguished for CER[EO], based on the degree of unsaturation (saturated saCER[EO] or monounsaturated muCER[EO]) and on the type of ester linked FFA residue (oleic acid [EO-18:1] or linoleic acid [EO-18:2]) as illustrated in **supplementary figure 1 g**. These four subgroups were analysed for the subclass EOS in NHS, FTM(20-), CC-FTM(20-) and CC-FTM(20+) (**Supplementary fig. 6**). However, saCER[EOS-18:2] and muCER[EOS-18:1] elute at the same retention time and share the same m/z, therefore these are presented as a mixed subgroup. When comparing the CER[EOS] subgroup profiles of NHS and control FTM(20-), a major difference was observed in the presence of saCER[EO-18:1]. Strikingly, this subgroup was substantially present in FTMs, whereas it was absent in NHS. This contributed to the increased overall presence of subclass [EOS] in the lipid matrix of FTMs as compared to NHS. Comparing the CER[EOS] subgroup profile between the various FTMs, only the subgroup of muCER[EOS-18:2] was increased in CC-FTM(20+) as compared to control FTM(20-) indicating a small difference between the subgroup profiles for CER[EOS] induced by the various optimization approaches.

The ω-hydroxyceramide (CER[O]) subclass was also detected by the lipidomics analysis. In-depth profiling was performed before in a recent study of Helder *et al.* (Helder *et al.*, submitted), where it was reported that the CER[OH] subclass serves as valuable indicator for the presence and composition of all CER[O] subclasses. Therefore, the CER[OH] profile was determined as percentage of the total quantified amount of ceramides in NHS, FTM(20-), CC-FTM(20-), and CC-FTM(20+) (**Fig. 2 h**). In NHS, mainly the saCER[OH] was detected, whereas in the various models the muCER[OH] was predominant, contributing to an overall increase of CER[OH] in the FTMs. When comparing the optimization approaches,

addition of the LXR antagonist significantly increased the amount of saCER[OH] and muCER[OH] in the lipid matrix of the SC.

In summary, we observed a substantially improved ceramide composition in the double targeting approach which involved inhibition of LXR as compared to control FTM(20-).

3.3. Lead optimization approaches improve organization of the lipid matrix

Complementary to the compositional analyses, we evaluated the lipid organization in the SC of FTMs developed with the lead optimization approaches. In all FTMs, the lipids assembled in lipid lamellae with repeat distances characteristic for the LPP, as detected in the SAXD diffraction profiles (**Fig. 3 a**). From the position of the peaks, the repeat distance of the LPP was calculated, which was similar for all conditions tested (**Fig. 3 b**). Nevertheless, the repeat distance in all FTMs was shorter than the reported LPP repeat distance of NHS. Additionally, the presence of the SPP was not observed in FTMs, although this is present in NHS [33].

The lateral lipid organization was examined by FTIR analyses. The spectrum of the methylene rocking vibrational mode is indicative for the orthorhombic lateral packing when there are two peaks present at 719 cm^{-1} and 730 cm^{-1}, whereas the hexagonal lateral packing is indicated by a single peak at 719 cm^{-1}. In the FTM(20-) at 10°C, the spectra showed a single peak at 719 cm^{-1}, indicating that lipids were predominantly arranged in the hexagonal lateral packing (**Fig. 3 c**). In CC-FTM(20-) and CC-FTM(20+), the peak at 730 cm^{-1} was stronger, indicating that a higher fraction of lipids adapted the orthorhombic lateral packing. Yet, in NHS the peak at 730 cm^{-1} was most intense, indicating that in NHS a higher fraction of lipids were predominantly arranged in the orthorhombic lateral packing.

In summary, our analyses showed that the lipid organization in the control FTM(20-) differs from that of NHS, which is partially restored in the lead optimization approached regarding the lipid lateral packing.

3.4. Lead targeted FTMs enhances barrier functionality

Evaluation of the barrier formation in the lead targeted FTMs was finalized by determination of the barrier functionality. For the outside-in barrier functionality assessment, benzocaine was used as model compound. The benzocaine flux values were lower for the lead optimization approaches as compared the control FTM(20-) (**Fig. 4 a**). Nevertheless, the flux values remained higher in all FTMs as compared to NHS. Next, the inside-out barrier functionality was examined by measuring the transepidermal water loss (TEWL) over time. This examination again revealed an impaired barrier functionality in control FTM(20-) as compared to NHS (**Fig. 4 b**). Importantly, the TEWL values were substantially lower in the

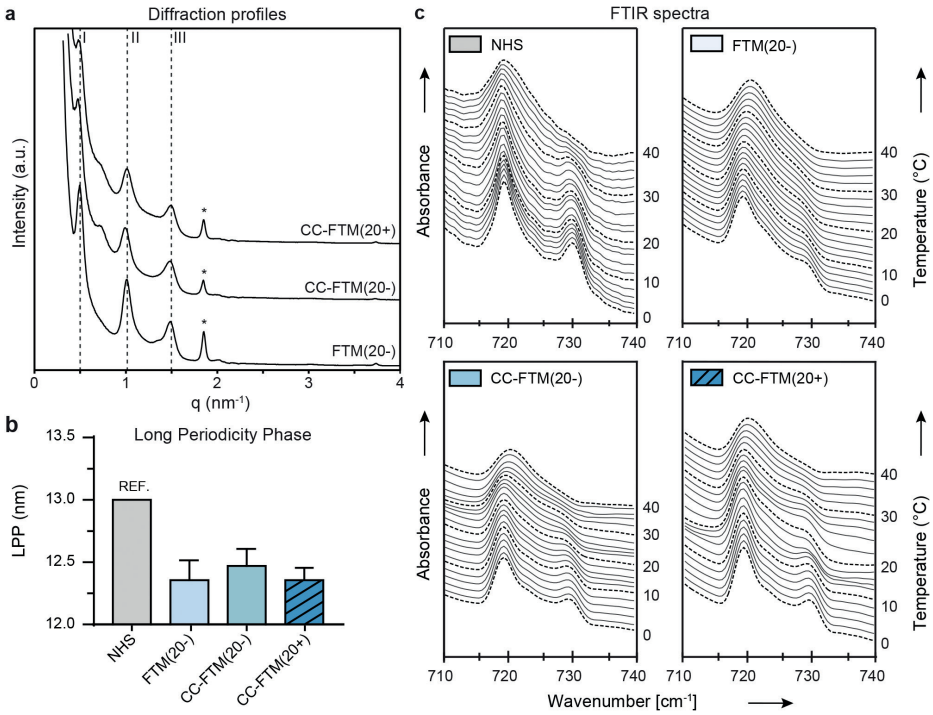


Figure 3. Lipid matrix organization in the SC of NHS and lead targeted FTMs. (a) Small angle X-ray diffraction profiles of selected single- and multitargeted full thickness models. Data is shown as intensity in arbitrary units (a.u.) on the y-axis and scattering vector q on x-axis. The position of the diffraction orders (I, II and III) are indicated by dashed lines, whereas cholesterol phase is indicated by the asterisk symbol (*). **(b)** Bar plot of calculated repeat distance of the LPP in FTMs. Values for NHS were obtained from reference Bouwstra *et al.* [33], data represents mean + s.d. **(c)** FTIR spectra of NHS and selected single- and multitargeted FTMs. Data is presented in absorbance (in a.u.) on the left y-axis over the wavenumber (in cm^{-1}) on the x-axis in the absorbance region corresponding to the methylene rocking vibrational mode. On the right y-axis, the temperature of measurement is shown (from 0°C to 40°C).

CC-FTM(20-) and CC-FTM(20+). These assessments revealed an enhanced barrier functionality in the lead optimization approaches.

4. Discussion

In this study, we unravelled that optimization of *in vitro* developed FTMs using advanced single, double, and triple targeted approaches resulted in better mimicking of NHS. The epidermal morphogenesis was improved after modification of the dermal ECM by chitosan. Furthermore, the lipid barrier composition was enhanced after inhibition of the liver-X-receptor. These effects

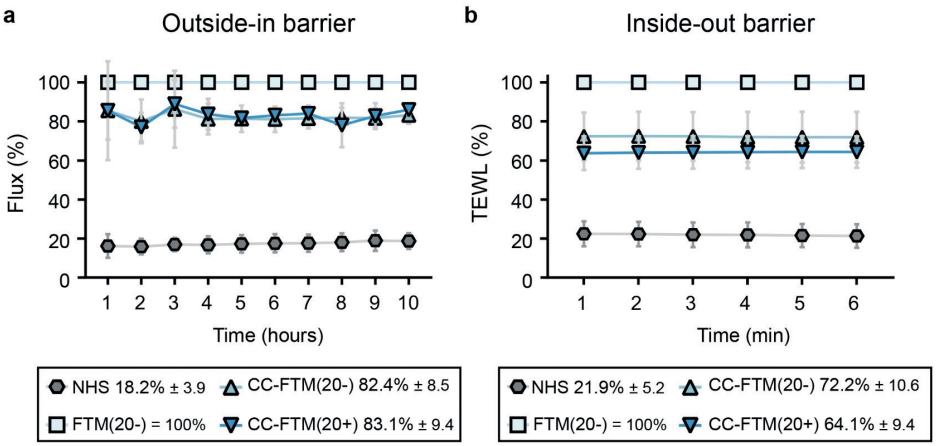


Figure 4. Barrier functionality in single and double targeted FTMs. (a) Evaluation of outside-in barrier functionality of NHS and of selected FTMs. The relative flux of benzocaine is plotted over time. Data is shown relative to FTM(20-), where 100% equals a benzocaine flux of 49,5 µg/cm²/h. **(b)** Evaluation of inside-out barrier functionality of NHS and of indicated FTMs. Transepidermal water loss (TEWL) is measured over time. Shown datasets are shown relative to FTM(20-), where 100% equals a TEWL of 12,7 g/m²/h. Data represents mean ± s.d., n≥3. Relative steady-state values are indicates in the figure legend.

persisted by targeting both factors, resulting in better functionality of the epidermal barrier and closer resemblance to NHS.

The presence of the four epidermal layers of NHS is mirrored in all FTMs, in agreement with results obtained in previous studies ([27], Mieremet *et al.* (chapter 5), and Helder *et al.* submitted). In addition, the epidermal morphogenesis of CC-FTM(20-) and CC-FTM(20+) better mimicked that of NHS, based on the reduced thickness of the viable epidermis, reduced thickness of granular cells, and lower epidermal activation as compared to FTM(20-). The morphogenesis of the double targeted CC-FTM(3-) and triple targeted CC-FTM(3+) showed a substantial thinner viable epidermis and lower proliferation in these models as compared to NHS. This is a result of the combinatory anti-proliferative effects of chitosan which allowed keratinocytes to better adhere and the lower oxygen level which reduced the cellular metabolism rate [34-36]. This shows that a combination of promising single targets could lead to suboptimal outcomes.

The CER composition was characterized for all single, double, and triple targeted approaches. The results clearly showed that inhibition of the nuclear receptor LXR increased the MCL of CER[non-EO] and reduced the level of monounsaturated CER [AS] and [NS], in line with previously obtained findings (Helder *et al.* submitted). These effects were present irrespective of dermal equivalent type (FTM or CC-FTM) or external oxygen level (20 or 3%), indicating the robustness of

the LXR inhibition by supplementation of the cell culture medium with GSK2033. Unfortunately, the alterations in CER composition induced by dermal equivalent type (FTM or CC-FTM) [27] or external oxygen level (20 or 3%) as observed in earlier studies (Mieremet *et al.* (chapter 5)) did not fully persist in this study. This could possibly be explained by donor variability, or batch-to-batch variations.

The lipid organization was studied for the lead optimization approaches, revealing similar lamellar and improved lateral lipid organization compared to control FTM(20-). Due to a lower level of monounsaturated CER[non-EO], a higher fraction of lipids was able to adapt the orthorhombic packing, although the hexagonal packing remained predominant [21]. In general, the level of monounsaturated CER[non-EO] reduced after LXR inhibition, but the increased presence of monounsaturated CER[O] partially counteracted this effect, leading to similar effects in the CC-FTM(20-) and CC-FTM(20+) on lateral organization. As the hexagonal packing was reduced but not to levels as observed in NHS, it implicates that other factors also contribute to formation of the hexagonal lateral packing, for example the reduced ratio of FFA to CER in FTMs compared to that in NHS (Mieremet and Helder *et al.*, (chapter 8)) [37, 38]. Future studies should aim to optimize the ratio of CER/FFA/cholesterol in HSEs, which could promote the formation of the orthorhombic lateral packing. Besides, it has been shown that CER[non-EO] with 34 carbon atoms as compared to CER[non-EO] with 42 carbon atoms in lipid membrane models modified the lipid organization and reduced the barrier functionality [39]. This is in line with our observations in HSEs, therefore reduction of CER[non-EO] with ≤40 carbon atoms in HSEs is an important issue for future research to improve lipid organization and barrier functionality. Moreover, the increased presence of CER[EO-18:1] in the lipid matrix also contributes to an altered barrier formation [40].

The increased presence of CER[EO-18:1] was also observed in fatty acid deficiency [41, 42], therefore the amount of supplemented linoleic acid is prone for optimization, thereby potentially reducing the presence of CER[EO-18:1] leading to improvements of barrier formation of HSEs. However, incorporation of linoleic acid into triglycerides instead of in CER[EO] remains a limiting factor [43]. Additionally, the increased presence of CER[O] in the lipid matrix after LXR inhibition is dissimilar to NHS. CER[O] is covalently bound to the cornified envelope, although it is also partially present in the lipid matrix. Previously, we investigated the mechanisms underlying the increased presence of CER[O] in the lipid matrix after LXR inhibition by examining the gene expression of major lipid processing enzymes involved in mediation of cross-linking CER[O] to the protein envelope (i.e. TGM-1, CYP4F22, PNPLA1, Alox-12B, and Alox-E3) (Helder *et al.*, submitted) [44-46]. As these enzymes were equally expressed in both conditions,

it remains to be elucidated why saturated and monounsaturated CER[O] are more present in the lipid matrix after LXR inhibition.

The barrier function was assessed in this study for the lead optimization approaches through an outside-in diffusion study with benzocaine. Benzocaine has a low molecular weight (165.189 g/mol) and medium lipophilicity (LogP = 1.9), thereby serving as ideal model compound which efficiently diffuses through the intercorneocyte space of the SC [32, 47, 48]. As the composition and organization of lipids showed improvements, this was accurately reflected by lower benzocaine diffusion fluxes in the corresponding HSEs. Nevertheless, it is of interest for follow-up studies to determine compound diffusion profiles for high MW or suboptimal lipophilicities in order to better understand barrier permeability in HSEs as compared to NHS. The inside-out barrier functionality is based on evaporation of water through the SC [49]. The results of TEWL revealed enhanced inside-out performances, corresponding to results of lipid composition. However, the lipid composition in CC-FTM(20-) in this study was to a certain degree improved as compared to FTM(20-), although previous reported findings showed more substantial improvements in the lipid composition of the CC-FTM [27]. As thereby the improved TEWL values are not clearly linked to the lipid profiles, it is therefore possible that also the formation of corneocytes is enhanced, which led to reduced water evaporation through the SC [50]. Moreover, a clear association of percutaneous penetration with TEWL in *in vitro* developed HSE is more difficult to ascertain [51], in contrast to an established correlation found in NHS [52, 53].

In conclusion, HSEs developed with advanced optimization approaches showed considerable improvements for epidermal morphogenesis in combination with enhanced lipid barrier formation and functionality, thereby better mimicking NHS.

5. Acknowledgments

This research was financially supported by Dutch Technology Foundation TTW (grant no. 13151), which is part of the Netherlands Organisation for Scientific Research (NWO), and which is partly funded by the Ministry of Economic Affairs. The personnel at European Synchrotron Radiation Facility working at the DUBBLE beam line (BM26) are thanked for their help with the SAXD measurements. We thank the company Evonik (Essen, Germany) for contribution of ceramides.

6. Competing interests

The authors have declared no conflicting interests.

7. Author contributions

AM, RWJH JAB and AEG designed the research study. AM, RWJH, AN, and GG performed the research. AM, RWJH, AN and WB performed the data analysis. AM and RWJH drafted the manuscript, which was commented on by JAB and AEG.

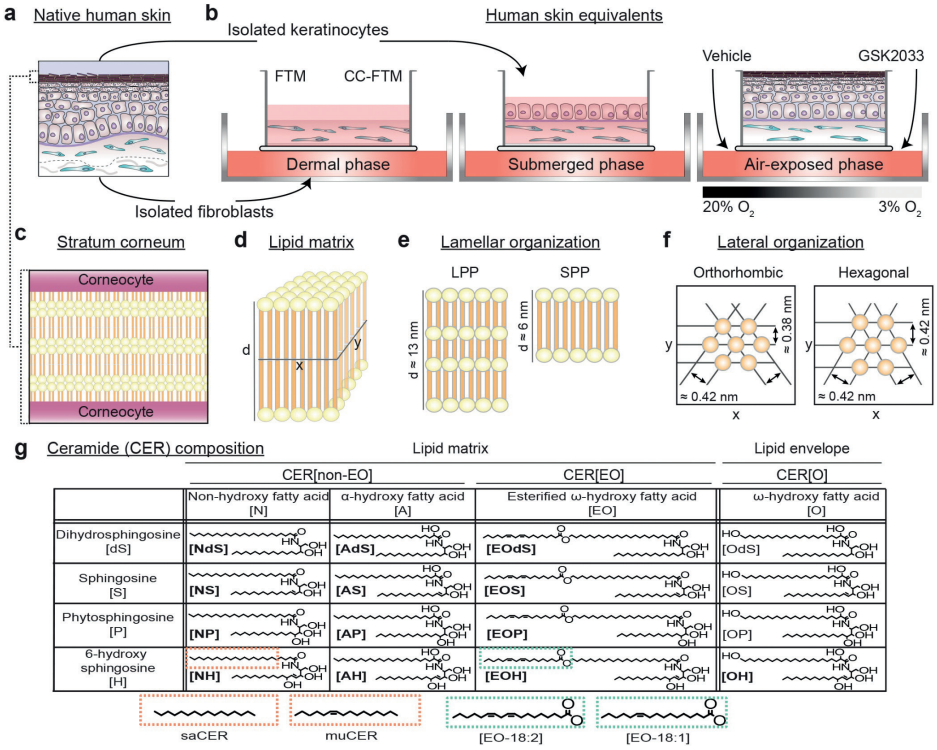
8. References

1. Mathes, S.H., H. Ruffner, and U. Graf-Hausner, The use of skin models in drug development. Advanced Drug Delivery Reviews, 2014. 69-70: p. 81-102.
2. Gordon, S., et al., Non-animal models of epithelial barriers (skin, intestine and lung) in research, industrial applications and regulatory toxicology. Alternatives to Animal Experimentation: ALTEX, 2015. 32(4): p. 327-378.
3. Niehues, H., et al., 3D skin models for 3R research: The potential of 3D reconstructed skin models to study skin barrier function. Experimental dermatology, 2018. 27(5): p. 501-511.
4. El Ghalbzouri, A., et al., Leiden reconstructed human epidermal model as a tool for the evaluation of the skin corrosion and irritation potential according to the ECVAM guidelines. Toxicology in Vitro, 2008. 22(5): p. 1311-1320.
5. Wufuer, M., et al., Skin-on-a-chip model simulating inflammation, edema and drug-based treatment. Scientific Reports, 2016. 6: p. 37471.
6. Sriram, G., et al., Full-thickness human skin-on-chip with enhanced epidermal morphogenesis and barrier function. Materials Today, 2018. 21(4): p. 326-340.
7. van den Broek, L.J., et al., Progress and Future Prospectives in Skin-on-Chip Development with Emphasis on the use of Different Cell Types and Technical Challenges. Stem Cell Reviews and Reports, 2017. 13(3): p. 418-429.
8. Thakoersing, V.S., et al., Unraveling Barrier Properties of Three Different In-House Human Skin Equivalents. Tissue Engineering Part C: Methods, 2012. 18(1): p. 1-11.
9. Schafer-Korting, M., et al., Reconstructed human epidermis for skin absorption testing: results of the German prevalidation study. ATLA, 2006. 34(3): p. 283.
10. Van Gele, M., et al., Three-dimensional skin models as tools for transdermal drug delivery: challenges and limitations. Expert Opinion on Drug Delivery, 2011. 8(6): p. 705-720.
11. Flaten, G.E., et al., In vitro skin models as a tool in optimization of drug formulation. European Journal of Pharmaceutical Sciences, 2015. 75: p. 10-24.
12. Planz, V., C.-M. Lehr, and M. Windbergs, In vitro models for evaluating safety and efficacy of novel technologies for skin drug delivery. Journal of Controlled Release, 2016. 242: p. 89-104.
13. Proksch, E., J.M. Brandner, and J.-M. Jensen, The skin: an indispensable barrier. Experimental Dermatology, 2008. 17(12): p. 1063-1072.
14. Feingold, K.R. and P.M. Elias, Role of lipids in the formation and maintenance of the cutaneous permeability barrier. Biochimica et Biophysica Acta - Molecular and Cell Biology of Lipids, 2014. 1841(3): p. 280-294.
15. van Smeden, J. and J.A. Bouwstra, Stratum Corneum Lipids: Their Role for the Skin Barrier Function in Healthy Subjects and Atopic Dermatitis Patients. Curr Probl Dermatol, 2016. 49: p. 8-26.
16. Bouwstra, J.A. and G.S. Gooris, The lipid organisation in human stratum corneum and model systems. The Open Dermatology Journal, 2010. 4(1).
17. Boncheva, M., The physical chemistry of the stratum corneum lipids. International journal of cosmetic science, 2014. 36(6): p. 505-515.
18. Masukawa, Y., et al., Comprehensive quantification of ceramide species in human stratum corneum. Journal of lipid research, 2009. 50(8): p. 1708-1719.
19. Boiten, W., et al., Quantitative analysis of ceramides using a novel lipidomics approach with three dimensional response modelling. Biochimica et Biophysica Acta - Molecular and Cell Biology of Lipids, 2016. 1861(11): p. 1652-1661.
20. t'Kindt, R., et al., Profiling and Characterizing Skin Ceramides Using Reversed-Phase Liquid Chromatography–Quadrupole Time-of-Flight Mass Spectrometry. Analytical Chemistry, 2012. 84(1): p. 403-411.
21. Mojumdar, E.H., et al., Monounsaturated Fatty Acids Reduce the Barrier of Stratum Corneum Lipid Membranes by Enhancing the Formation of a Hexagonal Lateral Packing. Langmuir, 2014. 30(22): p. 6534-6543.
22. Janssens, M., et al., Increase in short-chain ceramides correlates with an altered lipid organization and decreased barrier function in atopic eczema patients. Journal of lipid research, 2012. 53: p. 2755-2766.
23. Lee, M.H., et al., Effect of composition on water permeability of model stratum corneum lipid membranes. Soft Matter, 2012. 8(5): p. 1539-1546.
24. Ponec, M., et al., Barrier Function in Reconstructed Epidermis and Its Resemblance to Native Human Skin. Skin Pharmacology and Physiology, 2001. 14(Suppl. 1): p. 63-71.
25. Thakoersing, V.S., et al., Increased presence of monounsaturated fatty acids in the stratum corneum of human skin equivalents. Journal of Investigative Dermatology, 2013. 133(1): p. 59-67.

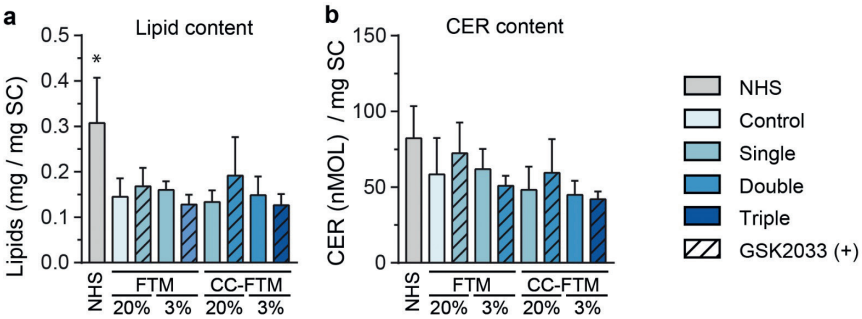
26. Netzlaff, F., et al., The human epidermis models EpiSkin®, SkinEthic® and EpiDerm®: An evaluation of morphology and their suitability for testing phototoxicity, irritancy, corrosivity, and substance transport. European Journal of Pharmaceutics and Biopharmaceutics, 2005. 60(2): p. 167-178.
27. Mieremet, A., et al., Improved epidermal barrier formation in human skin models by chitosan modulated dermal matrices. PLoS ONE, 2017. 12(3): p. e0174478.
28. Haisma, E.M., et al., Inflammatory and antimicrobial responses to methicillin-resistant Staphylococcus aureus in an in vitro wound infection model. PloS ONE, 2013. 8(12): p. e82800.
29. Ponec, M., et al., The formation of competent barrier lipids in reconstructed human epidermis requires the presence of vitamin C. Journal of Investigative Dermatology, 1997. 109(3): p. 348-355.
30. Berkers, T., et al., Topically applied fatty acids are elongated before incorporation in the stratum corneum lipid matrix in compromised skin. Experimental Dermatology, 2017. 26(1): p. 36-43.
31. Bligh, E.G. and W.J. Dyer, A rapid method of total lipid extraction and purification. Canadian journal of biochemistry and physiology, 1959. 37(8): p. 911-917.
32. de Jager, M., et al., A novel in vitro percutaneous penetration model: evaluation of barrier properties with p-aminobenzoic acid and two of its derivatives. Pharm Res, 2006. 23(5): p. 951-60.
33. Bouwstra, J.A., et al., Structural investigations of human stratum corneum by small-angle X-ray scattering. Journal of Investigative Dermatology, 1991. 97(6): p. 1005-12.
34. Howling, G.I., et al., The effect of chitin and chitosan on the proliferation of human skin fibroblasts and keratinocytes in vitro. Biomaterials, 2001. 22(22): p. 2959-2966.
35. Straseski, J.A., et al., Oxygen deprivation inhibits basal keratinocyte proliferation in a model of human skin and induces regio-specific changes in the distribution of epidermal adherens junction proteins, aquaporin-3, and glycogen. Wound Repair and Regeneration, 2009. 17(4): p. 606-616.
36. Chatelet, C., O. Damour, and A. Domard, Influence of the degree of acetylation on some biological properties of chitosan films. Biomaterials, 2001. 22(3): p. 261-268.
37. Gooris, G.S. and J.A. Bouwstra, Infrared Spectroscopic Study of Stratum Corneum Model Membranes Prepared from Human Ceramides, Cholesterol, and Fatty Acids. Biophysical Journal, 2007. 92(8): p. 2785-2795.
38. van Smeden, J., et al., The important role of stratum corneum lipids for the cutaneous barrier function. Biochimica et Biophysica Acta - Molecular and Cell Biology of Lipids, 2014. 1841(3): p. 295-313.
39. Pullmannová, P., et al., Permeability and microstructure of model stratum corneum lipid membranes containing ceramides with long (C16) and very long (C24) acyl chains. Biophysical Chemistry, 2017. 224: p. 20-31.
40. Bouwstra, J.A., et al., Phase Behavior of Stratum Corneum Lipid Mixtures Based on Human Ceramides: The Role of Natural and Synthetic Ceramide 1. Journal of Investigative Dermatology, 2002. 118(4): p. 606-617.
41. Wertz, P.W., E.S. Cho, and D.T. Downing, Effect of essential fatty acid deficiency on the epidermal sphingolipids of the rat. Biochimica et Biophysica Acta - Lipids and Lipid Metabolism, 1983. 753(3): p. 350-355.
42. Hansen, H.S. and B. Jensen, Essential function of linoleic acid esterified in acylglucosylceramide and acylceramide in maintaining the epidermal water permeability barrier. Evidence from feeding studies with oleate, linoleate, arachidonate, columbinate and α-linolenate. Biochimica et Biophysica Acta - Lipids and Lipid Metabolism, 1985. 834(3): p. 357-363.
43. Vičanová, J., et al., Incorporation of linoleic acid by cultured human keratinocytes. Archives of Dermatological Research, 1999. 291(7): p. 405-412.
44. Ohno, Y., et al., PNPLA1 is a transacylase essential for the generation of the skin barrier lipid ω-O-acylceramide. Nature communications, 2017. 8: p. 14610.
45. Ohno, Y., et al., Essential role of the cytochrome P450 CYP4F22 in the production of acylceramide, the key lipid for skin permeability barrier formation. PNAS, 2015. 112(25): p. 7707-7712.
46. Elias, P.M., et al., Formation and functions of the corneocyte lipid envelope (CLE). Biochimica et Biophysica Acta - Molecular and Cell Biology of Lipids, 2014. 1841(3): p. 314-318.
47. Naik, A., Y.N. Kalia, and R.H. Guy, Transdermal drug delivery: overcoming the skin's barrier function. Pharmaceutical Science & Technology Today, 2000. 3(9): p. 318-326.
48. Bolzinger, M.-A., et al., Penetration of drugs through skin, a complex rate-controlling membrane. Current Opinion in Colloid & Interface Science, 2012. 17(3): p. 156-165.
49. Akdeniz, M., et al., Transepidermal water loss in healthy adults: a systematic review and meta-analysis update. British Journal of Dermatology, 2018. 179: p. 1049-1055.
50. Hadgraft, J. and M.E. Lane, Transepidermal water loss and skin site: A hypothesis. International Journal of Pharmaceutics, 2009. 373(1): p. 1-3.

51. Chilcott, R.P., et al., Transepidermal water loss does not correlate with skin barrier function in vitro. Journal of Investigative Dermatology, 2002. 118(5): p. 871-875.
52. Levin, J. and H. Maibach, The correlation between transepidermal water loss and percutaneous absorption: an overview. Journal of Controlled Release, 2005. 103(2): p. 291-299.
53. Lotte, C., et al., In vivo relationship between transepidermal water loss and percutaneous penetration of some organic compounds in man: effect of anatomic site. Archives of dermatological research, 1987. 279(5): p. 351-356.
54. Motta, S., et al., Ceramide composition of the psoriatic scale. Biochimica et Biophysica Acta - Molecular Basis of Disease, 1993. 1182(2): p. 147-151.
55. Vávrová, K., A. Kováčik, and L. Opálka, Ceramides in the skin barrier. Acta Facultatis Pharmaceuticae Universitatis Comenianae, 2017. 64(2): p. 28-35.

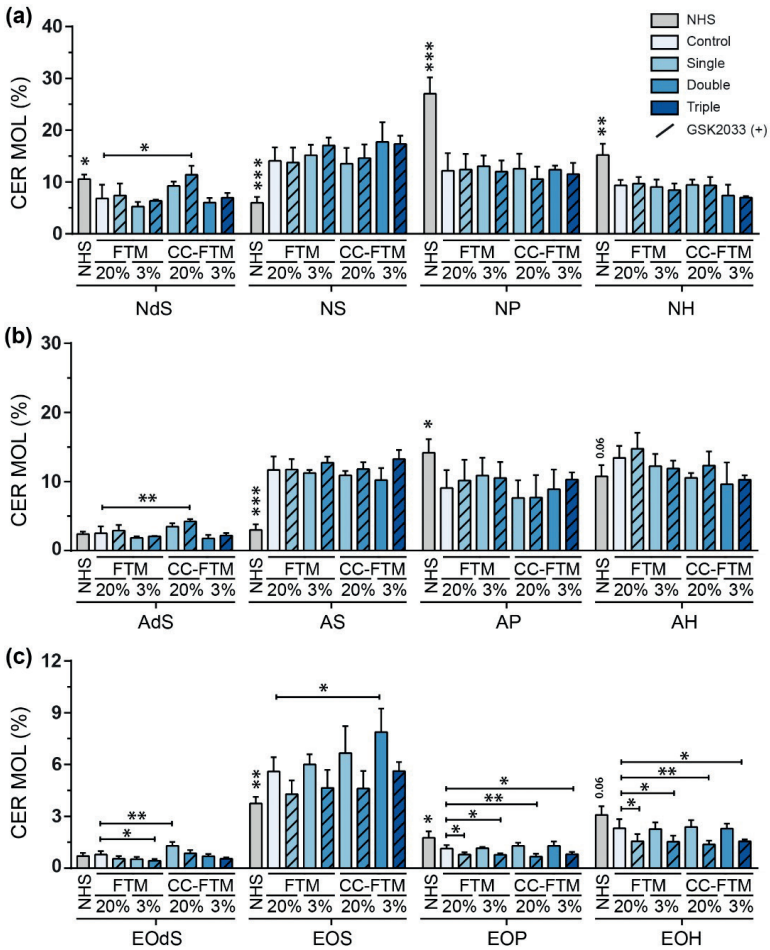
9. Supplementary information



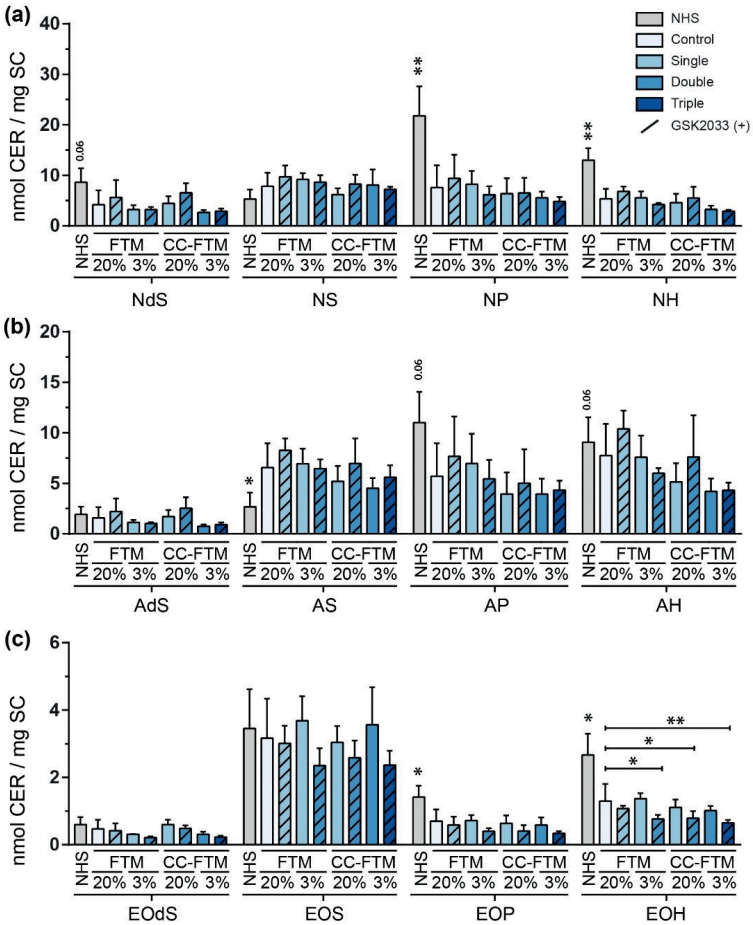
Supplementary figure 1. Illustration of study approach and key concepts of the lipid barrier. **(a)** Schematic overview of a cross section of the native human skin showing the dermis containing fibroblasts and the epidermis containing keratinocytes. **(b)** Study approach for the development of single- and multitargeted FTMs. Development of FTMs occurred in three main phases. 1) Dermal phase: isolated primary fibroblasts were seeded in a collagen or in a collagen-chitosan extracellular matrix, to develop FTMs or CC-FTMs respectively. 2) Submerged phase: isolated primary keratinocytes were seeded on top of the dermal equivalent. 3) Air-exposed phase: Differentiation occurred leading to full epidermal stratification. In this study, external oxygen level was reduced to 3% and/or LXR antagonist GSK2033 was added to the medium. **(c)** Schematic overview of the intercorneocyte lipid matrix of the stratum corneum. **(d)** Illustration of the lipid matrix. Hydrophilic head group regions and hydrophobic hydrocarbon chain regions were indicated by the yellow dots or orange columns respectively. **(e)** Simplified overview of the lamellar organization. Long periodicity phase (LPP) and short periodicity phase (SPP) as shown with characteristic repeat distance. **(f)** Lateral organization of the hydrocarbon chains. The orthorhombic organization is a very dense ordered packing, whereas the hexagonal organization is a dense ordered packing. **(g)** Ceramide composition with subclasses indicated and named after their combination of sphingosine base and free fatty acid chain, according to Motta *et al.* [54] and expanded as reviewed by Vávrová *et al.* [55]. Additional CER[non-EO] entities exist based on their saturated CER (saCER) or monounsaturated CER (muCER) hydrocarbon chains, whereas additional CER[EO] entities exist based on the esterified linoleic (CER[EO-18:2]) or oleic (CER[EO-18:1]) acid residue. In this study, the ceramide subclasses indicated in bold were analysed.



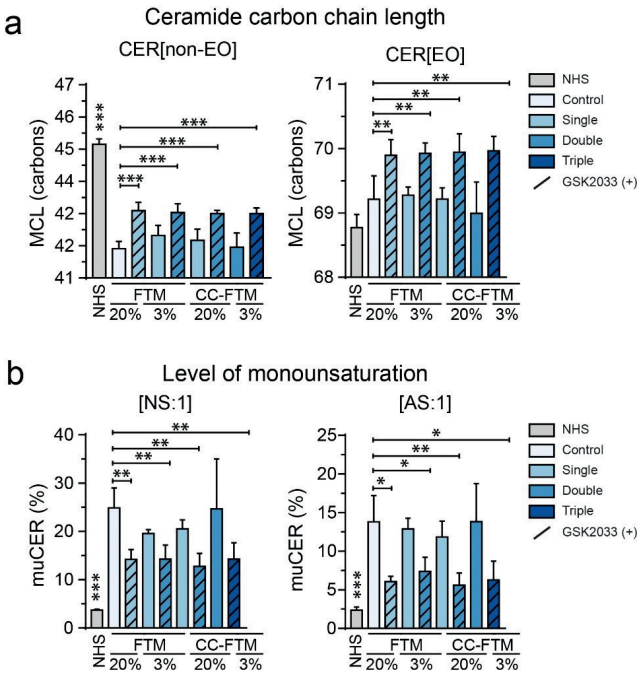
Supplementary figure 2. Total lipid and ceramide content in the SC of all single, double, and triple targeted FTMs. (a) Total lipids in the SC of NHS and all single- and multitargeted FTMs and NHS. **(b)** Absolute amount of CER in the SC as shown per mg SC of NHS and of all single- and multitargeted FTMs. Data represents mean + s.d., n≥4.



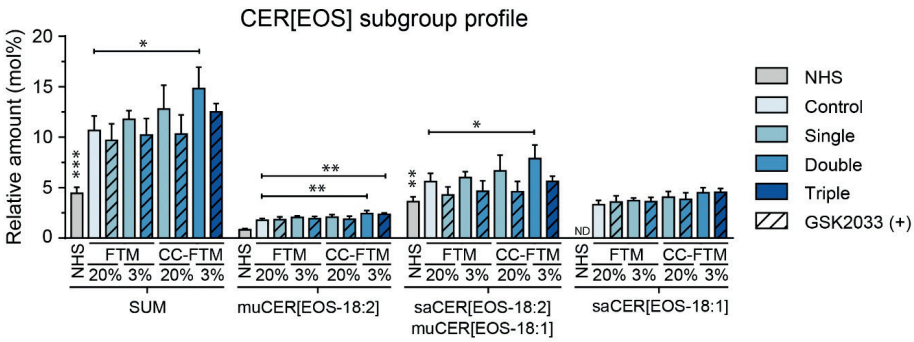
Supplementary figure 3. Relative ceramide subclass profiles of all single, double, and triple targeted FTMs. Relative amount of **(a)** non-hydroxy CER[non-EO], **(b)** alpha hydroxy CER[non-EO], and **(c)** esterified omega hydroxy CER[EO] in NHS and FTMs. Data represents saturated CERs and is presented in relative amounts as mean + s.d., n≥4.



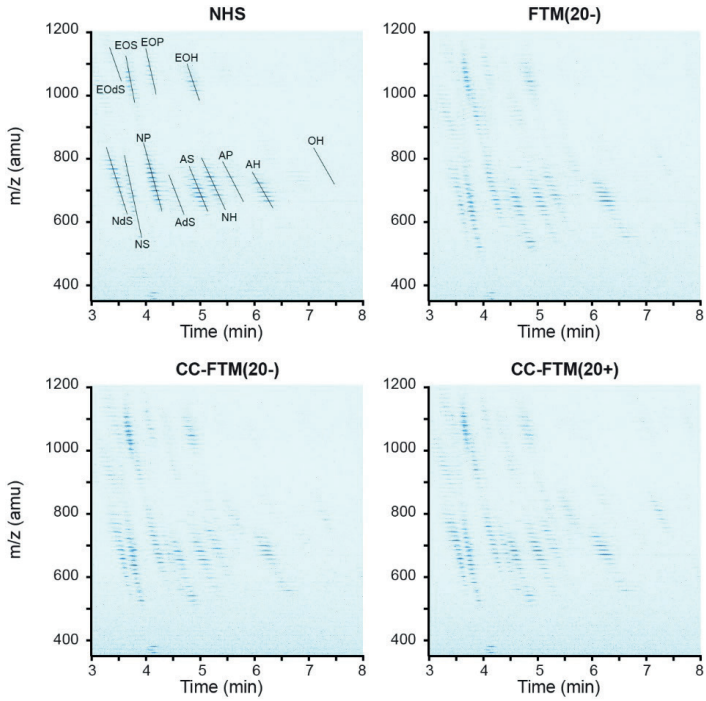
Supplementary figure 4. Quantitative ceramide subclass profiles of all single, double, and triple targeted FTMs. Quantitative amount of **(a)** non-hydroxy CER[non-EO], **(b)** alpha hydroxy CER[non-EO], and **(c)** esterified omega hydroxy CER[EO] in NHS and FTMs. Data represents saturated CERs and is presented in absolute amounts per mg SC as mean + s.d., n≥4.



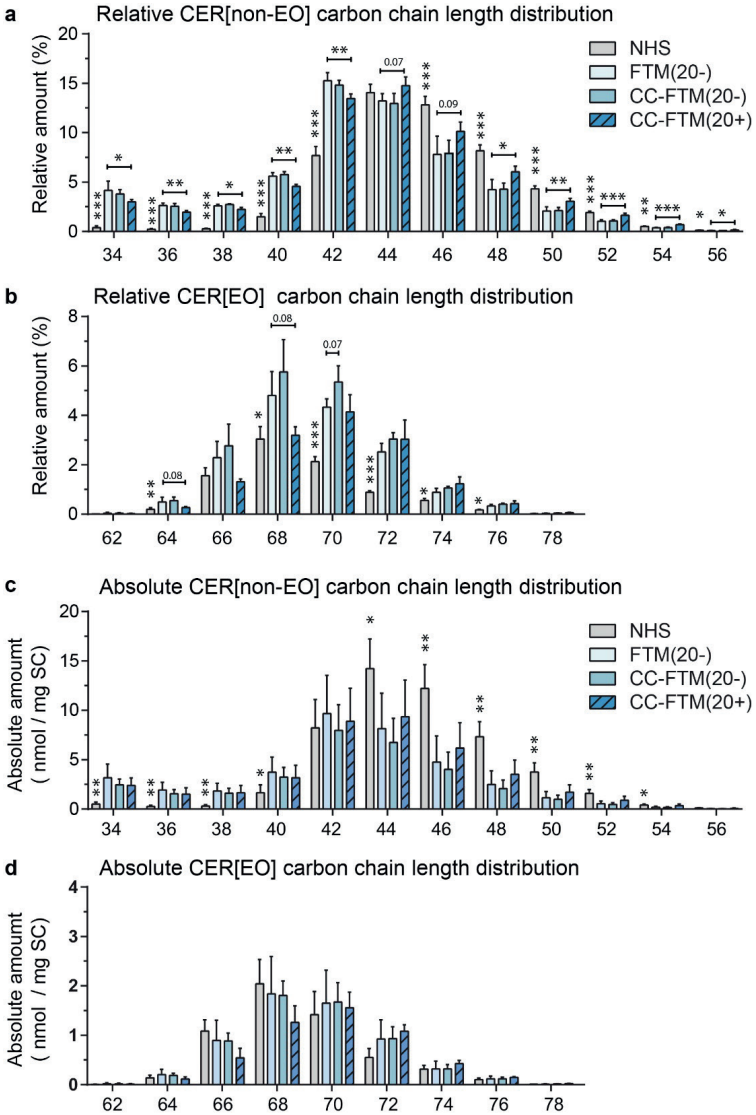
Supplementary figure 5. Mean ceramide carbon chain lengths and level of monounsaturation in all single, double, and triple targeted FTMs. (a) Mean carbon chain length of CER[non-EO] and of CER[EO]. **(b)** Level of monounsaturation presented as percentage of monounsaturated ceramide per subclass. The CER[NS:1] and CER[AS:1] are shown, which contain a single desaturation in their acyl chain. Data represents mean + s.d., n≥4.



Supplementary figure 6. Subgroup profile of subclass EOS in all single, double and triple targeted FTMs. Subgroups are created based on level of desaturation (saturated ceramide (saCER) and monounsaturated CER(muCER) and on type of esterified FFA residue (linoleic acid (18:2) or oleic acid (18:1)). This results in four subgroups for each CER[EO] subclass: muCER[EOS-18:2], muCER[EOS-18:1], saCER[EOS-18:2], and saCER[EOS-18:1]. No distinction can be made in detection between muCER[EOS-18:1] and saCER[EOS-18:2], therefore these are indicated as mixed subgroup. Relative amount of subclass [EOS] is presented as sum of all and per subgroup. Data represents percentage of the total quantified amount as mean + s.d., n≥4. ND indicates no detection.



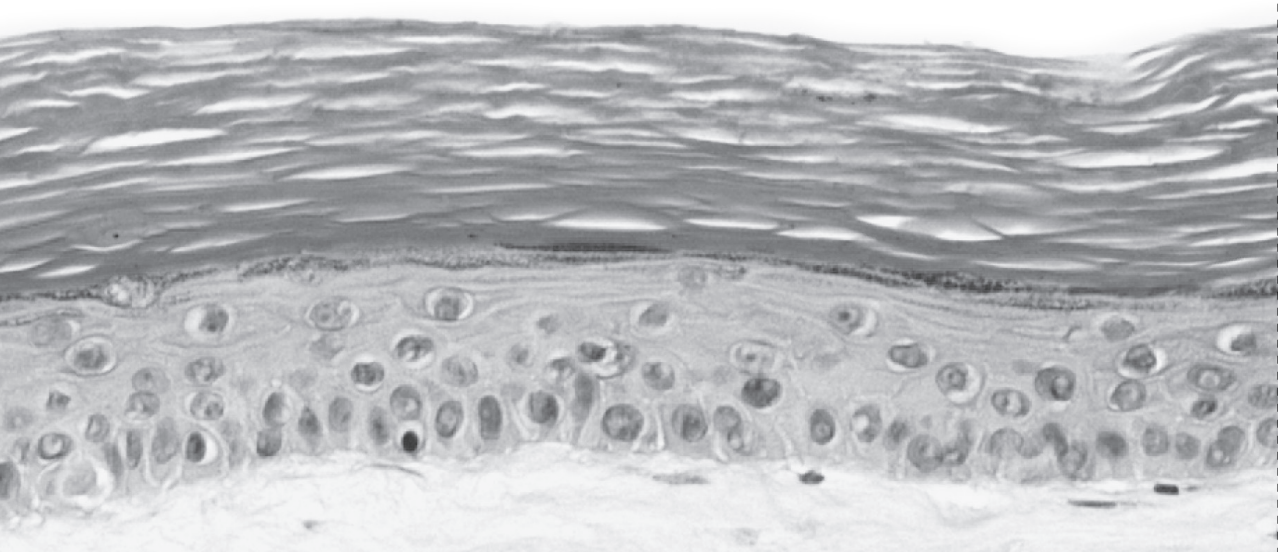
Supplementary figure 7. LC-MS ion maps of detected ceramides in lead optimization approaches. Two dimensional LC-MS ion maps with indicated position and nomenclature of the 13 studied CER subclasses in the ion map of NHS.



Supplementary figure 8. Ceramide carbon chain length distribution of lead optimization approaches. **(a)** Relative amount each ceramide with a specific amount of carbon atoms for CER[non-EO] and for **(b)** CER[EO] in NHS and in selected FTMs. **(c)** Quantitative amount each ceramide with a specific amount of carbon atoms for CER[non-EO] and for **(d)** CER[EO] in NHS and in selected FTMs. Data represents saturated CERs values in absolute amounts per mg SC as mean + s.d., n≥4.

10

Summary and perspectives



1. Summary

1.1. Introduction

Human skin consists of multiple layers, of which the dermis and epidermis form the outermost layers of the integumentary system. Main functions of the native human skin (NHS) skin are to protect the human body from water and heat loss, and to guard the body against pathogenic entrees or external aggravations. Multiple defence mechanisms are developed to efficiently perform these functions, including the microbial, chemical, immunological, and physical barrier. The uppermost layer of the epidermis is the stratum corneum (SC) [1]. This layer forms the physical skin barrier and can be considered as rampart of the body [2]. The SC consist of corneocytes embedded in a lipid matrix, often referred to as a brick and mortar structure [3, 4]. The corneocytes are highly keratinized cells which are almost impermeable. These are linked to an intercorneocyte lipid matrix, which is highly structured in the lamellar and lateral organization. This matrix is composed of ceramides, free fatty acids (FFAs), and cholesterol as main lipid classes [5, 6]. As the lipid matrix is the only continuous pathway through the SC, the structure and composition are crucial for the functionality of the skin barrier [7, 8].

Cell-based *in vitro* skin models were developed to facilitate screenings of compounds for therapeutic potential or toxicity and to enable scientific research aiming to expand knowledge on skin physiology and pathophysiology [1, 9-14]. Human skin equivalents (HSEs) are three dimensional (3D) models of NHS which are generated *in vitro* using primary cells. HSEs resemble NHS in many aspects, including dermal and epidermal architecture. However, a limitation is the altered lipid barrier formation which leads to a decreased barrier functionality [15-19]. This could be induced by the differences between *in vivo* and *in vitro* conditions, which include differences in cell microenvironment and in cell culture conditions. The former includes dissimilarities in cell-matrix interactions, as HSEs are developed in a short time frame with limited extracellular materials. The latter includes differences in skin temperature, oxygen levels, relative humidity, and exposure to sunlight between *in vivo* and *in vitro* settings, as these can only be partially mimicked in a cell culture incubator. Additionally, the NHS is nourished by manifold nutrients and signalling molecules, whereas the HSE is supported by cell culture medium which is composed of defined factors.

1.2. Aim of the thesis

In this thesis, the differences between *in vivo* and *in vitro* conditions were analysed to better understand which of these aspects play a crucial role for the barrier formation in HSEs. The primary aim of this research was to enhance the

morphogenesis and barrier formation of HSEs to better mimic that of NHS. The main objectives were:

a) to determine whether the dermal extracellular matrix (ECM) affects epidermal lipid barrier formation
b) to investigate if culture conditions during generation of HSEs affects lipid barrier formation
c) to generate HSEs with optimized dermal ECM and external culture conditions in combination with improved cell culture medium composition

1.3 Part I Optimization of the *in vitro* generated dermal equivalent

In part I, studies were conducted to address research questions related to the first objective: to determine whether the dermal ECM affects epidermal lipid barrier formation. These studies focussed on the dermal equivalent of full thickness models (FTMs), which consist of fibroblasts incorporated into a collagen type I/III matrix. This type of matrix is widely used in tissue engineering, but has several limitations including the contraction over time and animal protein as source. In addition, ECM components affect fibroblast proliferation, migration, collagen production, and differentiation potentially altering the epidermal morphogenesis and barrier formation due to extensive cellular communication.

In **chapter 2** the effect of the collagen source used for the dermal ECM on the morphogenesis and barrier formation of FTMs is presented. Properties of collagen vary between tissues and species, including variations in amino acid composition, thermal stability, and enzymatic resistance. Moreover, the animal origin of the collagens could induce a biologic response to primary human stromal cells. Therefore, the animal derived collagen (rat tail tendon) was compared to collagen obtained from human dermal tissue. To do so, a method was developed to obtain soluble collagen from the human abdominal dermis, which was successively used to generate human collagen full thickness models (hC-FTMs). Comparisons of dermal and epidermal morphology and lipid barrier formation between original FTMs and hC-FTMs revealed similarities for these characteristics. The animal material-free hC-FTM contains a dermal equivalent that mimics the native stromal tissue to a higher extent and provides a better alternative to animal testing.

In **chapter 3**, experiments are described on the modification of the dermal ECM by incorporation of chitosan in the collagen matrix isolated from rat tail tendon due to low batch-to-batch variability. Establishment of this reinforced ECM formed a novel type of HSE, named the collagen-chitosan full thickness model (CC-FTM). This CC-FTM was evaluated for dermal and epidermal morphogenesis characteristics and compared to the conventional FTMs and to NHS. In this

novel CC-FTM, the fibroblast distribution and BM deposition were not affected by the altered dermal ECM. Importantly, the morphology better resembled that of NHS based on the reduction of thickness of the viable epidermis, normalization of proliferation, and absence of epidermal activation. With respect to the lipid barrier composition in the CC-FTMs, the ceramide subclass profile and carbon chain length distribution better resembled that of NHS **(table 1)**. Accordingly, the lipid barrier organization and inside-out lipid barrier functionality were improved.

Overall, part I illustrated the importance of the dermal ECM and revealed novel insights on the influence hereof on epidermal morphogenesis and barrier formation of FTMs.

1.4. Part II Establishing external culture conditions favouring the barrier formation

In part II, studies were conducted to address research questions related to the second objective: to investigate if culture conditions during generation of HSEs affects lipid barrier formation. These studies focussed on the contribution of single external factors during generation of FTMs.

In **chapter 4** studies are presented comparing FTMs generated at body's core temperature (37°C) with FTMs generated at temperatures that approach skin surface temperature (35°C and 33°C). At these temperatures, the morphology and barrier formation of the FTMs were monitored during 4 weeks. Reduction of temperature to 35°C did not induce major differences, but reduction to 33°C led to increased epidermal thickness, disorganization of lower epidermal cell layers, and enlargement of granular cells. These substantial morphological differences were accompanied with moderate effects on lipid barrier formation **(table 1)**. This study emphasizes the importance of external factors during generation of FTMs, although reduction of external temperature did not lead to better resemblance of FTMs to NHS.

The *in vitro* oxygen level was assessed in the studies described in **chapter 5**. To determine the influence of oxygen level on generation of FTMs, the level of oxygen was reduced from conventional normoxia (20% O_2) to hypoxia (3% O_2). This reduction in oxygen level activated the hypoxia-inducible factor signalling pathway in monocultures of skin cells and in FTMs. In FTMs generated under hypoxia, epidermal thickness and proliferation were reduced, whereas terminal differentiation was enhanced. Also, the SC ceramide composition and lipid organization better mimicked that of NHS. This chapter revealed that oxygen level plays an important role in epidermal morphogenesis and barrier formation of FTMs.

The effect of the relative humidity (RH) as external factor on morphogenesis and lipid barrier formation in FTMs was described in **chapter 6**. To do so, FTMs and CC-FTMs were generated at 90% RH and 60% RH. Comparisons for the morphogenesis revealed that the uppermost epidermal layers are most affected by RH, including an enlargement of the granular layers at lower RH and induction of epidermal cell activation. Neither the composition of the lipids nor the organization of the lipid matrix was affected by reduced RH, despite a closer approximation of daily life RH levels.

The final external factor which was examined is the exposure to sunlight. However, in contrast to the assessments of other external factors, this was performed indirectly by supplementing the medium with an active metabolite of the sunlight-driven vitamin D pathway, which is $1,25(OH)_2D_3$. Results described in **chapter 7** show that supplementation with 1,25(OH)2D3 induced the activation of vitamin D receptor leading to upregulation of its target genes CYP24A and LL37. The epidermal morphogenesis of FTMs supplemented with $1,25(OH)_2D_3$ was similar as compared to control. The ceramide composition and chain length distribution were also similar. Comparing ultraviolet light exposed FTMs to non-exposed control FTMs, no difference in expression of lipid processing enzymes was detected, although at high dose UV-exposure the morphology of FTMs indicated more cell death. This study shows that the lack of vitamin D pathway activation during generation of FTMs is not contributing to the compromised barrier formation of FTMs.

In summary, part II demonstrated the pivotal role of external cell culture conditions on epidermal epidermal morphogenesis and the lipid barrier formation of FTMs (**table 1**).

1.5. Part III Combination of optimized cell culture with enhanced medium conditions

In part III, studies were conducted to address research questions related to the third objective: to generate HSEs with optimized dermal ECM and external culture conditions in combination with improved cell culture medium composition. These studies focussed on the contribution of culture medium supplements, and the combination of optimized external factors with optimized culture medium.

High levels of saturated FFA could lead to lipotoxic effects elevating the expression of stearoyl-CoA desaturase-1, an enzyme important for the synthesis of monounsaturated lipids. The mixture of FFAs supplemented in the culture medium was hypothesized to be in disbalance leading to the observed aberrations in the lipid barrier formation in FTMs. In studies described in **chapter 8**, the concentration of the saturated FFA palmitic acid (PA) was therefore reduced to

10% and 1% of the original concentration of 25 µM in the culture medium. When reducing the PA concentration to the lowest level, the morphology of the FTMs showed a delay in early differentiation and an increase in epidermal activation. Nevertheless, the composition of ceramides and FFAs in the SC was similar, irrespective of level of palmitic acid in the culture medium. Importantly, as this was the first time we quantified the FFA content, it was observed that the quantity of FFAs in the SC of FTMs was substantially lower than that of NHS, contributing to the altered barrier formation. In summary, this study showed that the level of supplemented palmitic acid to the cell culture medium adequately supports epidermal morphogenesis and barrier formation of FTMs.

A combination of optimized external conditions with an improved cell culture medium composition was reported in **chapter 9**. Herein, FTMs or CC-FTMs (**chapter 3**) were generated with inhibition of the nuclear liver X receptor by GSK2033 (work conducted by R. Helder) under normoxic or hypoxic conditions (**chapter 5**). Modulation of these single factors showed promising results regarding barrier formation in FTMs. Additional effects regarding the recapitulation of epidermal architecture in combination with enhanced lipid barrier formation were observed in the CC-FTM combined with LXR inhibition (i.e. enhanced morphogenesis, reduced level of monounsaturated lipids, improved lipid organization). Furthermore, the functionality of the epidermal barrier was assessed, which revealed improved functionality of the *in vitro* generated barrier, thereby more closely mimicking barrier formation and functionality of NHS. The developed HSE is of interest regarding drug development research and associated preclinical studies.

Overall, part III illustrated the importance of the medium composition with supplemented lipids in combination with optimized external conditions during generation of HSEs (**table 1**). The insights obtained in these studies showed again the complexity of optimization *in vitro* generation of HSEs. Multitargeted approaches serve as a valuable research method, resulting in the formation of HSEs with enhanced morphogenesis and lipid barrier formation better mimicking NHS.

1.6. Conclusions

The studies in this thesis describe optimization approaches for the dermal equivalent, external cell culture conditions, and combinatory methods with enhanced medium composition to better resemble the SC lipid barrier formation *in vitro*. The results indicate that modification of the dermal ECM by chitosan enhanced epidermal morphogenesis which was reflected in an improved barrier formation and functionality. Furthermore, the results indicate that external culture conditions affect the lipid barrier formation both positively and negatively,

emphasizing the difficulty in modulation of experimental conditions during *in vitro* generation of HSEs. By reduction of external oxygen, the epidermal morphogenesis and lipid barrier formation was shown to be improved, thereby better mimicking that of NHS. Combining CC-FTMs with a chemical antagonist of liver X receptor in a combinatory approach resulted in the formation of HSEs with epidermal morphogenesis and barrier formation that more closely resembles that of NHS.

2. Perspectives

The availability of preclinical skin models which better resemble NHS will lift the success rates in drug development, which is still a time-consuming procedure with high failure rates in clinical trials. Although generation of HSEs using optimized methods reveal promising results as described in this thesis, there are still limitations and challenges which need to be overcome [20]. In this section, an overview is provided on the prospects in skin tissue engineering based on the three main parts of this thesis, covering optimization strategies for the dermal ECM, cell culture conditions, and for multi-targeting approaches. Complementary, perspectives on using HSEs in the emerging fields of advanced high throughput screening and precision medicine is provided.

2.1 Optimization approaches for the dermal equivalent

A key component of 3D skin models is the ECM, which constitutes of collagen type I/III in the dermal equivalent of FTMs. Although primary fibroblasts rearrange collagen over time, the major biochemical composition cannot be altered resulting in definite physical and mechanical properties [21, 22]. This leads to restrictions in fully capturing cell-matrix signalling pathways. In this thesis, it is described that modification of the dermal ECM by chitosan leads to an improved dermal and epidermal morphogenesis and resulted in enhanced epidermal barrier formation. These results encourage further optimization of the dermal equivalent. Various factors are involved in this, which are the composition of the proteins, structure of the ECM, and presence of cell types in the dermal equivalent (**Fig. 1 a**).

The first factor is the composition of the ECM proteins. This can be fine-tuned mimicking the heterogeneous composition in NHS based on i) biological hydrogels derived from animal, plant or human sources, on ii) synthetic hydrogels based on non-natural or natural polymers, or on iii) composite materials which cover both natural and non-natural constituents [23, 24]. Additionally, the ECM could be optimized to better interact with growth factors (e.g. basic fibroblast growth factor (FGF-2) [25]), protect growth factors from degradation, and/or enhance their activity, which potentially improves the longevity of HSEs [26, 27]. The second factor is the structure of the ECM. Optimizations can be performed for porosity,

				Morphogenesis			
	Chapter	Study	Condition	Dermal	Proliferation (%)	Differentiation	Activation
General	2-9	All	NHS	Fib. Dis. [+] BM [+]	9,3 - 12,1	Early [+] Late [+]	Absent
			FTM	Fib. Dis. [±] BM [+]	10,5 - 22,7	Early [+]; Late [±]	Present K16 [+]
Part I	2	Human collagen	hC-FTM	Fib. Dis. [±] BM [+]	16,9 ± 4,4	Early [+]; Late [±]	Present K16 [+]
	3	Chitosan	CC-FTM	Fib. Dis. [±] BM [+]	12,3 ± 1,7	Early [+]; Late [+]	Absent
Part II	4	Temperature	35°C day 14	Fib. Dis. [±] BM [+]	11,9 ± 4,6	Early [±]; Late [±]	Present K16 [+]
			33°C day 14	Fib. Dis. [±] BM [±]	12,7 ± 6,4	Early [-]; Late [±]	Present K16 [+]
	5	Oxygen	3% O_2	Fib. Dis. [±] BM [+]	14,6 ± 4,5	Early [+]; Late [+]	Increased K16 [+]
	6	Relative humidity	FTM 60% RH	Fib. Dis. [±] BM [+]	12,6 ± 2,3	Early [+]; Late [±]	Present K16 [+]
			CC-FTM 60% RH	Fib. Dis. [±] BM [+]	4,4 ± 2,4	Early [+]; Late [±]	Increased K16 [+]
	7	Vitamin D	20 nM $1,25(OH)_2D_3$	N.D.	20,6 ± 8,7	Early [+]; Late [±]	Present K16 [+]
Part III	8	Palmitic acid	10% PA (2,5 µM)	Fib. Dis. [±] BM [+]	8,8 ± 2,3	Early [+]; Late [±]	Present K16 [+]
			1% PA (0,25 µM)	Fib. Dis. [±] BM [+]	9,1 ± 2,7	Early [-]; Late [±]	Present K16 [+]
	9	Multi-targeted	#CC-FTM(20-)	N.D.	9,3 ± 1,9	Early [+]; Late [+]	Absent
			#CC-FTM(20+)	N.D.	10,7 ± 0,8	Early [+]; Late [+]	Absent

Table 1. Summary of results for the optimization approaches in full thickness models as described in this thesis. Observations are described as compared to FTM, except for FTM itself which is described as compared to NHS. Arrows indicate a significant increase (↑) or significant decrease (↓). [+] = good, [±] = medium, [-] = poor. # = lead approach, N.D. = not determined, Fib. Dis. = Fibroblast distribution,

SC lipid composition			SC lipid organization		Additional remarks
Ceramide subclass profile	**Ceramide chain length distribution**	**muCER index (%)**	**Lamellar (nm)**	**Lateral**	
Benchmark	Benchmark	NS: 1,2 ± 0,4 AS: 0,8 ± 0,9	LPP ~ 13 nm SPP ~ 6 nm	Orthorhombic	
[Q] [NS]↑ [AS]↑ [EOS]↑ [NP]↓	C32-C40↑ C42-C54↓ C64-C74 equal	NS: 16,1 - 22,2 AS: 10,3 - 17,6	LPP 12,2 - 12,6 SPP absent	Hexagonal	Low FFA quantity Increased muFFA index
[NQ] Comparable [NS]↑	C34, C42, C66, C68↑ C46, C48↓	NS: 27,4 ± 4,9 AS: 19,2 ± 6,2	LPP 12,1 ± 0,3	N.D.	
[NQ] Improved [NP]↑ [NS]↓	C44, C46, C48↑ C34, C66, C68, C70↓	N.D.	LPP 12,6 ± 0,1	N.D.	TEWL improved
[Q] Equal	Equal	NS: 24,4 ± 4,7 AS: 18,0 ± 3,3	LPP 12,4 ± 0,2	N.D.	
[Q] Impaired [NS]↑ [AS]↑[EOS]↑	C34, C40, C66↑ C44, C46↓	NS: 34,1 ± 6,9 AS: 27,3 ± 6,1	LPP 12,2 ± 0,2	N.D.	
[Q] Improved [NP]↑	Equal	NS: 23,0 ± 10,5 AS: 19,0 ± 8,7	LPP 12,7 ± 0,2	Orthorhombic and hexagonal	
[Q] Equal	Equal	NS: 16,0 ± 1,9 AS: 10,3 ± 0,7	LPP 12,4 ± 0,1	Hexagonal	
[Q] Equal	Equal	NS: 17,5 ± 2,5 AS: 12,6 ± 1,4	LPP 12,4 ± 0,1	Hexagonal	
[NQ] Equal	Equal	NS: 31,4 ± 6,7 AS: 23,5 ± 4,7	LPP 12,0 ± 0,1	Hexagonal	
[Q] Equal	Equal	NS: 18,1 ± 4,1 AS: 16,1 ± 1,5	LPP 12,6 ± 0,1	Hexagonal	Equal FFA quantity Equal muFFA index
[Q] Equal	Equal	NS: 19,9 ± 2,9 AS: 8,9 ± 1,5	LPP 12,6 ± 0,1	Hexagonal	Equal FFA quantity Equal muFFA index
[Q] Comparable [EOdS]↑	Equal	NS: 19,4 ± 6,2 AS: 12,0 ± 3,7	LPP 12,5 ± 0,1	Orthorhombic and hexagonal	TEWL improved Diffusion equal
[Q] Comparable [NdS]↑[EOP]↓	C34-C42↓ C48-C56↑	NS: 12,4 ± 2,7 AS: 5,9 ± 2,1	LPP 12,4 ± 0,1	Orthorhombic and hexagonal	TEWL Improved Diffusion equal

BM = basement membrane, SG = Stratum granulosum, SC = Stratum corneum, LPP = Long Periodicity Phase, SPP = Short Periodicity Phase, TEWL = transepidermal water loss, muCER = monounsaturated ceramide, muFFA = monounsaturated free fatty acid. NQ = LC-MS data based on non-quantified AUC/ISTD data, Q = LC-MS data based on quantified values. Data represents mean ± SD.

density, and matrix stiffness. Structural factors are important for the maintenance of dermal homeostasis [28-30]. Fibroblasts can respond to mechanical forces, of which the stiffness can be modified based either the ECM material [31], or on (stimulated) increased or decreased secretion of ECM components and matrix metalloproteinases (e.g. MMP-1) [32]). Alternatively, recapitulation of the rete ridges macrostructure in an epidermal model revealed improved epidermal morphogenesis and epidermal barrier functionally [33]. The third factor is the presence of and interactions between stromal cell types in the dermal equivalent. These could be fibroblasts, adipocytes, nerve cells, endothelial cells, and skin-resident immune cells. Additionally, the fibroblast population is heterogeneous. It is therefore expected that reticular and papillary fibroblasts have a distinct reciprocal signalling pathways with epidermal keratinocytes, thereby it is likely that fibroblast subpopulations have diverge effects on the barrier formation of the epidermis [23]. Better recapitulation of the dermal architecture is therefore highly desired.

Development of innovative dermal equivalents harbouring modified dermal ECM composition with additional stromal cell types was recently shown by the Kaplan lab [34, 35], who described the utilization of silk-collagen cross linked matrix systems harbouring hypodermis, nerve and immune cells. Nevertheless, whether the incorporation of other stromal cell types affects not only the complexity of the HSE, but also the barrier formation remains topic for future studies.

The various features of the dermal equivalent are also of importance for the upcoming field of tissue engineering by 3D bioprinting [36]. As compared to traditional methods, the construction of the ECM can be better controlled using 3D bioprinting [37]. The ECM in bio-printed tissues is a result of the bioink materials, which should be tuneable to be suitable for bioprinting. Reproducing native ECM accurately for the physical, chemical, structural, and biological parameters is more likely to occur by 3D printing than in the conventional transwell system [38]. Yet, for 3D bioprinting many challenges exist in accurately reproducing the native cellular microenvironment, which should also be decoded for *in vitro* skin tissue engineering.

2.2 Perspectives to further improve skin cell culture conditions

A key aspect during generation of HSEs is the application of optimal cell culture conditions. The results described in this thesis add valuable information on the impact of various cell culture conditions on the generation of 3D models, especially with regards to the lipid barrier formation. Nevertheless, several optimization approaches regarding external cell culture conditions targeting specific factors of the skin tissue engineering protocol are still of high interest (**Fig. 1 b**).

The main focus of this thesis was to evaluate the lipid barrier formation based on optimization of the external cell culture conditions. Nevertheless, the results of the described studied were obtained primarily in FTMs. It would be of high interest to perform a validation study in other types of HSEs besides FTMs (i.e. explant model, Leiden epidermal model, or fibroblast-derived matrix model) [15]. Moreover, the SC is not only composed of lipids, as the corneocytes also play a vital role in the establishment of the skin barrier. Evaluation of the effects of external cell culture conditions on the protein barrier through examination of shape and maturation of corneocytes, formation of the cornified protein envelope, and formation of the bound lipids could reveal additional insights [39-42]. Furthermore, a limitation of HSEs is the lack of desquamation. Although some research has been performed aiming to initiate exfoliation based on mechanical or chemical removal of upper SC layers, normal shedding of superficial SC layer has not been observed *in vitro* [43]. Future attempts should focus on the induction of desquamation, as absence of it results in excessive accumulation of SC layers.

Up to now, HSEs based on primary cells most accurately reflected the NHS. As such, it is of interest to implement optimization strategies during isolation of primary keratinocytes [44, 45]. These should aim to apply optimized external cell culture conditions during the isolation procedure of primary cells, especially those which showed most promising results in 3D models. By application of these conditions during isolation of primary keratinocytes, cellular adaptation occurs favouring earlier onset of homeostasis. Additionally, exploratory studies regarding primary cell isolation procedure based on cell sorting technologies should be performed, which facilitates the expansion of specific primary cell subpopulations [46]. Alternatively, it has been shown that the undulating structure of the DEJ can be mimicked *in vitro* to improve the keratinocyte stem cell niche, resulting in optimized keratinocyte adhesion and proliferation [47]. These approaches could be important to enhance the capability of the primary cells to form 3D models in higher passages, which so far is limited for keratinocytes in their first or second passage.

Nevertheless, the primary cell isolation procedures are generally time-consuming, labour-intensive, and comes with inter-lab standardization and quality assurance challenges [48]. Immortalized cells or cell lines can also be utilized to form HSEs. By definition, these provide a nearly unlimited source of identical cells, which strongly improves the reproducibility and consistency of monocultures and HSEs. HaCaT, Near-diploid Immortal KeratinocyteS (NIKS), and N/TERT immortalized cell lines have been used for this purpose, revealing promising results although with high variations in barrier formation [49-53]. This suggests that only a limited subset of cell lines can fully differentiate into a stratified epidermis, most probably due to their high proliferative phenotype. Future endeavours should

also focus on establishment and characterization of induced immortalization of primary fibroblasts and keratinocytes, with focus on the barrier formation [54-56]. Moreover, the induced pluripotent stem cell (iPSC) technology has the potential to create all types of skin cells based on a single healthy or diseased donor [57-61]. This technology can also be employed to generate disease-specific skin cells, thereby having a high potential to explore the molecular mechanisms underlying various skin disorders in *in vitro* generated HSEs.

2.3 Future directions in multitargeted 3D HSE cultures

Another approach is to combine an optimized dermal equivalent with enhanced cell culture conditions and an improved composition of the cell culture medium. A so-called multitarget approach has been explored in this thesis and revealed the high potential of this method. Therefore, combinatory approaches should be applied in future studies (**Fig. 1 c**).

Consistent with the implementation of optimized cell culture condition, the optimization of cell culture medium composition has been tested during the air-exposed phase only in this thesis, instead of implementation during the primary cell isolation. By implementing optimized cell culture medium at an earlier stage, adaptation to it could induce improved homeostasis *in vitro*. Another critical part in the cell culture medium is animal-derived serum [62]. Avoiding the use of fetal bovine serum (FBS) during isolation of primary cells and generation of HSE by using chemically-defined media will lead to reduced batch to batch variability and provides a better alternative to animal testing by minimizing animal-derived components. Feasibility of using chemically-defined media in generation of HSEs has been explored and shown before [63], although more detailed information on the lipid barrier formation should be obtained in future studies to reveal insights on the influence of FBS on the lipid biosynthesis and lipid barrier formation.

Multitarget approach to improve the cell culture medium composition can be achieved by a better refreshment medium rate, preventing the reduced availability in nutrients and faster removal of waste products, limiting the activation of unwanted signalling pathways. As an increased manual refreshment rate is labour-intensive and prone for errors, automated microfluidic systems are sophisticated, suitable methods which better mimic the circulation. These so-called skin-on-a-chip can be generated based on 2D or 3D (co-)cultures [64-67].

Another approach to improve the lipid barrier formation of HSE is to better mimic the complex cell populations resident in NHS. To do so, co-cultures should be established of fibroblasts and keratinocytes with adipocytes, nerve cells, endothelial cells, and skin-resident immune cells of the dermis and epidermis [34, 68, 69]. This can be complemented by cells involved in hair follicle formation

and sebum production, as these cells produce and secrete lipid of the superficial sebum [61]. Also culturing (a selection) of skin-resident micro-organisms is of interest to further mimic NHS and host-microbiome interactions [1, 70, 71].

More insight on the differences between the lipid biosynthesis pathways forming the lipid barrier of HSEs as compared to NHS can be achieved by in-depth characterization. This can be performed by using comparative transcriptome, proteome, and/or metabolome analyses of HSEs and NHS [72, 73]. Using these unbiased approaches, more evidence is obtained about lipid processing enzymes or barrier

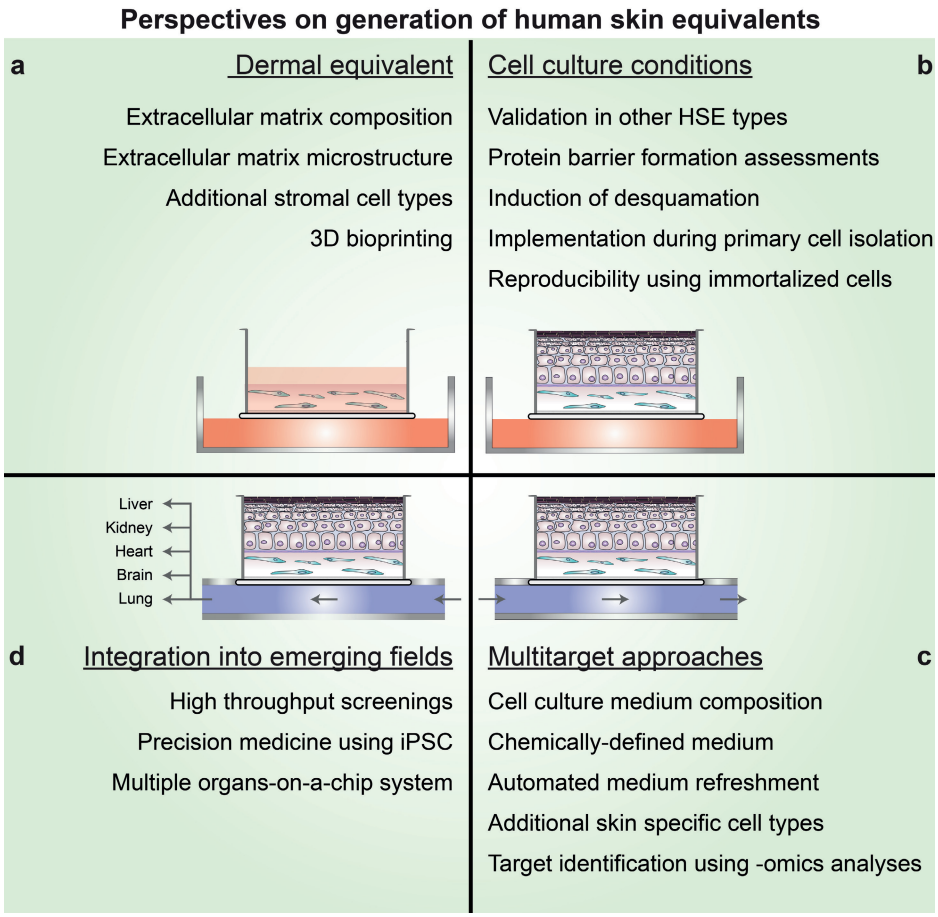


Figure 1. Overview of prospects on generation of human skin equivalents. Perspectives on **(a)** optimization of dermal equivalents, **(b)** studies regarding external cell culture conditions, **(c)** optimization of HSEs by multitargeted approaches, and **(d)** integration of HSEs into emerging fields of advanced high throughput screenings and precision medicine.

formation pathways. This will lead to more information on activation or deactivation of signalling pathways, identifying targets for future optimization studies. Target identification strategies should aim to normalize these persistent differences in the SC lipid composition.

2.4 Outlook on integration of HSEs in high throughput screenings and precision medicine

A closing perspective will be about integrating HSEs in the emerging fields of advanced high throughput screenings (HTS) and precision medicine (**Fig. 1 d**).

Currently, 2D cultures are used in HTS as these provide an easy cell culturing system with clear read-outs. Nevertheless, the relevance to physiology is much lower as compared to 3D models, especially for topical applied drug screenings. Therefore, the 3D models should also be applied in HTS [74]. It is also foreseen that disease specific HSEs will be applied in medium or low throughput screenings due to their restricted applicability.

The utilization of HSEs in precision medicine for drug research will be based on iPSC generated HSEs [61, 75-78]. These could be either a single or multi organ-on-a-chip, based on the relevance in a screening. Disease-on-a-chip methods could be established based on patient derived iPSC cells or by inducing a disease-specific mutation in the healthy cells based on clustered regularly interspaced short palindromic repeats (CRISPR)/CRISPR-associated protein 9 (CRISPR-Cas9) mediated genome engineering [79, 80]. By creating such a complex model, cell culture media and conditions should be optimal and not create a limiting factor in the applicability of these models. If possible, a full body-on-a-chip could be generated interconnecting multiple organotypic micro-organs or organoids [81]. HSEs will be integrally applied in future preclinical models monitoring the cutaneous effects of drugs and for modelling percutaneous drug absorption. Methods for rapid physicochemical characterization of lipid barrier formation matching HTS objectives will remain a challenge which needs to be addressed in future studies.

3. References

1. Niehues, H., et al., 3D skin models for 3R research: The potential of 3D reconstructed skin models to study skin barrier function. Exp Dermatol, 2018. **27**(5): p. 501-511.
2. Nishifuji, K. and J.S. Yoon, The stratum corneum: the rampart of the mammalian body. Veterinary dermatology, 2013. **24**(1): p. 60-e16.
3. Elias, P.M., Structure and function of the stratum corneum permeability barrier. Drug Development Research, 1988. **13**(2-3): p. 97-105.
4. Michaels, A.S., S.K. Chandrasekaran, and J.E. Shaw, Drug permeation through human skin: Theory and in vitro experimental measurement. AIChE Journal, 1975. **21**(5): p. 985-996.
5. Van Smeden, J., et al., The important role of stratum corneum lipids for the cutaneous barrier function. Biochimica et Biophysica Acta -Molecular Cell Biology of Lipids, 2014. **1841**(3): p. 295-313.
6. Weerheim, A. and M. Ponec, Determination of stratum corneum lipid profile by tape stripping in combination with high-performance thin-layer chromatography. Archives of dermatological research, 2001. **293**(4): p. 191-199.
7. Feingold, K.R., The outer frontier: the importance of lipid metabolism in the skin. Journal of lipid research, 2009. **50**(Supplement): p. S417-S422.
8. Feingold, K.R., P.M. Elias, and C.B.o. Lipids, Role of lipids in the formation and maintenance of the cutaneous permeability barrier. Biochimica et Biophysica Acta -Molecular, 2014. **1841**(3): p. 280-294.
9. Gordon, S., et al., Non-animal models of epithelial barriers (skin, intestine and lung) in research, industrial applications and regulatory toxicology. Alternatives to Animal Experimentation: ALTEX, 2015. **32**(4): p. 327-378.
10. Flaten, G.E., et al., In vitro skin models as a tool in optimization of drug formulation. European Journal of Pharmaceutical Sciences, 2015. **75**: p. 10-24.
11. Küchler, S., K. Strüver, and W. Friess, Reconstructed skin models as emerging tools for drug absorption studies. Expert opinion on drug metabolism & toxicology, 2013. **9**(10): p. 1255-1263.
12. Poumay, Y. and A. Coquette, Modelling the human epidermis in vitro: tools for basic and applied research. Archives of dermatological research, 2007. **298**(8): p. 361-369.
13. Van Gele, M., et al., Three-dimensional skin models as tools for transdermal drug delivery: challenges and limitations. Expert opinion on drug delivery, 2011. **8**(6): p. 705-720.
14. Mathes, S.H., H. Ruffner, and U. Graf-Hausner, The use of skin models in drug development. Adv Drug Deliv Rev, 2014. **69-70**: p. 81-102.
15. Thakoersing, V.S., et al., Unraveling barrier properties of three different in-house human skin equivalents. Tissue Eng Part C Methods, 2012. **18**(1): p. 1-11.
16. Ponec, M., et al., Lipid and ultrastructural characterization of reconstructed skin models. International journal of pharmaceutics, 2000. **203**(1-2): p. 211-225.
17. Kandarova, H., Evaluation and validation of reconstructed human skin models as alternatives to animal tests in regulatory toxicology. 2006: Freie Universität Berlin.
18. Lotte, C., et al., Permeation and skin absorption: reproducibility of various industrial reconstructed human skin models. Skin Pharmacology and Physiology, 2002. **15**(Suppl. 1): p. 18-30.
19. Schafer-Korting, M., et al., Reconstructed human epidermis for skin absorption testing: results of the German prevalidation study. Altern Lab Anim, 2006. **34**(3): p. 283-94.
20. Randall, M.J., et al., Advances in the Biofabrication of 3D Skin in vitro: Healthy and Pathological Models. Frontiers in bioengineering and biotechnology, 2018. **6**: p. 154-154.
21. Grinnell, F., Fibroblast biology in three-dimensional collagen matrices. Trends in Cell Biology, 2003. **13**(5): p. 264-269.
22. Miron-Mendoza, M., J. Seemann, and F. Grinnell, The differential regulation of cell motile activity through matrix stiffness and porosity in three dimensional collagen matrices. Biomaterials, 2010. **31**(25): p. 6425-6435.
23. Sriram, G., P.L. Bigliardi, and M. Bigliardi-Qi, Fibroblast heterogeneity and its implications for engineering organotypic skin models in vitro. Eur J Cell Biol, 2015. **94**(11): p. 483-512.
24. Yang, S., et al., The design of scaffolds for use in tissue engineering. Part I. Traditional factors. Tissue engineering, 2001. **7**(6): p. 679-689.
25. Walker, A., J.E. Turnbull, and J.T. Gallagher, Specific heparan sulfate saccharides mediate the activity of basic fibroblast growth factor. Journal of Biological Chemistry, 1994. **269**(2): p. 931-935.
26. Schultz, G.S. and A. Wysocki, Interactions between extracellular matrix and growth factors in wound healing. Wound Repair Regen, 2009. **17**(2): p. 153-62.
27. Briquez, P.S., J.A. Hubbell, and M.M. Martino, Extracellular Matrix-Inspired Growth Factor Delivery Systems for Skin Wound Healing. Advances in Wound Care, 2015. **4**(8): p. 479-489.

28. Ghosh, K., et al., Cell adaptation to a physiologically relevant ECM mimic with different viscoelastic properties. Biomaterials, 2007. **28**(4): p. 671-679.
29. Jiang, S., et al., Physical Properties of Implanted Porous Bioscaffolds Regulate Skin Repair: Focusing on Mechanical and Structural Features. Advanced healthcare materials, 2018. **7**(6): p. 1700894.
30. Planz, V., et al., Three-dimensional hierarchical cultivation of human skin cells on bio-adaptive hybrid fibers. Integrative Biology, 2016. **8**(7): p. 775-784.
31. Achterberg, V.F., et al., The Nano-Scale Mechanical Properties of the Extracellular Matrix Regulate Dermal Fibroblast Function. Journal of Investigative Dermatology, 2014. **134**(7): p. 1862-1872.
32. Petersen, A., et al., The Impact of Substrate Stiffness and Mechanical Loading on Fibroblast-Induced Scaffold Remodeling. Tissue Engineering Part A, 2012. **18**(17-18): p. 1804-1817.
33. Kumamoto, J., et al., Mathematical-model-guided development of full-thickness epidermal equivalent. Scientific Reports, 2018. **8**(1): p. 17999.
34. Lightfoot Vidal, S.E., et al., 3D biomaterial matrix to support long term, full thickness, immuno-competent human skin equivalents with nervous system components. Biomaterials, 2018.
35. Vidal Yucha, S.E., et al., Human Skin Equivalents Demonstrate Need for Neuro-Immuno-Cutaneous System. 2019. **0**(0): p. 1800283.
36. Vijayavenkataraman, S., W.F. Lu, and J.Y.H. Fuh, 3D bioprinting of skin: a state-of-the-art review on modelling, materials, and processes. Biofabrication, 2016. **8**(3): p. 032001.
37. Moroni, L., et al., Biofabrication strategies for 3D in vitro models and regenerative medicine. Nature Reviews Materials, 2018. **3**(5): p. 21-37.
38. Yan, W.-C., et al., 3D bioprinting of skin tissue: From pre-processing to final product evaluation. Advanced drug delivery reviews, 2018.
39. Elias, P.M., et al., Formation and functions of the corneocyte lipid envelope (CLE). Biochimica et Biophysica Acta (BBA) - Molecular and Cell Biology of Lipids, 2014. **1841**(3): p. 314-318.
40. Hirabayashi, T., et al., PNPLA1 has a crucial role in skin barrier function by directing acylceramide biosynthesis. Nature Communications, 2017. **8**: p. 14609.
41. Yokouchi, M., et al., Epidermal cell turnover across tight junctions based on Kelvin's tetrakaidecahedron cell shape. eLife, 2016. **5**: p. e19593.
42. Riethmüller, C., Assessing the skin barrier via corneocyte morphometry. Experimental Dermatology, 2018. **27**(8): p. 923-930.
43. Ponec, M., J. Kempenaar, and A. Weerheim, Lack of desquamation–the Achilles heel of the reconstructed epidermis. International journal of cosmetic science, 2002. **24**(5): p. 263-272.
44. Tjin, M.S., et al., Biologically relevant laminin as chemically defined and fully human platform for human epidermal keratinocyte culture. Nature communications, 2018. **9**(4432): p. 1-10.
45. Ścieżyńska, A., et al., Isolation and culture of human primary keratinocytes – a methods review. Experimental Dermatology, 2019. **28**(2): p. 107-112.
46. Li, A., P.J. Simmons, and P. Kaur, Identification and isolation of candidate human keratinocyte stem cells based on cell surface phenotype. Proceedings of the National Academy of Sciences, 1998. **95**(7): p. 3902-3907.
47. Helling, A.L., et al., Dynamic Culture Substrates That Mimic the Topography of the Epidermal–Dermal Junction. 2019. **0**(0): p. null.
48. Pamies, D., et al., Advanced good cell culture practice for human primary, stem cell-derived and organoid models as well as microphysiological systems. ALTEX-Alternatives to animal experimentation, 2018. **35**(3): p. 353-378.
49. Boelsma, E., M.C.H. Verhoeven, and M. Ponec, Reconstruction of a Human Skin Equivalent Using a Spontaneously Transformed Keratinocyte Cell Line (HaCaT). Journal of Investigative Dermatology, 1999. **112**(4): p. 489-498.
50. Allen-Hoffmann, B.L., et al., Normal Growth and Differentiation in a Spontaneously Immortalized Near-Diploid Human Keratinocyte Cell Line, NIKS. Journal of Investigative Dermatology, 2000. **114**(3): p. 444-455.
51. Smits, J.P., et al., Immortalized N/TERT keratinocytes as an alternative cell source in 3D human epidermal models. Scientific reports, 2017. **7**(1): p. 11838.
52. van Drongelen, V., et al., Barrier properties of an N/TERT-based human skin equivalent. Tissue Engineering Part A, 2014. **20**(21-22): p. 3041-3049.
53. M.A., R.C., et al., Development of a Full-Thickness Human Skin Equivalent In Vitro Model Derived from TERT-Immortalized Keratinocytes and Fibroblasts. Tissue Engineering Part A, 2015. **21**(17-18): p. 2448-2459.
54. Wagner, T., et al., Establishment of keratinocyte cell lines from human hair follicles. Scientific Reports, 2018. **8**(1): p. 13434.
55. Chapman, S., et al., Human keratinocytes are efficiently immortalized by a Rho kinase inhibitor. The Journal of Clinical Investigation, 2010. **120**(7): p. 2619-2626.

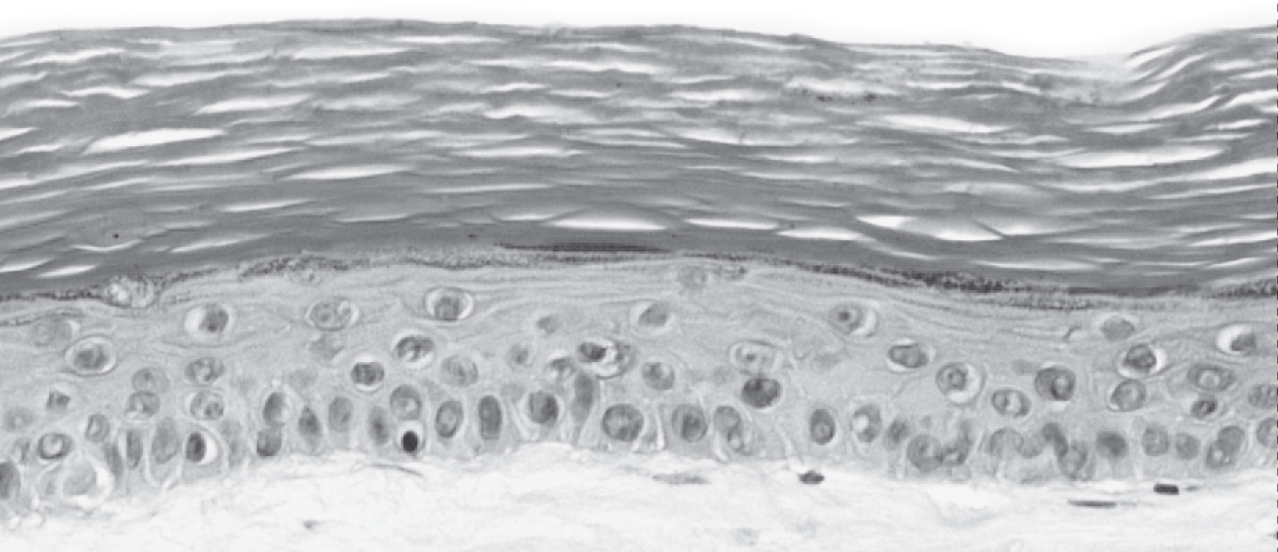
56. Choi, M. and C. Lee, Immortalization of Primary Keratinocytes and Its Application to Skin Research. Biomolecules & therapeutics, 2015. **23**(5): p. 391-399.
57. Takahashi, K. and S. Yamanaka, Induction of pluripotent stem cells from mouse embryonic and adult fibroblast cultures by defined factors. Cell, 2006. **126**(4): p. 663-676.
58. Ohyama, M. and H. Okano, Promise of Human Induced Pluripotent Stem Cells in Skin Regeneration and Investigation. Journal of Investigative Dermatology, 2014. **134**(3): p. 605-609.
59. Dinella, J., M.I. Koster, and P.J. Koch, Use of Induced Pluripotent Stem Cells in Dermatological Research. The Journal of investigative dermatology, 2014. **134**(8): p. e23-e23.
60. Devito, L., et al., Induced pluripotent stem cell line from an atopic dermatitis patient heterozygous for c.2282del4 mutation in filaggrin: KCLi001-A. Stem Cell Research, 2018. **31**: p. 122-126.
61. Lee, J., et al., Hair Follicle Development in Mouse Pluripotent Stem Cell-Derived Skin Organoids. Cell Reports, 2018. **22**(1): p. 242-254.
62. van der Valk, J., et al., Fetal bovine serum (FBS): past–present–future. ALTEX-Alternatives to animal experimentation, 2018. **35**(1): p. 99-118.
63. Stark, H.-J., et al., Organotypic Keratinocyte Cocultures in Defined Medium with Regular Epidermal Morphogenesis and Differentiation. Journal of Investigative Dermatology, 1999. **112**(5): p. 681-691.
64. Sriram, G., et al., Full-thickness human skin-on-chip with enhanced epidermal morphogenesis and barrier function. Materials Today, 2018. **21**(4): p. 326-340.
65. Abaci, H.E., et al., Pumpless microfluidic platform for drug testing on human skin equivalents. Lab on a Chip, 2015. **15**(3): p. 882-888.
66. Ataç, B., et al., Skin and hair on-a-chip: in vitro skin models versus ex vivo tissue maintenance with dynamic perfusion. Lab on a Chip, 2013. **13**(18): p. 3555-3561.
67. Maschmeyer, I., et al., A four-organ-chip for interconnected long-term co-culture of human intestine, liver, skin and kidney equivalents. Lab on a Chip, 2015. **15**(12): p. 2688-2699.
68. van den Bogaard, E.H., et al., Crosstalk between Keratinocytes and T Cells in a 3D Microenvironment: A Model to Study Inflammatory Skin Diseases. Journal of Investigative Dermatology, 2014. **134**(3): p. 719-727.
69. Ouwehand, K., et al., Technical Advance: Langerhans cells derived from a human cell line in a full-thickness skin equivalent undergo allergen-induced maturation and migration. Journal of leukocyte biology, 2011. **90**(5): p. 1027-1033.
70. van Drongelen, V., et al., Reduced filaggrin expression is accompanied by increased Staphylococcus aureus colonization of epidermal skin models. Clinical & Experimental Allergy, 2014. **44**(12): p. 1515-1524.
71. Rademacher, F., et al., Skin microbiota and human 3D skin models. Experimental Dermatology, 2018. **27**(5): p. 489-494.
72. Bachelor, M., et al., Transcriptional profiling of epidermal barrier formation in vitro. Journal of Dermatological Science, 2014. **73**(3): p. 187-197.
73. Winget, J.M., et al., Quantitative proteogenomic profiling of epidermal barrier formation in vitro. Journal of Dermatological Science, 2015. **78**(3): p. 173-180.
74. Schimek, K., et al., Bioengineering of a full-thickness skin equivalent in a 96-well insert format for substance permeation studies and organ-on-a-chip applications. Bioengineering, 2018. **5**(2): p. 43.
75. Ronaldson-Bouchard, K. and G. Vunjak-Novakovic, Organs-on-a-chip: a fast track for engineered human tissues in drug development. Cell stem cell, 2018. **22**(3): p. 310-324.
76. Petrova, A., et al., 3D In Vitro Model of a Functional Epidermal Permeability Barrier from Human Embryonic Stem Cells and Induced Pluripotent Stem Cells. Stem Cell Reports, 2014. **2**(5): p. 675-689.
77. van den Broek, L.J., et al., Progress and Future Prospectives in Skin-on-Chip Development with Emphasis on the use of Different Cell Types and Technical Challenges. Stem Cell Reviews and Reports, 2017. **13**(3): p. 418-429.
78. Kashpur, O., et al., 17 - Induced pluripotent stem cells to generate skin tissue models, in Skin Tissue Models, A.P. Marques, et al., Editors. 2018, Academic Press: Boston. p. 399-419.
79. Papapetrou, E.P., Patient-derived induced pluripotent stem cells in cancer research and precision oncology. Nature medicine, 2016. **22**(12): p. 1392.
80. Esch, E.W., A. Bahinski, and D. Huh, Organs-on-chips at the frontiers of drug discovery. Nature Reviews Drug Discovery, 2015. **14**: p. 248.
81. Huh, D., G.A. Hamilton, and D.E. Ingber, From 3D cell culture to organs-on-chips. Trends in cell biology, 2011. **21**(12): p. 745-754.

11

Nederlandstalige samenvatting (Dutch Summary)

Curriculum Vittea

List of Publications



NEDERLANDSTALIGE SAMENVATTING

De huid

De huid is het grootste orgaan van het lichaam. Ondanks dat het een relatief dunne beschermlaag is, heeft het vele belangrijke functies. Dit zijn onder andere het beschermen van het lichaam tegen micro-organismen of allergenen, en het voorkomen van warmteverlies en uitdroging [1].

Barrière van de humane huid

De huid is opgebouwd uit drie verschillende lagen. Van binnen naar buiten zijn dit: het onderhuids vetweefsel, de lederhuid (dermis), en de opperhuid (epidermis) (**figuur 1 a**). Het onderhuids vetweefsel en de dermis zijn belangrijk voor de vitaliteit van de opperhuid. Deze zorgen namelijk voor het transport van voldoende voedingsstoffen naar de epidermis, het afvoeren van afvalstoffen uit de epidermis, en de communicatie met andere organen in het lichaam. In de dermis zijn de fibroblasten de belangrijkste en meest voorkomende cellen. De eiwitten van het extracellulaire matrix (ECM) vormen een groot en belangrijk component van deze laag [2]. Tussen de dermis en epidermis bevindt zich het basaalmembraan. De epidermis, die voornamelijk uit keratinocyten bestaat, vormt de belangrijkste barrière van de huid en is opgebouwd uit vier epidermale lagen zoals weergegeven in **figuur 1 b**. De onderste epidermale laag is het *stratum basale* (de basale cellaag), waar de celdeling oftewel de proliferatie plaatsvindt. De proliferatie van de huid is sterk gereguleerd, omdat de huid zich continue moet vernieuwen om de afschilfering van dode huidcellen aan het oppervlakte te compenseren [3]. De tweede laag is het *stratum spinosum*, waarin de keratinocyten beginnen met het differentiatieproces [4]. Deze differentiatie zet zich voort in het *stratum granulosum*. Karakteristiek voor deze epidermale laag is de aanwezigheid van granulen en lamellaire bodies [5]. Deze bevatten verschillende lipiden die belangrijk zijn voor de vorming van de buitenste, verhoornde laag van de huid, het *stratum corneum*. Deze epidermale laag is het eindproduct van het differentiatieproces. Aan het huidoppervlakte schilferen de verhoorden huidcellen af, wat gecompenseerd wordt met de vorming van een nieuwe cellaag in het *stratum corneum*. Daarnaast bevat de huid ook haarvaten, zweetklieren en talgklieren, maar deze dragen minder bij aan de huidbarrière.

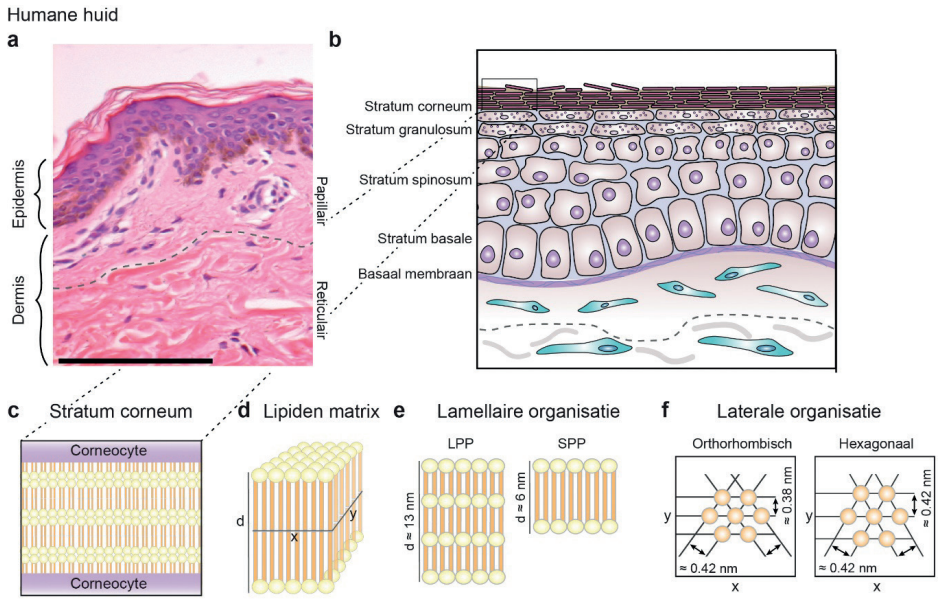
Het *stratum corneum* (afgekort tot SC) vormt veruit de sterkste barrière van de huid. De structuur van het SC kan vergeleken worden met een bakstenen muur, waar de corneocyten de bakstenen, en de lipiden het cement voorstellen [6, 7]. Dit betekent dat de corneocyten worden omsloten door een matrix van lipiden **(figuur 1 c)**. De lipiden matrix vormt een unieke en aaneengesloten structuur in het SC [8]. Dit is van belang voor het transport van geneesmiddelen door het SC die in een pleister, crème of zalf op de huid worden aangebracht.

De lipiden in het SC zijn zeer regelmatig gerangschikt **(figuur 1 d)** [9]. Ten eerste vormen de lipiden op elkaar gestapelde lagen. Deze structuur herhaalt zich over een bepaalde lengte, wat de repetitie afstand wordt genoemd. De stapeling van de lipiden wordt de lamellaire fase genoemd **(figuur 1 e)**. In het SC zijn er twee verschillende lamellaire fasen, namelijk de lange periodiciteit fase (LPP) en de korte periodiciteit fase (SPP). Ten tweede vormen de lipiden een organisatie met een bepaalde dichtheid, wat de laterale organisatie wordt genoemd **(figuur 1 f)**. Er zijn drie soorten structuren, welke variëren van een zeer dichte structuur naar een minder dichte structuur. Dit zijn de orthorhombische, hexagonale en de vloeibare laterale organisatie. Wetenschappelijke studies hebben aangetoond dat de functionaliteit van de huidbarrière afhankelijk is van de laterale en de lamellaire organisatie, die op hun beurt worden beïnvloed door de samenstelling van de lipiden [10].

De samenstelling van lipiden is onderverdeeld in hoofd- en subklassen [11]. De drie hoofdklassen zijn de ceramiden, de vrije vetzuren en het cholesterol. Deze hoofdklassen zijn aanwezig in ongeveer een gelijke molaire verhouding **(figuur 1 g)**. De molecuulstructuur van ceramiden bestaat uit een sphingoïde base gekoppeld aan een vetzuurketen. Omdat er verschillende typen sphingoïde basen en vetzuurketens zijn, bestaan er ook meerdere ceramide subklassen [12]. De vijftien meest voorkomende ceramide subklassen staan weergegeven in **figuur 1 g**. Daarnaast kan ook het aantal koolstofatomen variëren in zowel de sphingoïde base als in de vetzuurketen. Ook kunnen de koolstofketens dubbele bindingen bevatten, wat de mate van (on)verzadigdheid in de ceramiden bepaald. Dit resulteert in een groot aantal structuren binnen een ceramide subklasse. In de tweede belangrijke klasse, de vrije vetzuren, kunnen zowel het aantal koolstofatomen en de hoeveelheid aan dubbele bindingen variëren, wat resulteert in ruwweg drie verschillende vrije vetzuur subklassen **(figuur 1 g)**.

Humane huidequivalenten

Humane huidequivalenten zijn de meest geavanceerde modellen van de humane huid **(figuur 1 h)**. Ze lijken in veel aspecten op de humane huid en worden daarom voor een groot aantal toepassingen ingezet [14-19]. Voor fundamenteel onderzoek worden humane huidequivalenten gebruikt om de fysiologie en pathofysiologie van de huid (bijv. wondgenezing, huidveroudering, atopisch eczeem, psoriasis, huidkanker) beter te begrijpen [20, 21]. Ook kunnen ze ingezet worden voor preklinische studies om bijvoorbeeld nieuwe medicijnen te ontwikkelen en te testen. Daarnaast worden humane huidequivalenten ook gebruikt voor het testen van nieuwe cosmetica ingrediënten en het bepalen van het bijtend of irriterend vermogen van bepaalde chemicaliën. Tevens worden humane huidequivalenten gebruikt voor het vaststellen van de huidgevoeligheid voor sommige industriële materialen [22, 23].



Figuur 1 Aspecten van de morfologie en de lipiden barrière in de normale humane huid en in het humane huidequivalent. (a) Doorsnede van de humane huid. **(b)** Illustratie van de humane huid. De epidermale lagen, het basaalmembraan en de dermis zijn weergegeven. **(c)** Afbeelding van de lipiden matrix in het STRATUM CORNEUM (SC). **(d)** Driedimensionale structuur van de lipiden matrix. De gele cirkels geven de hydrofiele regionen weer en de oranje cilinders geven de hydrofobe regionen weer. **(e)** Schematische voorstelling van de lamellaire organisatie. De lange periodiciteit fase (LPP) en de korte periodiciteit fase (SPP) zijn weergegeven. **(f)** Laterale organisatie van de lipiden in het SC. De lipiden kunnen de meest compacte orthorhombische of de compacte hexagonale organisatie vormen.

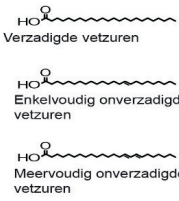
Er zijn een aantal soorten humane huidequivalenten ontwikkeld, waaronder de humane huidequivalenten van de Universiteit Leiden. Daarnaast worden ook verschillende humane huidequivalenten commercieel aangeboden. De verschillende soorten humane huidequivalenten zijn het epidermale model, het "full-thickness model" (FTM) bestaande uit een dermis en epidermis, en de geavanceerde humane huidequivalenten welke nog een extra celtype bevatten. Humane huidequivalenten bootsen veel eigenschappen van de humane huid nauwkeurig na, zoals de aanwezigheid van de vier epidermale lagen, de vorming van het basaalmembraan, en de aanwezigheid van fibroblasten met bijbehorend ECM-eiwitten in de dermis **(figuur 1 i)**. De SC lipiden in de humane huidequivalenten bestaan ook uit ceramiden, vrije vetzuren en cholesterol, wat leidt tot de vorming van lamellaire structuren [24]. Echter, er zijn ook verschillen tussen de humane huid en de humane huidequivalenten. Morfologisch gezien bevatten de humane huidequivalenten geen golvende structuren tussen de epidermis en dermis, is de celdeling verhoogd, bevinden de keratinocyten zich

g Lipiden samenstelling

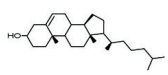
Ceramiden

	CER[non-EO]		CER[EO]	CER[O]
	Non-hydroxy vetzuur [N]	α-hydroxy vetzuur [A]	Esterificeerd ω-hydroxy vetzuur [EO]	ω-hydroxy vetzuur [O]
Dihydrosphingosine [dS]	[NdS]	[AdS]	[EOdS]	
Sphingosine [S]	[NS]	[AS]	[EOS]	[OS]
Phytosphingosine [P]	[NP]	[AP]	[EOP]	[OP]
6-hydroxy sphingosine [H]	[NH]	[AH]	[EOH]	[OH]

Vrije vetzuren

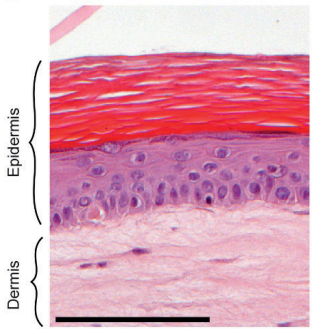


Cholesterol

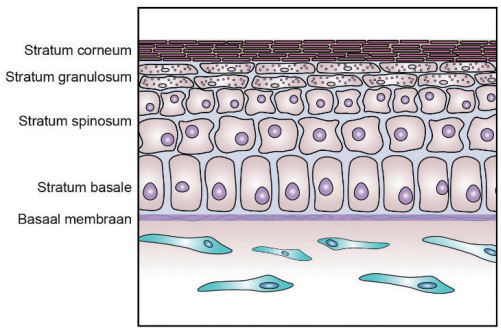


Humane huidequivalent

h



i



Figuur 1 Vervolg. **(g)** Samenstelling van de lipiden matrix met de hoofdklassen bestaande uit ceramiden, vrije vetzuren en het cholesterol. De ceramiden bestaan uit verschillende subklassen, weergegeven in een tabel op basis van de naamgeving volgens Motta *et al.* [13]. Structuurformules van de vrije vetzuren en het cholesterol zijn weergegeven. **(h)** Doorsnede van het humane huidequivalent. **(i)** Illustratie van het humane huidequivalent. Epidermale lagen, het basaalmembraan en de dermis zijn geïllustreerd. Schaal: 100µm.

in een geactiveerde staat en zijn de cellen van het *STRATUM GRANULOSUM* groter. Daarnaast functioneert de barrière van het humane huidequivalent niet zoals die van de humane huid. Uit recent onderzoek blijkt dat er verschillen zijn in de lipiden samenstelling en organisatie tussen de humane huidequivalenten en de humane huid [25, 26]. Dit betreft het profiel van de ceramide subklassen, een verhoogde aanwezigheid van ceramiden met korte koolstofketens, de verlaagde aanwezigheid van ceramiden met lange koolstofketens, en een verhoogde hoeveelheid ceramiden en vrije vetzuren met een enkelvoudig onverzadigde binding. Dit resulteert in een afwijkende lipidenorganisatie in het SC van humane huidequivalenten. De lipiden vormen een LPP met een kortere repetitie afstand, vormen geen SPP, en vormen voornamelijk de hexagonale laterale organisatie, in tegenstelling tot een orthorhombische laterale organisatie in het SC van de natieve humane huid. Deze veranderingen dragen bij aan een verminderde barrièrefunctie en dus een verhoogde diffusie van therapeutische moleculen door het SC en een verhoogd waterverlies. Dit kan mogelijk leiden tot misinterpretatie

van data tussen de humane huidequivalenten en de humane huid, wat kan leiden tot onder- of overschatting van therapeutische doseringen of toxiciteit van chemicaliën.

Doelstellingen

Het doel van het onderzoek beschreven in dit proefschrift is om de epidermale morfogenese en barrière vorming van de humane huidequivalenten te verbeteren, waardoor de barrière van de humane huid beter wordt nagebootst. In de beschreven studies worden geavanceerde technieken gebruikt om zowel de dermale als de epidermale morfogenese, SC lipiden samenstelling en organisatie, en functionaliteit van de barrière te onderzoeken. De doelstellingen van dit proefschrift zijn:

a) Onderzoeken of de dermale ECM de epidermale lipiden barrière kan beïnvloeden.
b) De celkweekcondities aanpassen met als doel de vorming van de lipiden huidbarrière tijdens het produceren van de humane huidequivalenten te verbeteren.
c) Gebaseerd op de uitkomsten van de voorgaande studies, de ontwikkeling van humane huidequivalenten waarin de verbeterde kweekcondities en optimale ECM leiden tot een verbeterde huid barrièrefunctie.

Deel I Optimalisatie van de dermale extracellulaire matrix in humane huidequivalenten

In deel I van het proefschrift zijn studies beschreven die geassocieerd zijn met de eerste doelstelling: "onderzoeken of de dermale ECM de epidermale lipiden barrière kan beïnvloeden". Het dermale compartiment van het FTM bestaat uit een collageen type I/III matrix waarin zich fibroblasten bevinden. Dit type ECM wordt vaak toegepast tijdens het kweken van orgaanmodellen, maar heeft een aantal nadelen waaronder de afkomst vanuit dierlijk materiaal en het ongecontroleerd krimpen van het collageen.

In **hoofdstuk 2** wordt het FTM (met collageen geïsoleerd uit rattenstaarten) vergeleken met een nieuw FTM, welke ontwikkeld is met humaan collageen in de dermis. Om dit te bewerkstelligen is een methode ontwikkeld om het humane collageen te isoleren. Vervolgens is dit collageen succesvol gebruikt voor de ontwikkeling van het humaan collageen full-thickness model (hC-FTM). Het nieuwe hC-FTM bevat een dermale matrix welke grote gelijkenissen vertoonde met die van het FTM. De morfologie, lipiden samenstelling, en lipiden organisatie waren vergelijkbaar met het FTM. Het ontwikkelde hC-FTM is daardoor een beter alternatief voor dierproeven dan het FTM, aangezien er geen dierlijk materiaal gebruikt wordt.

In **hoofdstuk 3** is een studie beschreven waarin het collageen (geïsoleerd uit rattenstaarten) gemengd wordt met het biopolymeer chitosan. Hierdoor is een nieuw type FTM ontwikkeld, welke het collageen-chitosan full thickness model (CC-FTM) is genoemd. In het CC-FTM was de verdeling van de fibroblasten en het genereren van het basaalmembraan niet verstoord door de aanwezigheid van chitosan. De epidermale morfogenese van het CC-FTM vertoonde grote gelijkenissen met die van de humane huid. Dit manifesteerde zich in een dunnere epidermis, normalisatie in celdeling en afwezigheid van een geactiveerde epidermis. De samenstelling van de ceramiden in het SC werd ook onderzocht. Zowel de ceramide koolstofketenlengte verdeling als de ceramide subklasse samenstelling leken meer op die van de humane huid in het CC-FTM dan in het FTM. Als gevolg van de verbetering in de lipiden samenstelling was ook de lipiden organisatie verbeterd en was het waterverlies door de huid verminderd, een aanwijzing dat de barrière functionaliteit in het CC-FTM is verbeterd.

Samenvattend, de studies beschreven in deel I laten zien dat de samenstelling van de dermis een belangrijke rol speelt in de epidermale morfogenese en barrière vorming van FTMs.

Deel II Optimalisatie van de celkweekcondities in humane huidequivalenten

In deel II staan studies beschreven die betrekking hebben op de tweede doelstelling: “de celkweekcondities aanpassen met als doel de vorming van de lipiden huidbarrière tijdens het produceren van de humane huidequivalenten te verbeteren”. In deze studies is er steeds één factor van de celkweekconditie gevarieerd tijdens het kweken van FTMs, om zo inzicht te verkrijgen in de bijdrage van elke specifieke parameter.

In **hoofdstuk 4** staan experimenten beschreven waarin de temperatuur tijdens de celkweek wordt onderzocht. De FTMs werden gekweekt bij lichaamstemperatuur (37°C) en bij lagere temperaturen, die beter de temperatuur van het huidoppervlak benaderden (35°C en 33°C). De FTMs werden geanalyseerd op morfologische eigenschappen en op lipiden en de daarmee samenhangende barrière karakteristieken tijdens een periode van vier weken. Een verlaging van temperatuur van 37°C naar 35°C leidde niet tot substantiële veranderingen. Echter, een verlaging van 37°C naar 33°C leidde tot een verandering in de epidermale morfogenese, wat zich manifesteerde in een dikkere epidermis, slechtere organisatie in de lagere epidermale lagen, en een verdikking van de granulaire cellen. Tevens werden kleine veranderingen in de samenstelling van de SC lipiden gevonden. De effecten van een verlaagde temperatuur waren vergelijkbaar na twee en na vier weken kweken, alhoewel het SC aanzienlijk dikker was na een langere celkweekperiode. Uit de resultaten van deze studie blijkt dat de temperatuur, een

invloed heeft op de morfogenetische eigenschappen en op de SC lipiden barrière vorming van het FTM.

Een andere belangrijke celkweekconditie is het zuurstofgehalte, wat beschreven staat in **hoofdstuk 5**. Om de invloed van het zuurstofgehalte op de morfogenese en SC lipiden van het FTM te onderzoeken, zijn 2D (monokweken van keratinocyten) en 3D (FTM) modellen geproduceerd met een zuurstofgehalte van 20% (normoxie, normale kweekconditie) of met een zuurstofgehalte van 3% (hypoxie). In de 2D en 3D modellen die gekweekt werden bij 3% zuurstof was het "hypoxia-inducible factor" (HIF) signaaltransductie mechanisme sterk geactiveerd. Dit werd aangetoond door een verhoogde expressie van een aantal genen die een belangrijke rol spelen in het metabolisme, waaronder pyruvaat dehydrogenase kinase (PDK-1), glucose transporter 1 (GLUT1), en vasculair endotheel groeifactor A (VEGFA). In het FTM geproduceerd met 3% zuurstof zijn er verbeteringen in de morfologie aangetoond, waardoor dit beter de humane huid nabootst. Deze veranderingen zijn de afname in dikte van de epidermis, reductie in celdeling, en een verbeterde structuur van de granulaire cellen. De samenstelling van SC lipiden was ook verbeterd en benaderde de ceramide samenstelling in humane huid beter. De studie die beschreven staat in **hoofdstuk 5** laat zien dat een lager zuurstofgehalte een positieve invloed heeft op de ontwikkeling van het FTM.

De invloed van relatieve luchtvochtigheid op de morfogenetische eigenschappen en lipidenbarrière karakteristieken van FTMs staat beschreven in **hoofdstuk 6**. Om dit te onderzoeken werden FTMs en CC-FTMs gekweekt bij een relatief luchtvochtigheidsgehalte van 90% en 60%. De morfologische eigenschappen werden het meest beïnvloed door een verlaging in relatieve luchtvochtigheid. De cellen van het *STRATUM GRANULOSUM* zijn vergroot, en de epidermis is meer geactiveerd. Een verandering van het relatieve luchtvochtigheidsgehalte leidde niet tot substantiële veranderingen in de lipidenbarrière karakteristieken van FTMs noch van CC-FTMs.

In **hoofdstuk 7** is een studie beschreven wat zich richtte op het effect van de afwezigheid van zonlicht tijdens het kweken van FTMs. Een van de belangrijkste effecten van zonlicht op de huid is de activatie van vitamine D. Om dit effect te imiteren werden FTMs geproduceerd met celkweekmedium wat verrijkt werd met een actieve vorm van vitamine D ($1,25(OH)_2D_3$). Deze toevoeging leidde tot activatie van het vitamine D signaaltransductie mechanisme in 2D en 3D modellen, waaronder een verhoogde expressie van een antibacterieel peptide (LL37). De toevoeging van $1,25(OH)_2D_3$ had geen invloed op de morfogenese, de ceramide subklassen samenstelling en de ceramide koolstofketenlengte verdeling Directe blootstelling van FTMs aan ultraviolet licht (UV) veranderde de morfologie en ceramiden samenstelling niet, alhoewel blootstelling aan een

hoge dosering UV-licht apoptose van de keratinocyten veroorzaakte. Hieruit blijkt dat een gebrek in blootstelling aan UV-licht in FTMs niet leidt tot een verandering in de barrière vorming van de huid.

Samenvattend, uit de studies in deel II blijkt dat een verandering in celkweekcondities direct de morfogenetische eigenschappen en lipiden barrière karakteristieken van FTMs kan beïnvloeden. De meest optimale omstandigheden voor de productie van FTMs de humane huid het best nabootsen zijn een temperatuur van 37°C, een zuurstofgehalte van 3%, en een luchtvochtigheidsgehalte van 90%. Optioneel kan er ook voor specifieke vraagstukken $1,25(OH)_2D_3$ toegevoegd worden aan het celkweekmedium.

Deel III Meervoudige combinaties om humane huidequivalenten te verbeteren

In deel III staan studies beschreven die geassocieerd zijn met de derde doelstelling: "Gebaseerd op de uitkomsten van de voorgaande studies, de ontwikkeling van humane huidequivalenten waarin de verbeterde kweekcondities en optimale ECM leiden tot een verbeterde huid barrièrefunctie". Om dit te realiseren is in hoofdstuk 8 de toevoeging van vrije vetzuren aan het celkweekmedium onderzocht. Vervolgens zijn in hoofdstuk 9 meervoudige veranderingen in kweekcondities gekozen om de optimale combinatie van het dermale ECM, de celkweekcondities, en het celkweekmedium te identificeren.

De studie beschreven in **hoofdstuk 8** richtte zich op de optimalisatie van de concentratie van het verzadigde vrije vetzuur palmitinezuur. In het onderzoek werd de concentratie van palmitinezuur (25 µM) verlaagd tot 10% en 1% van de originele hoeveelheid. In het FTM dat werd ontwikkeld met 1% palmitinezuur werden veranderingen in morfologie gevonden, waaronder een slechtere organisatie van de lagere epidermale lagen en een verhoging van de epidermale activatie. De samenstelling van de ceramiden en vrije vetzuren werd onderzocht. Deze werd niet beïnvloed door de hoeveelheid palmitinezuur in het medium. Tevens werd de absolute hoeveelheid ceramiden en vetzuren in de natieve humane huid en het FTM bepaald. Er werd een lagere absolute hoeveelheid vrije vetzuren in het SC van het FTM gevonden dan in het SC van de humane huid. Concluderend, deze studie toont aan dat de huidige toevoeging van vrije vetzuren aan het celkweekmedium adequaat de morfogenese en lipiden barrière vorming in het FTM ondersteunt.

Uit de voorgaande studies wordt een combinatie van veranderde kweekcondities gekozen, met als doel een FTM te ontwikkelen met een verbeterde morfologie en barrièrefunctie. Deze studie is beschreven in **hoofdstuk 9**. De veranderde kweekcondities zijn i) het modificeren van het dermale ECM met chitosan (hoofdstuk 3), ii) kweken met 3% zuurstof (hoofdstuk 5), en iii) het inhiberen

van de nucleaire receptor "liver X-receptor" (LXR) zoals beschreven door Helder *et al.* (nog niet gepubliceerd). Enkele combinaties van veranderde kweekcondities leiden tot een verdere verbetering van de morfogenese en lipidensamenstelling in het FTM waardoor de FTMs beter de eigenschappen van de humane huid nabootst. In meer detail zijn dit een vermindering in epidermale activatie, een lagere hoeveelheid van enkelvoudig onverzadigde ceramiden in het SC en een grotere fractie lipiden die een orthorhombische laterale organisatie vormen in het SC. Dit resulteerde in een verbetering in de barrière functionaliteit. Het CC-FTM gekweekt met inhibitie van de LXR imiteert de humane huid het beste. Dit type humane huidequivalent heeft daarom ook de grootste potentie voor toepassingen in studies naar nieuwe medicijnen die worden toegediend via de huid.

Kortom, de studies beschreven in deel III bevestigen het belang van een gebalanceerd celkweekmedium met een juiste hoeveelheid toegevoegde vrije vetzuren. Daarnaast is een combinatie van verbeterde celkweekcondities met een geoptimaliseerd celkweekmedium van cruciaal belang voor het creëren van humane huidequivalenten welke de humane huid het beste nabootsen. De nieuwe inzichten die in deel III zijn verkregen tonen ook de complexiteit aan van de optimalisatie van een *in vitro* gevormde kweekhuid. Een optimalisatie strategie waarbij verschillende factoren gecombineerd worden is een veelbelovende onderzoeksmethode, wat heeft geleid tot de ontwikkeling van humane huidequivalenten met verbeterde morfologie en lipide barrière eigenschappen.

Conclusies

In dit proefschrift worden studies beschreven met als doel een humane huidequivalent te ontwikkelen die beter de natieve humane huid nabootst. Dit resulteerde in humane huidequivalenten met een: veranderde dermale ECM, beter afgestemde celkweekcondities, en optimale combinatie van dermale ECM en kweekcondities. Uit deze studies blijkt dat verbeterde kweekcondities de morfologie en lipide barrière vorming in het humane huidequivalent verder kunnen verbeteren. Uit de studies blijkt ook de enorme complexiteit in de ontwikkeling van het humane huidequivalent en dat de verschillende cellulaire processen die hierbij betrokken zijn elkaar beïnvloeden. Belangrijke stappen zijn gezet in het begrijpen van deze processen en welke factoren een belangrijk rol spelen in de barrière vorming van lipiden. Het humane huidequivalent die het beste de humane huid nabootst betreffende de morfologie en lipide barrière vorming is het CC-FTM waarin de LXR werd geremd.

Referenties

1. Proksch, E., J.M. Brandner, and J.M. Jensen, The skin: an indispensable barrier. Experimental Dermatology, 2008. 17(12): p. 1063-1072.
2. Eckes, B., T. Krieg, and C.M. Niessen, Biology of the Skin, in Therapy of Skin Diseases: A Worldwide Perspective on Therapeutic Approaches and Their Molecular Basis. 2010, Springer: Berlin, Heidelberg, Germany. p. 3-14.
3. Blanpain, C. and E. Fuchs, Epidermal homeostasis: a balancing act of stem cells in the skin. Nature Reviews Molecular Cell Biology, 2009. 10: p. 207-217.
4. Simpson, C.L., D.M. Patel, and K.J. Green, Deconstructing the skin: cytoarchitectural determinants of epidermal morphogenesis. Nature Reviews Molecular Cell Biology, 2011. 12: p. 565.
5. Menon, G.K., S.E. Lee, and S.-H. Lee, An overview of epidermal lamellar bodies: Novel roles in biological adaptations and secondary barriers. Journal of Dermatological Science, 2018. 92(1): p. 10-17.
6. Michaels, A., S. Chandrasekaran, and J. Shaw, Drug permeation through human skin: theory and in vitro experimental measurement. AIChE Journal, 1975. 21(5): p. 985-996.
7. Elias, P.M., Epidermal lipids, barrier function, and desquamation. Journal of Investigative Dermatology, 1983. 80: p. S44-S49.
8. Bouwstra, J.A. and M. Ponec, The skin barrier in healthy and diseased state. Biochimica et Biophysica Acta - Biomembranes, 2006. 1758(12): p. 2080-2095.
9. Boncheva, M., The physical chemistry of the stratum corneum lipids. International Journal of Cosmetic Science, 2014. 36(6): p. 505-515.
10. Bouwstra, J.A. and G.S. Gooris, The lipid organisation in human stratum corneum and model systems. The Open Dermatology Journal, 2010. 4(1): p. 10-13.
11. van Smeden, J., et al., The important role of stratum corneum lipids for the cutaneous barrier function. Biochimica et Biophysica Acta - Molecular and Cell Biology of Lipids, 2014. 1841(3): p. 295-313.
12. Kihara, A., Synthesis and degradation pathways, functions, and pathology of ceramides and epidermal acylceramides. Progress in lipid research, 2016. 63: p. 50-69.
13. Motta, S., et al., Ceramide composition of the psoriatic scale. Biochimica et Biophysica Acta - Molecular Basis of Disease, 1993. 1182(2): p. 147-151.
14. Planz, V., C.-M. Lehr, and M. Windbergs, In vitro models for evaluating safety and efficacy of novel technologies for skin drug delivery. Journal of Controlled Release, 2016. 242: p. 89-104.
15. Mathes, S.H., H. Ruffner, and U. Graf-Hausner, The use of skin models in drug development. Advanced Drug Delivery Reviews, 2014. 69-70: p. 81-102.
16. Yun, Y.E., et al., Artificial skin models for animal-free testing. Journal of Pharmaceutical Investigation, 2018: p. 1-9.
17. Groeber, F., et al., Skin tissue engineering — In vivo and in vitro applications. Advanced Drug Delivery Reviews, 2011. 63(4): p. 352-366.
18. Niehues, H., et al., 3D skin models for 3R research: The potential of 3D reconstructed skin models to study skin barrier function. Experimental Dermatology, 2018: p. 501-511.
19. Rademacher, F., et al., Skin microbiota and human 3D skin models. Experimental Dermatology, 2018. 27(5): p. 489-494.
20. MacNeil, S., Progress and opportunities for tissue-engineered skin. Nature, 2007. 445: p. 874.
21. van Drongelen, V., et al., Reduced filaggrin expression is accompanied by increased Staphylococcus aureus colonization of epidermal skin models. 2014. 44(12): p. 1515-1524.
22. Gordon, S., et al., Non-animal models of epithelial barriers (skin, intestine and lung) in research, industrial applications and regulatory toxicology. Alternatives to Animal Experimentation : ALTEX 2015. 32(4): p. 327-378.
23. Bergers, L., et al., Immune-competent human skin disease models. Drug Discov Today, 2016. 21(9): p. 1479-1488.
24. Ponec, M., et al., Barrier function in reconstructed epidermis and its resemblance to native human skin. Skin Pharmacology Physiology, 2001. 14(Suppl. 1): p. 63-71.
25. Thakoersing, V.S., et al., Increased presence of monounsaturated fatty acids in the stratum corneum of human skin equivalents. Journal of Investigative Dermatology, 2013. 133(1): p. 59-67.
26. Thakoersing, V.S., et al., Unraveling barrier properties of three different in-house human skin equivalents. Tissue Engineering Part C: Methods, 2011. 18(1): p. 1-11.

Curriculum vitae

Arnout Mieremet was born in Delft, the Netherlands on August 25th 1990. After graduating from Christelijk Lyceum Delft in 2008, he started his study Bio-Pharmaceutical Sciences at Leiden University. After obtaining the Bachelor degree in 2011, he continued his master education in Bio-Pharmaceutical Sciences with the research track Biopharmaceutical Sciences and Drug Delivery. During his master, Arnout performed two internships, of which the first was performed at the department of Drug Delivery Technology of the Leiden Academic Centre for Drug Research under the supervision of Prof. J. Bouwstra. During this internship, he developed a barrier repair model using explant skin cultures and characterized the morphogenesis and lipid barrier formation. In addition, he determined whether knockdown of filaggrin affected the barrier in HSEs based on the N/TERT cell line. Arnout performed his second internship at the department of Pharmacy and Biotechnology at the University of Bologna under supervision of Prof. S. Spampinato. During this internship, he investigated the role of serotonin in astroglial cells in a cell-based model of neuropathic pain. He completed his master Bio-Pharmaceutical Sciences cum laude in 2014. He started his PhD in May 2014 at the department of Dermatology at the LUMC in collaboration with the department of BioTherapeutics at the LACDR under supervision of Prof. J. Bouwstra and dr. A. El Ghalbzouri, which resulted in this thesis. From May 2019 he started as postdoctoral associate in the lab of Dr. V. de Waard, department of Medical Biochemistry at the Amsterdam UMC, focusing on the development of *in vitro* models of the rare disease Marfan syndrome.

List of publications

Mieremet, A. and Helder, R., A. Nadaban, W. Boiten, G. Gooris, A. El Ghalbzouri, and J.A. Bouwstra. "Multitargeted optimization approaches of culture media and external factors improves morphogenesis and barrier formation in human skin equivalents." (*in preparation*).

Mieremet, A. and Helder, R., A. Nadaban, G. Gooris, J. A. Bouwstra, and A. El Ghalbzouri "Contribution of palmitic acid to epidermal morphogenesis and lipid barrier formation in human skin equivalents." (*submitted*).

Mieremet, A., W. Boiten, R. van Dijk, G. Gooris, H.S. Overkleeft, J.M.F.G. Aerts, J.A. Bouwstra, and A. El Ghalbzouri (2019). "Unravelling effects of relative humidity on lipid barrier formation in human skin equivalents."Archives of Dermatological Research (*in press*).

Mieremet, A., A. Vázquez García, W. Boiten, R. van Dijk, G. Gooris, J.A. Bouwstra, and A. El Ghalbzouri (2019). "Human skin equivalents cultured under hypoxia display enhanced epidermal morphogenesis and lipid barrier formation." Scientific Reports 9: 7811.

Mieremet, A., R. van Dijk, W. Boiten, G. Gooris, J.A. Bouwstra, and A. El Ghalbzouri (2019). "Characterization of human skin equivalents developed at body's core and surface temperatures." Journal of Tissue Engineering and Regenerative Medicine 13(7): 1122-1133.

Mieremet, A., R. van Dijk, G. Gooris, J. A. Bouwstra, and A. El Ghalbzouri (2019). "Shedding light on the effects of 1,25-dihydroxyvitamin D3 on epidermal lipid barrier formation in three-dimensional human skin equivalents." The Journal of Steroid Biochemistry and Molecular Biology 189: 19-27.

Mieremet, A., M. Rietveld, R. van Dijk, J. A. Bouwstra, and A. El Ghalbzouri (2018). "Recapitulation of Native Dermal Tissue in a Full-Thickness Human Skin Model Using Human Collagens." Tissue Engineering Part A 24(11-12): 873-881.

Mieremet, A., M. Rietveld, S. Absalah, J. van Smeden, J. A. Bouwstra, and A. El Ghalbzouri (2017). "Improved epidermal barrier formation in human skin models by chitosan modulated dermal matrices." PloS one 12(3): e0174478.

Danso, M. O., T. Berkers, **A. Mieremet**, F. Hausil, and J. A. Bouwstra (2015). "An *ex vivo* human skin model for studying skin barrier repair." Experimental dermatology 24(1): 48-54.

van Drongelen, V., M. O. Danso, A. Mulder, **A. Mieremet**, J. van Smeden, J. A. Bouwstra, and A. El Ghalbzouri (2014). "Barrier properties of an N/TERT-based human skin equivalent." Tissue Engineering Part A 20(21-22): 3041-3049.

van Drongelen, V., M. Alloul-Ramdhani, M. O. Danso, **A. Mieremet**, A. Mulder, J. van Smeden, J. A. Bouwstra, and A. El Ghalbzouri (2013). "Knock-down of filaggrin does not affect lipid organization and composition in stratum corneum of reconstructed human skin equivalents." Experimental Dermatology 22(12): 807-812.